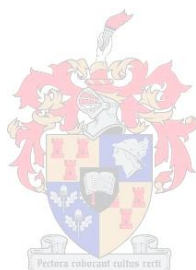# Computational study of anion-anion intermolecular interactions between I_3^- ions in the gas phase, solution and solid state

by
Ferdinand George Groenewald

Thesis presented in partial fulfilment of the requirements for the degree Master of Science in Chemistry at the University of Stellenbosch

Supervisor: Prof. Catharine Esterhuysen
Co-supervisor: Prof. Jan Dillen
Faculty of Science
Department of Chemistry & Polymer Science

December 2012

Declaration

By submitting this thesis/dissertation electronically, I declare that the entirety of the work contained therein is my own, original work, that I am the sole author thereof (save to the extent explicitly otherwise stated), that reproduction and publication thereof by Stellenbosch University will not infringe any third party rights and that I have not previously in its entirety or in part submitted it for obtaining any qualification.

December 2012

Abstract

A theoretical study of the I_3^- ion and $I_3^- \cdots I_3^-$ interactions within a dimer of ions was performed using various levels of theory and basis sets. Optimisations in the gas phase and in an implicit polarisable continuum solvent model with a variety of solvents showed that there is a significant dependence of the $I_3^- \cdots I_3^-$ interaction energy on the solvent used. We found that MP2/cc-pVTZ-pp was found to consistently outperform the other methods tested, yielding the most satisfactory results for the I-I bond length and the $I_3^- \cdots I_3^-$ intermolecular distance when compared to the calculated Cambridge Structural Database (CSD) averages (I-I bond length is 2.92 Å and $I_3^- \cdots I_3^-$ distance is 3.80 Å). Additionally, MP2/cc-pVTZ-pp yields results most comparable to the benchmark CCSD/aug-cc-pVTZ-pp//MP2/cc-pVTZ-pp $I_3^- \cdots I_3^-$ interaction energy. A total of 21 Density Functional Theory (DFT) functionals (4 GGAs, 11 Hybrid GGAs, 1 meta-GGA and 5 containing DFT-D2 corrections) were tested and compared to the calculated CSD averages and benchmark $I_3^- \cdots I_3^-$ interaction energy. Comparable results were relatively easily obtained for the geometrical parameters for a few DFT functionals, although only one single DFT functional did not underestimate the $I_3^- \cdots I_3^-$ interaction energy.

A substantial dependence of the $I_3^- \cdots I_3^-$ interaction energy and also the stabilisation provided by the solvent (ΔE_S) on the dielectric constant were observed. This could be seen in the potential energy surface (PES) in a number of solvents at various levels of theory.

Two other alternative stabilising electrostatic environments, namely the electric field and various crystal structure models, were tested yielding structures and energies that correlate to the previous results.

The $I^- \cdots I_2$ and $I_3^- \cdots I_3^-$ interactions were analysed utilising the Atoms in Molecules (AIM) theory where three properties (the electron density, the Laplacian of the electron density and also the total energy density) were investigated at particular critical points. The results for the $I^- \cdots I_2$ and $I_3^- \cdots I_3^-$ interactions are consistent with our other findings as well as work done by others.

The presence of the σ-hole at the tip of the I_3^- ion was identified when the electrostatic surface potential (ESP) was investigated. When the ESP of the σ-hole was analysed as a function of the surroundings the trend observed was consistent with our previously found results for the $I_3^- \cdots I_3^-$ interaction energy and ΔE_S. In addition, the electrostatic surface potential shows a direct relation to the $I_3^- \cdots I_3^-$ interaction energy and even more so to the stabilisation energy. The ESP of the σ-hole in *n*-methylformamide-mixture differs only 2 % from what is found in the solid state for the I_3^- ion. Furthermore, it was found that the surrounding cations in the solid state contribute approximately 10 kcal/mol of stabilisation over that of the *n*-methylformamide-mixture solvent.

Uittreksel

'n Teoretiese studie van die I_3^- ioon en $I_3^- \cdots I_3^-$ intermolekulêre interaksies is uitgevoer deur gebruik te maak van 'n verskeidenheid vlakke van teorie en basisstelle. Die optimiserings is uitgevoer in die gasfase asook in oplosmiddel, waar die oplosmiddel voorgestel word deur 'n implisiete kontinuum polariseerbare oplosmiddelmodel. 'n Aansienlike afhanklikheid van die $I_3^- \cdots I_3^-$ interaksie-energie op die oplosmiddel is waargeneem. Die MP2/cc-pVTZ-pp het die mees akkuraatste resultate gelewer vir die I-I bindingsafstand en die $I_3^- \cdots I_3^-$ intermolekulêre afstand wanneer dit vergelyk word met die berekende Cambridge Structural Database (CSD) gemiddeldes. MP2/cc-pVTZ-pp het ook die akkuraatste $I_3^- \cdots I_3^-$ interaksie-energie gelewer wanneer dit vergelyk word met die CCSD/aug-cc-pVTZ-pp//MP2/cc-pVTZ-pp maatstaf. Uit 21 digtheidsfunksionale teorie (DFT) funksionale (4 GGAs, 11 Hybrid GGAs, 1 meta-GGA met 5 wat die DFT-D2 korreksie inkorporeer) getoets, het daar net een (PBE-D2) vergelykbare resultate gelewer vir die $I_3^- \cdots I_3^-$ interaksie-energie, waar die ander DFT funksionale die interaksie-energie onderskat. Die DFT funksionale is meer suksesvol in die modellering van die geometriese parameters, naamlik die I-I bindingsafstand en die $I_3^- \cdots I_3^-$ intermolekulêre afstand, as die $I_3^- \cdots I_3^-$ interaksie-energie.

'n Aansienlike afhanklikheid is waargeneem vir die $I_3^- \cdots I_3^-$ interaksie-energie en die stabiliseringsenergie van die dielektriese konstante van die oplosmiddel. Hierdie afhanklikheid van die dielektriese konstante is ook geobserveer by 'n verskeidenheid vlakke van teorie wanneer daar na die potensiële energie oppervlak gekyk is.

Twee ander elektrostatiese omgewings is getoets, naamlik 'n elektriese veld asook verskeie kristal struktuurmodelle waar daar gevind was dat die resultate saamstem met ons ander bevindinge.

Die $I^- \cdots I_2$ en $I_3^- \cdots I_3^-$ interaksies is verder ondersoek deur gebruik te maak van die "Atoms in Molecules" teorie, waar daar na 3 eienskappe gekyk is naamlik die elektron digtheid, die Laplaciaan van die elektron digtheid en die totale energie digtheid by spesifieke kritieke bindingspunte. Ons resultate is in lyn met ons ander resultate, asook werk wat gedoen is deur ander.

Die "σ-hole" is geidentifiseer vir die I_3^- ioon dmv die analise van die elektrostatiese oppervlak potensiaal (EOP). Die elektrostatiese potentiaal van die oppervlak by die "σ-hole" het 'n aansienlike afhanklikheid op die dielektriese konstante getoon, maar is nogsteeds konsistent met die $I_3^- \cdots I_3^-$ interaksie-energie en die stabiliseringsenergie. Verder, het ons ontdek dat die EOP van die "σ-hole" in die kristal verskil maar net 2 % vanaf die "σ-hole" in die mees polêre

oplosmiddel getoets (*n*-metiel-formamied-mengsel), asook dat die kristal 10 kcal/mol meer stabilisering lewer as vir 'n enkele I_3^- ioon.

Acknowledgements

First and foremost, I would like to thank my highly skilled and wise supervisors, Prof. Catharine Esterhuysen and Prof. Jan Dillen for their guidance and support during the past two years. Thank you for always being there to answer all of my questions regarding the subject and helping me make sense of my results. I would also like to thank you for providing the necessary tools and computational resources enabling me to do the work shown in this dissertation, which would not have been possible otherwise.

I would like to extend my thanks to my family and friends for the support and for the countless philosophical discussions we had about my work. Furthermore, I would like to show my gratitude towards the Supramolecular Materials Chemistry group at the University of Stellenbosch for welcoming me to their group and the support they showed me during my MSc.

Finally, I would like to thank the University of Stellenbosch for providing the necessary facilities and the NRF for funding.

Publications and Posters

Publications

This study

Groenewald F, Esterhuysen C, Dillen J, Theo Chem Acc, *Extensive theoretical investigation: Influence of the electrostatic environment on the $I_3^- \cdots I_3^-$ anion-anion interaction*, In press, DOI: 10.1007/s00214-012-1281-0

Other work

Groenewald F, Dillen J, Struct Chem, *Conformational analysis of caprolactam, cycloheptene and caprolactone,* DOI 10.1007/s11224-011-9921-x

Groenewald F, Dillen J, Mateura M, Struct Chem, *A computational investigation of the effect of the double bond on the conformations of seven membered rings*, DOI 10.1007/s11224-012-0073-4

Conferences

This work was presented as a poster at Indaba 7 held in the Kruger National Park in 2012 entitled: *Computational investigation of $I_3^- \cdots I_3^-$ interactions*

Glossary

a-DZ	aug-cc-pVDZ-pp
AIM	Atoms in Molecules
a-TZ	aug-cc-pVTZ-pp
BCP	Bond Critical Point
BSSE	Basis set superposition error
cc	Correlation consistent
CC	Coupled Cluster
CP	Critical Points
CSD	Cambridge Structural Database
CT	Charge Transfer
CT-TBP	Charge transfer trigonal bipyramidal adducts
DZ	cc-pVDZ-pp
DFT	Density Functional Theory
dTZ	Def2-TZVP
$d(I_3^- \cdots I_3^-)$	$I_3^- \cdots I_3^-$ Intermolecular distance
E_C	Correlation energy
ECP	Electrostatic Core Potential
E_{INT}	$I_3^- \cdots I_3^-$ interaction energy
ESP	Electrostatic Surface Potential
E_{XC}	Exchange-correlation energy
E_X	Exchange energy
GEA	Gradient Expansion Approximation
GGA	Generalised Gradient Approximation
GTO	Gaussian Type Orbitals
HF	Hartree-Fock
IEF-PCM	Integral equation formalism polarisable continuum model
MP2	Møller-Plesset 2nd order perturbation theory
PES	Potential energy Surface
PCM	polarisable continuum model
pp	pseudo potentials
QM	Quantum Mechanics

SAS	Surface Analysis Suite
STO	Slater Type Orbitals
TZ	cc-pVTZ-pp
vdW	van der Waals
WFT	Wave Function Theory
ΔE_S	Stabilisation Energy

Table of Contents

CHAPTER 1

Introduction

1.1. Background on the I_3^- ion

Triiodides exist in the solid state and in solution as approximately linear molecules which can be symmetric or asymmetric depending on the surroundings. They can generally be formed by mixing an iodide salt (e.g. CsI) with iodine crystals (I_2), similarly to the rest of the polyiodide family where one polyiodide can consist of up to 27 iodine atoms [1-3]. Triiodides are generally found to be disordered in the solid state and it has been suggested that this disorder may even be dynamic [2, 4]. Due to hypervalency, triiodide or more generally trihalogen (X_3^-) systems, violate the Lewis octet rule. As a result, particular interest has been shown towards these ions in a number of molecular orbital studies found in the literature [5-7]. The bonds found in I_3^- have been referred to as "secondary bonds", since they are longer (3 - 4 Å) than a normal I_2 covalent bond (2.72 Å). The I_3^- ion itself is formed by a dative bond formed between the I^- and I_2 fragment, sometimes referred to as a charge-transfer complex [8]. In a theoretical study on the bonding of the I_3^- ion Kloo, Rosdahl and Svensson [8] pointed out that the triiodide ion can either by centrosymmetric with an I-I bond length of 2.91 Å, or has asymmetric I-I bond lengths which range from 2.85 Å to 3.00 Å, i.e. less than the sum of the van der Waals (vdW) radius of iodine of 4.3 Å. The authors came to the conclusion that the formation of these I-I bonds in the I_3^- ion can be adequately described in terms of intramolecular bonding with additional dispersion interactions between the I_2 and I^- fragments. They also noted that when the I_2 and I^- are separated by less than 4 Å, there is a significant overlap in electron density. Part of their study looked at the potential energy surface (PES) where they found that the preferred structure for I_3^- in the gas phase is centrosymmetric ($D_{\infty h}$). To our knowledge, probably the only gas phase data available for the I_3^- ion was obtained by Topol in 1971 [9], where the author managed to obtain a heat of formation for the I_3^- ion in the gas phase, with a value of -24 kcal/mol, while later in 1973, Downs and Adams deduced a similar value, -25 kcal/mol, for the formation energy of triiodide ion in the gas phase [10].

Nuclear Quadrupole Resonance experiments performed by Harada and co-workers [11] to analyse the triiodide ion's charge distribution in various crystals showed that the symmetric I_3^- ion also has a symmetrical charge distribution where the charges are approximately -0.5 e and 0.08 e on the terminal and central iodine atoms, respectively. They also found that when the triiodide is asymmetric the terminal iodine furthest away from the central iodine has the highest charge.

In 1978 Datta and co-workers [12] carried out a theoretical study on I_3^- by constructing a flexible counterion framework and studying its effects. They showed that the I_3^- ion is

symmetric in the gas phase and in solution, where the solution was simulated by constructing a flexible counterion framework. Furthermore, symmetric and asymmetric rigid counterion frameworks were also investigated, to simulate a crystalline environment, where they found the I_3^- ion to be symmetric or asymmetric depending on the symmetry of the framework. Interestingly, the authors pointed out that there is a decrease in the bond length of the I_3^- ion when it is placed in a symmetric flexible framework. They concluded that the I_3^- ion is basically symmetric unless the surroundings induce asymmetry.

Another theoretical investigation [13] mentioned that the asymmetry found in linear anions is strictly related to the surrounding cation distribution in the solid state. Furthermore, the authors pointed out that the orbitals of an I^- ion are stabilised differently by the surrounding cation distributions, thus influencing its donor abilities and explaining the asymmetry present in the solid state. This also explains why there is such a wide range of bond lengths observed for the I_3^- ion in the solid state. Also, previous work has shown that the PES of the $I_2 \cdots I^-$ interaction is very flat and that a small amount of energy is needed to change the bond length [14]. Novoa *et al.* [5] performed a theoretical study investigating the stability of trihalogen systems in the presence of neighbouring cations utilising *ab initio* methods, where they concluded that all the X_3^- ions have $D_{\infty h}$ symmetry and are stable against dissociation into I^- and I_2 fragments.

A UV-Vis study [15] showed that solvent selection has a significant influence on the electronic transition energies of trihalides including the I_3^- ion ($\sigma_g \rightarrow \sigma_u^*$ and $\pi_g \rightarrow \sigma_u^*$). These transition energies decrease as the donor ability of the solvent increases either due to the destabilisation of the ground state (σ_g or π_g) or the stabilisation of the excited state (σ_u^*). Gabes and Stufkens [16] conducted a UV-Vis study where it was shown that the observed electronic transitions can be assigned to the symmetry or asymmetry of the trihalide ions in the solid state or solution. They pointed out that some bands appear weaker in the solution spectra when compared to solid state spectra, due to a lowering of symmetry which occurs in the solid state. Myers [17] performed a study, in 1958, on the kinetics of the I_3^- ion in aqueous solution utilising ^{127}I NMR. He found that the quadrupole couplings are so strong that the iodine resonance line is broadened to such an extent that it is undetectable. Unfortunately, no I_3^- dimer formation was reported. Sato *et al.* [18] found that the free-energy profile of the I_3^- ion in acetonitrile is similar to that found in the gas phase, consistent with experimental results. They did, however, mention that this free-energy profile changes drastically in aqueous solution with an enhanced probability of finding geometries of lower symmetry. An investigation studying the Raman spectra of triiodide ions in solution showed that when the iodide concentration is increased, a peak at 155 cm^{-1} is observed. The presence of this peak

indicates the presence of higher polyiodides, and not the asymmetry of the triiodide ion [3]. In 2007 Clark and co-workers [19] proposed the existence of a "σ-hole" on halogen atoms induced by a partially occupied p-orbital, which creates a positive electrostatic potential at the tip of the halogen atom. This was proven shortly afterwards in an overview paper written by Politzer and co-workers [20]. It has been shown that the surface potential at the σ-hole plays an important role in formation of the σ-hole bond. Furthermore, the directional nature of the halogen bonding caused by σ-holes indicate an electrostatic origin [21]. Halogen bonding has been detected in solution using NMR showing that the solvent has a significant influence on the strength of this intermolecular interaction [22, 23].

Several theoretical studies have been done on electrostatic and dispersion bound complexes where a dependence of the intermolecular interaction on the solvent used was noted. Furthermore, all of these studies obtained consistent results regarding the dependence of the strength of a dimer's intermolecular interaction on the solvent [24-29]. In an extensive review article on the polyiodide series [1] it was shown that the average bond length and $I_3^-\cdots I_3^-$ intermolecular distance are 2.92 Å and ≥3.6 Å, respectively, for approximately 500 triiodides. Since this study was conducted the structures of approximately 280 triiodides added to the Cambridge Structural Database (CSD) have also been found agree with the results obtained by Svensson & Kloo. We note, however, that the calculated average I-I bond length for the I_3^- ion utilising the CSD data, agrees with the postulate of Slater [30] based on experimental data, made in 1959, where he argued that there is a critical I-I bond length for the I_3^- ion, 2.92 Å. This is identical to the evidence we obtained for over 700 triiodides in the solid state.

Several theoretical studies of the I_3^- ion in gas phase and solution have, however, yielded different results. One study using the PW91 functional with various basis sets in the gas phase calculated bond lengths equal to and greater than 2.97Å [31]. Other studies found the optimised bond lengths for the I_3^- ion in the gas phase at the HF, MP2, CCSD, CCSD(T) CISD and QCISD(T) levels of theory to be 2.965, 2.943, 2.964, 2.982, 2.979 and 3.002 Å, respectively [8, 18, 32].

Some crystals contain one-dimensional $[I_3^-]_\infty$ chains, with the $I_3^-\cdots I_3^-$ intermolecular distances in the range of 3-4 Å [8] which have been shown to possess interesting properties such as conductivity. This was verified by a theoretical study performed by Alvarez, Novoa and Mota, who proposed mechanisms for the electric conductivity along these $[I_3^-]_\infty$ chains. One method they suggested was ion migration along the chains, which requires little activation since the ions propagate relatively easily through the chain. The authors further pointed out that the hypervalency in I_3^- facilitates ion migration [4]. Another study by Forsyth *et al.* [33]

showed that polyiodides can be used as doping agents for an insulating polymer matrix, where in some cases only the I_3^- ion acts as the conducting species.

As can be seen from previous work discussed in this section, a large amount of theoretical and experimental work has been done on the I_3^- ion in solution and in the gas phase, where the $I_2\cdots I^-$ intramolecular interaction was subject to investigation. However, we observe in the solid state [2] that these I_3^- ions exhibit the ability to form long linear $[I_3^-]_\infty$ chains, but to our knowledge, no theoretical investigation has been conducted on the nature and origin of these $I_3^-\cdots I_3^-$ interactions present between the triiodide ions in the solid state. Furthermore, no adequate theoretical methods have been identified to model these $I_3^-\cdots I_3^-$ interactions.

1.2. Overview of theoretical methods

In this section we will briefly point out some important points within the Density Functional Theory (DFT) theory. Also, we will briefly look at the most simplistic Wave Function Theory (WFT) method, HF, to point out fundamental differences between the two theories. All of the following equations and explanations used for the DFT and HF explanations are taken from ref. [34]. A brief overview of the basis sets used in this thesis is also included in order to point out significant differences. Most of the basis set theory was taken from ref. [35]. Other overviews include an introduction to the solvent model used, how computational performance of a method is measured, the DFT dispersion problem, the electrostatic surface potential and the Atoms in Molecules theory.

1.2.1. Quantum mechanics (QM) overview

The goal of most quantum mechanical approaches is the approximate solution of the time-dependent, non-relativistic Schrödinger equation:

$$\hat{H}\Psi_i(\vec{x}_1, \vec{x}_2, \dots \vec{x}_n, \vec{R}_1, \vec{R}_2, \dots \vec{R}_M) = E\Psi_i(\vec{x}_1, \vec{x}_2, \dots \vec{x}_n, \vec{R}_1, \vec{R}_2, \dots \vec{R}_M) \qquad \text{(eq. 1)}$$

with $\hat{H}$ as the Hamilton operator for a molecule consisting of M nuclei, and n electrons in a vacuum with no external magnetic or electric fields present. The *x* vectors define 3N spatial coordinates and the N spin coordinates of all the electrons and the R vectors define 3M spatial coordinates of the nuclei.

The Hamilton operator yields all the needed information to obtain the total energy of a molecule, and consists of:

$$\hat{H} = -\frac{1}{2}\sum_{i=1}^{N}\nabla_i^2 - \frac{1}{2}\sum_{A=1}^{M}\frac{1}{M_A}\nabla_A^2 - \sum_{i=1}^{N}\sum_{A=1}^{M}\frac{Z_A}{r_{iA}} + \sum_{i=1}^{N}\sum_{j>1}^{N}\frac{1}{r_{ij}} + \sum_{A=1}^{M}\sum_{A>B}^{M}\frac{Z_a Z_b}{R_{AB}} \qquad \text{(eq. 2)}$$

Kinetic Energy of the electrons (*N*) and nuclei (*M*)

Potential Energy: Electrostatic electron-nucleus (N-M), electron-electron (N-N), nuclei-nuclei (M-M) interactions

5

Here, A and B run over the M nuclei, while i and j denote the number of N electrons in the molecule. M_A is the mass of nucleus A as a multiple of the mass of an electron, since the equations in this discussion have been simplified by applying the system of atomic units to appear in a compact form. Equation 2 can be simplified by applying the *Born-Oppenheimer* approximation, where the positions of the nuclei are kept fixed in space, thus making the kinetic energy of the nuclei zero and as a result the potential energy of the nuclei-nuclei repulsion is merely a constant. Thus, it reduces to the electronic Hamiltonian:

$$\hat{H}_{elec} = -\frac{1}{2}\sum_{i=1}^{N}\nabla_i^2 - \sum_{i=1}^{N}\sum_{A=1}^{M}\frac{Z_A}{r_{iA}} + \sum_{i=1}^{N-1}\sum_{j>1}^{N}\frac{1}{r_{ij}} = \hat{T} + \hat{V}_{Ne} + \hat{V}_{ee} \qquad \text{(eq. 3)}$$

This means that the solution of the Schrödinger equation when the electronic Hamiltonian is applied to the electronic wave function Ψ_{elec} is E_{elec}. Since the nuclear repulsion term is not explicitly part of the electronic Hamiltionian, it should be added to E_{elec} to give E_{tot}.

To summarise:

$$\hat{H}_{elec}\Psi_{elec} = E_{elec}\Psi_{elec}$$

and

$$E_{tot} = E_{elec} + E_{nuc}$$

The electronic wave function itself is not an observable; only if the square of the wave function is taken does it represent the probability of finding electrons $1, 2…$N simultaneously in a volume defined by $d\vec{x}_1 d\vec{x}_2 … d\vec{x}_N$,

$$|\Psi(\vec{x}_1, \vec{x}_2, … \vec{x}_N)|^2 d\vec{x}_1 d\vec{x}_2 … d\vec{x}_N \qquad \text{(eq. 4)}$$

The integration of eq. 4 over a full range of variables should be equal to 1, for it to be normalised, implying that the probability of finding an electron at any point in space should be equal, resulting in

$$\int … \int |\Psi(\vec{x}_1, \vec{x}_2, … \vec{x}_N)|^2 d\vec{x}_1 d\vec{x}_2 … d\vec{x}_N = 1 \qquad \text{(eq. 5)}$$

This brings us to the variational principle, where in order to solve $\hat{H}_{elec}$ specifically for a particular molecule, the part of the Hamiltonian that will vary as the molecule changes has to be identified. If we inspect eq. 3, we see that the number of electrons, N, and the attractive electrostatic interactions of the electrons with the nuclei, M, is given by the $\hat{V}_{Ne}$ operator. The $\hat{V}_{Ne}$ term is also termed as the external potential ($\hat{V}_{ext}$) in DFT. The external potential is not always limited to the nuclear field, but may include other external fields such as magnetic or electric fields. The kinetic energy operator ($\hat{T}$) and the electron-electron repulsion potential energy operator ($\hat{V}_{ee}$) are independent of the molecule under investigation.

The variational principle enables one to systematically approach the wave function of the ground state Ψ_0 to obtain the lowest energy (E_0) for a molecule. This means that a trial wave function (Ψ_{trial}) is generated, where an appropriate operator is applied which will yield an

6

energy (E_{trial}). Naturally, this implies that $E_{trial} > E_0$. The goal is to get as close as possible to the ground state wave function, resulting in the lowest energy for a molecule.

This can be mathematically represented as:

$$\langle \Psi_{trial} | \widehat{H} | \Psi_{trial} \rangle = E_{trial} \geq E_0 = \langle \Psi_0 | \widehat{H} | \Psi_0 \rangle$$

1.2.2. Hartree-Fock (HF)

As mentioned above, a trial wave function has to be constructed in order to obtain the wave function of the ground state (Ψ_0), so that the ground state energy (E_0) can be approximated. But in order to do so, a starting point has to be obtained. Since this is WFT, this is done by approximating the N-electron wave function by an antisymmetrised product of N one-electron wave functions $\chi_i(\vec{x}_i)$, which is usually called the Slater determinant, Φ_{SD}:

$$\Psi_0 \approx \Phi_{SD} = \frac{1}{\sqrt{N!}} \begin{vmatrix} \chi_1(\vec{x}_1) & \chi_2(\vec{x}_1) \dots & \chi_N(\vec{x}_1) \\ \chi_1(\vec{x}_2) & \chi_2(\vec{x}_2) & \chi_N(\vec{x}_2) \\ \vdots & \vdots & \vdots \\ \chi_1(\vec{x}_N) & \chi_2(\vec{x}_N) & \chi_N(\vec{x}_N) \end{vmatrix}$$

This equation simplifies to the product of the diagonal elements:

$$\Phi_{SD} = \frac{1}{\sqrt{N!}} det\{\chi_1(\vec{x}_1)\, \chi_2(\vec{x}_2) \dots \chi_N(\vec{x}_N)\}$$

The one electron functions $\chi_i(\vec{x}_i)$ are called spin orbitals; these spin orbitals exist as spatial orbitals ($\phi(\vec{r})$) that have either an α(s) or β(s) spin function.

$$\chi(\vec{x}_i) = \phi(\vec{r})\sigma(s); \ \sigma = \alpha, \beta$$

The spin functions are defined to be orthonormal, while the spin orbitals are also chosen to be orthonormal.

$$\mathrm{E}_{HF} = min_{\Phi_{SD} \to N} E[\Phi_{SD}]$$

$$\mathrm{E}_{HF} = \langle \Phi_{SD} | \widehat{H} | \Phi_{SD} \rangle = \sum_i^N \left(i \big| \widehat{h} \big| i \right) + \frac{1}{2} \sum_i^N \sum_j^N (ii|jj) - (ij|ji)$$

The HF method will not be discussed in full, due to the length of the mathematics, however it is based on an iterative process (self-consistent field procedure) to determine the energy of the set of orbitals.

The basic difference between HF and DFT is that HF calculates the energy from orbitals, whereas DFT calculates the energy as a function of the electron density. This means that in order to obtain the minimum energy, different approximations have to be made for each method. In addition, HF can quickly become computationally very expensive if there is an increase in the number of electrons. Since WFT generates a wave function from orbitals, and

the basis sets determine the size of the wave function, a high basis set dependence can be expected for WFT methods. This makes basis set selection an important aspect. The HF potential does not cover electron correlation (dispersion interactions). Electron correlation is the interaction between instantaneous dipoles, created by fluctuations in the electron density, yielding a stabilising effect. Koch and Holthausen mention that when HF is considered pictorially, the electrons often get too close to one another, since HF treats the electrostatic interactions as an average. As a result, the electron-electron repulsion is too large, resulting in E_{HF} always being larger than E_0.

1.2.3. Density Functional Theory (DFT)

One of the main mathematical concepts of density functional theory is where a number (E_{trial}) is assigned to a function (Ψ_{trial}), this is then called a functional.

A functional, *F[f(x)]*, uses a function, *f(x)*, as input which then yields a number (*a*) as output:

$$F[f(x)] \rightarrow a \qquad \text{(eq. 6)}$$

The aim is to minimise the functional, i.e. E[Ψ], by searching through all possible N electron wave functions that are acceptable and get as close as possible to E_0. For a wave function to be acceptable and to ensure these functionals makes physical sense, it has to be continuous everywhere and quadratically integrable. This can be represented mathematically by:

$$E_0 = \min_{\Psi \rightarrow N} E[\Psi] = \min_{\Psi \rightarrow N} \langle \Psi | \hat{T} + \hat{V}_{Ne} + \hat{V}_{ee} | \Psi \rangle \qquad \text{(eq. 7)}$$

From eq. 4, which gives the probability of finding an electron in a defined volume, the electron density is defined by integrating over the spin coordinates and over all electrons, but only one of the spatial variables,

$$\rho(\vec{r}_1) = N \int \dots \int |\Psi(\vec{x}_1, \vec{x}_2, \dots \vec{x}_N)|^2 dx_1 d\vec{x}_2 \dots d\vec{x}_N \qquad \text{(eq. 8)}$$

$\rho(\vec{r}_1)$ determines the probability of finding an electron (of the N electrons) within $d\vec{r}_1$ space with N-1 electrons having arbitrary positions and spin in the state represented by the wave function (Ψ). The $\rho(\vec{r}_1)$ is actually the probability density, but it is common practice to call it the electron density. However, since electrons are indistinguishable, the probability of finding an electron would be N times the probability of finding one particular electron. It is clear that the electron density is either positive or zero in space, thus making it a non-negative function. As a result, the following equations apply.

$$\rho(\vec{r}_1 \rightarrow \infty) = 0$$

$$\int \rho(\vec{r}_1) \, d\vec{r}_1 = N$$

The first theorem that made way for modern day density functional theory, is the Hohenberg-Kohn theorem. This theorem proved that the external potential, $\hat{V}_{ext}(\vec{r})$, is a unique functional

8

of $\rho(\vec{r})$, and since $\hat{V}_{ext}(\vec{r})$ fixes $\hat{H}$ (see eq.3) we see that the ground state of a molecule is a unique functional for $\rho(\vec{r})$.

Kohn-Sham density functional theory is widely used for self-consistent-field calculations. In this theory only the exchange-correlation energy (E_{XC}), which is the sum of the exchange energy (E_X) and the correlation energy (E_C) as a functional of the electron spin densities $n_\uparrow(\mathbf{r})$ and $n_\downarrow(\mathbf{r})$ must be approximated. Most DFT functionals employ the Generalised Gradient Approximation (GGA) which can be generically written as:

$$E_{xc}^{GGA}[\rho_\uparrow, \rho_\downarrow] = \int f(\rho_\uparrow, \rho_\downarrow, \nabla\rho_\uparrow, \nabla\rho_\downarrow) \, d\vec{r}$$

$$E_{xc}^{GGA} = E_x^{GGA} + E_c^{GGA}$$

The exchange energy is also formally defined as the Fermi hole function, which is the hole in the probability density of electrons due to the Pauli principle, and applies to electrons with the same spin. This means that this function integrates to the probability distribution of N-1, since there is one electron, with a particular spin, occupying a point in space, thus the Fermi hole would always have a negative charge. The exchange energy, which is described by the Fermi hole function, accounts for interactions that are electrostatic in nature. This applies to hydrogen bonding and halogen bonding, for example. The correlation energy is a result for electrons of either spin, defined by the Coulomb hole function. The Coulomb hole refers to electrons interacting with antiparallel spin, resulting in the Coulomb hole having no charge. The correlation functional describes the weaker, van der Waals type interactions. GGA is an improvement on the gradient expansion approximation (GEA), which is shown to apply to systems where the electron density is not uniform, but varying slowly. What GGA does is apply restrictions on the GEA method, that are valid for true Fermi and Coulomb holes. So, if the GEA exchange hole (Fermi hole) violates the requirement of being negative at any point in space, it is set to zero. To correct the sum rule behaviour of GEA, the exchange holes are truncated to having one electron charge, and the correlation holes (Coulomb holes) are truncated to having zero electron charge.

So usually when one selects a functional, the exchange and correlation functionals can be chosen independently from each other, e.g. BLYP, where the B (Becke) functional describes the exchange energy (E_X) and the LYP (Lee-Yang-Parr) correlation energy (E_C). This splits the functional into two different functionals that separately truncate cases that violate the exchange and correlation sum rule behaviour.

Another type of DFT functional is the Hybrid density functional, where the E_X and E_C contributions are scaled by a parameter (λ), where λ is between 0 and 1, thus determining which hole contributes the most to the total energy. One of the most popular hybrid

9

functionals is known as the B3LYP functional [36-38]. It is also called a hybrid functional due to the fact that the functional has an exchange functional consisting of a pure DFT exchange and an exact Hartree-Fock exchange.

It should be pointed out that we are dealing with mathematically complex constructs which have been chosen such that boundary conditions are satisfied and the results obtained are satisfactory. In other words, the actual mathematics used does not aid in the understanding of the physics these functionals are trying to describe. Rather, the physics are modelled utilising mathematical equations such that the desired boundary conditions are met.

1.2.4. Basis sets

Basis sets are used to describe the orbitals at particular points in space that coincide with atoms, which if bonded contribute to the molecular orbitals. Thus the larger the basis set, the better representation is given of all the orbitals in a molecule; so naturally, if the basis is small, the representation of the molecular orbitals is poorer. Ideally, one would use an infinite number of basis functions to describe each atom, however this is impossible in actual calculations. The type of basis functions used influences the accuracy. The better a selected basis function can reproduce an unknown function, the fewer basis functions are then needed to yield an accurate result.

The most popular functions used to describe orbitals are the Gaussian Type Orbitals (GTO), derived from Slater type orbitals (STO) and written as follows for Cartesian coordinates:

$$\chi_{\zeta,l_x,l_y,l_z}(x,y,z) = Nx^{l_x}y^{l_y}z^{l_z}e^{-\zeta r^2}$$

N is the normalisation constant and l_x, l_y and l_z determine the type of orbital

(e.g. $l_x + l_y + l_z = 0$ an s-orbital). The smallest number of functions that can be used to describe the electrons in an atom is called the minimum basis set, which consists of a single basis function for each of the orbitals, e.g. the hydrogen atom would have a single *s*-function. An improvement on this is the double-zeta basis sets, which will have two basis functions representing each orbital, e.g. the hydrogen atom would now be represented by two *s*-functions (1s and 1s'). The improvement on the double-zeta is the triple-zeta, which consists of three times the number of basis functions than the minimum basis set.

There are also polarisation functions that can be added to these basis sets to increase the accuracy. Consider for example H-CN, where the orbitals making up the C-H bond are an s-orbital for H and the s- and p_z orbitals for C. In order to increase the accuracy of the C-H bond, a basis function has to be added that will enable a change in the electron distribution of the C-H bond. This is done by adding a p-function to the H atom, more specifically, a p_z

function. This addition of a 'p$_z$-orbital' to the hydrogen atom will enable the electron density on H to be polarised along the C-H bond, thus yielding a better description of the bond. This example illustrates the polarisation of the s-orbital(s). This can also be applied to other orbitals, e.g. p-orbitals can be polarised by d-orbitals, and d-orbitals can be polarised by f-orbitals, etc.

If large atoms are under investigation, i.e. atoms larger than krypton, effective core potential (ECP) or pseudopotential type basis sets are employed to decrease the computational cost.

In this study we used three types of basis sets and will briefly discuss each:

1.2.4.1. Pople-style basis sets

Different types of Pople-style basis sets exist, however, we will only briefly discuss the basis set that was used in this study and what the notation means. In this dissertation, the 6-311G** basis set was utilised.

The number 6 indicates that the core electrons are represented by six primitive Gaussian type orbitals. The number 311 indicates that the valence electrons are split into three, i.e. a triple split valence basis which is represented by 3, 1 and 1 primitive GTOs. The ** indicates that two polarisation functions are used, one where p-functions are added to hydrogen atoms and the other being the addition of d-functions to heavier atoms.

1.2.4.2. Correlation consistent (cc) basis set

The cc-type basis sets were initially designed by Dunning; these basis sets were modified for larger atoms in 2003 [39], where pseudo potentials (pp) were introduced, also referred to as containing effective core potentials (ECP).

These basis sets have ECPs for large atoms and are geared towards recovering the correlation energy of the valence electrons. Several different cc basis sets are available and are known by their acronyms: cc-pVDZ-pp, cc-pVTZ-pp, cc-pVQZ-pp, cc-pV5Z-pp, cc-pV6Z-pp (correlation consistent polarised Valence Double/Triple/Quadruple/Quintuple/Sextuple Zeta pseudopotentials). The pseudopotential functional only applies to the inner electrons and is given by:

$$V_{PP}(\boldsymbol{r}) = -\frac{Q}{r} + \sum_{ljk} B_{lj}^{k} \exp(-\beta_{lj}^{k} r^2) P_{lj}$$

where Q is the inner-core charge and the sum is over Gaussian expansion (index k) of semilocal short-range radial potentials, which are different for different orbital angular-momentum quantum numbers l. For a given l the j is given by $\pm \frac{1}{2}$. P_{lj} is the projector onto the complete space of functions with angular symmetry l,j around a core under investigation.

11

The constants B_{lj}^k and β_{lj}^k are adjusted by a least-squares fit so that V_{PP} yields results as close as possible to the all-electron reference data [39]. Additional diffuse functions (basis functions with small exponents) can be added (indicated with the *aug-* prefix) and are important if loosely bound electrons are present, e.g. in the study of anions.

1.2.4.3. The def2-TZVP basis set

The def2-TZVP basis set consists of contracted GTOs. This basis set has a slightly modified ECP obtained from LanL2DZ. The 'def' is an abbreviation for default and the 'def2' is a slightly modified/improved basis set of the same type. The TZV indicates that it is a triple zeta valence quality basis set, while the P indicates that a polarisation function has been added [34].

1.2.5. Implicit solvent model

There are two main types of solvent models developed in recent decades, which are the continuum solvent models and the discrete solvent models. In this dissertation a continuum solvent model was employed. The continuum models treat the solvent as a continuum, where the solute is placed in a cavity and then surrounded by a uniform non-directional distribution of point charges. The solvent model used here falls under the apparent surface charge (ASC) category [40]. The polarisability of the solvent is indicated by the dielectric constant (ε), which is a unique macroscopic property of the solvent. There are a few possible variations on the size of the cavity and the reaction field. In this study the Integral Equation Formalism Polarisable Continuum Model (IEF-PCM) was used, where the cavity is generated by overlapping spheres, see ref. [34].

1.2.6. Performance

The performance of a theoretical model, DFT or WFT, is usually investigated by subjecting the method to a variety of tests. Different methods yield different accuracies for different tests.

These tests include:

- Comparison of molecular structures and vibrational frequencies;
- Relative Energies and Thermochemistry;
- Electric properties;
- Magnetic Properties;
- Hydrogen bonds and weakly bound systems;
- Chemical reactivity: exploring the potential energy surface.

In our study of the I_3^- ion and the $I_3^- \cdots I_3^-$ interaction, we are particularly interested in the molecular structure and also the interaction energies various methods yield for these anion-anion interactions, and we will thus use these aspects as tests for the accuracy of the methods investigated.

In general in the field of theoretical chemistry, the more expensive a method is, the higher the accuracy thereof. The crucial task in computational chemistry is to find a compromise between computational cost and the accuracy obtained. Theoretical methods are usually compared to the most accurate method available, which is also the most expensive method: the CCSD(T) method which is a WFT method, which has been referred to as the "gold standard" [41]. Since WFT methods are referred to as *ab initio* methods, where *ab initio* translates to "from scratch", they are generally expected to outperform DFTs, since DFTs are parameterised and thus inherently 'biased'.

1.2.7. The DFT dispersion energy problem

Dispersion interactions, also referred to as London forces, are weak long range intermolecular interactions that are a result of electron correlation. This correlation between the electron densities of neighbouring molecules induces an instantaneous dipole moment. These interactions are always present, since they are a result of electrons of the opposite spin interacting. These forces are known to be purely quantum mechanical. Dispersion is known to be a non-local interaction, which makes it extremely difficult, if not impossible, for DFT functionals to model it correctly, seeing that density functional theory has local exchange and correlation functionals. The correlation functional, which 'accounts' for the dispersion type interactions, is considered to be mathematically local, since it describes properties local to the molecule or atom.

13

1.2.8. Electrostatic surface potential (ESP)

The WFA Surface Analysis Suite (SAS) software package [42] describes the electrostatic potential on the surface of a molecule, where the surface is defined at an electron density of $\rho(\mathbf{r}) = 0.001$ a.u. as proposed by Bader *et al.* [43, 44] such that it contains 95-98 % of a molecule's electron density and 97 % of a molecule's electronic charge [45, 46]. The electrostatic potential created by the nuclei and electrons of a molecule at any point **r** is given by

$$V\left(r\right) = \sum_A \frac{Z_A}{|R_A - r|} - \int \frac{\rho(r')dr\prime}{r' - r}$$

where Z_A is the charge on the nucleus A, located at $\mathbf{R}_A$, and $\rho(\mathbf{r})$ is the molecule's electron density. The authors mention that V(**r**) is a physical observable and can be obtained experimentally by diffraction methods [46]. They also mention that in order to predict interactive behaviour V(**r**) has to be analysed at a defined surface, referred to as $V_S(\mathbf{r})$. The most positive (least negative) and least positive (most negative) values, are defined as $V_{S,\,MAX}$ and $V_{S,\,MIN}$, respectively. For further details see ref. [42-44, 46].

1.2.9. Atoms in Molecules (AIM)

In 1987 Bader [47] published a paper entitled "Atoms in molecules" where he explains AIM and the accuracy thereof. He postulated that an approximate quantum mechanical state function not only gives the energy of a given molecular structure, it also "contains the necessary information to both define the atoms in a molecule and determine their average properties." The state functions also indicate where electronic charge is locally concentrated and depleted. The author mentions that a postulate of quantum mechanics is that the value of a physical quantity can be obtained by applying a corresponding operator to the state function. Thus quantum mechanics is concerned with observables that can be obtained by applying a particular operator (which corresponds to a particular physical property) to a state function. The 'sharp' or 'average' values some observables yield are dependent on the nature of the state function, so that the change in these observables with time is given by what is called a Heisenberg equation of motion. The theorems in quantum mechanics (the virial theorem and Ehrenfest relations) are derived from this equation and relate various average values. Furthermore, in his paper Bader answers the question "Are there atoms in molecules?", where he explains how this is defined using the state function to partition a molecule into subsystems. We will only briefly highlight a few points to serve as background to our AIM results.

The gradient vector ($\nabla\rho$) is the first derivative of the electron/charge density and describes the change in the electron density; the nature and value of the gradient vector are used to define the quantum subsystem (splitting the molecule into atoms). The zero flux surface is when the gradient vector of the charge density yields a scalar product equal to zero with the unit vector of the electron density. The zero flux surface partitions the system (molecule) and or charge distribution into atoms (subsystems). Also, if the zero flux line passes through a point where $\nabla\rho = 0$, it is called a *critical point* (3, -1), where the 3 indicates the rank/dimension, i.e. 3D, and "-1" indicates that the point is at a 2D maximum and 1D minimum (-1 + -1 + 1 = -1). The "-1" can be pictured as the summation of the sign (-1 or +1) of the three second derivatives of the electron density (one for each dimension), where +1 indicates a minimum and -1 indicates a maximum if the second derivative is considered. See Fig. 1.1.
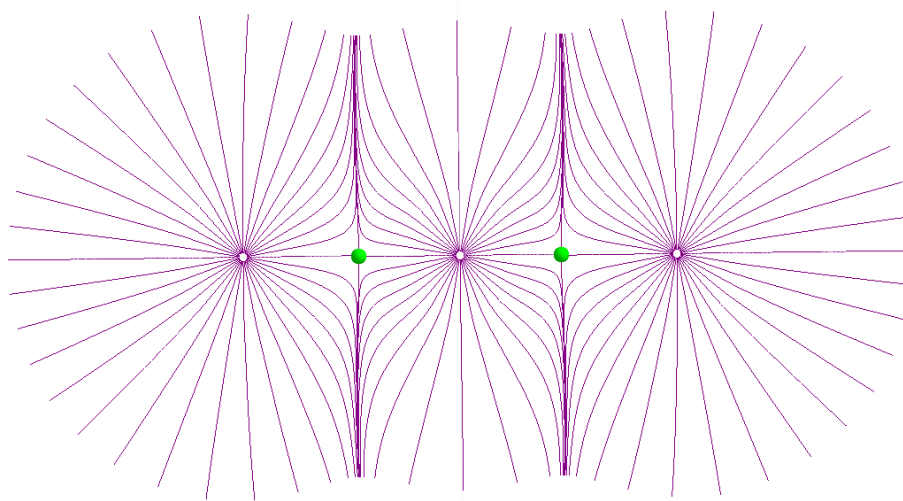
Fig. 1.1 – Illustration of the gradient pathways for the I_3^- ion in the gas phase at the MP2/a-TZ level of theory with the (3, -1) critical points shown in green. This figure shows that all the gradient pathways terminate at the nucleus (nuclear attractors) shown as white dots.

The two BCPs shown in Fig. 1.1 can be seen as 1D minima, positioned along the bond path, between two atoms.

There are four critical points with rank three [48]. They are:

(3, -3)   All curvatures of the electron density are negative indicating a local
                 3D maximum;

(3, -1)   Two curvatures are negative, indicating a 2D-maximum, while one is positive
                 and showing a 1D minimum perpendicular to the associated plane defined by
                 the negative curvatures;

(3, +1)   Two curvatures are positive, i.e. a 2D-minimum while one curvature is
                 negative at a 1D maximum;

(3, +3)   All three curvatures are positive at a local 3D-minimum.

The nucleus of an atom is defined by a local 3D maximum, since the electron density decreases as one moves away from the position of the nucleus in any direction. This also means that all the nearby gradient paths terminate at the nucleus. Nuclei are referred to as nuclear attractors (NA) with a critical point defined by (3, -3), and there is only one attractor per atomic basin which defines the atoms in 3D space.

A molecular bond is defined by a pathway of maximum electron density between nuclei and is called *bond path*, where the local minimum on that line between the bonded nuclei is called a *bond critical point* (BCP), which is defined by a critical point (3, -1). Furthermore, ring critical (3, +2) points and cage critical (3, +3) points also exist but will not be discussed since they are not relevant to this study. Bader concluded: "…the theory now offers the possibility of relating the properties of atoms to the properties of their bonds." (see ref.[47] and references therein)

The Laplacian is the second derivative of the electron density and indicates where the electron density is locally depleted and concentrated. The Laplacian is given by:

$$L(\boldsymbol{r}) = -\frac{1}{4}\nabla^2\rho(\boldsymbol{r}) \tag{5}$$

This definition of the Laplacian was chosen since at $\nabla^2\rho(\boldsymbol{r}) < 0$, the electron density is concentrated at point **r**, and where $\nabla^2\rho(\boldsymbol{r}) > 0$, the electron density is depleted [48]. If $L(\boldsymbol{r})$ is at a maximum, the electron density is also at a maximum.

An essay written by Bader and co-workers (see [49] and references therein) entitled "Chemical bonding: From Lewis to Atoms in Molecules" raises a few interesting issues which we will briefly highlight. They mention that there are three terms which account for the bonding present between atoms: electron-electron, nuclear-nuclear and electron-nuclear electrostatic forces, which are the only forces present within a field-free molecule. They quoted Lennard-Jones and Pople by saying that the only source of attraction between two atoms is the force between the electrons and nucleus. Furthermore, the authors point out that there are three destabilising terms that counteract the stabilising electron-nucleus interactions: 1) nucleus-nucleus repulsion 2) electron-electron repulsion and 3) the kinetic energy of the electrons increasing in the formation of a chemical bond. Thus the forces responsible for binding can be explained by the Feynman and Ehrenfest theorems where the former describes the forces acting on the nuclei and the latter describes the forces acting on the electrons. Bader and co-workers also mention that the bond energy for a diatomic molecule over a range of intermolecular separations is a result of the attractive Feynman forces acting on the nuclei. Furthermore they quote Feynman: "It becomes clear why the strongest and most important

attractive forces arise when there is a concentration of charge between two nuclei." Chemical bonding can therefore be seen as a result of overall attractive electrostatic forces exerted on the nuclei by the electron density accumulated between the nuclei. Bader and co-workers concluded that "The consequences of the accumulation of density in the binding region on the total energy and its kinetic and potential contributions are fully accounted for by the virial and the Feynman and Ehrenfest force theorems."

1.3. Aims

Although the $I_3^- \cdots I_3^-$ interaction has been referred to as a weak interaction [5-7, 18, 31, 50-54], to our knowledge there have been no studies regarding the qualitative or quantitative nature of this interaction. Therefore, the aim of this study is to understand the driving force behind the formation of $[I_3^-]_\infty$ chains by finding a global energy minimum for a pair of I_3^- ions in a variety of environments. A further aim is to study the effect a non-directional electrostatic environment (solvent) and a directional electrostatic environment (crystalline environment) have on the geometry of the I_3^- ion, the $I_3^- \cdots I_3^-$ intermolecular distance and the $I_3^- \cdots I_3^-$ interaction strength. Furthermore, it is important to find suitable computational methods that could reproduce experimental structural properties of the I-I bond length and $I_3^- \cdots I_3^-$ intermolecular distance averages, as well as the $I_3^- \cdots I_3^-$ interaction energy as calculated at the CCSD/a-TZ//MP2/TZ level of theory.

Additionally, the aim is also to compare the implicit solvent model and the solid state as electrostatic environments and study the influences they might have on the I_3^- ion at a wide variety of levels of theory. In particular, an attempt will be made to quantify the differences between these two electrostatic environments and to investigate the possible presence of $I_3^- \cdots I_3^-$ interactions in the solid state to determine how favourable these $I_3^- \cdots I_3^-$ interactions possibly are. Method dependence of the relevant parameters will also investigated and compared, in order to verify observed trends.

In Chapter 2 a description will be given of the methodologies used, while the results of modelling the I_3^- ion and the I_3^- dimer utilising a variety of methods and basis sets in the gas phase and in several solvents will be given in Chapter 3. Alternative electrostatic environments to the implicit solvent model are utilised in Chapter 4 to investigate their effects on the optimised structures of the I_3^- ion and I_3^- dimer. In Chapter 5 the electrostatic surface potential of the I_3^- ion is investigated and correlated to the calculations done in solution. Three properties of the AIM theory are utilised in Chapter 6 to characterise and correlate the $I_2 \cdots I^-$ and the $I_3^- \cdots I_3^-$ interactions at various levels of theory to the work described in this dissertation, as well as by others. In Chapter 7 a crystalline electrostatic environment is

studied by means of analysing the electrostatic surface potential of the I_3^- ion and comparing it to what was found in solution. Furthermore, analyses of three AIM parameters of the I_3^- ion and I_3^- dimer in a crystal were compared to solution. In the final chapter, we conclude and list possible future work based on the results given in this dissertation.

References

1.   Svensson, P.H. and L. Kloo, *Synthesis, Structure, and Bonding in Polyiodide and Metal Iodide−Iodine Systems.* Chemical Reviews, 2003. **103**(5): p. 1649-1684.

2.   Allen, F., *The Cambridge Structural Database: a quarter of a million crystal structures and rising.* Acta Crystallographica Section B, 2002. **58**(3 Part 1): p. 380-388.

3.   Loos, K.R. and A.C. Jones, *Structure of triiodide ion in solution. Raman evidence for the existence of higher polyiodide species.* The Journal of Physical Chemistry, 1974. **78**(22): p. 2306-2307.

4.   Alvarez, S., J. Novoa, and F. Mota, *The mechanism of electrical conductivity along polyhalide chains.* Chemical Physics Letters, 1986. **132**(6): p. 531-534.

5.   Novoa, J.J., F. Mota, and S. Alvarez, *Structure and stability of the X3- systems (X = fluoride, chloride, bromide, iodide) and their interaction with cations.* The Journal of Physical Chemistry, 1988. **92**(23): p. 6561-6566.

6.   Gabes, W. and M.A.M. Nijman-Meester, *Semiempirical molecular orbital calculation of symmetrical trihalide ions.* Inorganic Chemistry, 1973. **12**(3): p. 589-592.

7.   Tasker, P.W., *A calculation of the electronic states of the trihalide anions.* Molecular Physics, 1977. **33**(2): p. 511-518.

8.   Kloo, L., J. Rosdahl, and Per H. Svensson, *On the Intra- and Intermolecular Bonding in Polyiodides.* European Journal of Inorganic Chemistry, 2002. **2002**(5): p. 1203-1209.

9.   Topol, L.E., *Thermodynamic studies in the tetramethylammonium iodide-polyiodide and tetraethylammonium iodide-polyiodide systems.* Inorganic Chemistry, 1971. **10**(4): p. 736-740.

10.   Downs AJ, A.G., in *Comprehensive Inorganic Chemistry*, E.H. Bailor JC, Nyholm R, Trotman-Dickenson AF, Editor 1973, Pergamon: Oxford.

11.   Harada, H., D. Nakamura, and M. Kubo, *Nuclear quadrupole resonance of iodine in some polyiodides.* Journal of Magnetic Resonance (1969), 1974. **13**(1): p. 56-67.

12.   Datta, S.N., C.S. Ewig, and J.R. Van Wazer, *The geometric and electronic structures of I3− and I5− from effective-potential calculations.* Journal of Molecular Structure, 1978. **48**(3): p. 407-416.

13.   Manca, G., A. Ienco, and C. Mealli, *Factors Controlling Asymmetrization of the Simplest Linear I3– and I42– Polyiodides with Implications for the Nature of Halogen Bonding.* Crystal Growth & Design, 2012. **12**(4): p. 1762-1771.

14.   Aragoni, M.C., et al., *Adducts of S/Se Donors with Dihalogens as a Source of Information for Categorizing the Halogen Bonding.* Crystal Growth & Design, 2012. **12**(6): p. 2769-2779.

15.   Detellier, C. and P. Laszlo, *Solvent effect on the electronic transitions of the triiodide anion.* The Journal of Physical Chemistry, 1976. **80**(22): p. 2503-2506.

16.   Gabes, W. and D.J. Stufkens, *Electronic absorption spectra of symmetrical and asymmetrical trihalide ions.* Spectrochimica Acta Part A: Molecular Spectroscopy, 1974. **30**(9): p. 1835-1841.

17.   Myers, O.E., *Kinetics of the Triiodide Equilibrium.* The Journal of Chemical Physics, 1958. **28**(6): p. 1027-1029.

18.   Sato, H., F. Hirata, and A.B. Myers, *Theoretical Study of the Solvent Effect on Triiodide Ion in Solutions.* The Journal of Physical Chemistry A, 1998. **102**(11): p. 2065-2071.

19.   Clark, T., et al., *Halogen bonding: the σ-hole.* Journal of Molecular Modeling, 2007. **13**(2): p. 291-296.

20.   Politzer, P., et al., *An overview of halogen bonding.* Journal of Molecular Modeling, 2007. **13**(2): p. 305-311.

21.   Mohajeri, A., A.H. Pakiari, and N. Bagheri, *Theoretical studies on the nature of bonding in σ-hole complexes.* Chemical Physics Letters, 2009. **467**(4–6): p. 393-397.

22.   Metrangolo, P., et al., *Perfluorocarbon–hydrocarbon self-assembly: Part 16. 19F NMR study of the halogen bonding between halo-perfluorocarbons and heteroatom containing hydrocarbons.* Journal of Fluorine Chemistry, 2002. **114**(1): p. 27-33.

23.   Bertrán, J.F. and M. Rodríguez, *Detection of halogen bond formation by correlation of proton solvent shifts. 1. Haloforms in n-electron donor solvents.* Organic Magnetic Resonance, 1979. **12**(2): p. 92-94.

24.   Aquino, A.J.A., et al., *Solvent Effects on Hydrogen BondsA Theoretical Study.* The Journal of Physical Chemistry A, 2002. **106**(9): p. 1862-1871.

25.   Lu, Y., et al., *Effects of solvent on weak halogen bonds: Density functional theory calculations.* International Journal of Quantum Chemistry, 2012. **112**(5): p. 1421-1430.

26.   Gora, R.W., et al., *Intermolecular interactions in solution: Elucidating the influence of the solvent.* The Journal of Chemical Physics, 2004. **120**(6): p. 2802-2813.

27.   Cammi, R., F.J.O. del Valle, and J. Tomasi, *Decomposition of the interaction energy with counterpoise corrections to the basis set superposition error for dimers in*

solution. Method and application to the hydrogen fluoride dimer. Chemical Physics, 1988. **122**(1): p. 63-74.

28.   Contador, J.C., et al., *A theoretical study of hydrogen-bonded complexes in solution: BSSE and decomposition of interaction energy.* Journal of Molecular Structure: THEOCHEM, 1994. **314**(1–2): p. 229-239.

29.   Riley, K.E., J. Vondrasek, and P. Hobza, *Performance of the DFT-D method, paired with the PCM implicit solvation model, for the computation of interaction energies of solvated complexes of biological interest.* Physical Chemistry Chemical Physics, 2007. **9**(41): p. 5555-5560.

30.   Slater, J., *Note on the interatomic spacings in the ions, I3-, FHF.* Acta Crystallographica, 1959. **12**(3): p. 197-200.

31.   Md Asaduzzaman, A. and G. Schreckenbach, *Computational study of the ground state properties of iodine and polyiodide ions.* Theoretical Chemistry Accounts: Theory, Computation, and Modeling (Theoretica Chimica Acta), 2009. **122**(3): p. 119-125.

32.   Danovich, D., J. Hrušák, and S. Shaik, *Ab initio calculations for small iodo clusters. Good performance of relativistic effective core potentials.* Chemical Physics Letters, 1995. **233**(3): p. 249-256.

33.   Forsyth, M., et al., *Conductivity percolation in polyiodide/polymer complexes.* Chemistry of Materials, 1993. **5**(8): p. 1073-1077.

34.   Koch W, H.M., *A Chemist's guide to Density Functional Theory.* Vol. 1. 2000: Wiley-VCH.

35.   Frank, J., *Introduction to Computational Chemistry*1999: Wiley.

36.   Becke, A.D., *Density-functional thermochemistry. III. The role of exact exchange.* The Journal of Chemical Physics, 1993. **98**(7): p. 5648-5652.

37.   Lee, C., W. Yang, and R.G. Parr, *Development of the Colle-Salvetti correlation-energy formula into a functional of the electron density.* Physical Review B, 1988. **37**(2): p. 785-789.

38.   Miehlich, B., et al., *Results obtained with the correlation energy density functionals of becke and Lee, Yang and Parr.* Chemical Physics Letters, 1989. **157**(3): p. 200-206.

39.   Peterson, K.A., et al., *On the Spectroscopic and Thermochemical Properties of ClO, BrO, IO, and Their Anions.* The Journal of Physical Chemistry A, 2006. **110**(51): p. 13877-13883.

40.   Tomasi, J., B. Mennucci, and R. Cammi, *Quantum Mechanical Continuum Solvation Models.* Chemical Reviews, 2005. **105**(8): p. 2999-3094.

41. Riley, K.E., et al., *Stabilization and Structure Calculations for Noncovalent Interactions in Extended Molecular Systems Based on Wave Function and Density Functional Theories.* Chemical Reviews, 2010. **110**(9): p. 5023-5063.

42. Bulat FA, T.-L.A., *WFA: A suite of programs to analyse wavefunctions*: unpublished.

43. Bader, R.F.W., W.H. Henneker, and P.E. Cade, *Molecular Charge Distributions and Chemical Binding.* The Journal of Chemical Physics, 1967. **46**(9): p. 3341-3363.

44. Bader, R.F.W., et al., *Properties of atoms in molecules: atomic volumes.* Journal of the American Chemical Society, 1987. **109**(26): p. 7968-7979.

45. Murray JS, P.P., *Molecular Surfaces, van der Waals Radii and Electrostatic Potentials in Relation to Noncovalent Interactions.* Croatia Chemica Acta, 2009. **82**: p. 267-275.

46. Bulat, F., et al., *Quantitative analysis of molecular surfaces: areas, volumes, electrostatic potentials and average local ionization energies.* Journal of Molecular Modeling, 2010. **16**(11): p. 1679-1691.

47. Bader, R.F.W., *Atoms in molecules.* Accounts of Chemical Research, 1985. **18**(1): p. 9-15.

48. Bader, R.F.W., *Atoms in Molecules*, in *Encyclopedia of Computational Chemistry*, A.N. Schleyer PvR, Kollman PA, Clark T, Schaefer HFS, Gasteiger J, Schreiner PR, Editor 1998, Wiley-VCH: Chichester. p. 64-87.

49. Bader, R.F.W., Hernández-Trujillo J, Cortés-Guzmán F, *Chemical bonding: From Lewis to Atoms in Molecules.* Journal of Computational Chemistry, 2006. **28**: p. 4-14.

50. Gomes, A.S.P., et al., *The electronic structure of the triiodide ion from relativistic correlated calculations: A comparison of different methodologies.* The Journal of Chemical Physics, 2010. **133**(6): p. 064305-12.

51. Saethre LJ, G.O., Sletten J, *Structure and Bonding in Linear Polyiodine Compounds. A Theoretical Investigation.*, in *Acta Chemica Scandinavica*1988. p. 16-26.

52. Starikov, E.B., *Polyiodide chains in crystalline organic iodides: Ab initio Hartree–Fock crystal orbital study.* International Journal of Quantum Chemistry, 1997. **64**(4): p. 473-479.

53. Sharp, S.B. and G.I. Gellene, *Ab Initio Calculations of the Ground Electronic States of Polyiodide Anions.* The Journal of Physical Chemistry A, 1997. **101**(11): p. 2192-2197.

54. Brown, R. and E. Nunn, *The effect of ionic lattices on the electronic structures of polyatomic ions. I. The triiodide ion.* Australian Journal of Chemistry, 1966. **19**(9): p. 1567-1576.

CHAPTER 2

Methodology

2.1. Modelling of the I_3^- ion and $I_3^- \cdots I_3^-$ in the gas phase and in an implicit solvent model

All calculations were performed with the Gaussian 09 rev. B.01 package [1]. All the basis sets used for the calculations were downloaded from the EMSL database [2, 3]. Wave function theory (WFT) geometry optimisations were performed for the I_3^- ion and the I_3^- dimers using 2nd-order Møller-Plesset Perturbation theory, MP2 [4, 5] in combination with the def2-TZVP (dTZ) [6], aug-cc-pVTZ-pp (a-TZ), cc-pVTZ-pp (TZ), aug-cc-pVDZ-pp (a-DZ) and cc-pVDZ-pp (DZ) basis sets [7]. All of these basis sets include an electrostatic core potential (ECP) for iodine to decrease the cost of computation and take relativistic effects into account. The Hartree-Fock (HF) interaction energies were obtained by using the MP2 optimised geometry with the same basis set. All calculations were either performed in the gas phase or in an implicit solvation model, the polarisable continuum model [8, 9]. Additional coupled cluster with single and double excitations (CCSD) [10] geometry optimisations were performed for the I_3^- ion in the gas phase and implicit solvent model.

All calculations at the CCSD level of theory for the I_3^- dimer were done as single-point calculations using optimised geometries at the MP2/a-TZ level of theory for the gas-phase and in ethanol (ε=24.852) and water (ε=78.3553). Additional CCSD single-point calculations were performed using optimised geometries at the MP2/TZ level of theory in chloroform (ε=4.7113), ethanol (ε=24.852), water (ε=78.3553) and n-methylformamide-mixture (ε = 181.56). The CCSD/a-TZ//MP2/TZ single point calculations were performed to calculate the $I_3^- \cdots I_3^-$ interaction energy. We did attempt to perform geometry optimisations at the CCSD/a-TZ level of theory for the I_3^- dimer in chloroform, ethanol, water and n-methylformamide-mixture, however our resources were insufficient to allow the calculation to run to completion. Counterpoise corrections [11, 12] were done only for the gas-phase optimisations. We did not apply this basis set superposition error (BSSE) correction (1.38 kcal/mol for CCSD/a-TZ//MP2/a-TZ) to the solvated ions due to the spurious nature of the stationary point in the gas phase and the magnitude of the $I_3^- \cdots I_3^-$ interaction energy (see Section 3.1.2 & 3.1.3). The only stationary point found in the gas phase was at the MP2/a-TZ level of theory, which is considered to be an artefact since it severely overestimates the $I_3^- \cdots I_3^-$ interaction energy in solution. This means that the accuracy of the counterpoise corrections at this point is questionable and since counterpoise corrections cannot be performed when using a PCM model, it was decided not to apply this spurious correction to other methods and basis sets.

DFT geometry optimisations were performed in gas-phase and implicit solvent model using the PBE [13, 14], wB97X [15], wB97XD [16], B971[17], B97D [18], BP86 [19, 20], B3LYP [21-23], TPSS [24], BLYP [19, 22, 23], PBE0 (PBE1PBE) [25], M06 [26], M06-HF [26],

24

M06-2X [27], LC-ωPBE [28-31], B972 [32] and X3LYP [33] functionals in combination with the a-TZ and dTZ basis sets. We also incorporated a dispersion correction in the abovementioned functionals as published by Grimme [18] in 2006, and denoted by DFT-D2 e.g. BP86-D2. The following equations were taken from Grimme's paper and will not be discussed; for further details please see Grimme's paper.

The total energy is given by

$$E_{DFT\text{-}D} = E_{KS\text{-}DFT} + E_{disp} \qquad (1)$$

where $E_{KS\text{-}DFT}$ is the usual Kohn-Sham energy as obtained by the chosen DFT, and E_{disp} is given by:

$$E_{disp} = -s_6 \sum_{i=1}^{N-1} \sum_{j=i+1}^{N} \frac{C_6^{ij}}{R_{ij}^6} f_{damp}(R_{ij}) \qquad (2)$$

Here s_6 is the global scaling factor that only depends on the density functional used, N is the number of atoms, C_6^{ij} denotes the dispersion coefficient for atom pair ij given by the equation $C_6^{ij} = \sqrt{C_6^i C_6^j}$, and R_{ij} is the interatomic distance. A damping function is included to avoid near singularities, given by

$$f_{damp}(R_{ij}) = \frac{1}{1+e^{-a\left(\frac{R_{ij}}{R_r}-1\right)}} \qquad (3)$$

where R_r is the sum of the atomic radii and a is a constant equal to 20

The $I_3^-\cdots I_3^-$ interaction energy (E_{int}) and (ΔE_s) were calculated as follows:

E_{INT} = Energy $(I_3^-\cdots I_3^-)$ – 2×Energy (I_3^-)

ΔE_s = Energy (solvated I_3^-) – Energy (gas phase I_3^-)

The coordinates, frequencies and energies of the optimised structures are included in the supplementary information.

2.1.1. E_{INT} in SETHAB

The $I_3^- \cdots I_3^-$ interaction energies (E_{INT}) in the *n*-methylformamide-mixture solvent were calculated employing the geometry of the I_3^- ion and $I_3^- \cdots I_3^-$ obtained from SETHAB, utilising the implicit solvent model. Single point energy calculations were performed for I_3^- and $I_3^- \cdots I_3^-$ for HF, MP2, PBE-D2 and B97D utilising the a-TZ basis set. Additional single point calculations were performed for I_3^- and $I_3^- \cdots I_3^-$ at the MP2/TZ level of theory, included as reference for the $I_3^- \cdots I_3^-$ interaction energies shown in Chapter 7.

The $I_3^- \cdots I_3^-$ interaction energies are given by:

$$E_{INT} = \text{Energy} (I_3^- \cdots I_3^-) - 2 \times \text{Energy} (I_3^-)$$

2.2. CSD searches

Structural data were obtained from the May 2012 update of the Cambridge Structural Database V5.33 utilising the ConQuest V1.15 search program [34]. The search for the I_3^- ion consisted of only an I-I-I fragment. Chains of I_3^- ions were identified by searching for a fragment containing two I-I-I ions with an intermolecular contact less than the sum of the van der Waals distance between the terminal I atoms on the two triiodides. Crystal structures containing I^-, I_2 and polyiodides were excluded. Crystal structures containing chains of I_3^- ions were identified by inspection. One crystal structure, SETHAB [35] was also identified suitable for further modelling of the crystallographic environment.
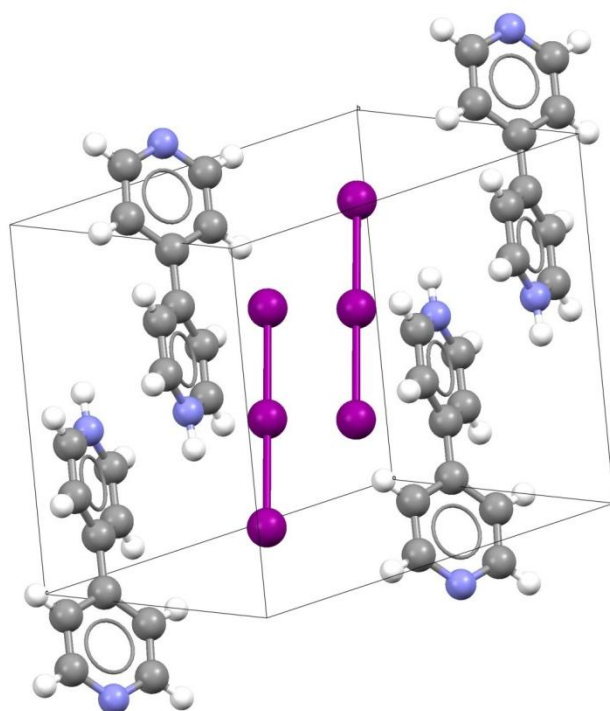
Fig. 2.1 – Expanded unit cell of the selected SETHAB crystal, where Iodine is shown in purple, carbon in grey, nitrogen in blue and hydrogen in white.

2.3. PES curves

The Potential Energy (PES) scans where performed by taking the optimised structure for an isolated I_3^- at a selected level of theory in a particular solvent or gas phase, where the only variable in the scan is the $I_3^- \cdots I_3^-$ intermolecular distance. (see Fig. 2.2) The scan was performed by doing an array of single point calculations of the I_3^- dimer with a intermolecular distance of 3 Å to 10 Å in steps of 0.1 Å to obtain the PES in a variety of solvents for various levels of theory. For all of the gas phase and chloroform PES curves we used the energy of two I_3^- ions at infinite separation as our relative minimum. For all the other solvents we used the last single point energy calculation of the scan as our relative minimum where the I_3^- has a intermolecular distance of 10 Å.

θ

Intermolecular distance (Å)
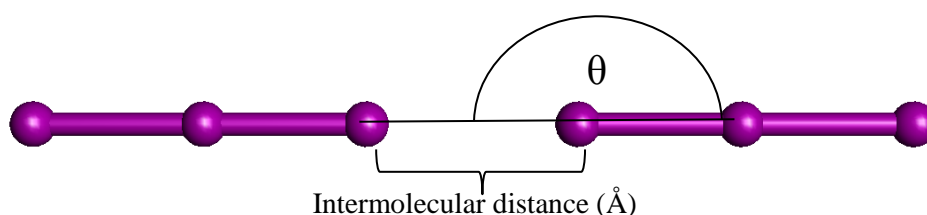
Fig. 2.2 − Illustration of the scan performed where the θ remained a constant equal to 180˚ where the PES was constructed by an array of single point calculations as a function of the intermolecular distance. The geometries for each of the I_3^- ions was obtained from the optimised structure for an isolated I_3^- ion in the respective phase.

2.4. Electrostatic Surface Potential (ESP) analysis

2.4.1. The I_3^- ion in solution

Analysis of the surface potential was carried out, on the optimised structure of the I_3^- ion, by utilising the WFA Surface Analysis Suite (SAS), designed by Bulat and Toro-Labbe [36, 37]. The iso-surface was selected to be defined at an electron density of 0.001 au.

All geometry optimisations and the writing of the corresponding *.wfn and *.cube files were performed using the Gaussian 09 rev.B.01 package utilising the all-electron basis set 6-311G** basis set [38], obtained from the EMSL basis set exchange [2, 3]. Since, the WFA SAS cannot utilise wave functions (*.wfx files) generated from basis sets containing ECPs. All the wave functions (*.wfn) and cube files (*.cube) were generated utilising the corresponding optimised structures, which is needed as input by the WFA SAS program to calculate the values for V(**r**) and generate the images for the ESP surface. All I_3^- and $I_3^- \cdots I_3^-$ geometries in the gas phase, chloroform, ethanol, water and *n*-methylformamide-mixture used were optimised using MP2, PBE-D2, B97D, TPSS, TPSS-D2 utilising the 6-311G** basis set.

2.4.2. The I_3^- ion in a crystal

The surface of the I_3^- ion was analysed utilising the WFA Surface Analysis Suite, with the isosurface defined at an electron density of 0.001 au. Single point calculations were performed utilising the B97D and the PBE-D2 functionals for the expanded unit cell (shown in Fig. 2.3). Charges were calculated for the expanded unit cell (shown in Fig. 2.3). Charge set **1** and **2** were calculated from the same geometry, where the C-H bonds were optimised with Molecular Mechanics (MM), utilising the UFF force field, and the N-H bond was not optimised and kept at 0.99 Å to investigate the influence this would have on the surface analysis of the I_3^- ion. Charge set **1** was calculated utilising the 6-311G** basis set for the I_3^- ion and the 3-21G basis set for the C, N and H atoms. Charge set **2** was calculated with the 6-311G** basis set for all the atoms (I, C, N, H) [39], downloaded from the EMSL basis set exchange.

Charge set **3** was obtained from a geometry obtained from an expanded unit cell with the C-H bonds optimised using the UFF force field in Cerius^2 and the N-H bond length was set to 1.12 Å (see Fig. 2.4).
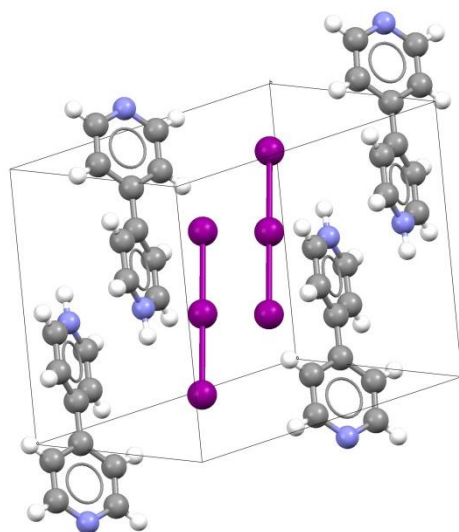
Fig. 2.3 – Expanded unit cell used to obtained Mulliken charges for the charge sets, for various methods. Iodine atoms are shown in purple, carbon in grey, nitrogen in blue and hydrogen in white.

The coordinates of the point charges were obtained by expanding the expanded unit cell $3\times3\times3$ super cell and consisting of 1674 atoms. All but the central I_3^- ion were then replaced with their corresponding point charges as calculated at various levels of theory. Charges were extracted from charge sets for a single cation and anion, which was then used for the point charges of the super cell so that all the cations have the same Mulliken charges and so does the anions.

28

2.5. Atoms in molecules (AIM) analysis

2.5.1. AIM analysis in solution

All geometries used for the I_3^- ion and the $I_3^- \cdots I_3^-$ for MP2 and various DFT functionals were optimised using the Gaussian 09 rev.B.01 package. All the wave functions generated from the utilisation of basis sets containing ECPs (*.wfx files) used to perform the AIM analysis were generated using the corresponding optimised structure in Gaussian 09 rev.B.01 package. The AIM analysis was performed utilising the AIMAll (v.11.04.03) [40] software package, including figures of various two-dimensional contour plots. The total energy density [H(*r*)] is given by -1.0*K(*r*), where K(*r*) is a selected output of the AIMAll software package. All the wave function integrations were performed using the default settings.

All geometry optimisations of I_3^- and $I_3^- \cdots I_3^-$ using MP2 were performed utilising the a-TZ basis set containing ECP obtained from [2, 3] were performed in the gas phase, chloroform, ethanol, water and *n*-methylformamide-mixture.

The DFT optimisations of the I_3^- ion in the gas phase were performed with the M06-2X, ωB97X, M06-HF, LC-ωPBE, BLYP, B3LYP, PBE-D2 and TPSS-D2 functionals utilising the a-TZ basis set. The DFT optimisations of $I_3^- \cdots I_3^-$ were done in *n*-methylformamide-mixture employing the PBE-D2 and TPSS-D2 DFT functionals in combination with the a-TZ basis set.

2.5.2. AIM analysis of SETHAB

Geometry of $I_3^- \cdots I_3^-$ was obtained from the CSD for the SETHAB crystal structure. Wave functions were generated for $I_3^- \cdots I_3^-$ in the gas phase, in *n*-methylformamide-mixture (ε = 181.56) and crystal point charge environment, utilising the Gaussian09 Rev.B.01 software package at the MP2/TZ level of theory. The TZ basis set was obtained from EMSL basis set exchange. The default implicit solvent model (IEF-PCM) was selected for *n*-methylformamide-mixture.

The Mulliken charge distribution utilised in charge set **4** was obtained from the extended unit cell (shown in Fig 2.3) at the PBE-D2/6-311G** level of theory, where the C-H bonds were optimised utilising the Cerius[2] [41] software package, utilising the UFF force field and the N-H bond length was set to 1.12 Å (N-H bond length obtained from Section 2.7 where the N-H bond was optimised with the B971 functional in combination with the dTZ and D95V [42] basis set for iodine and C, N, H, respectively. See Fig. 2.4). The coordinates for the point charges were obtained by expanding the unit cell 3×4×3, since the $[I_3^-]_\infty$ chains extend along the crystallographic *b*-axis, with $I_3^- \cdots I_3^-$ positioned at the centre of the crystal, with the C-H bonds optimised with the UFF force field in Cerius[2] and the N-H bond was set to 1.12 Å.

2.6. Electric field optimisations

All the optimisations performed in various electric dipole fields were done using Gaussian09 Rev.B.01. All optimisations were performed utilising MP2 in combination with the a-TZ, TZ, a-DZ, DZ basis set obtained from the EMSL basis set exchange.

2.7. Crystal optimisations

All the quantum mechanical optimisations were performed with the Gaussian09 Rev.B.01 software package. All the MM optimisations of the positions of the hydrogen atoms were performed with the Cerius[2] software package, utilising the default force field (UFF). Small models of the crystal containing various ions surrounding the central I_3^- ion were identified. All the hydrogen positions of the cations in the crystal models **1**, **2**, **3** were optimised with MM. However, the UFF was unable to correctly model one of the hydrogen atoms in **4** (indicated in orange in Fig. 2.4). Hence, to determine the position of the hydrogen atom bonded to the nitrogen, an optimisation of only the hydrogen atom was performed utilising the B971 functional in combination with the dTZ and D95V [42] basis set for the triiodide and cations, respectively.
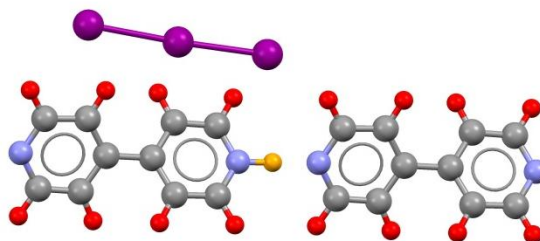
Fig. 2.4 – The structure used to optimise the hydrogen atom position (shown in orange) bonded to the nitrogen atom. The hydrogen atoms shown in red were optimised using molecular mechanics (UFF force field). Carbon atoms are shown in grey and nitrogen in blue.

Optimisations of all the crystal models the positions of the cations were kept stationary while the position of the I_3^- ions was optimised freely.

In crystal model **1**, the positions of the cations were kept stationary and only the I_3^- ions were allowed to optimise their positions utilising the HF, MP2, B3LYP and B97D methods with the 3-21G [43-48] basis set utilised for I, C, N and H. Furthermore, the I_3^- ions were also optimised at the B971/dTZ level of theory and the D95V basis set for C, N and H.

For optimisations of crystal models **2** and **3** the HF and B3LYP methods in combination with the 3-21G basis set were utilised, in addition to the B971 functional where the dTZ basis set was used for the iodine atoms and the D95V basis set for C, N and H.

The optimisations using crystal model **4** were performed with the B971 and the PBE-D2 functionals, where the dTZ basis set was employed for I_3^- ions and the B95V basis set for the C, N and H atoms.

2.8. Stabilisation of the I_3^- ion in the crystal

The positions of the hydrogen atoms were optimised, as before, with MM, utilising the UFF force field in Cerius[2]. The position of the proton bonded to the nitrogen was left as found in the crystal structure (N-H = 0.99 Å). The stabilisation provided by the crystal environment was calculated utilising the MP2 method with the a-TZ basis set for the I atoms, and the 3-21G basis set used for the C, N and H atoms.

The stabilisation energy was calculated by:

Stabilisation Energy = Energy (AB) – Energy (A+B)

References

1.   Frisch, M.J., et al., *Gaussian 09, Revision B.01*, 2009: Wallingford CT.

2.   Feller, D., *The role of databases in support of computational chemistry calculations.* Journal of Computational Chemistry, 1996. **17**(13): p. 1571-1586.

3.   Schuchardt, K.L., et al., *Basis Set Exchange: A Community Database for Computational Sciences.* Journal of Chemical Information and Modeling, 2007. **47**(3): p. 1045-1052.

4.   Møller, C. and M.S. Plesset, *Note on an Approximation Treatment for Many-Electron Systems.* Physical Review, 1934. **46**(7): p. 618-622.

5.   Binkley, J.S. and J.A. Pople, *Møller–Plesset theory for atomic ground state energies.* International Journal of Quantum Chemistry, 1975. **9**(2): p. 229-236.

6.   Weigend, F. and R. Ahlrichs, *Balanced basis sets of split valence, triple zeta valence and quadruple zeta valence quality for H to Rn: Design and assessment of accuracy.* Physical Chemistry Chemical Physics, 2005. **7**(18): p. 3297-3305.

7.   Peterson, K.A., et al., *On the Spectroscopic and Thermochemical Properties of ClO, BrO, IO, and Their Anions.* The Journal of Physical Chemistry A, 2006. **110**(51): p. 13877-13883.

8.   Tomasi, J., B. Mennucci, and R. Cammi, *Quantum Mechanical Continuum Solvation Models.* Chemical Reviews, 2005. **105**(8): p. 2999-3094.

9.   Miertuš, S., E. Scrocco, and J. Tomasi, *Electrostatic interaction of a solute with a continuum. A direct utilizaion of AB initio molecular potentials for the prevision of solvent effects.* Chemical Physics, 1981. **55**(1): p. 117-129.

10.   Scuseria, G.E. and H.F. Schaefer Iii, *Is coupled cluster singles and doubles (CCSD) more computationally intensive than quadratic configuration interaction (QCISD)?* The Journal of Chemical Physics, 1989. **90**(7): p. 3700-3703.

11.   Boys, S.F. and F. Bernardi, *The calculation of small molecular interactions by the differences of separate total energies. Some procedures with reduced errors.* Molecular Physics, 1970. **19**(4): p. 553-566.

12.   Simon, S., M. Duran, and J.J. Dannenberg, *How does basis set superposition error change the potential surfaces for hydrogen-bonded dimers?* The Journal of Chemical Physics, 1996. **105**(24): p. 11024-11031.

13.   Perdew, J.P., K. Burke, and M. Ernzerhof, *Generalized Gradient Approximation Made Simple.* Physical Review Letters, 1996. **77**(18): p. 3865-3868.

14. Perdew, J.P., K. Burke, and M. Ernzerhof, *Generalized Gradient Approximation Made Simple [Phys. Rev. Lett. 77, 3865 (1996)].* Physical Review Letters, 1997. **78**(7): p. 1396-1396.

15. Chai, J.-D. and M. Head-Gordon, *Systematic optimization of long-range corrected hybrid density functionals.* The Journal of Chemical Physics, 2008. **128**(8): p. 084106-15.

16. Chai, J.-D. and M. Head-Gordon, *Long-range corrected hybrid density functionals with damped atom-atom dispersion corrections.* Physical Chemistry Chemical Physics, 2008. **10**(44): p. 6615-6620.

17. Hamprecht, F.A., et al., *Development and assessment of new exchange-correlation functionals.* The Journal of Chemical Physics, 1998. **109**(15): p. 6264-6271.

18. Grimme, S., *Semiempirical GGA-type density functional constructed with a long-range dispersion correction.* Journal of Computational Chemistry, 2006. **27**(15): p. 1787-1799.

19. Becke, A.D., *Density-functional exchange-energy approximation with correct asymptotic behavior.* Physical Review A, 1988. **38**(6): p. 3098-3100.

20. Perdew, J.P., *Density-functional approximation for the correlation energy of the inhomogeneous electron gas.* Physical Review B, 1986. **33**(12): p. 8822-8824.

21. Becke, A.D., *Density-functional thermochemistry. III. The role of exact exchange.* The Journal of Chemical Physics, 1993. **98**(7): p. 5648-5652.

22. Lee, C., W. Yang, and R.G. Parr, *Development of the Colle-Salvetti correlation-energy formula into a functional of the electron density.* Physical Review B, 1988. **37**(2): p. 785-789.

23. Miehlich, B., et al., *Results obtained with the correlation energy density functionals of becke and Lee, Yang and Parr.* Chemical Physics Letters, 1989. **157**(3): p. 200-206.

24. Tao, J., et al., *Climbing the Density Functional Ladder: Nonempirical Meta–Generalized Gradient Approximation Designed for Molecules and Solids.* Physical Review Letters, 2003. **91**(14): p. 146401.

25. Adamo, C. and V. Barone, *Toward reliable density functional methods without adjustable parameters: The PBE0 model.* The Journal of Chemical Physics, 1999. **110**(13): p. 6158-6170.

26. Zhao, Y. and D. Truhlar, *The M06 suite of density functionals for main group thermochemistry, thermochemical kinetics, noncovalent interactions, excited states, and transition elements: two new functionals and systematic testing of four M06-class*

functionals and 12 other functionals. Theoretical Chemistry Accounts: Theory, Computation, and Modeling (Theoretica Chimica Acta), 2008. **120**(1): p. 215-241.

27.   Zhao, Y. and D.G. Truhlar, *Comparative DFT Study of van der Waals Complexes: Rare-Gas Dimers, Alkaline-Earth Dimers, Zinc Dimer, and Zinc-Rare-Gas Dimers.* The Journal of Physical Chemistry A, 2006. **110**(15): p. 5121-5129.

28.   Tawada, Y., et al., *A long-range-corrected time-dependent density functional theory.* The Journal of Chemical Physics, 2004. **120**(18): p. 8425-8433.

29.   Vydrov, O.A. and G.E. Scuseria, *Assessment of a long-range corrected hybrid functional.* The Journal of Chemical Physics, 2006. **125**(23): p. 234109-9.

30.   Vydrov, O.A., et al., *Importance of short-range versus long-range Hartree-Fock exchange for the performance of hybrid density functionals.* The Journal of Chemical Physics, 2006. **125**(7): p. 074106-9.

31.   Vydrov, O.A., G.E. Scuseria, and J.P. Perdew, *Tests of functionals for systems with fractional electron number.* The Journal of Chemical Physics, 2007. **126**(15): p. 154109-9.

32.   Wilson, P.J., T.J. Bradley, and D.J. Tozer, *Hybrid exchange-correlation functional determined from thermochemical data and ab initio potentials.* The Journal of Chemical Physics, 2001. **115**(20): p. 9233-9242.

33.   Xu, X. and W.A. Goddard, *The X3LYP extended density functional for accurate descriptions of nonbond interactions, spin states, and thermochemical properties.* Proceedings of the National Academy of Sciences of the United States of America, 2004. **101**(9): p. 2673-2677.

34.   Allen, F., *The Cambridge Structural Database: a quarter of a million crystal structures and rising.* Acta Crystallographica Section B, 2002. **58**(3 Part 1): p. 380-388.

35.   Kochel, A., *4-(4-Pyridyl)pyridinium triiodide.* Acta Crystallographica Section E, 2006. **62**(12): p. o5605-o5606.

36.   Bulat FA, T.-L.A., *WFA: A suite of programs to analyse wavefunctions*: unpublished.

37.   Bulat, F., et al., *Quantitative analysis of molecular surfaces: areas, volumes, electrostatic potentials and average local ionization energies.* Journal of Molecular Modeling, 2010. **16**(11): p. 1679-1691.

38.   Glukhovtsev, M.N., et al., *Extension of Gaussian-2 (G2) theory to bromine- and iodine-containing molecules: Use of effective core potentials.* The Journal of Chemical Physics, 1995. **103**(5): p. 1878-1885.

39. Krishnan, R., et al., *Self-consistent molecular orbital methods. XX. A basis set for correlated wave functions.* The Journal of Chemical Physics, 1980. **72**(1): p. 650-654.

40. Keith, T.A., *AIMAll* 2012 TK Gristmill Software: Overland Park KS, USA.

41. Inc., M.S., *Cerius^2 modelling environment*, 1998, Molecular Simulations Inc.: San Diego.

42. Dunning Jr. TH, H.P., in *Modern Theoretical Chemistry*, S.I. HF, Editor 1976, Plenum: New York. p. 1-28.

43. Binkley, J.S., Pople JA, Hehre WJ, *Self-consistent molecular orbital methods. 21. Small split-valence basis sets for first-row elements.* Journal of the American Chemical Society, 1980. **102**: p. 939-947.

44. Gordon MS, B.J., Pople JA, Pietro WJ and Hehre WJ, *Self-consistent molecular orbital methods. 22. Small split-valence basis sets for second-row elements.* Journal of the American Chemical Society, 1982. **104**: p. 2797-2803.

45. Pietro WJ, F.M., Hehre WJ, Defrees DJ, Pople JA, Binkley JS, *Self-Consistent Molecular Orbital Methods. 24. Supplemented small split-valence basis-sets for 2nd-row elements.* Journal of the American Chemical Society, 1982. **104**: p. 5039-5048.

46. Dobbs KD, H.W., *Molecular-orbital theory of the properties of inorganic and organometallic compounds. 4. Extended basis-sets for 3rd row and 4th row, main-group elements.* Journal of Computational Chemistry, 1986. **7**: p. 359-378.

47. Dobbs KD, H.W., *Molecular-orbital theory of the properties of inorganic and organometallic compounds. 5. Extended basis-sets for 1st-row transition-metals.* Journal of Computational Chemistry, 1987. **8**: p. 861-879.

48. Dobbs KD, H.W., *"Molecular-orbital theory of the properties of inorganic and organometallic compounds. 6. Extended basis-sets for 2nd-row transition-metals.* Journal of Computational Chemistry, 1987. **8**: p. 880-893.

CHAPTER 3

Modelling of the I_3^- ion and $I_3^- \cdots I_3^-$ in the gas phase and in an implicit solvent model

Introduction

In this chapter we investigate the ability of various wave function theory (WFT) methods and Density Functional Theory (DFT) functionals to reproduce selected geometrical parameters using calculated CSD averages for the I-I bond length and the $I_3^- \cdots I_3^-$ intermolecular distance as reference. In particular, the investigation of the $I_3^- \cdots I_3^-$ interaction energy will be investigated by employing various WFT methods and DFT functionals and compared to the CCSD/a-TZ//MP2/TZ benchmark for the $I_3^- \cdots I_3^-$ interaction energy. In addition, we aim to explore possible dependency of these above mentioned parameters on the solvent used.

3.1. Wave function Theory (WFT)

3.1.1. I_3^- ion bond length

The I_3^- ion decomposes into I_2 and I^- at temperatures equal to or greater than room temperature, according to an extensive review article on polyiodides [1], thus it has not been possible to obtain any experimental information on the bond length of the I_3^- ion other than what has been found in the solid state. However, previous studies have shown that the symmetry of the I_3^- ion in solution is dependent on the solvent used, where the induced asymmetry can facilitate forbidden transitions visible in Raman spectra [2, 3]. This influence of asymmetry on spectra has also been observed in a UV-Vis study on compounds in both the solid state and in solution [4].

Average geometrical parameters for the I_3^- ion obtained from the CSD were reported in 2003 as 2.92 Å [1], however, since then there have been approximately 200 additional characterisations of triiodides. We therefore repeated the analysis using the May 2012 update of the CSD [5], where we obtained 787 hits for the discrete I_3^- ion of which only 675 contain bond length information, and 98 hits for $[I_3^-]_n$, with n ≥ 2, where 36 form $[I_3^-]_\infty$ chains. The bond length of the triiodide ion varies in the solid state from 2.53 Å to 3.21 Å, however, we found the CSD average to be 2.92 Å. This range observed for the bond length of the triiodide ion in the solid state can be attributed to changes in the surrounding chemical environment where only a few kcal/mol are needed to shift the I-I bond from its equilibrium distance [6]. For the intermolecular distance the CSD average was determined for 36 structures containing $[I_3^-]_\infty$ chains and was found to be 3.8 Å, within a range of 3.58 Å to 3.96 Å. Furthermore, considering that less than 5 % of all the structural data available for the I_3^- ion contains structural information for $[I_3^-]_\infty$ chains, the distribution over this range has low frequencies with the global maximum occurring at the mean.

Table 3.1 – CSD averages for the I_3^- bond length (Å) and $I_3^-\cdots I_3^-$ intermolecular distance (Å), with comparative CCSD and MP2 geometries from optimisations utilising various basis-sets, and interaction energies (kcal/mol) at the CCSD, MP2 and HF (in parenthesis) levels of theory.

Method	Basis set	Bond length (Å)			$d(I_3^-\cdots I_3^-)$ (Å)			E_{INT} (kcal/mol)		
		gas	ethanol	water	gas	ethanol	water	gas	ethanol	water
CCSD	a-TZ	2.946[d]	2.936[d]	2.936[d]		-		-	-	-
CCSD	a-TZ		-			-		34.381[a,c]	-0.264[a]	-1.279[a]
	a-TZ		-			-		-	**-0.802[b]**	**-1.797[b]**
MP2	dTZ	2.910	2.905	2.905	-	3.637	3.634	-	-1.651	-2.670
								-	4.940	4.024
	a-TZ	2.924	2.915	2.915	3.901	3.561	3.562	[c]33.170	-3.187	-4.219
								[c](36.658)	(6.035)	(5.043)
	TZ	2.921	2.912	2.911	-	3.788	3.778	-	-0.769	-1.788
								-	(4.002)	(3.090)
	a-DZ	2.996	2.985	2.985	-	3.786	3.777	-	-1.973	-2.975
								-	(3.896)	(2.989)
	DZ	2.988	2.978	2.978	-	4.018	4.008	-	-0.055	-1.049
								-	(2.538)	(1.594)
CSD average		**2.92(5)**			**3.80(10)**			-	-	-

HF interaction energies obtained from MP2 optimised geometries using the same basis set.

[a]CCSD/a-TZ//MP2/a-TZ optimised geometry in the gas phase, ethanol and water.

[b]CCSD/a-TZ// MP2/TZ optimised geometry in ethanol and water.

[c]Counterpoise corrected

[d]Optimised geometries at the CCSD/a-TZ level of theory

Previous theoretical studies of symmetrical I_3^- ions in the gas phase at the CCSD and CCSD(T) levels of theory yielded bond lengths of 2.964 Å and 2.982 Å, respectively [7, 8]. However, the influence of a changing electrostatic environment on the bond length at these levels of theory was not investigated.

In Table 3.1 we have summarised the computational results for two geometrical parameters: the I_3^- bond length and the $I_3^-\cdots I_3^-$ intermolecular distance, with the CSD averages indicated for reference, where the optimised structure of the I_3^- ion being centrosymmetric in the gas phase, ethanol (ε=24.852) and water (ε=78.3553). In addition, the CCSD/a-TZ interaction energy for the I_3^- dimer has been included as a benchmark. If the optimised I-I bond length of the I_3^- ion in the gas phase at the CCSD/a-TZ level of theory listed in Table 3.1 is compared to previously reported [7, 8] optimisations performed for the I_3^- ion, we observe a decrease in the I-I bond length where the results reported here are closer to the calculated CSD average. In the gas phase, MP2 in combination with the dTZ, a-TZ and TZ basis sets gives bond lengths comparable to the CSD average for I_3^- (2.92 Å) with the best result obtained for MP2/TZ (2.921 Å). If the I_3^- ion is placed in ethanol or water, with increasing dielectric constants, there is a decrease in the bond length of approximately 0.01 Å for all basis sets such that the MP2/a-TZ results (2.915 Å in the solvent) are closest to the CSD value. Here,

we see that MP2/TZ outperforms CCSD/a-TZ in the gas phase and in solution for the I-I bond length of the I_3^- ion if the CSD average is considered, even though the deviation of CCSD/a-TZ is less than 1 % from the CSD average. Suffice it to say MP/TZ yields results comparable to the CCSD/a-TZ level of theory and that both methods exhibit a decrease of about 0.01 Å when the bond length of the I_3^- ion is modelled in an electrostatic environment. Furthermore, MP2 in combination with the double-zeta basis sets gives elongated I-I distances when compared to the larger triple-zeta basis sets. This basis set dependence can be attributed to MP2 overestimating the dispersion contribution, (see Section 3.1.3). This statement is supported by a previous theoretical study of the $I^- \cdots I_2$ bond [7] which identified additional dispersion interactions between the two fragments.

However, if one considers the greatest deviation being 3 % from the CSD average for the I_3^- bond length it is clear that all these basis sets in combination with MP2 perform very well in reproducing the experimental structures, with the CCSD method deviating by less than 1%. Although all of these geometry optimisations yielded symmetrical I_3^- ions, when optimised as a dimer the geometries of the individual I_3^- ions are asymmetric, while the total length of the molecule elongates by a negligible amount (~0.01 Å), see Table S1 in the Supplementary Information. Very recently, Aragoni and co-workers [6] studied triatomic linear molecules and their bond length deviations in CSD data, where they found I_3^- has a normalised elongation (δ_{I-I}) $\leq$ 0.36 when the bond length d(I-I) is $\leq$ 3.6 Å. They also calculated the PES of the I_3^- ion and concluded that the PES is extremely flat and that only a few kilocalories of energy are needed to impose a change in the bond length.
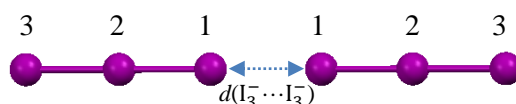
Fig. 3.1 – General geometry of the stationary point found for the I_3^- dimer. Note that $d(I_1\text{-}I_2)$ is shorter than $d(I_2\text{-}I_3)$, but the $d(I_1\text{-}I_3)$ in a dimer is elongated by a negligible amount when compared to a single optimised I_3^- ions.

3.1.2. Intermolecular distance $d(I_3^- \cdots I_3^-)$

It is clear from Table 3.1 that the $I_3^- \cdots I_3^-$ distances deviate much more from the CSD average than the I-I intramolecular distances for the I_3^- ion. This also agrees with what is observed experimentally where the standard deviation for the $I_3^- \cdots I_3^-$ intermolecular distance is twice that of the intramolecular I-I bond length. In the gas phase only the a-TZ basis set yields a stationary point (see Fig. 3.2), which can be attributed to the fact that MP2 overestimates the dispersion interaction. However, this is clearly not a minimum energy conformation thus in the gas phase, only repulsive interactions exist between I_3^- ions. The stationary point is

therefore actually an artefact (see Section 3.1.3.) although the intermolecular distance (3.901 Å) is slightly greater than the CSD average of 3.8 Å. This slight deviation of the intermolecular distance for the gas phase dimer from the CSD average can be attributed to the inability of MP2 to model dispersion interactions, thus changing the PES sufficiently enabling us to identify a stationary point (shown in Fig. 3.2). Therefore, at the CCSD/a-TZ//MP2/a-TZ level of theory this stationary point is approximately 34 kcal/mol higher in energy than two I_3^- ions at infinite separation. Nevertheless, the repulsive interaction energy of the I_3^- dimer in the gas provides insight into the severity of the repulsion present without the presence of an electrostatic environment.
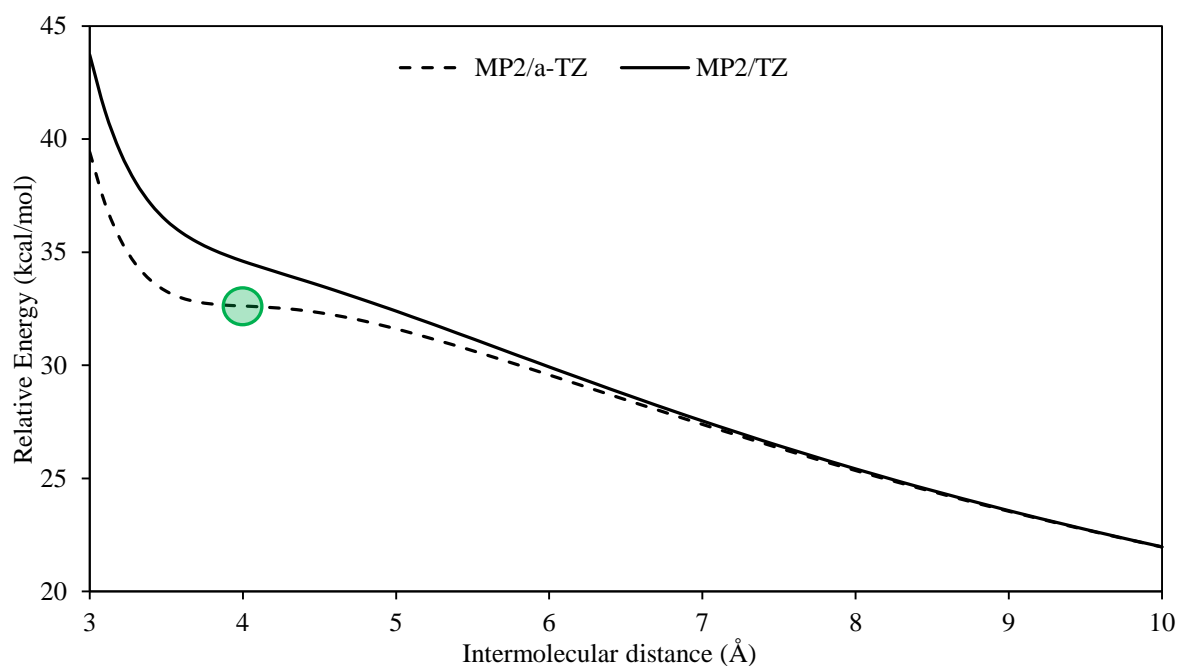
Fig. 3.2 – The PES of the I_3^- dimer in the gas phase with the stationary point represented as a green circle.

When the dimer is placed in an electrostatic environment we observe a decrease in the intermolecular distance of 0.34 Å at the MP2/a-TZ level, although the distances are almost identical in ethanol and water. With the other basis sets (except for dTZ), on the other hand, there is a decrease of 0.1 Å in the intermolecular distance in ethanol as compared to water. This decrease in the $I_3^- \cdots I_3^-$ distance in water as compared to ethanol is due to the added stabilisation provided by water as a solvent (see Section 2.1).

MP2/TZ reproduces the CSD average most closely. The a-TZ and dTZ basis sets underestimate the intermolecular distance whereas the double-zeta basis sets overestimate it.

3.1.3. The $I_3^- \cdots I_3^-$ interaction energy

To our knowledge there are no experimental or theoretical values available for the $I_3^- \cdots I_3^-$ interaction energy; even a paper on the kinetics of the triiodide ion in aqueous solution using [127]I NMR, unfortunately does not report any dimer formation [9]. Thus we consider the CCSD/a-TZ//MP2/TZ interaction energy to be our benchmark, since CCSD(T)/a-TZ//MP2/a-TZ is computationally too expensive when the dimer is considered. A geometry optimisation of the I_3^- dimer at the CCSD/a-TZ level of theory was attempted, but was found to be computationally too expensive.

The CCSD/a-TZ//MP2/a-TZ results are included in Table 3.1 as an illustration of the substantial dependence of the value obtained for the interaction energy on the geometry used. At the MP2/a-TZ level of theory the $I_3^- \cdots I_3^-$ distance is shorter than that at the MP2/TZ level due to the overestimation of the dispersion interaction. This overestimation of the dispersion interaction at the MP2/a-TZ level can also be observed in the gas phase when the PES is investigated, as shown in Fig. 3.2, where MP2/a-TZ yields a more stabilising PES curve when compared to MP2/TZ. The PES curves will be discussed in more detail later in Section 3.4. The shorter $I_3^- \cdots I_3^-$ distance obtained from the MP2/a-TZ level of theory results in CCSD/a-TZ giving a less stabilising $I_3^- \cdots I_3^-$ interaction energy in ethanol (-0.264 kcal/mol) and water (-1.279 kcal/mol) than with the MP2/TZ geometry. The MP2/TZ geometry was used for further energy calculations since it is closer to the CSD average and also yields a higher $I_3^- \cdots I_3^-$ interaction energy (-0.802 kcal/mol) in ethanol and water (-1.797 kcal/mol), when the MP2/TZ optimised geometry is used for CCSD/a-TZ single point calculations. These substantial differences in the interaction energies at the CCSD/a-TZ level of theory illustrate exactly how important is geometry selection in constructing a benchmark for complexes bound by a weak interaction energy as a result of electron correlation.

It was found that MP2/TZ delivered an $I_3^- \cdots I_3^-$ interaction energy of -0.77 kcal/mol with a deviation in ethanol of 5 % from our benchmark of -0.80 kcal/mol. This difference, however, decreased when modelled in a solvent with a higher dielectric constant, resulting in a deviation of only 0.01 kcal/mol from the CCSD benchmark. Our results coincide with a previous study regarding the ability of MP2 to model non-covalent interactions, which concluded that cc-pVTZ-pp gave the most balanced description of the electrostatic and dispersion interactions [10].

It has previously been reported [11] that the ratio of the MP2 and HF interaction energies, $\Delta E(HF)/\Delta E(MP2)$, can be employed to determine the dominant contributing interaction (electrostatic or dispersion) for various protein-ligand systems. The authors found that when the ratio was positive the interaction was mainly electrostatic in nature, while a negative value

41

indicated mainly dispersive interactions. The reason for this characteristic is the inability of HF to model dispersion interactions due to the absence of dynamical correlation in the wave function [12]. If we now consider the HF interaction energies summarised in Table 3.1 it can be seen that the interaction appears to remain repulsive regardless of the phase, although the repulsion decreases from 36.7 to 6.0 kcal/mol. In addition, the sign of the $\Delta E(HF)/\Delta E(MP2)$ ratio suggests that the repulsive $I_3^- \cdots I_3^-$ interaction in the gas phase is electrostatic, whereas in ethanol and water the interaction is mainly due to electron correlation. Furthermore, since the stationary point in the gas phase is considered to be an artefact, these results show that $I_3^- \cdots I_3^-$ interaction has to be studied in a controlled electrostatic environment.

3.2. Density Functional Theory (DFT)

3.2.1. I_3^- ion bond length

The variation of the I_3^- ion's bond length when using various functionals in different polarisable continuum media is illustrated in Table 3.2 and Table 3.3. It can be seen that all DFT functionals overestimate the bond length, except for the M06-HF and LC-ωPBE functionals.

Table 3.2 – I_3^- bond lengths (Å), $I_3^- \cdots I_3^-$ distances (Å) and interaction energies (kcal/mol) for various functionals the a-TZ basis set. CSD average distances and the CCSD/a-TZ interaction energy are included for comparison.

Method/Functional	basis-set	Bond length(Å)			$d(I_3^- \cdots I_3^-)$ (Å)		E_{INT} (kcal/mol)	
		gas	ethanol	water	ethanol	water	ethanol	water
CCSD	**a-TZ**	**2.946**[a]	**2.936**[a]	**2.936**[a]	-		-	
CCSD	**a-TZ**	-			-		**-0.264**[b]	**-1.279**[b]
	a-TZ	-			-		**-0.802**[c]	**-1.797**[c]
PBE	a-TZ	2.976	2.966	2.967	3.705	3.696	0.307	-0.712
PBE-D2		2.978	2.968	2.968	3.856	3.848	-0.813	-1.824
ωB97X		2.943	2.933	2.933	3.925	3.889	-0.435	-1.410
ωB97XD		2.949	2.940	2.940	4.219	4.212	0.202	-0.782
B971		2.965	2.955	2.955	4.063	4.043	0.551	-0.451
B97D		3.029	3.015	3.015	4.003	3.997	-0.600	-1.586
BP86		2.987	2.978	2.977	3.730	3.723	1.100	0.088
BP86-D2		2.990	2.979	2.979	3.887	3.881	-0.517	-1.515
B3LYP		2.994	2.983	2.983	-	4.631	-	0.532
B3LYP-D2		2.997	2.986	2.986	4.034	4.029	0.027	-0.966
TPSS		2.979	2.969	2.969	3.729	3.719	0.961	-0.056
TPSS-D2		2.981	2.971	2.971	3.899	3.886	-0.571	-1.581
BLYP		3.044	3.030	3.030	-	-	-	-
BLYP-D2		3.049	3.036	3.036	3.994	3.995	-0.083	-1.064
PBE0		2.938	2.929	2.929	3.977	3.956	0.832	-0.181
M06		2.972	2.961	2.961	3.927	3.925	-0.173	-1.179
M06-HF		2.841	2.835	2.834	3.880	3.879	1.161	0.113
M06-2X		2.924	2.916	2.916	3.890	3.888	0.234	-0.792
LC-ωPBE		2.898	2.890	2.890	4.361	4.334	1.282	0.316
B972		2.958	2.948	2.948	-	4.505	-	0.286
X3LYP		2.990	2.979	2.979	4.474	4.366	1.293	0.323
CSD average		**2.92(5)**			**3.80(10)**		-	

[a]Optimised at the CCSD/a-TZ level of theory

[b]CCSD/a-TZ//MP2/a-TZ

[c]CCSD/a-TZ//MP2/TZ

In Table 3.2 we have included the CSD averages listed in Table 3.1, as discussed in Chapter 3.1.1. The I-I bond lengths obtained for various DFT functionals with the a-TZ basis set listed in Table 3.2 will be discussed first.

The I-I bond lengths calculated using the M06-2X functional are most comparable to the CSD average (2.92 Å), with a deviation of 0.004 Å in the gas phase. The bond length shortening of 0.008 Å from the gas phase is similar for ethanol and water, irrespective of the electrostatic environment. The ωB97X, PBE0, LC-ωPBE functionals also give comparable results with deviations that are less than 1 % from the CSD average with differences in bond lengths being 0.023 Å, 0.028 Å and 0.022 Å, respectively. The ωB97X and ωB97XD functionals yield bond lengths almost identical to the CCSD/a-TZ level of theory with deviations of 0.003 Å. In

general, all of the selected DFT functionals perform extremely well with the a-TZ basis set, considering that the largest deviation from the calculated CSD average is less than 5 %.

Table 3.3 – I_3^- bond lengths (Å), $I_3^- \cdots I_3^-$ distances (Å) and interaction energies (kcal/mol) for various functionals with the dTZ basis set.

Method/Functional	Basis-set	Bond length(Å)			$d(I_3^- \cdots I_3^-)$ (Å)		E_{INT} (kcal/mol)	
		gas	ethanol	water	ethanol	water	ethanol	water
CCSD	**a-TZ**	**2.946**[a]	**2.936**[a]	**2.936**[a]			**-**	
CCSD	**a-TZ**		**-**			**-**	**-0.264**[a]	**-1.279**[a]
	a-TZ		-			-	**-0.802**[c]	**-1.797**[c]
PBE	dTZ	2.974	2.963	2.963	3.683	3.675	0.232	-0.780
PBE-D2		2.976	2.965	2.965	3.845	3.838	-0.875	-1.877
ωB97X		2.941	2.930	2.930	3.877	3.874	-0.424	-1.400
ωB97XD		2.947	2.936	2.936	4.219	4.212	0.221	-0.755
B971		2.963	2.952	2.952	4.029	4.013	0.502	-0.492
B97D		3.027	3.012	3.012	3.991	3.990	-0.640	-1.616
BP86		2.985	2.973	2.974	3.709	3.700	1.056	0.047
BP86-D2		2.988	2.975	2.976	3.887	3.875	-0.517	-1.540
B3LYP		2.993	2.980	2.980	-	4.495	-	0.483
B3LYP-D2		2.996	2.983	2.983	4.024	4.019	-0.065	-1.048
TPSS		2.977	2.965	2.965	3.716	3.706	0.901	-0.109
TPSS-D2		2.979	2.967	2.968	3.894	3.881	-0.624	-1.624
BLYP		3.042	3.028	3.028	-	-	-	-
BLYP-D2		3.048	3.033	3.033	3.985	3.984	-0.197	-1.166
PBE0		2.935	2.925	2.925	3.956	3.934	0.782	-0.224
M06		2.971	2.959	2.958	3.854	3.854	-0.189	-1.189
M06-HF		2.838	2.831	2.831	3.895	3.893	1.137	0.079
M06-2X		2.922	2.913	2.913	3.881	3.879	0.216	-0.804
LC-ωPBE		2.896	2.887	2.887	4.739	3.992	1.271	0.332
B972		2.956	2.945	2.945	-	4.472	-	0.260
X3LYP		2.988	2.976	2.976	4.384	4.291	1.228	0.262
CSD average		**2.92(5)**			**3.80(10)**		-	

[a]Optimised at the CCSD/a-TZ level of theory

[b]CCSD/a-TZ//MP2/a-TZ

[c]CCSD/a-TZ//MP2/TZ

As with Table 3.2 we included the CSD averages and benchmark interaction energies in Table 3.3 for comparison. The dTZ basis set compares well to the a-TZ basis set, but gives slightly shorter bond lengths in each case. Again, the M06-2X functional yields results closest to the CSD average with a 0.002 Å deviation from the CSD average (2.92 Å), while ωB97X, PBE0 and LC-ωPBE functionals also yielded comparable results with deviations (< 1 %) from the CSD average of 0.021 Å, 0.015 Å and 0.024 Å when the gas phase is considered, respectively.

If we consider the I_3^- bond length obtained using the ωB97X and PBE0 functionals it can be

seen that the dTZ basis set yields results more comparable to the CSD average when compared to the a-TZ basis set. However, this is the exact opposite for the LC-ωPBE functional due to the increase in the underestimation of the I_3^- bond length when the dTZ basis set is used. When the dTZ basis set is utilised with the ωB97XD functional, we see that the functional yields results virtually identical to the calculated bond length at the CCSD/a-TZ level of theory.

By comparing the calculated bond lengths listed in Table 3.2 and Table 3.3 to the CSD average it can be seen that there is a general overestimation of the bond lengths by all the DFT functionals, with the exceptions being the M06-HF and LC-ωPBE functionals. We believe this overestimation of the I_3^- bond length seen for the DFT functionals when compared to the CSD average, is a result of the additional dispersion interactions present in the intramolecular bonding of I_3^- [7]. However, reasons for M06-HF and LC-ωPBE giving shorter I_3^- bond lengths than the CSD average are unclear.

It can be seen in both Table 3.2 and Table 3.3 that the BLYP functional yielded the least comparable bond length (3.049 Å and 3.042 Å) to the CSD average in the gas phase, with the addition of the D2 correction elongating the I_3^- bond length even further, thus increasing the deviation from the CSD average. Despite the elongation of the I_3^- bond length present for the BLYP functional, including the additional elongation induced by the D2 correction, the distance is nevertheless still within 5 % of the CSD average.

3.2.2. Intermolecular distance $d(I_3^- \cdots I_3^-)$

As with the WFT methods in Section 3.1.2 (Fig. 3.1) individual I_3^- ions are asymmetric when optimised as a dimer, although the I_3^- ion's total length elongates by a negligible amount (~0.01 Å) compared to a discrete I_3^- ion, see Tables S2, S3, S4, S5. Since, as mentioned before, the stationary point found in the gas phase is an artefact, we did not perform any optimisations of the I_3^- dimer in the gas phase for the DFT functionals. To support this decision, the PES curves for two DFT functionals including a dispersion correction (PBE-D2 and B97D) and one without the dispersion correction (PBE) are shown in Fig. 3.3, where it can be seen that the PES surfaces described by the DFT functionals in the gas phase does not yield a stationary point.
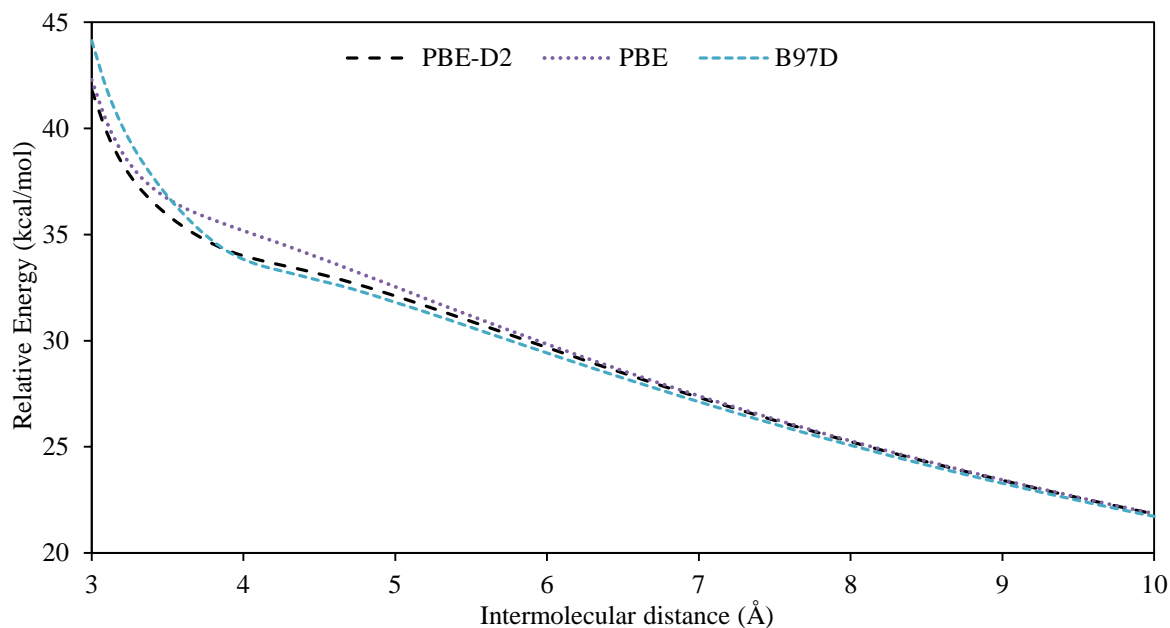
Fig. 3.3 – The PES curves for the I_3^- dimer in the gas phase employing various DFT functionals and utilising the a-TZ basis set.

Now, let us first consider the $I_3^- \cdots I_3^-$ intermolecular distance summarised in Table 3.2 where it can be seen that there is a modest decrease (from 0.001 Å to 0.108 Å) in the intermolecular distance with the increase in the dielectric constant, with the one exception being BLYP-D2. The average decrease in the $I_3^- \cdots I_3^-$ intermolecular distance (0.014 Å) in ethanol compared to water is consistent with the results for the WFT methods (see Section 3.1.2.). Three functionals (B972, BLYP, B3LYP) could not describe the PES sufficiently when modelled in ethanol and were unable to identify a minimum. However, when the electrostatic environment was changed to water the PES changed significantly, enabling us to find stationary points for two (B972, B3LYP) of these three functionals. Nevertheless, the intermolecular distances at these stationary points are severely overestimated, thus not providing accurate results. This proves that the electrostatic environment influences the PES significantly and that care should be taken when modelling in solvents with relatively low dielectric constants. The PBE-D2, BP86 and the meta-GGA, TPSS, functionals yielded results most comparable to the CSD average of the intermolecular distance with less than a 2 % deviation from the CSD average with the a-TZ basis set. However, it was possible to identify 5 functionals that gave an $I_3^- \cdots I_3^-$ distance in ethanol and water within the standard deviation obtained from the CSD: PBE, BP86, TPSS, M06-2X and M06-HF. The X3LYP functional produces results that deviate most from the CSD average for the $I_3^- \cdots I_3^-$ distances, with 18 % and 14 % overestimation of the intermolecular distance in ethanol and water, respectively. If we consider the intermolecular distances summarised in Table 3.3 for various DFT functionals utilising the dTZ basis set, a similar dependency of the intermolecular distance on

46

the basis set to that observed for the I-I distances in I_3^- is obtained, where the dTZ results are consistently shorter when compared to the a-TZ results listed in Table 3.2. This means that the DFT functionals that overestimate the intermolecular distance when combined with the a-TZ basis set yield results with the dTZ basis set that are more comparable to the CSD average for the intermolecular distance. However, the opposite is true for DFT functionals that underestimate the intermolecular distance when using the a-TZ basis set, seeing that the utilisation of the dTZ basis set generally yields a shorter intermolecular distance for a particular functional, when compared to the CSD average for the $I_3^- \cdots I_3^-$ distance. As before, a similar trend can be seen where there is a modest decrease (between 0.001 Å and 0.09Å) in the intermolecular distance in ethanol as compared to water, with the exception being the M06 and LC-ωPBE functionals. This decrease is also consistent with what was found for the WFT methods in Section 3.1.2.

Noticeably, even though a different basis set (dTZ) was utilised, the B972, BLYP and B3LYP functionals were unable to describe the PES sufficiently, thus not yielding a stationary point for the dimer in ethanol. However, when changing the solvent to water, only the BLYP functional was unable to describe the PES sufficiently and did not yield a stationary point for the I_3^- dimer. In general, the results listed in Table 3.3 are consistent with the results in Table 3.2.

Despite this general decrease in the intermolecular distance when results of the a-TZ basis set are compared to the results of the dTZ basis set for a particular DFT functional, the PBE-D2 functional in combination with the dTZ basis set maintains its less than 2 % deviation from the CSD average for the $I_3^- \cdots I_3^-$ intermolecular distance. However, the decrease in intermolecular distance due to the dTZ basis set resulted in the BP86-D2 and M06-2X functionals also yielding results (both 3.881 Å) more comparable to the CSD average for the intermolecular distance when considered in ethanol. The X3LYP functional yielded the least comparable results for the intermolecular distance for the dimer in ethanol and water when the CSD average is considered. The LC-ωPBE functional yields the least comparable result only in ethanol; reasons for this are unclear.

To summarise, no substantial dependence of the I_3^- bond length and $I_3^- \cdots I_3^-$ intermolecular distance on the electrostatic environment was observed, provided the latter is non-directional as is the case with the implicit continuum solvent model. These solvent results suggest that any significant changes in the geometry of the I_3^- ion itself or the intermolecular distance between the I_3^- ions can mostly be attributed to the asymmetry of the electrostatic environment, which agrees with what has been found previously [13].

3.2.3. The $I_3^- \cdots I_3^-$ interaction energy

In Section 3.1.3 we presented evidence that the attractive nature of the $I_3^- \cdots I_3^-$ interaction energy is due to the dispersion interaction. The inability of DFT functionals to model dispersion type non-covalent interactions has been proven to be the biggest shortcoming of GGA type DFT functionals although a number of 'remedies' have been proposed to solve this problem [14]. In order to determine whether the $I_3^- \cdots I_3^-$ interaction is similarly poorly modelled we performed an extensive study testing a variety of functionals. Furthermore, the lack of theoretical data available for the $I_3^- \cdots I_3^-$ interactions requires an expansion of this investigation to computationally less expensive methods such as DFT functionals, since these can also be employed in quantum mechanical investigations of the I_3^- ion in the solid state where the crystal structures show $I_3^- \cdots I_3^-$ interactions to be present [5].

There is a clear dependence of the interaction energy on the dielectric constant as seen in Table 3.2, where we have summarised the interaction energies for various DFT functionals utilising various basis sets. This trend can be observed for all the used DFT functionals where the interaction energy is approximately 1 kcal/mol more attractive in water than in ethanol. We found that the PBE-D2/a-TZ functional yields an interaction energy which is within 2 % of the CCSD/a-TZ//MP2/TZ interaction energy in both ethanol and water.

Despite the accuracy displayed by the PBE-D2 functional, we should mention the study carried out by Johnson *et al.* where they explicitly point out PBE giving 'dispersion-like' binding near minimum energy intermolecular distances which is spurious in nature and is "directly related to the asymptotic behaviour of the exchange enhancement factor" (see ref. [15] and references therein). It is not clear if the success of PBE-D2 is solely a result of this exchange enhancement factor or only the dispersion correction, or if it is the combination of the two. However, without the D2 correction PBE underbinds in ethanol by approximately 140 % which suggests the success is primarily a result of the D2 correction. The only other functionals that perform similarly well to PBE-D2 are the B97D, TPSS-D2 and BP86-D2 functionals, which underestimate the interaction energy in ethanol by roughly 25 %, 28 % and 36 %, respectively.

It was found that the X3LYP functional, as before with the $I_3^- \cdots I_3^-$ intermolecular distance, yields the least comparable results when the CCSD/a-TZ//MP2/TZ benchmark for the $I_3^- \cdots I_3^-$ interaction energy in ethanol and water is considered, with deviations of 261 % and 118 %, respectively. Furthermore, we found that the B3LYP functional only yielded a stationary point for the I_3^- dimer in water with the least comparable E_{INT} (0.532 kcal/mol) which deviates 130 % from our CCSD/a-TZ//MP2/TZ benchmark. Our findings concur with what Černý and Hobza [16] found in their investigation of the X3LYP functional and its ability to model

48

particular non-covalent interactions, where the functional can accurately model H-bonded dimers but fails when dispersion dominated dimers (stacking) are considered. They did, however, point out that even if a particular functional performs well for He and Ne dimers (or any atom pairs consisting of the first 10 atoms in the periodic table) it does not imply it has the ability to model dispersion bound dimers and thus the rare-gas dimers used to test the ability of a functional to model dispersion interactions do not provide a good enough representation of London forces in general between atoms and molecules. They suggested that the testing of DFT functionals with regards to non-covalent interactions should include polyatomic systems with delocalised π-electrons [16, 17].

The substantial difference the inclusion of the D2 correction makes on the calculation of the $I_3^- \cdots I_3^-$ interaction energy is evident when we consider the B3LYP and BLYP functionals, where stationary points could only be identified with the addition of the D2 correction. The addition of a dispersion correction was not successful in every case, however; for instance when we compare the $I_3^- \cdots I_3^-$ interaction energy of the ωB97X (-0.435 kcal/mol) functional to that of the ωB97XD (0.202 kcal/mol) functional with the a-TZ basis set in ethanol, it can be seen that the dispersion correction significantly decreases the accuracy of the method. However, it should be pointed out that the dispersion correction in ωB97XD is identical to the D2 correction with regards to the formula used, with the major differences being that the dispersion correction in ωB97XD omits the total scaling factor (s_6) and the constant a is different, see equation 2 in Chapter 2 and references [18, 19].

In Table 3.3 we have listed the $I_3^- \cdots I_3^-$ interaction energies for various DFT functionals utilising the dTZ basis set. Interestingly, with the PBE-D2 functional the $I_3^- \cdots I_3^-$ interaction energy became 8 % and 4 % more stabilising for ethanol and water, respectively. Although the magnitude of the additional stability calculated with a specific basis set is functional dependent, we found that the E_{INT} is calculated as being generally more stabilising when using the dTZ basis set with all the selected DFT functionals listed in Table 3.3 as compared to those obtained with the a-TZ basis set.

We are unsure of why the dTZ basis set consistently yields a more stabilising $I_3^- \cdots I_3^-$ interaction energy than the a-TZ basis set, however, the authors of the dTZ basis set mention that this basis set yields results "not too far from the DFT basis set limit" [20]. There are, however, cases where dTZ in combination with certain DFT functionals yields an E_{INT} less stabilising when compared to their a-TZ basis set counterparts, i.e. the ωB97X and ωB97XD functionals.

3.3. Dependence of the $I_3^- \cdots I_3^-$ interaction energy (E_{INT}) on the electrostatic environment

As discussed above, the $I_3^- \cdots I_3^-$ interaction energies in ethanol and water summarised in Tables 1, 2 and 3 show a substantial dependence on the environment. In order to further investigate this effect, we have added chloroform (ε=4.7113) and *n*-methylformamide-mixture (ε=78.3553) as solvents.

In Table 3.4 we summarise the $I_3^- \cdots I_3^-$ interaction energies (E_{INT}) and energy of stabilisation by the solvent (ΔE_S) values for our selected solvents, while selected results are represented graphically in Fig. 3.4 and Fig. 3.5.

Table 3.4 – E_{INT} and ΔE_S (in italics) (kcal/mol) for chloroform, ethanol, water and *n*-methylformamide-mixture using the a-TZ, TZ and dTZ basis sets.

Solvent	[a]CCSD	[b]MP2	MP2	[c]HF	PBE-D2	[d]PBE-D2	TPSS-D2	[d]TPSS-D2	B97D	[d]B97D
	$I_3^- \cdots I_3^-$ Interaction Energy (kcal/mol) and ΔE_S (kcal/mol)									
Chloroform (ε = 4.7113)	5.31	5.52	3.18	11.89	5.43	5.32	5.65	5.55	5.50	5.42
	-33.16	*-34.03*	*-33.11*	*-33.18*	*-33.05*	*-33.80*	*-33.28*	*-33.90*	*-32.95*	*-33.96*
Ethanol (ε = 24.852)	-0.80	-0.77	-3.19	6.04	-0.81	-0.87	-0.57	-0.62	-0.60	-0.64
	-40.53	*-41.56*	*-40.48*	*-40.55*	*-40.47*	*-41.36*	*-40.74*	*-41.47*	*-40.34*	*-41.47*
Water (ε = 78.3553)	-1.80	-1.79	-4.22	5.04	-1.82	-1.88	-1.58	-1.62	-1.59	-1.62
	-41.72	*-42.77*	*-41.66*	*-41.73*	*-41.66*	*-42.58*	*-41.94*	*-42.69*	*-41.72*	*-42.68*
n-methyl-formamide-mixture (ε = 181.56)	-2.06	-2.06	-4.48	4.78	-2.09	-2.14	-1.85	-1.89	-1.85	-1.88
	-42.03	*-43.09*	*-41.98*	*-42.05*	*-41.98*	*-42.90*	*-42.26*	*-43.01*	*-42.03*	*-43.00*

[a]CCSD/a-TZ//MP2/TZ

[b]MP2/TZ

[c]HF/a-TZ//MP2/a-TZ

[d]dTZ basis sets

It is clear from both Table 3.4 and Fig. 3.4 that there is a substantial dependence of the $I_3^- \cdots I_3^-$ interaction energy on the dielectric constant. In Table 3.4 we list results for three WFT methods and three DFT methods with CCSD/a-TZ//MP2/TZ as reference, where we see that the ΔE_S values of the listed methods compare well to one another for a particular solvent. Downs and Adams [21] reported that the hydration (ΔH^o) of the gaseous I_3^- ion to be -44.0 kcal/mol, where it can be seen that all the methods listed in Table 3.4 yield comparable results. This similarity of ΔE_S values for the various methods suggests that all the methods account for the effect the solvent has on the I_3^- ion, but not necessarily for the $I_3^- \cdots I_3^-$ interaction energy. Results for MP2/TZ have also been included since this was the WFT method that yields results for the $I_3^- \cdots I_3^-$ interaction energy most comparable to the CCSD/a-TZ//MP2/TZ benchmark (see Section 3.1.3).

We also included E_{INT} and ΔE_S values for the three listed DFT functionals utilising the dTZ basis set. It can be seen that the E_{INT} is stabilised by between approximately 2 % and 10 % and the ΔE_S by approximately 2 % when the dTZ basis set is utilised. We believe this increase in stabilisation found for E_{INT} and ΔE_S is a result of what was discussed earlier in Section 3.2.3, namely that the dTZ basis set yields results closer to the DFT basis set limit [20].

In Fig. 3.4 three WFT methods (CCSD, MP2 and HF) were included alongside one DFT functional (TPSS-D2) to demonstrate that both WFT and DFT methods exhibit similar dependence on the dielectric constant even though the E_{INT} differs for a particular method for each of the solvents for comparison we have only included data obtained with the a-TZ basis set although in the Section 3.1.3 we concluded that MP2/TZ gives the most comparable results to our CCSD/a-TZ//MP2/TZ benchmark. The exclusion of MP2/TZ from Fig. 3.4 was done for clarity, seeing that MP2/TZ directly overlays with our CCSD/a-TZ//MP2/TZ benchmark. In Fig. 3.4 the TPSS-D2 result is shown rather than the better PBE-D2 result for clarity, since the PBE-D2 result exactly overlays the benchmark CCSD result. In Section 3.1.3 we observed that the HF $I_3^-\cdots I_3^-$ interaction energy remains repulsive in both ethanol and water, which is also shown here in Table 3.4 and Fig. 3.4 with two additional solvents (chloroform and *n*-methylformamide-mixture). Despite the increase of the dielectric constant to ~181 the E_{INT} (4.78 kcal/mol) for the HF method remains repulsive. Thus, we conclude that the $I_3^-\cdots I_3^-$ interaction energy for HF will always remain repulsive regardless of the environment. We believe this is a result of the inability of HF to model dispersion interactions and also proves that highly repulsive electrostatic forces in general, can be 'damped', in particular the electrostatic forces present between the terminal atoms of the I_3^- dimer.

In Fig. 3.4 we notice almost identical behaviour exhibited by CCSD/a-TZ and TPSS-D2/a-TZ when E_{INT} is considered as a function of the dielectric constant. Furthermore, the graph suggests that a dielectric constant of ~20 is needed for this $I_3^-\cdots I_3^-$ interaction energy to become favourable, if the CCSD and TPSS-D2 methods are considered. If MP2/a-TZ is considered in Fig. 3.4, we observe that a lower dielectric constant of ~10 is needed before the $I_3^-\cdots I_3^-$ interaction energy becomes favourable. This decrease in the minimum required dielectric constant needed for the $I_3^-\cdots I_3^-$ interaction energy to become favourable is a result of MP2's overestimation of dispersion interactions which is exposed when the a-TZ basis set is used, as is visible in Fig. 3.4 for the calculated $I_3^-\cdots I_3^-$ interaction energies.

To our knowledge the only previously reported theoretical study on the interactions between ions with the same sign of charge was carried out by Grimme and Djukic [22] in 2011, where they studied cation-cation interactions between rhodium complexes utilising the COSMO

solvent model. The authors mentioned that the dispersion corrections are essential when utilising DFT functionals to study these complexes and they proved that the driving force behind the formation of their doubly charged complex can be attributed to dispersion interactions. Furthermore, they pointed out that the repulsion present for the equilibrium structure is 40 kcal/mol, which concurs with our 34 kcal/mol. In an extensive review article written by Pyykkö [23], in 1996, summarising numerous examples of closed-shell interactions stated that "When no other obvious bonding contributions exist, one finds at the *ab initio* level that the attraction is due to correlation effects" [23].
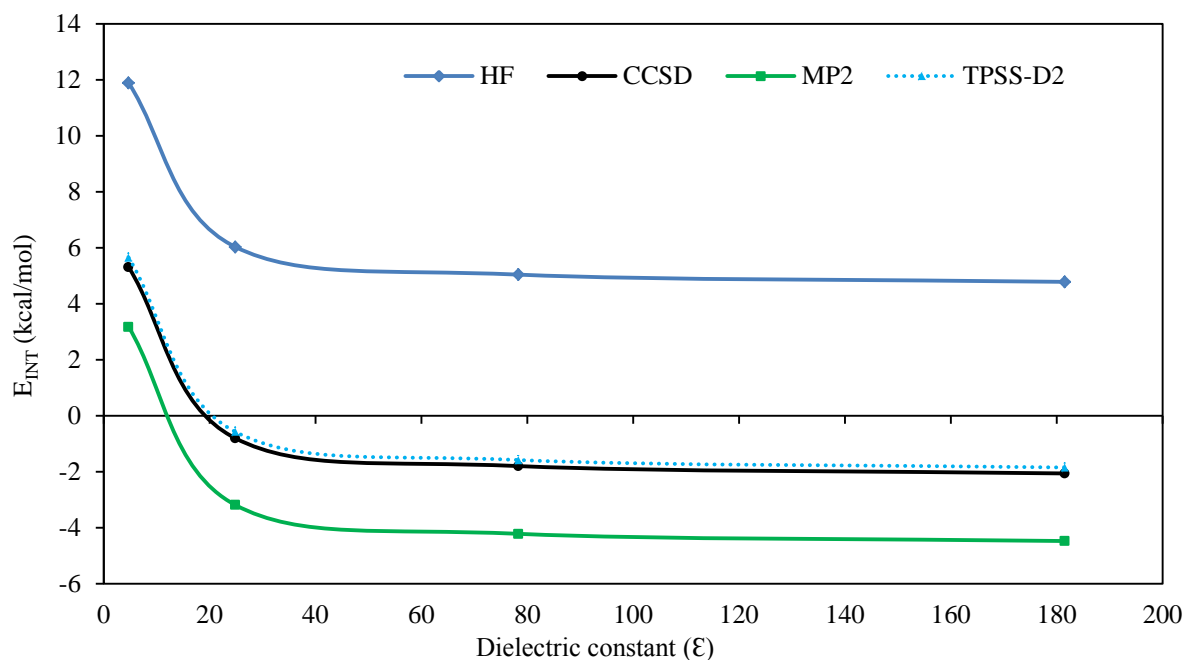
Fig. 3.4 – E_{INT} for the I_3^- dimer in various solvents: chloroform, ethanol, water and *n*-methyl-formamide utilising the a-TZ basis set. PBE-D2 results are not shown, see text.

A theoretical study performed by Aquino *et al.*[24] investigating the dependence of hydrogen bonding on the solvent used, concluded that as the dielectric constant increases the intermolecular interaction decreases. A similar theoretical study was performed by Lu *et al.*[25] on halogen bonding (X-B) in solution, where they found similar solvent dependent behaviour to that found for hydrogen bonding. Furthermore, they showed that the X-B interaction is 1 kcal/mol less stabilising in solvent than in the gas phase. This contrasts considerably with what we have found for our study of the I_3^-, where a stabilisation of 35 kcal/mol is provided by the solution if E_{INT} is considered. Gora *et al.*[26] elucidated the influence of the solvent on intermolecular interactions, where they showed that the observed trend is a result of the decrease in the contribution of the electrostatic interactions to the total interaction energy as the dielectric constant increases. They also mentioned that their results were generally consistent with what Cammi *et al.* [27] and Contador *et al.* [28] found for

hydrogen bonded complexes. Riley, Vondrášek and Hobza [29] studied interaction energies of biological interest using DFT-D in gas phase and solution where they found a similar dependence of the electrostatic component on the dielectric constant. Furthermore, they investigated the dependence of the interaction energy on the damping parameter (S_R), found in the damping function, where they showed it changed very little from the gas phase to a highly polar environment. However, we should mention they also studied dispersion bound complexes and found that there is an inverse relationship between the dielectric constant and the interaction energy, i.e. opposite to our study. Although the $I_3^- \cdots I_3^-$ dimer is an example of a dispersion bound complex we suspect that this difference is due to the attractive nature of the electrostatic contribution to the total attractive interaction energy. Their results correlate to what we are seeing with the $I_3^- \cdots I_3^-$ intermolecular interaction, the electrostatic interaction (repulsive) contribution decreases and as a result the total interaction energy increases. We believe this trend is applicable to any system where repulsive electrostatics are present, which is also observed for the cation-cation interactions present in the rhodium complexes, mentioned earlier [22]. Furthermore, cation-cation and anion-anion interactions have been observed in solution using NMR during a study investigating the hydration of oxidised metals and chloride anions [30].
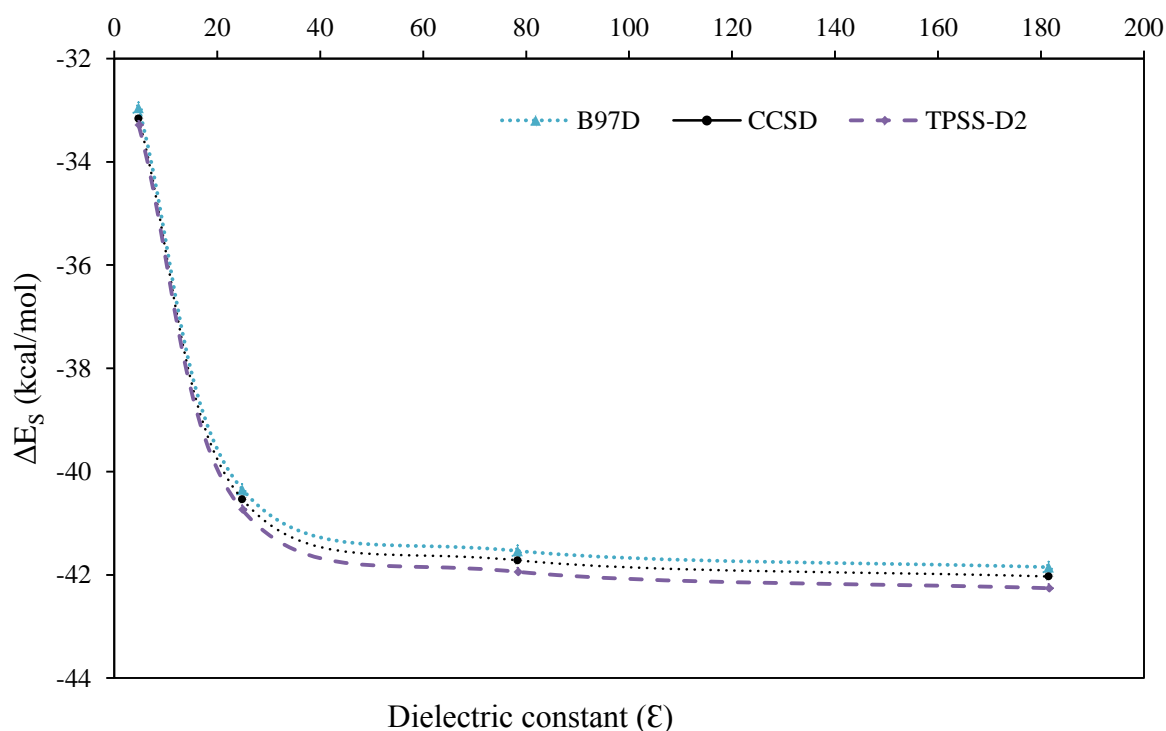

Fig. 3.5 – ΔE_S values calculated for I_3^- in implicit solvent models for chloroform, ethanol, water and *n*-methyl-formamide-mixture utilising the a-TZ basis set.

In Fig. 3.5 we graphically represent selected results listed in Table 3.4, showing the stabilisation provided by the solvent (ΔE_S) against the dielectric constant, where it can be seen

that the behaviour of ΔE_S with changing dielectric constant is similar to that of the $I_3^- \cdots I_3^-$ interaction dependence. The dielectric constant represents the polarity of the solvent, which is implicitly modelled by surrounding the solute with a polarisable charge distribution, thus the higher the dielectric constant the higher the electrostatic interaction between the solute and solvent [31]. The similarities in the dependence on the dielectric constant between Fig. 3.4 and Fig. 3.5 suggests that this increase in stability of the I_3^- ion provided by the solvent decreases the electrostatic repulsion between the I_3^- ions and as a result stabilises the $I_3^- \cdots I_3^-$ interaction. The similar ΔE_S results for all the methods listed in Table 3.4 suggest that the similarity can be assigned to the ability of each of the methods to model electrostatic interactions, in particular solute-solvent interactions, which explains the trends seen in both Fig. 3.4 and Fig. 3.5 (see ref. [29] and references therein).

It was mentioned earlier that Fig. 3.4 shows that a dielectric constant of about 20 is needed for this $I_3^- \cdots I_3^-$ interaction to become favourable. In Fig. 3.5 we can associate a dielectric constant of 20 to a stabilisation (ΔE_S) of about 40 kcal/mol, which is then what is needed for a single I_3^- ion to change the $I_3^- \cdots I_3^-$ interaction from repulsive to attractive. Thus in solid state one would expect this stabilisation to be equal to or greater than what is found in a solvent environment. It is therefore reasonable to postulate that if the stabilisation in the solid state is more than what is found for *n*-methylformamide-mixture ($\Delta E_S = 42$ kcal/mol), it can be suspected that the E_{INT} will be equal to or less stabilising than -2.0 kcal/mol (see Table 3.4) assuming the geometry is comparable.

3.4. Influence of the solvent on the PES
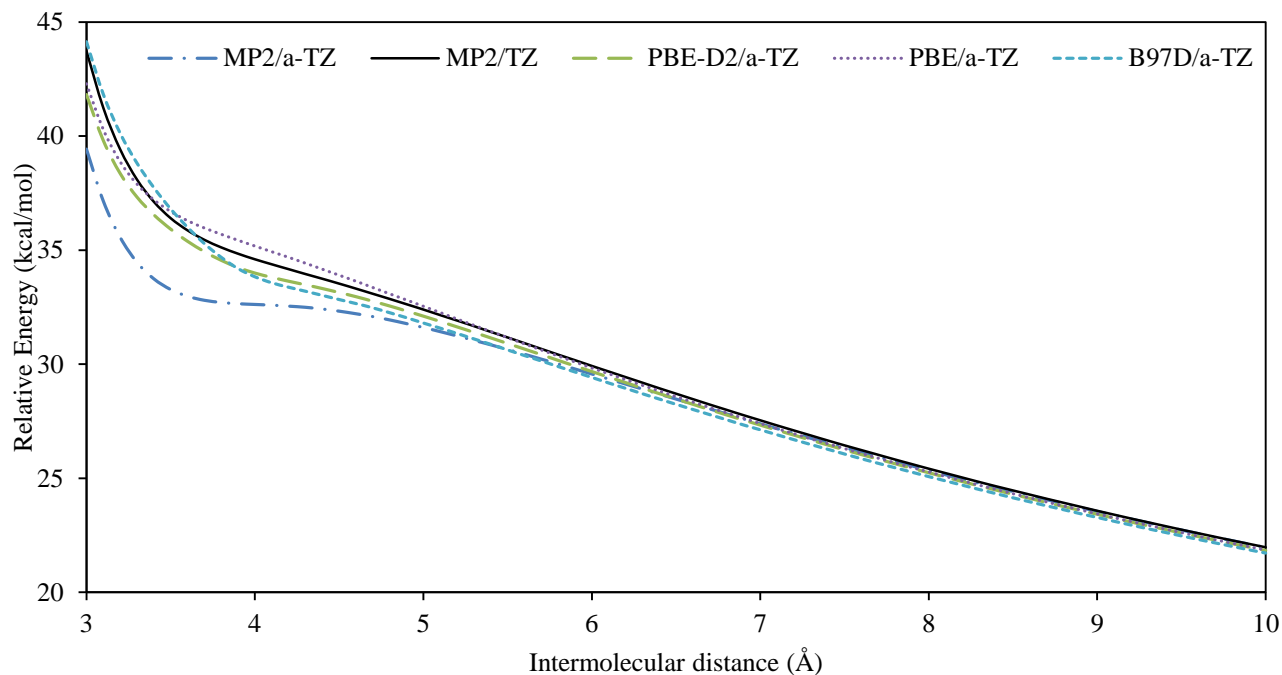
Fig. 3.6 – The PES curve of the I_3^- dimer in the gas phase at various levels of theory.

In Fig. 3.6 the PES curves for MP2 and three DFT functionals of the I_3^- dimer in the gas phase are included where the relative energy, also referred to as the interaction energy, is represented as a function of the $I_3^- \cdots I_3^-$ intermolecular distance. Here we see that MP2 utilising the a-TZ basis set describes the gas phase as having a spurious stationary point at ~4 Å, as well as exhibiting the least repulsive relative energy at 3 Å, which are both a result of the overestimation of the $I_3^- \cdots I_3^-$ interaction energy discussed in Section 3.1. However, when using the TZ basis set the PES changes so that no stationary point could be obtained. When we consider the PES curves for the three selected DFT functionals, we see that they behave similarly to MP2/TZ in the gas phase, describing the PES of the I_3^- dimer in the gas phase without any stationary points. Fig. 3.6 also illustrates how highly repulsive the $I_3^- \cdots I_3^-$ electrostatic interaction is in the gas phase and the linear behaviour of the potential energy as a function of the intermolecular distance, at relatively large distances, corresponds to electrostatic repulsion between same charge ions. Even at an intermolecular distance of 10 Å the repulsive interaction energy remains approximately 21 kcal/mol.

Fig. 3.7 – PES of the I_3^- dimer at the MP2/TZ level of theory for chloroform ($\varepsilon = 4.7113$), ethanol ($\varepsilon = 24.852$), water ($\varepsilon = 78.3553$) and *n*-methyl-formamide-mixture ($\varepsilon = 181.56$).

In Fig. 3.7 the PES curves obtained by performing a linear scan of the I_3^- dimer at the MP2/TZ level of theory are shown for a variety of solvents with a dielectric constant that ranges from approximately 5 to 182. Fig. 3.7 illustrates the dependence of the PES on the solvent used, which is clearly visible when the position of the respective stationary points (where the intermolecular distance is approximately 3.8 Å) on the PES curves of the I_3^- dimer in chloroform and ethanol is compared, where the value of the relative energy (also referred to as $I_3^- \cdots I_3^-$ interaction energy) changes from repulsive to attractive, respectively (also see Table 3.4). We observe that there is a less substantial change in the PES curves of the I_3^- dimer when water and *n*-methylformamide-mixture are compared as solvents. However, we should mention the discrepancies of the stationary points present for the PES curves for the I_3^- dimer in Fig. 3.7 are a result of our methodology in the calculation of the relative energy. All the PES curves were constructed by calculating the total energy of the I_3^- dimer by varying only the $I_3^- \cdots I_3^-$ intermolecular distance from 3 Å to 10 Å, keeping in mind that each of the I_3^- ions geometry are kept stationary with the geometry obtained from the optimised geometry of the I_3^- ion for a particular method (see Section 2.3). This explains why the relative energies of our various stationary points are slightly different in Fig. 3.7 than our calculated $I_3^- \cdots I_3^-$ interaction energies in Table 3.4.

Furthermore, the $I_3^- \cdots I_3^-$ intermolecular distances are similar for the various PES curves in Fig. 3.7 with regards to the stationary point. Also, the intermolecular distances for the stationary points present in the PES curves in Fig. 3.7 concur with the results listed in Table 3.2 for the optimised I_3^- dimer in ethanol and water, where the optimised structure for the I_3^- dimer yielded an intermolecular distance of approximately ~3.8 Å, comparable to the CSD average for the $I_3^- \cdots I_3^-$ intermolecular distance.

We should mention that we did not include the CCSD/a-TZ//MP2/TZ level of theory used in previous sections as a benchmark in studying the PES of the I_3^- dimer in solution due to the computational cost. Therefore, we are using the MP2/TZ as a benchmark when we compare PES curves of various methods.
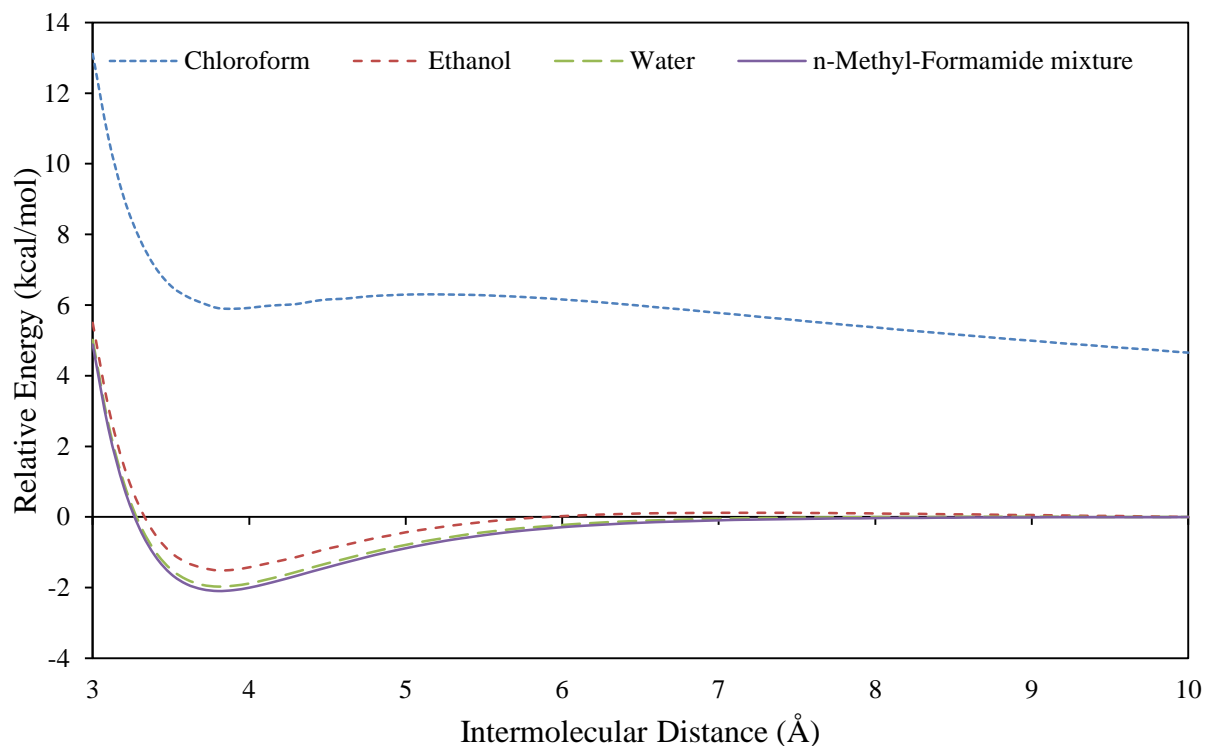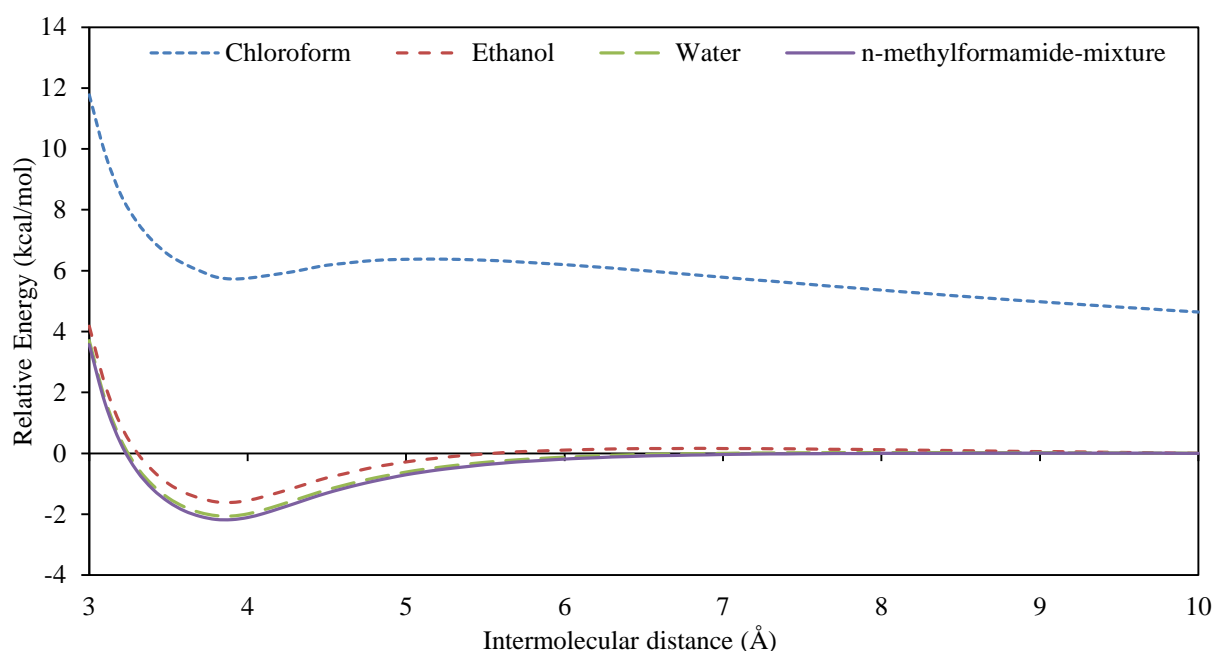

Fig. 3.8 – PES of the I_3^- dimer at the PBE-D2/a-TZ level of theory for chloroform ($\epsilon = 4.7113$), ethanol ($\epsilon = 24.852$), water ($\epsilon = 78.3553$) and *n*-methylformamide-mixture ($\epsilon = 181.56$).

Fig. 3.8 shows the PES curves of the DFT functionals which gave results most comparable to our CCSD/a-TZ//MP2/TZ benchmark $I_3^- \cdots I_3^-$ interaction energies (see Table 3.2 and 3.4). Here we see that these PES curves of PBE-D2 exhibits a similar solvent dependence to what was found for the *ab initio* method used in Fig. 3.7. When we compare the position of the energy minima of all the PES curves in Fig. 3.8 we see no substantial change in the $I_3^- \cdots I_3^-$ intermolecular distance; as before the values are comparable to one another and the CSD average. However, when we consider the value of the relative energy of the stationary points, we see that there is slight destabilisation present for chloroform and, the opposite is true for ethanol, water and *n*-methylformamide-mixture when we compare it to the E_{INT} found in Table 3.4. As mentioned earlier, these discrepancies are a result of the way in which we

calculate the relative energies. When Fig. 3.7 and Fig. 3.8 are compared to Fig. 3.6 the significant influence the solvent has on the PES is clearly visible. Let us consider the PES curves of the I_3^- dimer in the gas phase at various levels of theory shown in Fig. 3.6: no stationary point exists except for the spurious one obtained at the MP2/a-TZ level of theory. Furthermore, we observe in the gas phase a repulsive interaction energy at a $I_3^- \cdots I_3^-$ intermolecular distance of 10 Å of approximately 22 kcal/mol, where this interaction decreases to approximately 5 kcal/mol when modelled in chloroform at the MP2/TZ and PBE-D2/a-TZ levels of theory shown in Fig. 3.7 and Fig. 3.8, respectively. However, at a $I_3^- \cdots I_3^-$ intermolecular distance of 3.2 Å this repulsion present between the two I_3^- ions is decreased to zero when modelled in *n*-methylformamide-mixture. Also, we see that when the I_3^- dimer is considered in a solvent with a low dielectric constant, chloroform, the entire PES curve remains repulsive up to an intermolecular distance of 10 Å although substantially lower than what we found for the gas phase. Similar PES curves were obtained by Grimme and Djukic [22] in their study of the cation-cation between rhodium complexes for the gas phase and in solution.
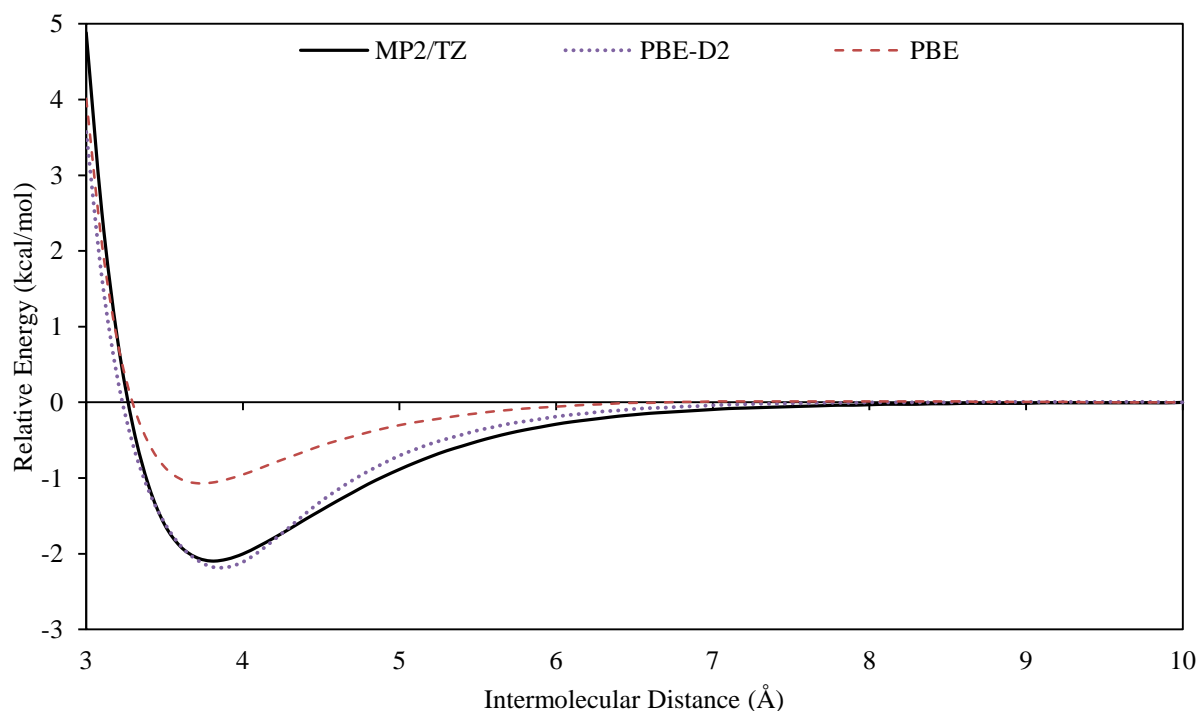
Fig. 3.9 – PES curves of MP2/TZ and the PBE, PBE-D2 DFT functionals for the I_3^- dimer in *n*-methylformamide-mixture utilising the a-TZ basis set.

The PES curves for the PBE and PBE-D2 DFT functionals using the a-TZ basis set with MP2/TZ as reference in the *n*-methylformamide-mixture solvent shown in Fig. 3.9. This graph was constructed to compare the best performing density functional (PBE-D2), when compared to the CCSD/a-TZ//MP2/TZ benchmark for the $I_3^- \cdots I_3^-$ interaction energy, to our

58

PES curve reference (MP2/TZ) and also to illustrate the influence of the D2 dispersion correction on the PES curve. Furthermore, we selected the *n*-methylformamide-mixture as solvent due its high dielectric constant and the influence the dielectric constant has on the strength $I_3^- \cdots I_3^-$ interaction energy, as well as the fact that the stabilisation of the interaction energy is mainly a result of electron correlation.

In Fig. 3.9 we see that where the $I_3^- \cdots I_3^-$ intermolecular distance is 3 - 3.2 Å, where both density functionals underestimate the repulsion relative to MP2/TZ and from 4.4 – 8.6 Å the opposite is true. When we consider the PES curves for the two density functionals the substantial difference the D2 correction makes to the surface can be seen, where the relative energy of the stationary point is almost 100 % more stabilising. Furthermore, the stationary point on the PES curves all exhibit comparable $I_3^- \cdots I_3^-$ intermolecular distances of approximately 3.8 Å when the CSD average is considered.

To summarise, an array of geometry optimisations were performed on the I_3^- ion and $I_3^- \cdots I_3^-$ in the gas phase and in selected solvents with a wide range of dielectric constants at various levels of theory. The optimised I-I bond lengths and the $I_3^- \cdots I_3^-$ intermolecular distances were compared to the calculated averages utilising the CSD. In particular, the nature of the $I_3^- \cdots I_3^-$ interaction was identified and the ability of various methods to model the $I_3^- \cdots I_3^-$ interaction was investigated in the gas phase and in solution, and then compared to the CCSD/a-TZ//MP2/TZ benchmark. Furthermore, the influence of the solvent on the $I_3^- \cdots I_3^-$ interaction energy was investigated at various levels of theory.

It was found that MP2 in combination with the TZ basis set yields results for the I-I bond length and the $I_3^- \cdots I_3^-$ intermolecular distance most comparable to the calculated CSD averages with deviations of 1 % from the I-I bond length of 2.52(5) Å and the $I_3^- \cdots I_3^-$ intermolecular distance of 3.80(10) Å. Furthermore, MP2/TZ also yields the most comparable $I_3^- \cdots I_3^-$ interaction energy, with deviations less than 4 % when the CCSD/a-TZ//MP2/TZ benchmark is considered. This makes MP2/TZ the best performing method when all three defined parameters are considered.

For the DFT results it was found that when the I-I bondlength of the I_3^- ion is considered the M06-2X outperforms the other DFT functionals with deviations of less than 1 %, with the PBE-D2, BP86 and TPSS functionals yielding the best results for the $I_3^- \cdots I_3^-$ intermolecular distance with deviations less than 2 % when the calculated CSD averages are considered. It was found that the only DFT functional that does not underestimate the $I_3^- \cdots I_3^-$ interaction energy, and may thus be considered as the most successful DFT functional is PBE-D2 with deviations less than 2 % from the CCSD/a-TZ//MP2/TZ benchmark. Considering the nature of the $I_3^- \cdots I_3^-$ interaction and the shallow PES, it seems reasonable to conclude that the

success of a DFT functional does not only depend in its ability to model the I-I bond length and the $I_3^- \cdots I_3^-$ intermolecular distance, but is rather determined by its ability to model the $I_3^- \cdots I_3^-$ interaction. Furthermore, when the calculated CSD averages for the I-I bond length and the $I_3^- \cdots I_3^-$ intermolecular distance are considered, most of the DFT functionals tested yield results with deviations less than 5 % and 10 %, respectively.

Additionally, it was shown that the $I_3^- \cdots I_3^-$ interaction energy increases as the dielectric constant increases for both WFT and DFT methods, corresponding to an increase in the stabilisation of the I_3^- ion provided by the solvent. The nature of the $I_3^- \cdots I_3^-$ interaction energy was concluded to be dispersion type interactions, which was proven in selected solvents with the aid of the HF method, which is well known to only account for electrostatic interactions [12]. Furthermore, the $I_3^- \cdots I_3^-$ interaction energy calculated by the HF method showed that the (repulsive) electrostatic component decreases as the dielectric constant increases. To conclude, the results shown in this chapter and the structures observed in the CSD, where these ions are known to pack in $[I_3^-]_\infty$ chains with intermolecular distances less than twice the vdW radii, suggest similarities with regards to the influence of electrostatic interactions between the I_3^- ion its surroundings for solvent and crystalline environments, where the stabilising interactions with its surroundings results in the decrease of the repulsion between the I_3^- ions, since the I_3^- ion is usually surrounded by cations in the solid state. This will be described in the next chapters.

References

1. Svensson, P.H. and L. Kloo, *Synthesis, Structure, and Bonding in Polyiodide and Metal Iodide−Iodine Systems.* Chemical Reviews, 2003. **103**(5): p. 1649-1684.

2. Loos, K.R. and A.C. Jones, *Structure of triiodide ion in solution. Raman evidence for the existence of higher polyiodide species.* The Journal of Physical Chemistry, 1974. **78**(22): p. 2306-2307.

3. Johnson, A.E. and A.B. Myers, *Solvent Effects in the Raman Spectra of the Triiodide Ion: Observation of Dynamic Symmetry Breaking and Solvent Degrees of Freedom.* The Journal of Physical Chemistry, 1996. **100**(19): p. 7778-7788.

4. Gabes, W. and D.J. Stufkens, *Electronic absorption spectra of symmetrical and asymmetrical trihalide ions.* Spectrochimica Acta Part A: Molecular Spectroscopy, 1974. **30**(9): p. 1835-1841.

5. Allen, F., *The Cambridge Structural Database: a quarter of a million crystal structures and rising.* Acta Crystallographica Section B, 2002. **58**(3 Part 1): p. 380-388.

6. Aragoni, M.C., et al., *Adducts of S/Se Donors with Dihalogens as a Source of Information for Categorizing the Halogen Bonding.* Crystal Growth & Design, 2012. **12**(6): p. 2769-2779.

7. Kloo, L., J. Rosdahl, and Per H. Svensson, *On the Intra- and Intermolecular Bonding in Polyiodides.* European Journal of Inorganic Chemistry, 2002. **2002**(5): p. 1203-1209.

8. Sharp, S.B. and G.I. Gellene, *Ab Initio Calculations of the Ground Electronic States of Polyiodide Anions.* The Journal of Physical Chemistry A, 1997. **101**(11): p. 2192-2197.

9. Myers, O.E., *Kinetics of the Triiodide Equilibrium.* The Journal of Chemical Physics, 1958. **28**(6): p. 1027-1029.

10. Riley, K.E. and P. Hobza, *Assessment of the MP2 Method, along with Several Basis Sets, for the Computation of Interaction Energies of Biologically Relevant Hydrogen Bonded and Dispersion Bound Complexes.* The Journal of Physical Chemistry A, 2007. **111**(33): p. 8257-8263.

11. Riley, K.E. and P. Hobza, *Strength and Character of Halogen Bonds in Protein–Ligand Complexes.* Crystal Growth & Design, 2011. **11**(10): p. 4272-4278.

12. Johnson, E.R., I.D. Mackie, and G.A. DiLabio, *Dispersion interactions in density-functional theory.* Journal of Physical Organic Chemistry, 2009. **22**(12): p. 1127-1135.

13. Datta, S.N., C.S. Ewig, and J.R. Van Wazer, *The geometric and electronic structures of I3− and I5− from effective-potential calculations.* Journal of Molecular Structure, 1978. **48**(3): p. 407-416.

14. Riley, K.E., et al., *Stabilization and Structure Calculations for Noncovalent Interactions in Extended Molecular Systems Based on Wave Function and Density Functional Theories.* Chemical Reviews, 2010. **110**(9): p. 5023-5063.

15. Johnson, E.R., et al., *Oscillations in meta-generalized-gradient approximation potential energy surfaces for dispersion-bound complexes.* The Journal of Chemical Physics, 2009. **131**(3): p. 034111-7.

16. Cerny, J. and P. Hobza, *The X3LYP extended density functional accurately describes H-bonding but fails completely for stacking.* Physical Chemistry Chemical Physics, 2005. **7**(8): p. 1624-1626.

17. Xu, X. and W.A. Goddard, *The X3LYP extended density functional for accurate descriptions of nonbond interactions, spin states, and thermochemical properties.* Proceedings of the National Academy of Sciences of the United States of America, 2004. **101**(9): p. 2673-2677.

18. Grimme, S., *Semiempirical GGA-type density functional constructed with a long-range dispersion correction.* Journal of Computational Chemistry, 2006. **27**(15): p. 1787-1799.

19. Chai, J.-D. and M. Head-Gordon, *Long-range corrected hybrid density functionals with damped atom-atom dispersion corrections.* Physical Chemistry Chemical Physics, 2008. **10**(44): p. 6615-6620.

20. Weigend, F. and R. Ahlrichs, *Balanced basis sets of split valence, triple zeta valence and quadruple zeta valence quality for H to Rn: Design and assessment of accuracy.* Physical Chemistry Chemical Physics, 2005. **7**(18): p. 3297-3305.

21. Downs AJ, A.G., in *Comprehensive Inorganic Chemistry*, E.H. Bailor JC, Nyholm R, Trotman-Dickenson AF, Editor 1973, Pergamon: Oxford.

22. Grimme, S. and J.-P. Djukic, *Cation−Cation "Attraction": When London Dispersion Attraction Wins over Coulomb Repulsion.* Inorganic Chemistry, 2011. **50**(6): p. 2619-2628.

23. Pyykkö, P., *Strong Closed-Shell Interactions in Inorganic Chemistry.* Chemical Reviews, 1997. **97**(3): p. 597-636.

24. Aquino, A.J.A., et al., *Solvent Effects on Hydrogen BondsA Theoretical Study.* The Journal of Physical Chemistry A, 2002. **106**(9): p. 1862-1871.

25. Lu, Y., et al., *Effects of solvent on weak halogen bonds: Density functional theory calculations.* International Journal of Quantum Chemistry, 2012. **112**(5): p. 1421-1430.

26. Gora, R.W., et al., *Intermolecular interactions in solution: Elucidating the influence of the solvent.* The Journal of Chemical Physics, 2004. **120**(6): p. 2802-2813.

27. Cammi, R., F.J.O. del Valle, and J. Tomasi, *Decomposition of the interaction energy with counterpoise corrections to the basis set superposition error for dimers in solution. Method and application to the hydrogen fluoride dimer.* Chemical Physics, 1988. **122**(1): p. 63-74.

28. Contador, J.C., et al., *A theoretical study of hydrogen-bonded complexes in solution: BSSE and decomposition of interaction energy.* Journal of Molecular Structure: THEOCHEM, 1994. **314**(1–2): p. 229-239.

29. Riley, K.E., J. Vondrasek, and P. Hobza, *Performance of the DFT-D method, paired with the PCM implicit solvation model, for the computation of interaction energies of solvated complexes of biological interest.* Physical Chemistry Chemical Physics, 2007. **9**(41): p. 5555-5560.

30. Friedman, H.L., *R. A. Robinson Memorial Lecture. Hydration of cation-cation and anion-anion pairs.* Faraday Discussions of the Chemical Society, 1988. **85**: p. 1-11.

31. Miertuš, S., E. Scrocco, and J. Tomasi, *Electrostatic interaction of a solute with a continuum. A direct utilizaion of AB initio molecular potentials for the prevision of solvent effects.* Chemical Physics, 1981. **55**(1): p. 117-129.

<div align="right">

CHAPTER 4

</div>

Electric field and crystal structure optimisations of I$_3^-$

Introduction

In this chapter we will study the influence of alternative electrostatic environments i.e. the electric field and various partial crystal structure models on both the geometry of the I_3^- ion and also the I_3^- dimer. These studies were carried out in order to see if other alternative electrostatic environments could be used other than the implicit solvent model used in Chapter 3 to aid in the study of these I_3^- ions and the $I_3^- \cdots I_3^-$ interactions. This study will consist of two parts, where the first part will investigate if the I_3^- ion and the I_3^- dimer can be modelled in an electric field with various strengths and orientations, by looking at the bond lengths and Mulliken charge distributions as parameters. Ideally, one would prefer an electric field that induces a minimum amount of change on the geometry and bond length of the I_3^- ion, since we saw in Chapter 3 that the I_3^- ion in optimised I_3^- dimer prefers a linear geometry and a disruption in the geometry can change the PES substantially in such a way that no stationary point can be obtained. Therefore, a stationary point would be more likely to find in a geometry that is closest to the optimised geometries in Chapter 3. The acquisition of a stationary point would enable us to calculate the $I_3^- \cdots I_3^-$ interaction energy. In part two the effect of changing the model of a crystal structure (ref. code SETHAB) on the bond length of the I_3^- ion will be studied at various levels of theory. Furthermore, the influence of each of the selected partial crystal structure models on the I_3^- ion will be investigated by comparing the optimised structure of the I_3^- ion in the selected crystal model to the optimised geometry of the I_3^- ion in the gas phase. The success of a method will be determined by the comparability of the optimised I_3^- ion in the selected crystal model to the experimental crystal.

4.1. Electric field results

4.1.1. The I_3^- ion

The first controlled electrostatic environment we will discuss is an electric field, which is defined by two parameters: direction and strength. Since our molecule is linear, it was orientated along the *z*-axis in standard orientation. This leaves us with two possible orientations for the electric field relative to the I_3^- ion, i.e. along the *z*-axis (shown in Fig. 4.1) or along the *x* or *y* axes (shown in Fig. 4.2), since these are equivalent.
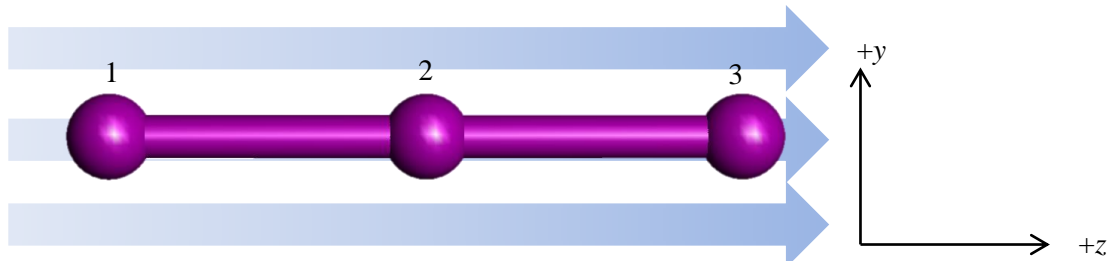
Fig. 4.1 – Direction of the electric field shown as arrows in the *z*-direction relative to the I_3^- ion's orientation.

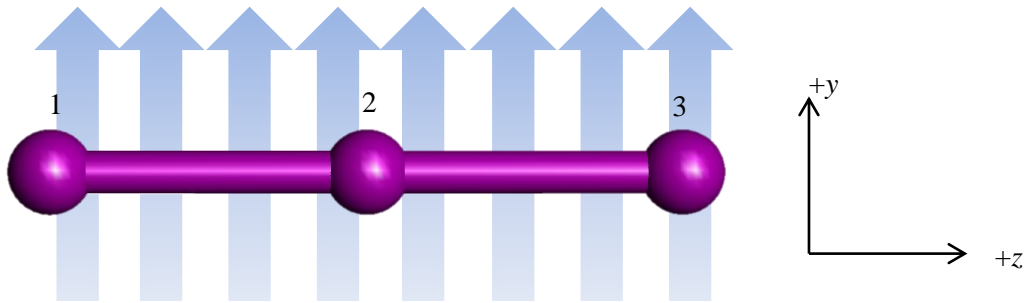**Fig. 4.2** – Direction of the electric field shown as arrows in the *y*-direction relative to the I_3^- ion's orientation.

Now that we have defined the two orientations of the electric field relative to the position of the I_3^- ion, we must investigate the influence the strength of the field has on the I_3^- ion and what determine the usable ranges of electric field strength, i.e. at what field strength the I-I bond breaks.

Table 4.1 – Bond lengths (Å) and Mulliken charges (*e*) of the optimised I_3^- ion in various electric field strengths (au) in the *z*-direction utilising MP2 with various basis sets.

Basis set	Electric Field Strength (au) *z*-axis direction	Bond length (Å)		Mulliken charges (*e*)		
		r_{12}	r_{23}	I_1	I_2	I_3
a-TZ	0	2.924	2.924	-0.63	0.25	-0.63
	0.001	2.902	2.946	-0.59	0.25	-0.66
	0.005	2.834	3.096	-0.42	0.24	-0.82
	0.009	Breaks into I_2 and I^-				
TZ	0	2.921	2.921	-0.54	0.09	-0.54
	0.001	2.900	2.944	-0.50	0.09	-0.58
	0.005	2.835	3.092	-0.33	0.07	-0.74
	0.009	Breaks into I_2 and I^-				
a-DZ	0	2.996	2.996	-0.57	0.14	-0.57
	0.001	2.975	3.025	-0.52	0.14	-0.61
	0.005	2.895	3.211	-0.32	0.14	-0.81
	0.009	Breaks into I_2 and I^-				
DZ	0	2.990	2.990	-0.54	0.08	-0.54
	0.001	2.971	3.017	-0.50	0.08	-0.58
	0.005	2.902	3.177	-0.33	0.07	-0.74
	0.009	Breaks into I_2 and I^-				

Optimised bond lengths and corresponding Mulliken charges for the I_3^- ion, calculated utilising MP2 with various basis sets to investigate possible basis set dependence on the outcome of the optimised geometry and charge distribution with respect to the electric field strength are listed in Table 4.1. The field direction relative to the I_3^- ion and atom numbering as illustrated in Fig. 4.1. If we consider the results listed in Table 4.1, we see that if the electric field is along the same axis as the I_3^- ion (*z*-axis), we observe breaking of the I-I bond at an electric field strength of 0.009 au. We observe that all the basis sets tested exhibit similar, comparable behaviour with respect to the electric field strength, where the asymmetry of the I_3^- ion increases as the electric field increases and ultimately one I-I bond breaks. Furthermore, in Table 4.1 we see that the magnitude of the Mulliken charges are basis set dependent, with the augmented basis sets yielding Mulliken charges larger in magnitude than the results with unaugmented basis sets. We also observe that as one I-I bond increases in length, as a result of the electric field pulling at one of the terminal iodine atoms, the other I-I bond decreases in length as the ability of the I^- to donate into the anti-bonding orbital of I_2 is decreased due to the pull of the electric field, as noted by others in the study of the I_3^- ion and its orbitals [1-3].

The effect of an electric field perpendicular to the orientation of the I_3^- ion (shown in Fig 4.2) was subsequently studied for comparison (see Table 4.2).

Table 4.2 – Bond lengths (Å), I-I-I angles (deg) and Mulliken charges (*e*) of the optimised I_3^- ion in various electric field strengths (au) in the *y*-direction utilising MP2 with various basis sets.

Electric field strength (au)			Bond length (Å)		Mulliken charges (*e*)		
Basis set	*y*-axis direction	Angle (I-I-I) (deg)	r_{12}	r_{23}	I_1	I_2	I_3
a-TZ	0	180	2.924	2.924	-0.63	0.25	-0.63
	0.001	178.8	2.919	2.920	-0.63	0.25	-0.63
	0.005	173.2	2.914	2.931	-0.61	0.25	-0.64
	0.009	166.4	2.896	2.966	-0.58	0.25	-0.67
	0.013		Breaks into I_2 and I^-				
TZ	0	180	2.921	2.921	-0.54	0.09	-0.54
	0.001	178.7	2.918	2.919	-0.54	0.09	-0.54
	0.005	173.1	2.913	2.929	-0.53	0.09	-0.56
	0.009	166.4	2.895	2.963	-0.50	0.11	-0.60
	0.013		Breaks into I_2 and I^-				
a-DZ	0	180	2.996	2.996	-0.57	0.14	-0.57
	0.001	178.7	2.995	2.995	-0.57	0.14	-0.57
	0.005	172.3	2.986	3.010	-0.55	0.14	-0.59
	0.009	164.0	2.961	3.062	-0.51	0.17	-0.66
	0.013		Breaks into I_2 and I^-				
DZ	0	180	2.99	2.99	-0.54	0.08	-0.54
	0.001	178.6	2.989	2.989	-0.54	0.08	-0.54
	0.005	172.2	2.982	3.002	-0.53	0.09	-0.56
	0.009	164.3	2.960	3.050	-0.49	0.10	-0.61
	0.013		Breaks into I_2 and I^-				

The bond lengths and Mulliken charge distributions for the optimised geometries of the I_3^- ion in various electric fields strengths in the direction of the *y*-axis are listed in Table 4.2, with the direction of the electric field shown in Fig. 4.2. We observe that when the electric field is orientated along the *y*-axis instead of along the *z*-axis, the maximum field strength tolerable before the I-I bond breaks increases from 0.009 au to 0.013 au. Furthermore, due to the directionality of the electric field relative to the I_3^- ion there is less asymmetry present with regard to the bond lengths, although at the MP2/a-TZ level of theory angle deformations of 1.3˚, 6.8 ˚ and 13.6˚ are observed for field strengths of 0.001 au, 0.005 au and 0.009 au, respectively. This decrease in the I-I-I angle can be seen for all the listed basis sets in Table 4.2 where the terminal iodine atom with the relatively more elongated I-I bond has the highest charge, which occurs as the I_3^- ion becomes asymmetric due to a decrease in the donation of electrons of the I^- into the anti-bonding orbital of I_2. Furthermore, we see that as the electric field strength increases the I-I-I angle decreases and so does the asymmetry of the I_3^- ion with

67

regards to the bond length, where all the listed basis sets in Table 4.2 exhibit this behaviour. This increase in asymmetry as the I-I-I angle decreases may be a result of the repulsion present between the terminal iodine atoms.

As before, the basis set dependence can be seen where the augmented basis sets yield charges that are larger in magnitude when compared to their unaugmented counterparts. We have thus confirmed that when an electric field is applied along the same axis on which the I_3^- ion is placed the largest change in the geometry is induced, far more than when the orientation of the electric field is perpendicular to the I_3^- ion (as shown in Fig. 4.2). Furthermore, we observe a relatively small change of 1.3˚ in the I-I-I angle when an electric field strength of 0.001 au is applied.

We will now extend our study to weaker electric fields to investigate the possibility of minimal distortion in the geometry. As mentioned before, the aim is to obtain an electric field with an orientation and strength that induces a minimum change in the optimised geometry of the I_3^- ion. The optimised geometries for the I_3^- dimer in Chapter 3 showed that the I_3^- ions are linear, thus ideally if this linearity is preserved for the I_3^- ions the results in Chapter 3 can be reproduced using an alternative electrostatic environment, i.e. the electric field, to the implicit solvent model.

Table 4.3 – Bond lengths (Å), I-I-I angles (deg) and Mulliken charges (*e*) of the optimised I_3^- geometry in various electric field strengths (au) in the *y*-direction utilising MP2 with various basis sets.

Basis set	Electric Field Strength (au) *y*-axis direction	Angle (I-I-I) (deg)	Bond lengths (Å)		Mulliken charges (*e*)		
			r_{12}	r_{23}	I_1	I_2	I_3
a-TZ	0	180.0	2.924	2.924	-0.63	0.25	-0.63
	0.0002	179.7	2.919	2.919	-0.63	0.25	-0.63
	0.0004	179.5	2.920	2.920	-0.63	0.25	-0.63
	0.0006	179.2	2.920	2.920	-0.63	0.25	-0.63
	0.0008	178.9	2.919	2.919	-0.63	0.25	-0.63
TZ	0	180.0	2.921	2.921	-0.54	0.09	-0.54
	0.0002	179.8	2.918	2.918	-0.54	0.09	-0.54
	0.0004	179.5	2.918	2.918	-0.54	0.09	-0.54
	0.0006	179.2	2.918	2.918	-0.54	0.09	-0.54
	0.0008	178.9	2.918	2.919	-0.54	0.09	-0.54
a-DZ	0	180.0	2.996	2.996	-0.57	0.14	-0.57
	0.0002	179.8	2.995	2.995	-0.57	0.14	-0.57
	0.0004	179.4	2.994	2.995	-0.57	0.14	-0.57
	0.0006	179.2	2.995	2.995	-0.57	0.14	-0.57
	0.0008	178.9	2.995	2.995	-0.57	0.14	-0.57
DZ	0	180.0	2.990	2.990	-0.54	0.08	-0.54
	0.0002	179.8	2.988	2.988	-0.54	0.08	-0.54
	0.0004	179.4	2.988	2.988	-0.54	0.08	-0.54
	0.0006	179.1	2.988	2.989	-0.54	0.08	-0.54
	0.0008	178.8	2.988	2.989	-0.54	0.08	-0.54

Angles, bond lengths and the Mulliken charge distributions for the I_3^- ion in various electric fields are listed in Table 4.3, where we see similar trends as before with respect to the I-I-I angle decreasing as the field strength increases. We also observe a negligible decrease in the bond length, while the Mulliken charge distribution remains constant.

We are therefore able to utilise field strengths of 0.001 au and 0.005 au along the *z*-axis and 0.0002 au, 0.0004 au and 0.001 au along the *x*-axis in order to mimic the behaviour of the I_3^- in solvent, since these electric field strengths induce a minimum change in the optimised geometry. We can now extend our investigation to the I_3^- dimer in these selected electric fields.

4.1.2. The I_3^- dimer

We will now continue our investigation to see if the electric field will provide the needed stabilisation so that the PES of the I_3^- dimer changes substantially from the gas phase, to yield a stationary point. From the investigation done in Chapter 3, we know that MP2/a-TZ yields a stationary point in the gas phase that is spurious in nature. This is why the TZ, a-DZ and DZ basis sets were included to verify whether or not a stationary point found for the a-TZ basis set is an artefact or not. The validity of the MP2/a-TZ method can be verified by the presence of a stationary point for each of the other basis sets, as was the case with the results in Table 3.1 where all the listed basis sets yield a stationary point in the selected solvents.
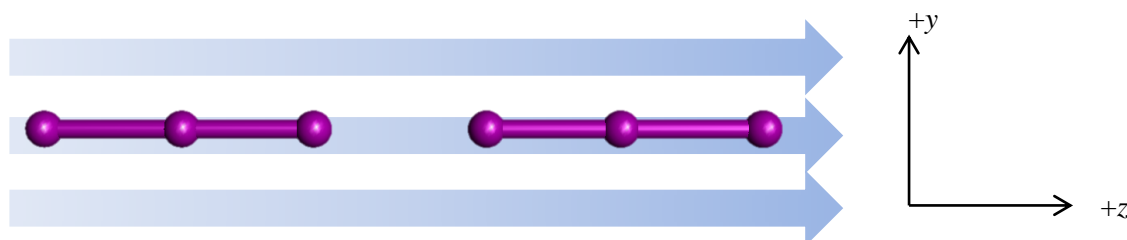
Fig. 4.3 – Direction of the electric field shown as arrows in the z-direction relative to the I_3^- dimer's orientation.
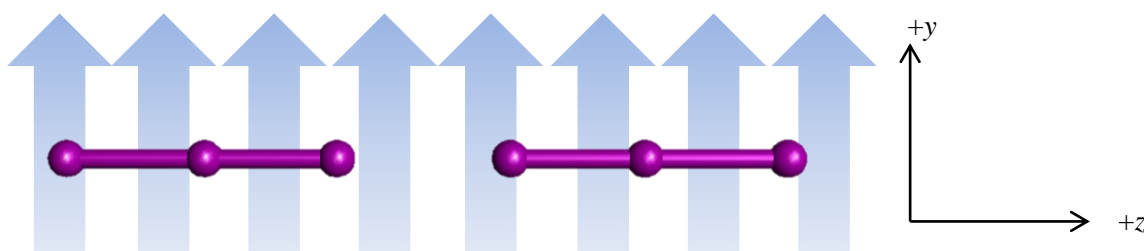
Fig. 4.4 – Direction of the electric field shown as arrows in the y-direction relative to the I_3^- dimer's orientation.

In Fig. 4.3 and Fig. 4.4 we show, as before with the I_3^- ions, the two directions of the electric field utilised for this investigation. In Table 4.4 we list all the various optimisations performed within the various electric field strengths and also the orientation of the electric field relative to the linear $I_3^- \cdots I_3^-$.

70

Table 4.4 – Various directions and magnitudes of the electric fields tested for the $I_3^- \cdots I_3^-$ complex utilising MP2 with various basis sets.

MP2	Electric Field Strength (au)	
basis set	*z*-axis direction	*x*-axis direction
a-TZ	0.001	0.0002
	0.005	0.0004
		0.001
TZ	0.001	0.0002
	0.005	0.0004
		0.001
a-DZ	0.001	0.0002
	0.005	0.0004
		0.001
DZ	0.001	0.0002
	0.005	0.0004
		0.001

When the electric field was applied to $I_3^- \cdots I_3^-$ in the *z*-direction, with both strengths 0.001 au and 0.005 au, the outcome was that the triiodides repelled one another leading to an increase in the $I_3^- \cdots I_3^-$ intermolecular distance with every optimisation step such that the minimum energy would be found at infinite separation.

Fig. 4.5 – Geometry of I_3^- dimer at the end of the attempted optimisation cycle at the MP2/a-TZ level of theory with an electric field strength of 0.01 au along the *y*-axis.

On the other hand, if the electric field is applied to $I_3^- \cdots I_3^-$ in the *y*-direction, we see that as before with the I_3^- ion, the electric field induces a bent geometry (shown in Fig. 4.5) and no stationary point could be obtained for an electric field strength 0.001 au, 0.0002 au, 0.0004 au due to the geometry oscillating. We observe that even at the MP2/a-TZ level of theory, no stationary point could be obtained. Furthermore, the other basis sets yielded geometries, at the end of their optimisations, with the ions at infinite separation. This illustrates that the electric field, for the orientations and strengths tested, is not sufficient in stabilising the I_3^- in such a way that the $I_3^- \cdots I_3^-$ interaction is favourable. The results suggest that we are unable to obtain any stationary points for the I_3^- dimer, due to the changes in the I_3^- ion's geometry induced by the electric field.

4.2. Crystal optimisations

One crystal in particular was investigated, with reference code: SETHAB [4]. Details are given in Table 4.5.

This crystal was selected since:

1) It did not exhibit disorder (more than one coordinate for a particular atom) when the structure was analysed utilising the molecular modelling software package, Cerius[2], the only crystal structure to exhibit this characteristic despite the fact that our CSD search explicitly excluded disordered structures.

2) The cation is small and organic, thus containing as few as possible electrons to reduce the computational expense of the quantum mechanical QM calculations.

Table 4.5 – Crystallographic data obtained from the CSD for SETHAB.

Chemical formula:	$C_{10}H_9N_2^+ \cdot I_3^-$
Name:	4-(4-Pyridyl) pyridinium triiodide
Space group:	$P\bar{1}$
Cell Lengths (Å):	**a** 8.8399(9); **b** 9.6529(8); **c** 9.7154(7)
Cell Angles (deg):	**α** 107.743(7); **β** 104.709(7); **γ** 110.791(8)
Cell volume ($Å^3$):	674.382
R-Factor:	3.6
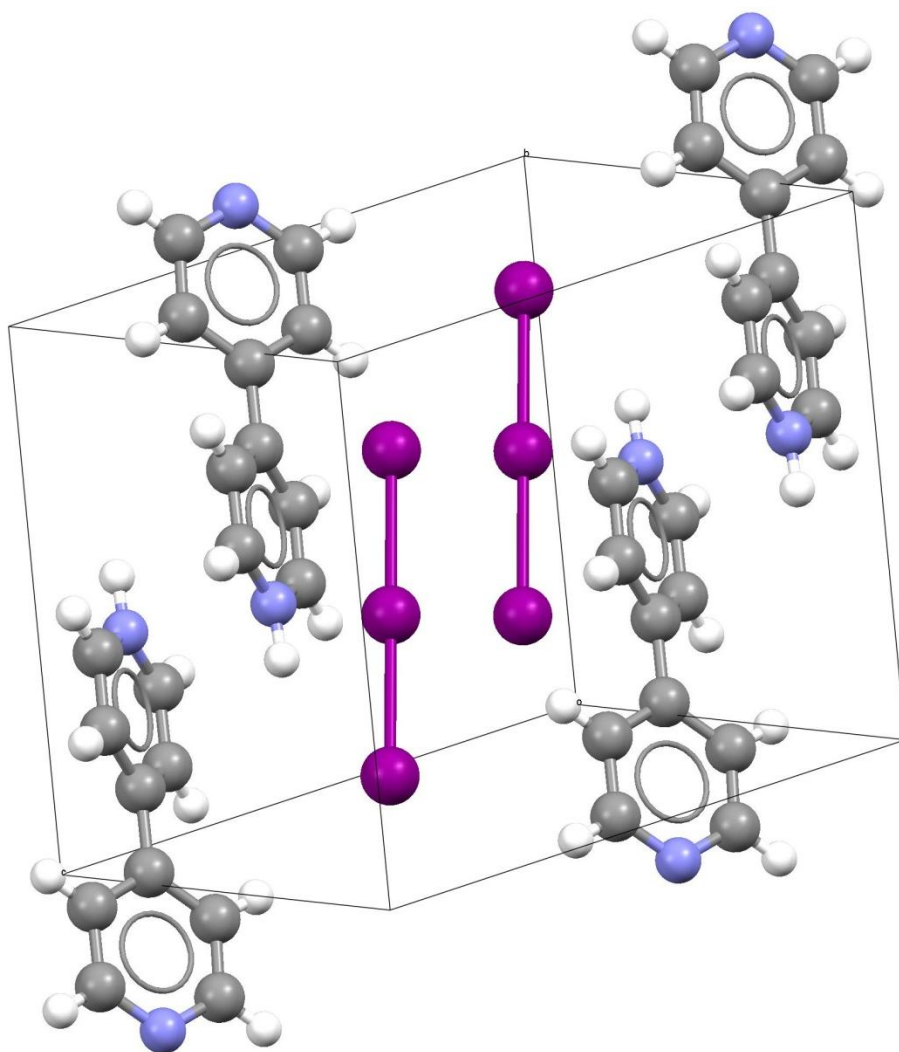
Fig. 4.6 – Expanded unit cell of SETHAB shown with two anions (I_3^-) and four cations ($C_{10}H_9N_2^+$), with the asymmetric unit consisting of one anion and one cation.

4.2.1. The I_3^- in SETHAB

Ideally, in order to obtain a realistic representation of the electrostatic interactions in a crystal structure a large number of molecules should be included in a model. However, when using QM methods such as WFTs and DFTs, one is limited by time constraints and computational cost. In particular, the widely used WFT method, MP2, was found to be too computationally expensive when studying crystals containing numerous atoms and thus alternative methods were investigated, such as the least expensive WFT method, HF, and various DFT functionals with relatively small basis sets. The B97D was included due to the dispersion correction, B971 due to its success in reproducing the I-I bond length in SETHAB, while B3LYP was included since it is a hybrid functional known to give accurate results for energetics of structural properties of molecules and solids (see [5] and references therein). In order to minimise computational cost, the selected crystal structures were optimised utilising the

73

minimum number of molecules required to model the electrostatic interactions. In this section we describe the investigation of various models of the crystal structure SETHAB [4] obtained from the CSD [6]. All the optimisations were performed by keeping the coordinates of the cations <u>stationary</u> and optimising <u>only</u> the positions of the I_3^- ions at various levels of theory. We were particularly interested in observing how the geometries of the triiodides change as a function of the selected partial packing arrangements and methods used. A further aim was to see if the I-I bond lengths found in the crystal structure could be reproduced.
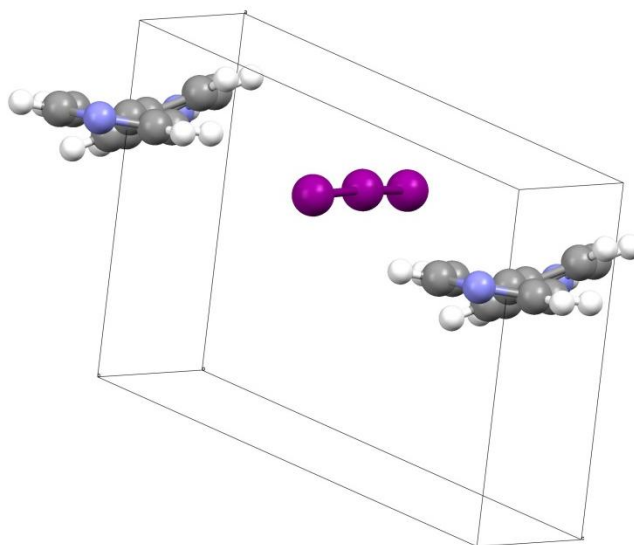
Fig. 4.7 – Selected partial crystal structure model (**1**), serving as input coordinates for triiodide optimisations listed in Table 4.6.

In Fig. 4.7 we show partial crystal structure model **1**, which serves as the input geometry for the optimisation of the I_3^- ion's geometry. The optimised bond lengths and deviations are listed in Table 4.6. The experimental structure of this particular I_3^- ion in **1** is asymmetric with I-I bond lengths of 2.951 Å and 2.938 Å in the solid state, and we would expect this asymmetry to be mimicked in the optimised geometry of the I_3^- ion in **1**. Although model **1** should be expanded substantially to provide a more realistic crystal structure environment, it was decided to limit the number of molecules in the QM investigation of SETHAB to a computationally manageable amount. In all the following SETHAB optimisations described the positions of the cations are kept stationary and only the I_3^- positions are optimised. In Table 4.6 we have listed the optimised triiodide positions for the input coordinates obtained from **1**, with the B971 optimised structures shown in Fig. 4.8.

Table 4.6 – Optimised bond lengths (Å) with the corresponding percentage deviation from the I-I bond length of the I_3^- ion in crystal **1**, utilising various methods in combination with the 3-21G basis set.

Method/DFT functional	I_3^- Bond lengths (Å)			
Crystal structure	**2.951**	% Deviation	**2.938**	% Deviation
[a]HF	-	-	-	-
MP2	3.161	7.13	3.133	6.63
B3LYP	3.162	7.14	3.133	6.63
B97D	3.188	8.04	3.166	7.75
[b]B971	2.967	0.55	2.935	0.10

[a]Stationary point could not be obtained

[b]dTZ basis set used for triiodide and the D95V basis set for C, H, N

If we consider the optimised bond lengths for the I_3^- ion listed in Table 4.6, we observe that all the methods yield an asymmetric I_3^- ion, coinciding with the solid state and demonstrating the influence of the surrounding cations on the I_3^- ion's geometry. This agrees with a previous theoretical study [2] where the influence of the electrostatic environment on the symmetry of the I_3^- ion was investigated. The authors pointed out that when the I_3^- ion is placed in asymmetric counterion framework it yielded slightly bent optimised geometry with unequal bond lengths.

A variety of methods were selected to investigate possible method dependence, while a small basis set (3-21G) was chosen to decrease computational cost. All methods listed in Table 4.6 overestimate the I-I bond lengths, with B3LYP yielding the most comparable results to MP2. We observe that optimising the I-I bond lengths for **1** at the B971/dTZ level of theory (shown in Fig. 4.8), yields results most comparable to those found experimentally for SETHAB.
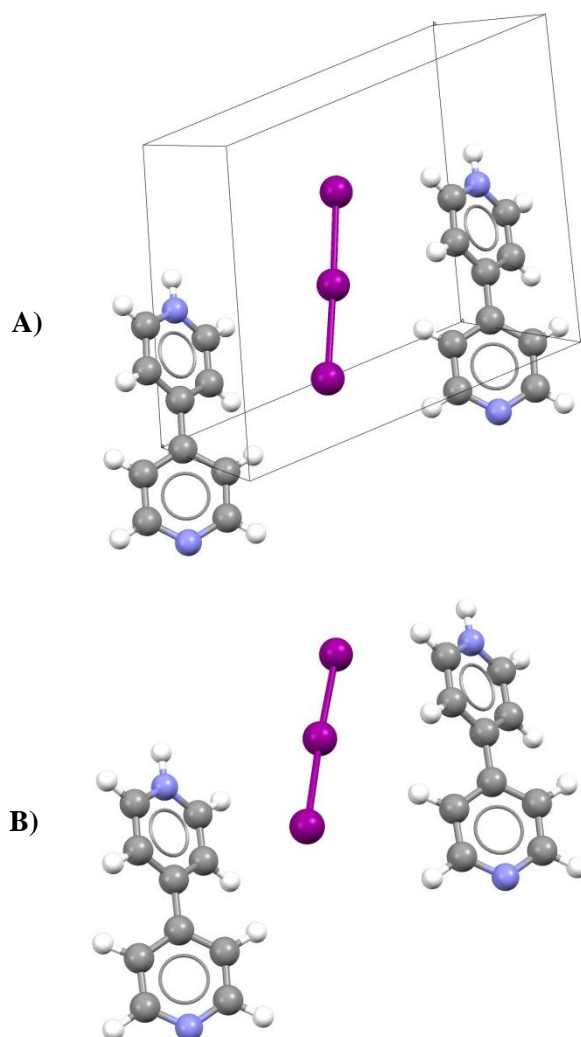
Fig. 4.8 – A) The input coordinates obtained from the CSD for crystal model 1; B) The optimised I_3^- position at the B971/dTZ level of theory.

In Fig. 4.8 B it can be seen that for the optimised structure using the method, B971, which yields results most comparable to the experimental structure shown in Fig. 4.8 A, the I_3^- ion has slightly moved away from the cations, rotating clockwise towards the adjacent protonated cation (NH^+ moiety).

The optimised I-I bond lengths in the gas phase and model **1** at various levels of theory are listed in Table 4.7. Also included are the percentage differences between the optimised I-I bond length in the gas phase from the optimised bond length in crystal model **1**, for a particular level of theory, which are all less than 1 %. This suggests that the optimised I-I bond length in crystal model **1** is mainly determined by the level of theory.

Table 4.7 - Average bond lengths (Å) for the I_3^- ion in the gas phase, partial crystal structure **1** with percentage deviation from one another utilising the 3-21G basis set.

Method/DFT functional	Average I_3^- bond length (Å)		
	Gas Phase	[a]Optimised in Crystal	% Difference
MP2	3.161	3.147	0.4
B3LYP	3.160	3.147	0.4
B97D	3.204	3.177	0.9
[b]B971	2.963	2.951	0.4

[a]Average bond length obtained using optimised bond lengths for **1**, listed in Table 4.6

[b]Optimised with the dTZ basis set

This high comparability of the I-I bond length of the isolated I_3^- ion to the I_3^- ion in model **1** illustrates the importance of the selection of the computational method. However, the effect of the choice of the partial crystal structure should be further investigated by expanding the size of the model, while considering the computational cost and time constraints.
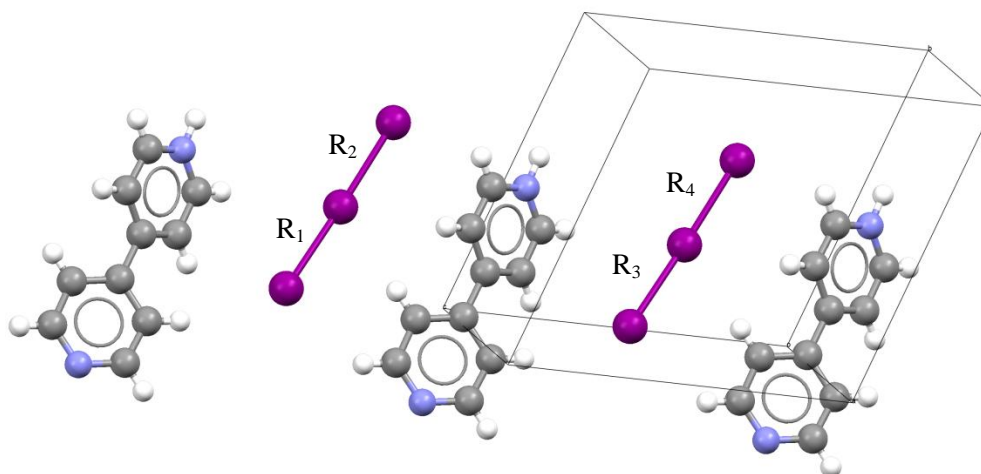
Fig. 4.9 – Partial crystal model **2** selected from SETHAB used as input coordinates for optimisations listed in Table 4.8 with the four I-I bonds indicated as R_1, R_2, R_3 and R_4 where $R_1 = R_3 = 2.951$ Å and $R_2 = R_4 = 2.938$ Å.

Consequently, the investigation was expanded by increasing the size of the crystal structure to the partial crystal structure model **2** (shown in Fig. 4.9). This expansion was done by adding one anion and one cation to model **1**. The optimised and non-optimised structures for the input coordinates shown in Fig. 4.9 are listed in Table 4.8 at various levels of theory, where we omitted the B97D method due to poor comparability to the I-I bond length found experimentally for SETHAB. The fact that the B3LYP hybrid functional did not yield a stationary point may be a result of the percentage overestimation of the I-I bond length.

Table 4.8 – Optimised and non-optimised bond lengths (Å) and their corresponding percentage deviation from the crystal model **2** utilising various methods in combination with the 3-21G basis set.

Method	R_1	% Deviation	R_2	% Deviation	R_3	% Deviation	R_4	% Deviation
				I_3^- Bond lengths (Å)				
Crystal Structure	**2.951**	-	**2.938**	-	**2.951**	-	**2.938**	-
HF	3.159	7.1	3.056	4.0	3.118	5.7	3.101	5.5
B3LYP[a]	3.172	7.5	3.122	6.3	3.148	6.7	3.152	7.3
B971[b]	2.978	0.9	2.924	0.5	2.965	0.5	2.946	0.3
Optimised I_3^- bond length in the gas phase		% Difference						
HF	3.161[c]	7.3[d]						
B3LYP[c]	3.118[c]	5.9[d]						
B971[b, c]	2.963[c]	0.6[d]						

[a]Non-optimised bond length

[b]Utilised the dTZ basis set for triiodide and the D95V basis set for C, N, H atoms

[c]Optimised bond length in the gas phase

[d]Percentage difference calculated of the I_3^- ion in the gas phase from the average I-I bond length of SETHAB

The optimised structures of **2** at the HF/3-21G and B971/dTZ level of theory are shown in Fig. 4.10. The non-optimised bond lengths for B3LYP were included in Table 4.8 to show that even though a stationary point could not be obtained, the I-I bond lengths are within 10 % from what is experimentally found for SETHAB. The percentage deviations in Table 4.8 indicate the deviation between the optimised I-I in the crystal model **2** from the crystal structure. At the bottom of Table 4.8 the optimised I-I bond lengths in the gas phase are included for HF, B3LYP and B971 with their respective percentage difference of the optimised I-I bond length in the gas phase to what is found experimentally for SETHAB.

We note, as before, that the percentage deviation are comparable to percentage difference, which indicates that the optimised I-I bond length in the crystal model **2** are also mainly determined by the level of theory.

When the results of B971 functional are considered, we observe that I-I bond lengths in the gas phase and in crystal model **2** with deviations less than 1 % from what is found experimentally for SETHAB. This accuracy of the B971 functional is consistent with the results in Table 4.6.
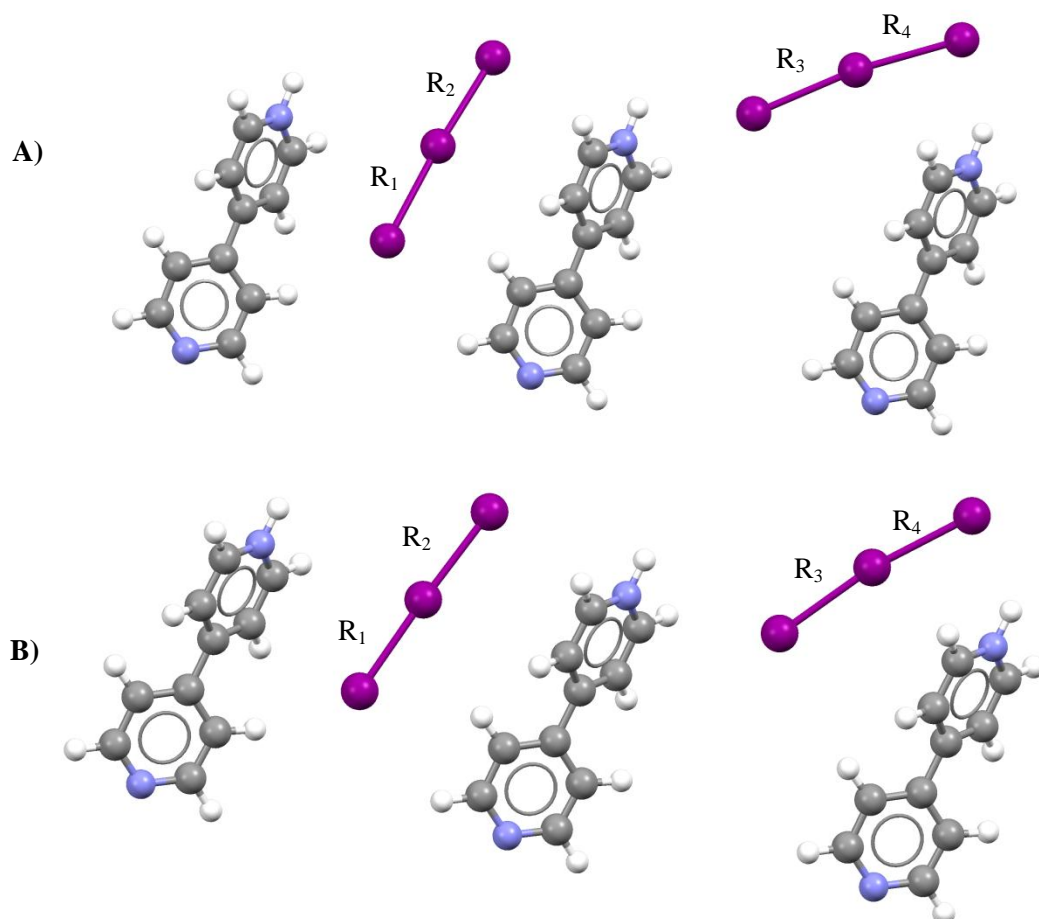
Fig. 4.10 – Graphical representations of the optimised triiodides in the partial structure **2** listed in Table 4.8 where **A)** is the optimised structure at the HF/3-21G level of theory and **B)** the optimised structure of the B971 functional utilising the dTZ basis set for iodine atoms and the D95V basis set for the C, N and H atoms. Both optimisations were performed using the initial model shown in Fig. 4.9.

However, if we compare the spatial arrangement of the optimised structure of the I_3^- ions at the HF/3-21G level of theory to the optimised structure of the I_3^- ions at the B971/dTZ level of theory as shown in Fig. 4.10, we observe that both methods yield similar structures with regards to the spatial arrangement of the molecules, with one I_3^- ion moving away from the neighbouring I_3^- ion. The optimised structures in Fig. 4.10 suggest that the environment determines the spatial arrangement of the molecules relative to one another and the level of theory affects the calculated I-I bond length.
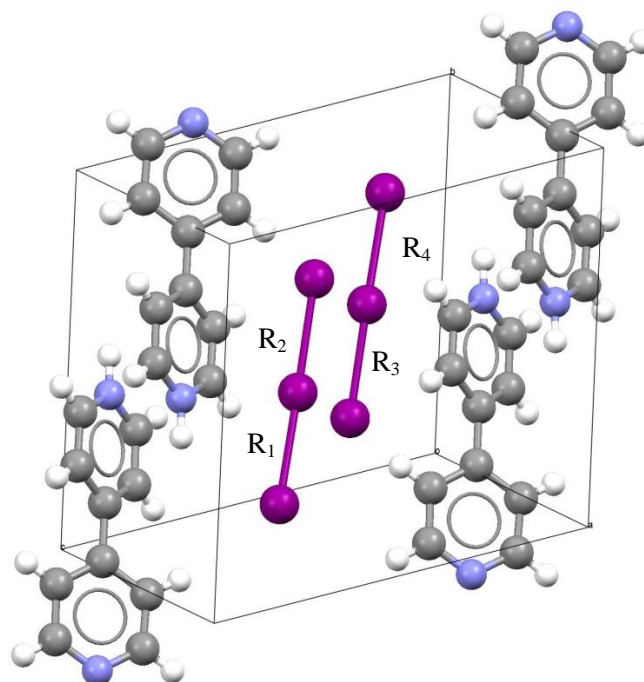
Fig. 4.11 – Selected partial crystal structure **3**, used as input coordinates selected from SETHAB for optimisations listed in Table 4.9 for the four I-I bond lengths.

In Fig. 4.11 crystal structure model **3** is shown, which is an expanded unit cell and consists of four cations surrounding two anions. This was selected to investigate whether the selected number of cations provide the necessary stabilisation to overcome the repulsive interactions between the I_3^- ions, and how this repulsion affects the I-I bond length.

Table 4.9 – I-I Bond lengths (Å) of the I_3^- ion in SETHAB, optimised I-I bond lengths (Å) of the I_3^- ion in the crystal environment and the optimised I-I bond lengths of the I_3^- ion in the gas phase with their corresponding deviations from the SETHAB crystal described by model **3** for various methods utilising the 3-21G basis set are listed. Additionally, the corresponding deviations from the solid state I-I bond length are listed.

Method	R_1	% Deviation	R_2	% Deviation	R_3	% Deviation	R_4	% Deviation
				I_3^- Bond lengths (Å)				
Crystal Structure	**2.951**	-	**2.938**	-	**2.951**	-	**2.938**	-
HF	3.124	5.9	3.082	4.9	3.124	5.9	3.082	4.9
B3LYP	3.225	9.3	3.073	4.6	3.225	9.3	3.073	4.6
B971[a]	3.036	2.9	2.870	2.3	3.037	2.9	2.870	2.3

Optimised I_3^- bond length in the gas phase	% Difference
HF	3.161	7.3[b]
B3LYP	3.118	5.9[b]
B971[a]	2.963	0.6[b]

[a]Utilised the dTZ basis set for triiodide and the D95V basis set for C, N, H atoms

[b]Percentage difference calculated for the I_3^- ion in the gas phase from the average I-I bond length of SETHAB
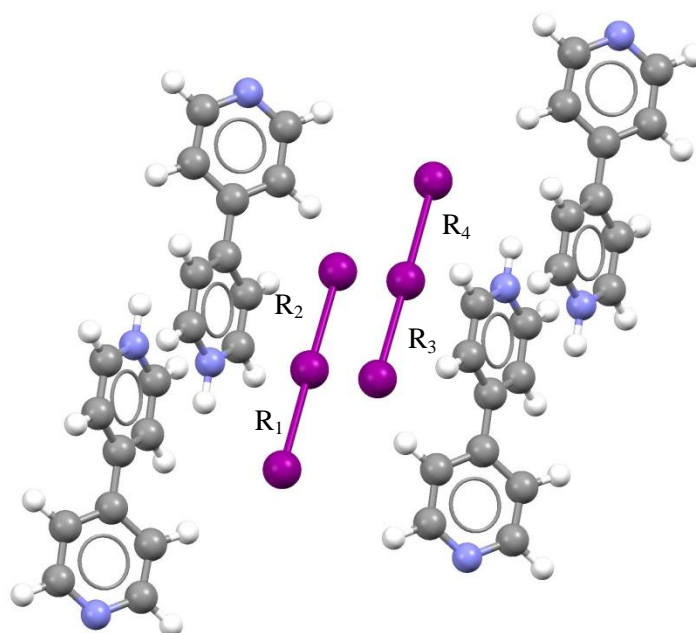
Fig. 4.12 – Graphical representation of the optimised structure at the B971/dTZ level of theory, listed in Table 4.9, with the bond lengths being $R_1 = R_4 = 3.036$ Å and $R_2 = R_3 = 2.87$ Å.

The optimised I-I bond lengths for the I_3^- ions including their corresponding deviations from the experimental bond lengths in **3** are listed in Table 4.9, with the input coordinates shown in Fig. 4.11. The optimised structure of the I_3^- ions at the B971/dTZ level of theory are shown in Fig. 4.12, where we it seems that the optimised structure is comparable to the crystal

81

structure, shown in Fig. 4.11. If we consider the optimised bond lengths for the I_3^- ions listed in Table 4.9, we see that B971 yields I-I bond lengths most comparable to the SETHAB crystal structure. Furthermore, note the slightly higher deviations from the I-I bond length in **3** than for what we have seen for the previous crystal models **1** and **2**. These deviations from crystal model **3** for all three DFT functionals are listed in Table 4.9 and are due to the change of the crystal structure environment, in particular the nearby triiodide ion, when compared to the previous examples.

As noted before, the B971 functional is the most successful in reproducing the I-I bond lengths for both the gas phase and the crystal structure environment when compared to that obtained experimentally in the solid state. All the optimisations performed thus far in Section 4.2. indicate that one should select a level of theory that yields a comparable I-I bond length in the gas phase to the crystal structure under investigation. The B971 functional consistently outperformed the other tested methods in all the crystal models (**1**, **2** and **3**). Furthermore, the optimisation results indicate that the surroundings alone determine the relative orientation of the I_3^- ion.

The second part of this investigation to see if the number of molecules present in the selected models obtained from the experimental crystal structure are sufficient to stabilise the $I_3^- \cdots I_3^-$ interaction is described in the next section.

4.2.2. The $I_3^-\cdots I_3^-$ interaction in the solid state
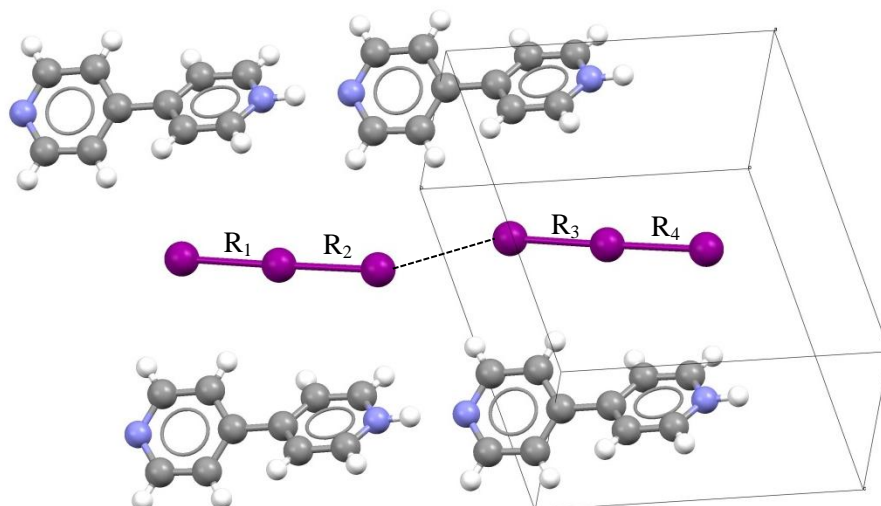
Fig. 4.13 – Selected partial crystal structure **4**, with the input coordinates obtained from the CSD for the SETHAB crystal with the four I-I bonds numbered as R_1, R_2, R_3 and R_4, where $R_1 = R_3 = 2.951$ Å, $R_2 = R_4 = 2.938$ Å, with the $I_3^-\cdots I_3^-$ intermolecular distance shown as black dotted line.

The $I_3^-\cdots I_3^-$ interaction was studied by choosing a model of the crystal structure **4** that contained two I_3^- ions surrounded by four cations (see Fig 4.13).

The optimised triiodide bond lengths and their corresponding deviations from the initial geometry of **4** are listed in Table 4.10. The PBE functional with the added D2 dispersion correction was included specifically to study the influence the D2 correction has on the optimised $I_3^-\cdots I_3^-$ geometry. We were also interested whether the inclusion of the dispersion term adds substantially to the accuracy of the optimised structures, since the presence of dispersion interactions between $I_3^-\cdots I_3^-$ have been proven to be the only attractive force between the I_3^- ions in solution (see Chapter 3 and 6). As it was found in Chapter 3, the PBE-D2 yields the most accurate $I_3^-\cdots I_3^-$ interaction energy when compared to the CCSD/a-TZ//MP2/TZ benchmark. In this section, we only selected the B971 and the PBE-D2 functional for comparison, where B971 yields the most comparable I-I bond length to what is found experimentally for SETHAB (but does not account for dispersion interactions) while PBE-D2 accounts for dispersion interactions.

Table 4.10 – Optimised bond lengths (Å) of the I_3^- ions shown in Fig. 4.13 with corresponding percentage deviations from SETHAB.

	Bond length (Å)							
	R_1	% Deviation	R_2	% Deviation	R_3	% Deviation	R_4	% Deviation
Crystal Structure	**2.951**	-	**2.938**	-	**2.951**	-	**2.938**	-
B971[a]	2.871	2.7	3.048	3.7	2.999	1.6	2.927	0.4
PBE-D2[a]	2.914	1.2	3.014	2.6	2.970	0.6	2.956	0.6

[a]dTZ basis set is used for the triiodides and the D95V basis set for C, H and N

In Table 4.10 we see that both functionals yield values for the optimised I-I bond length R_1 that are shorter than for R_2, which is opposite to the crystal structure where R_1 is larger than R_2. However, when we consider R_3 and R_4 we see that the deviations have decreased substantially (ranging from 0.4 % to 2 %, as opposed to 1 % and 4 % for R1 and R2), and the bond lengths have the same relationship as found in the crystal structure. Reasons why the bond lengths of only one I_3^- ion (on the left-hand side of Fig. 4.14) change substantially in **4** are unclear. Possible explanations could be that the I_3^- on the left is being repelled by lone pairs of the nearby unprotonated nitrogen atom, consequently pushing the neighbouring I_3^- ion towards the protonated cation.

Table 4.11 – Optimised I-I bond lengths (Å) for two DFT functionals in the gas phase utilising the dTZ basis set with their percentage deviation from the average I-I bond length in SETHAB.

DFT functional	Optimised I_3^- bond length in the gas phase	% Deviation
B971	2.963	0.6
PBE-D2	2.976	1.1

In Table 4.11 we have listed the optimised I-I bond lengths for the B971 and PBE-D2 functionals in the gas phase with their percentage deviation from the initial coordinates of **4**, where it can be seen that both DFT functionals yield comparable bond lengths with deviations less than 1.2 %. Note that when the I_3^- ion is optimised in the gas phase the B971 functional yields an I-I bond length closest to that found in the SETHAB crystal, so one would expect this accuracy to be seen when optimising I_3^- within a model of the crystal environment. Surprisingly, if the deviations in Table 4.10 are considered, we note that of the two DFT functionals, B971 yields less accurate bond lengths. This may be due to the absence of the dispersion correction in B971. Nevertheless, both functionals yield very similar I-I bond lengths that are also very close to the experimental values.

84
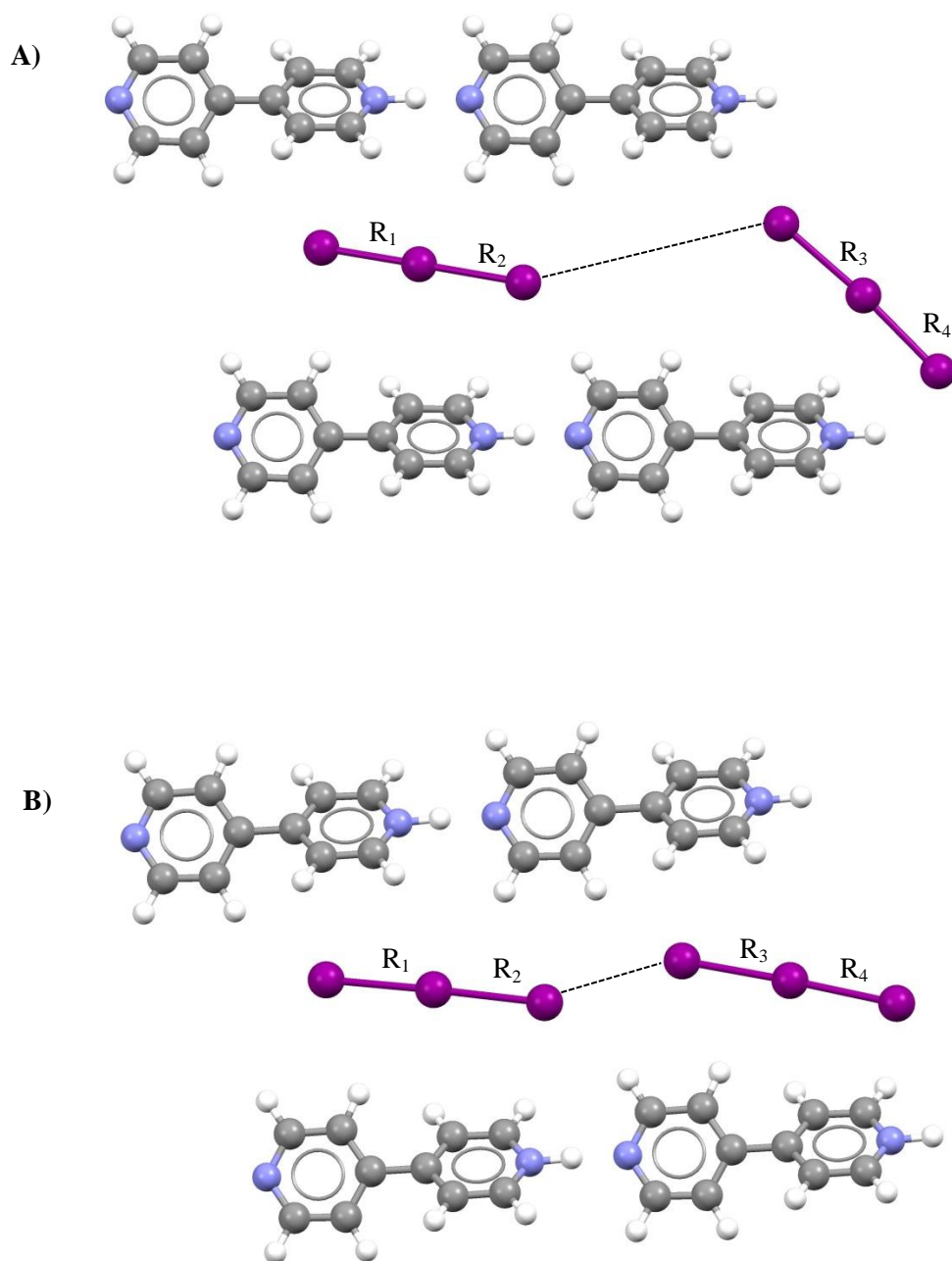
Fig. 4.14 – The optimised structures for **4** utilising A) the B971 and B) PBE-D2 functionals with the four I-I bond lengths R_1, R_2, R_3 and R_4. The $I_3^- \cdots I_3^-$ intermolecular distance is represented by a black dotted line.

In Fig. 4.14 we show the optimised structures obtained with the B971 and PBE-D2 functionals with the optimised I-I bond lengths given in Table 4.10 and the optimised $I_3^- \cdots I_3^-$ intermolecular distances listed below in Table 4.11, with the PBE-D2 results for the I_3^- dimer in *n*-methylformamide-mixture included in parenthesis for comparison.

Table 4.11 – The optimised $I_3^-\cdots I_3^-$ intermolecular distance (Å) (shown in Fig. 4.13 as the dotted black line) between the I_3^- ions in Fig. 4.14 at the B971 and PBE-D2 levels of theory.

	$d(I_3^-\cdots I_3^-)$ (Å)	% Deviation
Crystal Structure	**3.888**	-
B971	7.341	88.8
PBE-D2	3.853	0.9
	[a](3.836)	(1.3)

[a]$I_3^-\cdots I_3^-$ intermolecular distance of the I_3^- dimer in n-methylformamide-mixture with the dTZ basis set

When we consider the optimised triiodide positions in Fig. 4.14, we see that in this particular instance the D2 correction makes a significant difference with regards to the $I_3^-\cdots I_3^-$ intermolecular distance, while B971 does not account for the $I_3^-\cdots I_3^-$ interaction, thus yielding a structure considerably different to that found in the crystal. The difference can also be seen when the percentage deviation is considered for the $I_3^-\cdots I_3^-$ intermolecular distance listed in Table 4.11: 89 % and 1 % for the B971 and PBE-D2 functionals, respectively. Furthermore, we see that PBE-D2 yielded a $I_3^-\cdots I_3^-$ intermolecular distance in solution with deviations less than 2 %.

When the results were considered in Chapter 3, we observed that the ability of a particular functional to yield a stationary point was dependent on the solvent used, or rather if the needed stabilisation was provided by the solvent to change the PES sufficiently to enable the method to yield a stationary point. This may be the case for B971in model **4**, where the surroundings did not supply sufficient stabilisation for the functional to yield a stationary point. Considering the fact that B971 does not model dispersion interactions accurately (see Chapter 3), whereas PBE-D2 does account for dispersion interactions, this is not unexpected.

To conclude, four different crystal models were constructed and tested utilising various levels of theory. All the optimisations performed on the I_3^- ion at various levels of theory for the four crystal structure models indicate that there is a general decrease in the optimised I-I bond length within the crystal model, for a particular level of theory, when compared to the I-I optimised bond length in the gas phase at the same level of theory. Furthermore, even though all the crystal structure models chosen for the optimisation of the I_3^- ion can be considered as a non-realistic representation of a crystal structure, the results presented in this section are comparable to what was found experimentally.

All of these optimisations described in Chapter 4.2 indicate that when selecting a level of theory to model a particular crystal, the method should:

1) Yield an optimised I-I bond length in the gas phase comparable to the crystal of interest;

2) be capable of accounting for dispersion interactions, which could substantially influence the outcome of the optimised I_3^- positions in order to model the $[I_3^-]_\infty$ chains in the solid state;

3) yield comparable results for the $I_3^- \cdots I_3^-$ intermolecular distance in a highly polar solvent (e.g. *n*-methylformamide-mixture) ;

4) yield comparable results for the$I_3^- \cdots I_3^-$ interaction energy in a highly polar solvent when the CCSD/a-TZ//MP2/TZ benchmark is considered.

References

1.	Kloo, L., J. Rosdahl, and Per H. Svensson, *On the Intra- and Intermolecular Bonding in Polyiodides.* European Journal of Inorganic Chemistry, 2002. **2002**(5): p. 1203-1209.

2.	Datta, S.N., C.S. Ewig, and J.R. Van Wazer, *The geometric and electronic structures of I3− and I5− from effective-potential calculations.* Journal of Molecular Structure, 1978. **48**(3): p. 407-416.

3.	Novoa, J.J., F. Mota, and S. Alvarez, *Structure and stability of the X3- systems (X = fluoride, chloride, bromide, iodide) and their interaction with cations.* The Journal of Physical Chemistry, 1988. **92**(23): p. 6561-6566.

4.	Kochel, A., *4-(4-Pyridyl)pyridinium triiodide.* Acta Crystallographica Section E, 2006. **62**(12): p. o5605-o5606.

5.	Civalleri, B., et al., *B3LYP augmented with an empirical dispersion term (B3LYP-D*) as applied to molecular crystals.* CrystEngComm, 2008. **10**(4): p. 405-410.

6.	Allen, F., *The Cambridge Structural Database: a quarter of a million crystal structures and rising.* Acta Crystallographica Section B, 2002. **58**(3 Part 1): p. 380-388.

CHAPTER 5

Surface analysis of the I_3^- ion in the gas phase and in solution

In this Chapter the surface of the I_3^- ion is investigated in various environments ranging from the gas phase to a highly polar solvent such as *n*-methylformamide-mixture, with the electrostatic potential (ESP) of the surface studied at various levels of theory to inspect possible method dependence. In particular, the ESP of the σ-hole is investigated to expand the understanding of the $I_3^- \cdots I_3^-$ interaction energy in these various electrostatic surroundings. Furthermore, possible dependence between the ESP of the σ-hole and the stabilisation energy (ΔE_S) provided by the solvent and also the $I_3^- \cdots I_3^-$ interaction energy (E_{INT}) was explored. In order to analyse the effect the solvent has on the molecular surface of the I_3^- ion the program, WFA "Surface Analysis Suite" (SAS), was utilised and developed by Bulat and co-workers [1, 2]. The molecular surface is defined at an electron density of 0.001 au (electrons/bohr^3), which contains 97 % of a molecule's charge and 95-98 % of a molecule's electron density [1, 3]. In addition, the electrostatic potential of the surface of a molecule is defined by $V_S(\mathbf{r})$, which has been shown to be a physical observable and is effective for non-covalent interactions that are mainly electrostatic in nature (e.g. halogen bonding) [1]. The use of the electrostatic potential at the defined surface of a molecule has been utilised to explain halogen bonding (as a result of the "σ-hole" [4] which is a positive region, relative to the rest of the molecule, at the tip of the halogen atom when the electrostatic potential of surface is considered). Since, the σ-hole is relatively the most positive region of molecule, it is assigned as having the maximum value of the electrostatic potential ($V_{S, MAX}$). Values for $V_{S, MAX}$ at the σ-hole have been shown to correlate with trends seen in the calculated interaction energies between these sites and a given Lewis base (see ref. [1] and references therein). Another theoretical investigation performed by Politzer and co-workers [5] showed that as the polarisability increases and the electronegativity decreases from fluorine to iodine, one would expect the $V_{S, MAX}$ to be relatively more positive in the order F < Cl < Br < I, where in general fluorine has an entirely negative surface potential and that chlorine has a negative $V_{S, MAX}$. This is why fluorine and chlorine are rarely seen to form halogen bonds with Lewis bases. Since the σ-hole is a depletion of charge at the tips of a halogen atom the electron density is affected such that the radii perpendicular to the bond are larger than along the axis. This was generally referred to as polar flattening before Clark *et al.* [4] labelled it as a "σ-hole".

Mohajeri *et al.* [6] concluded in their theoretical study on the nature of bonding in σ-hole complexes that the $V_{S, MAX}$ value of the σ-hole can determine if one or more hydrogen bonds can be formed. They also stated that this dependence of the strength of the halogen bond on the electrostatic potential of the σ-hole indicates that it is electrostatically dominant.

In section 3.3 the influence of the solvent on the $I_3^- \cdots I_3^-$ interaction energy was investigated, where it was shown that the total $I_3^- \cdots I_3^-$ interaction energy increases as the dielectric constant increases which is a result of the decrease in the contribution of the (repulsive) electrostatic interaction term to the total interaction energy. The surface of the I_3^- ion was investigated using the WFA SAS software package to see if this decrease in repulsion between $I_3^- \cdots I_3^-$ could be observed as a function of the dielectric constant.

Gas phase

Chloroform

Ethanol

Water

n-methylformamide-
mixture
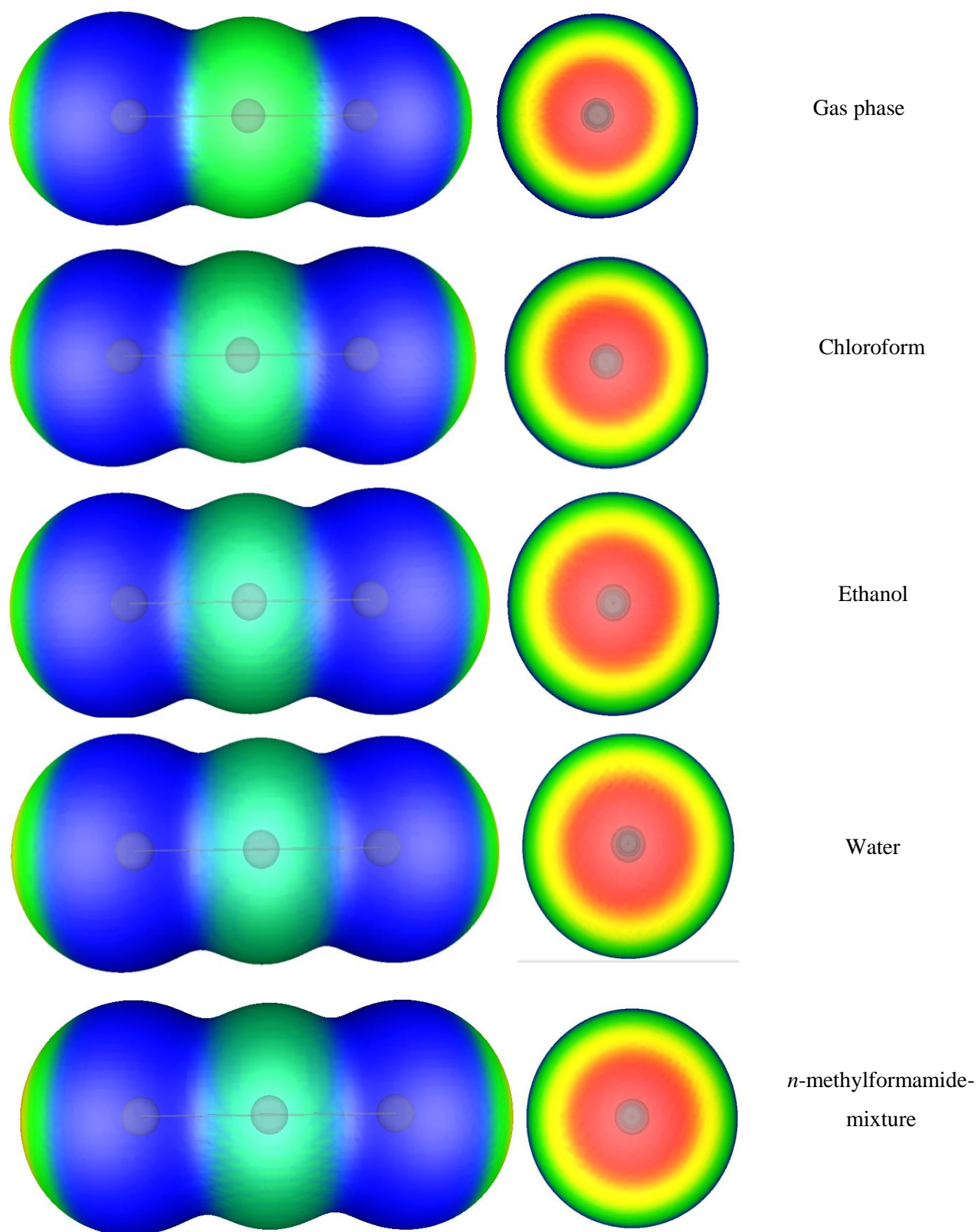
Fig. 5.1 – Calculated electrostatic potential (ESP) on the molecular surface of the I_3^- ion in the gas phase, chloroform, ethanol, water and *n*-methylformamide-mixture at the MP2/6-311G** level of theory. The red areas indicate the less negative regions (greater than -79 kcal/mol) of the molecule and the blue regions indicate the more negative (greater than -90 kcal/mol) electrostatic potential regions on the surface of the I_3^- ion.

The electrostatic potential on the molecular surface (ESP) of the I_3^- ion in the gas phase and various solvents for the WFT method (MP2/6-311G**) is shown in Fig. 5.1 The various images in Fig. 5.1 suggests that the size of the σ-hole, indicated in red, increases as the dielectric constant of the surroundings increases from the gas phase to a highly polar solvent. If we consider the size of the σ-hole for all the I_3^- ions shown in Fig. 5.1, the most prominent difference can be seen between the I_3^- ion in the gas phase and in the most polar solvent, *n*-methylformamide-mixture. In order to investigate whether DFT functionals are able to model a similar dependence of the σ-hole on the solvent, only the I_3^- ion in the gas phase and in *n*-methylformamide-mixture will be considered, since the σ-hole exhibits the most noticeable change.

Gas phase

n-methylformamide-mixture
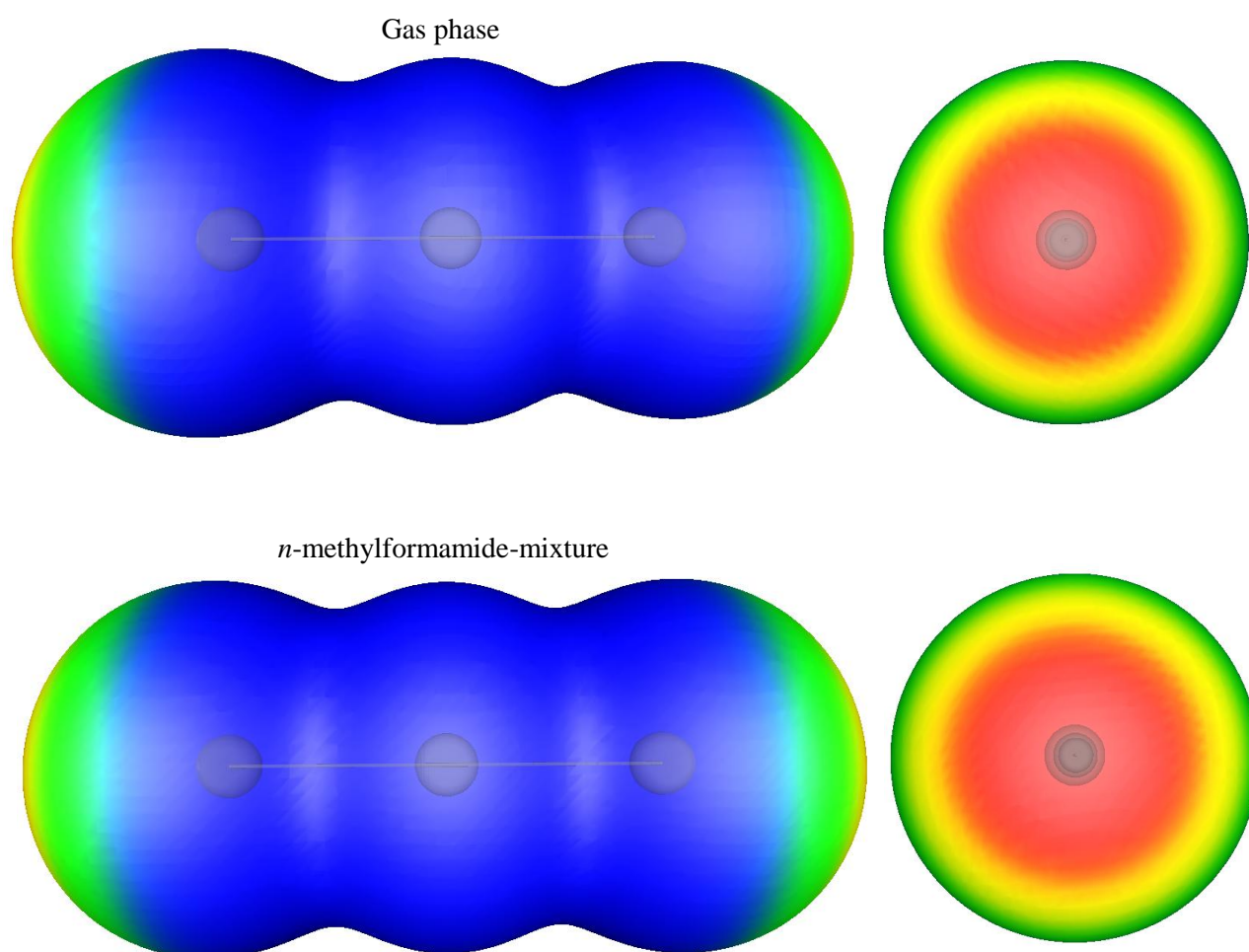
Fig. 5.2 – Calculated ESP on the molecular surface of the I_3^- ion in the gas phase and in *n*-methylformamide-mixture at the PBE-D2/6-311G** level of theory, where red is the relatively positive regions (greater than -79 kcal/mol) and blue is the relatively negative regions (greater than -92 kcal/mol).

The ESP surface of the I_3^- ion at the PBE-D2/6-311G** level of theory was calculated (see Fig. 5.2). The PBE-D2 DFT functional was selected to compare to the MP2 WFT method due to the DFT functional's ability to accurately model the $I_3^- \cdots I_3^-$ interaction energy in comparison to the CCSD/a-TZ//MP2/TZ benchmark. When we compare the ESP on the

molecular surface of the I_3^- ions in Fig. 5.1 to Fig. 5.2 we observe that the less negative region situated on the central iodine atom present for the MP2 method is absent when the PBE-D2 DFT functional is used. This is a result of the dependence of the Mulliken charge distribution on the method used, where the MP2 and the PBE-D2 methods yield positive (0.130 e) and negative (-0.071 e) Mulliken charge distribution for the central iodine atom, respectively. However, even though the electrostatic potential of the central atom is dependent on the method used, both methods exhibit similar dependence when the size of the σ-hole is considered, even though the PBE-D2 functional does seems to be less dependent on the solvent than MP2.

After observing this change induced by the solvent on the ESP surface of the I_3^- ion, we decided to investigate how the potential of the σ-hole changes quantitatively as a function of the solvent used, by utilising the $V_{S,\,MAX}$ values at the critical points (CP), shown in Fig. 5.3, on the surface of the I_3^- ion in the gas phase and in various solvents.
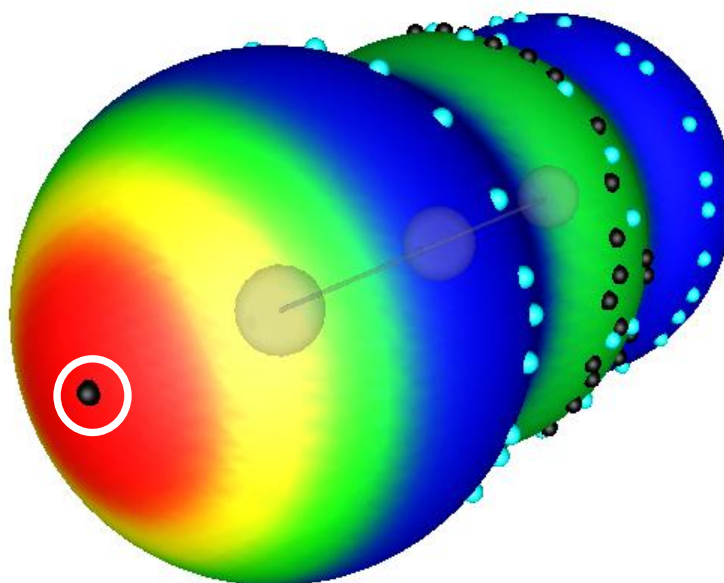
Fig. 5.3 – Calculated ESP surface of the I_3^- ion, with critical points (CP) indicated as black and light blue spheres, in the gas phase at the MP2/6-311G** level of theory.

All the CPs are shown in Fig. 5.3, where there will only be focusing on the CP in the middle of the σ-hole for the I_3^- ion which is encircled in white. As mentioned earlier, the red areas indicate the less negative regions of the molecule and the blue indicates the more negative regions of the ESP on the molecular surface.

Table 5.1 – $V_{S, MAX}$, ΔE_S and E_{INT} (kcal/mol) at various levels of theory for the gas phase and various solutions utilising the 6-311G** basis set.

	[a]MP2	PBE-D2	B97D	TPSS	TPSS-D2
Solvent	**Average $V_{S, MAX}$ (kcal/mol)**				
Gas	-75.31	-71.54	-71.22	-72.00	-71.95
Chloroform	-74.72	-70.04	-69.80	-70.57	-70.51
Ethanol	-74.42	-69.34	-69.14	-69.91	-69.84
Water	-74.37	-69.20	-69.00	-69.77	-69.71
n-methylformamide-mixture	-74.35	-69.16	-68.96	-69.74	-69.68
	ΔE_S (kcal/mol)				
gas	0.00	0.00	0.00	0.00	0.00
Chloroform	-33.39	-33.63	-33.48	-33.70	-33.69
Ethanol	-40.76	-41.12	-40.93	-41.19	-41.18
Water	-41.95	-42.33	-42.13	-42.40	-42.39
n-methylformamide-mixture	-42.26	-42.65	-42.45	-42.71	-42.70
	$I_3^- \cdots I_3^-$ Interaction Energy (E_{INT}) (kcal/mol)				
Gas	*33.17[b]*	-	-	-	-
Chloroform	*3.18*	5.56	5.58	-	5.76
Ethanol	*-3.19[b]*	-0.62	-0.45	-	-0.41
Water	*-4.22[b]*	-1.62	-1.43	0.16	-1.41
n-methylformamide-mixture	*-4.48*	-1.89	-1.69	-0.10	-1.67

[a]E_{INT} was calculated utilising the a-TZ basis set (in italics)

[b]E_{INT} are at the MP2/a-TZ level of theory, obtained from Table 1

Table 5.1 shows the average $V_{S,MAX}$ of the σ-hole, the stabilising energy (ΔE_S) provided by the solvent for the I_3^- ion and also the $I_3^- \cdots I_3^-$ interaction energy at various levels of theory [two GGAs (B97D, PBE-D2), one meta-GGA (TPSS/TPSS-D2) and with MP2 as reference] utilising the all-electron 6-311G** basis set except the $I_3^- \cdots I_3^-$ interaction energies of MP2 were calculated using the a-TZ basis set (see Table 5.1). The E_{INT} was not calculated at the MP2/6-311G** level of theory due to the computational cost.

In general the iodine atom has an relatively more positive $V_{S, MAX}$ value for the σ-hole when compared to other halogens (F, Br and Cl) and is in general positive for neutral molecules. However, to put this in perspective, we have highly negative values for the electrostatic potential of the σ-hole. If we compare the magnitude of the least positive $V_{S, MAX}$ value Politzer and co-workers [5] obtained, we see that the authors calculated a $V_{S, MAX}$ for the fluorine atom (usually the least positive of all the halogens) in CH_3F as -21 kcal/mol using a hybrid DFT functional. The most positive $V_{S, MAX}$ they calculated was for the NC-Br molecule with a calculated value of 42.1 kcal/mol.

When we consider the $V_{S,MAX}$ of all the methods in the various solvents we observe that all the calculated $V_{S, MAX}$ values are substantially more negative when compared to CH_3F (-21 kcal/mol) and considering the fact that it is iodine. The $V_{S,MAX}$ values for the DFT functionals varies between 5-8 % relative to MP2 in the gas phase or for a particular solvent. Furthermore, we notice that the $V_{S,MAX}$ of the I_3^- ion for MP2 and for the various DFT functionals becomes less negative from the gas phase to *n*-methylformamide-mixture by approximately 1.3 % and 3.3 %, respectively. This proves that a change of 1-3 % in the $V_{S,MAX}$ value for the σ-hole present at both ends of the I_3^- ion shown in Fig. 5.3, is sufficient to substantially change the $I_3^- \cdots I_3^-$ interaction energy from highly repulsive to attractive (see Table 5.1). If we consider $V_{S, MAX}$ of the TPSS functional with and without the dispersion correction listed in Table 5.1, we see that the difference in energy due to the D2 correction is negligible and could thus be considered equal. Furthermore, this negligible difference of $V_{S, MAX}$ could be a result of the change in geometry of the I_3^- ion induced by the D2 correction which we discussed earlier in Section 3.2.1.

If we consider the ΔE_S values listed in Table 5.1 we see that all the methods are comparable to one another, which was also seen in Table 4 and discussed in Section 2.1. Furthermore, we note that, as before with the $V_{S, MAX}$, the D2 correction has a negligible influence on the calculated ΔE_S results.

Also listed in Table 5.1 are the $I_3^- \cdots I_3^-$ interaction energies for various methods, where we see that the $I_3^- \cdots I_3^-$ interaction energies of the listed DFT functionals are underestimated when we utilise the all-electron 6-311G** basis set when the CCSD/a-TZ//MP2/TZ benchmark is considered. Here, we observe once again the substantial influence the D2 correction has on the PES, more specifically the $I_3^- \cdots I_3^-$ interaction energy when the TPSS functional is considered with and without the D2 correction. Without the D2 correction, the TPPS functional obtained stationary points for the I_3^- dimer in the two solvents with the highest dielectric constants: water and *n*-methylformamide-mixture. Since we can see from Table 5.1 that, it can be assumed the previously obtained TPSS results can be extended to TPSS-D2, the $V_{S, MAX}$ and ΔE_S values are independent of the D2 correction, thus enabling us to study the $I_3^- \cdots I_3^-$ interaction energy as an additional parameter for all four solvents listed in Table 5.1.
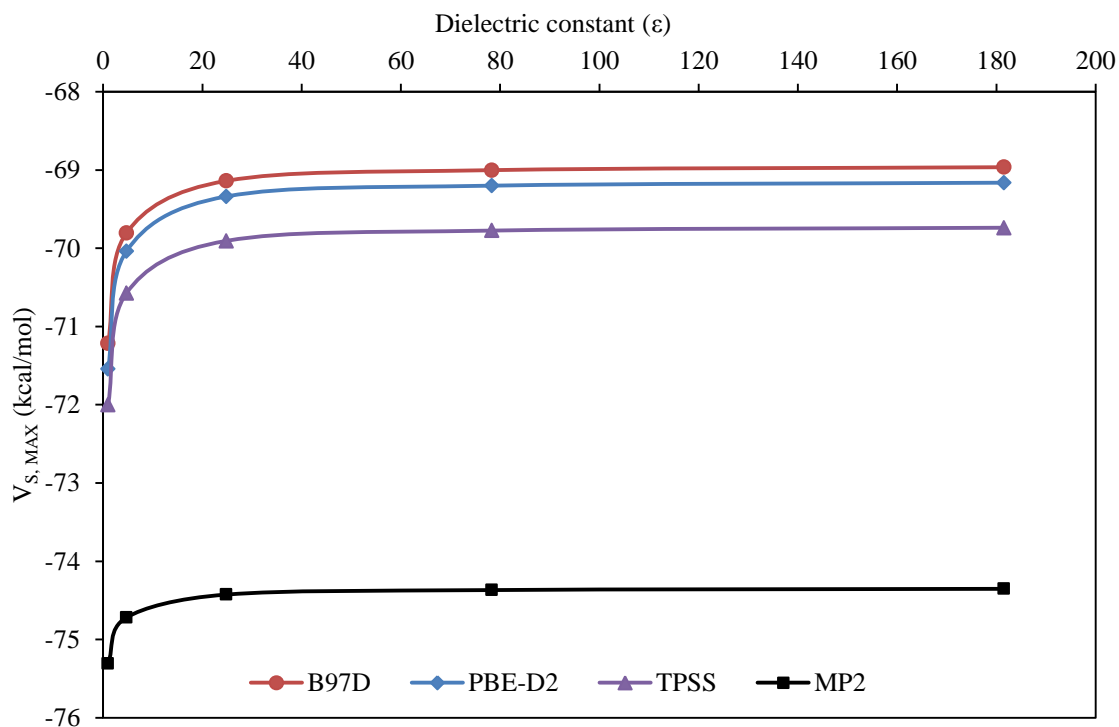
Fig. 5.4 – $V_{S, MAX}$ (kcal/mol) of the σ-hole of the I_3^- ion in the gas phase, chloroform, ethanol, water and *n*-methyl-formamide-mixture at various levels of theory utilising the 6-311G** basis set.

Fig. 5.4 is a visual representation of the data listed in Table 5.1, where we see that the solvent has a substantial influence on the calculated $V_{S, MAX}$ and that this exhibits a trend almost exactly opposite to what was found earlier for E_{INT} and ΔE_S in Fig. 3.4 and Fig. 3.5, respectively. This trend illustrates that as the dielectric constant of the solvent increases, resulting in an increase in the stabilisation provided by the solvent, the electrostatic potential on the surface of the I_3^- ion becomes less negative, thus decreasing the repulsion between the I_3^- ions when the dimer is considered. Furthermore, the authors [1] of the software package used to calculate these $V_{S, MAX}$ values state explicitly that the software package is suitable for studying non-covalent interactions that are electrostatic in nature. The trend observed in Fig. 5.4 coincides with what was observed earlier for the HF $I_3^-\cdots I_3^-$ interaction energy illustrated in Fig. 3.4 and listed in Table 3.4 (see Section 2.1), where there is a decrease of the electrostatic component of the total interaction energy, which we have shown to be repulsive for the case of the $I_3^-\cdots I_3^-$ interaction energy. It has been previously noted [4, 7] that the electrostatic surface potential of the σ-hole at the tip of the halogen atom becomes more positive as the remainder of the molecule becomes more electron withdrawing. Interestingly, we observe that the surface potential of the σ-hole at the tips of the I_3^- ion (shown in Fig. 5.3)

97

becomes less negative due to a change in the surroundings and not a change in the electron withdrawing capabilities of the remainder of the molecule.

$y = -0.0924x - 72.9$
$R^2 = 0.9986$

$y = -0.0961x - 73.272$
$R^2 = 0.9991$

$y = -0.0916x - 73.663$
$R^2 = 0.9991$

$y = -0.0408x - 76.081$
$R^2 = 0.9991$
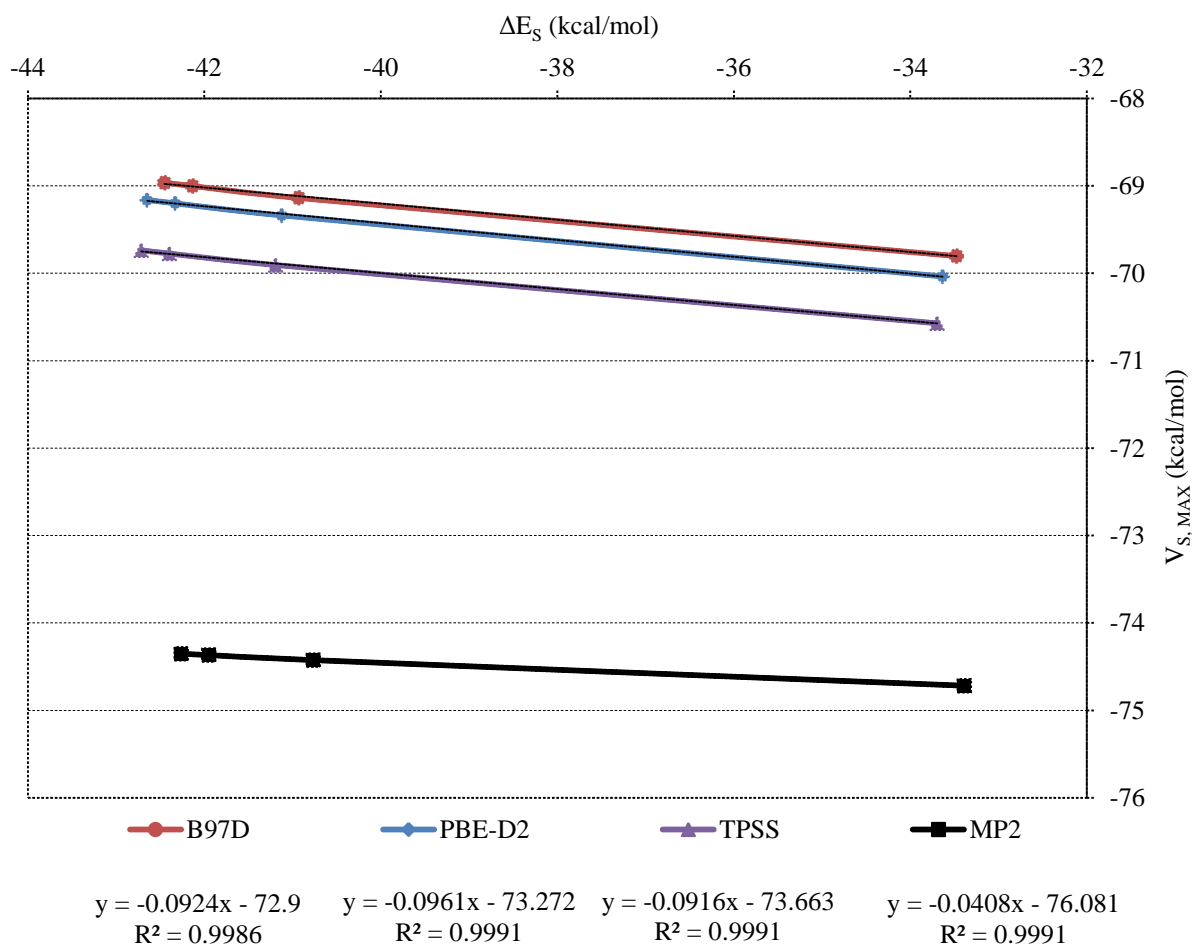
Fig. 5.5 – ΔE_S plotted against $V_{S,MAX}$ (kcal/mol) for chloroform, ethanol, water and *n*-methyl-formamide-mixture at various levels of theory utilising the 6-311G** basis set.

Fig. 5.5 is a graphical representation of ΔE_S plotted against $V_{S,\,MAX}$ in kcal/mol for the four selected solvents, where it can be seen that there is a linear dependence with a very high R^2 value for all the methods. This shows that the $V_{S,\,MAX}$ can be linked to the stabilisation provided by an electrostatic environment. We see that the MP2 method calculates a greater negative value for $V_{S,\,MAX}$ for each of the solvents relative to the DFT functionals. All the DFT functionals exhibit similar relationships between ΔE_S and $V_{S,\,MAX}$ to that shown by the WFT method, MP2, with the DFT functionals yielding comparable gradients. We see that the meta-GGA, TPSS, is the DFT functional which yields $V_{S,\,MAX}$ values closest to MP2, with B97D yielding the least accurate results when compared to MP2 and also with the lowest R^2 value (worst fit to the data).
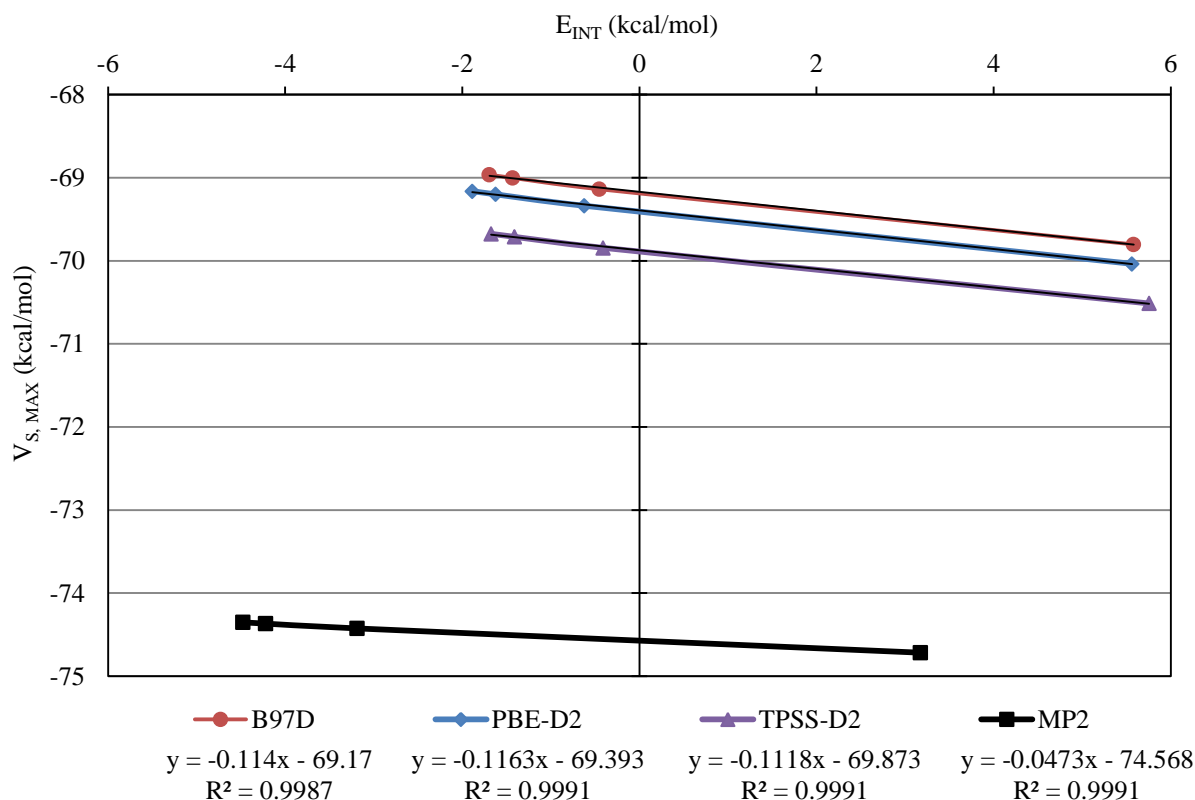
Fig. 5.6 − E_{INT} vs $V_{S, MAX}$ (kcal/mol) for chloroform, ethanol, water and *n*-methyl-formamide-mixture for the B97D, PBE-D2, TPSS-D2 DFT functionals utilising the 6-311G** basis set with E_{INT} of MP2 calculated with the a-TZ basis set.

The E_{INT} values are plotted against $V_{S, MAX}$ in Fig. 5.6 three DFT functionals with MP2 as reference listed in Table 5.1. Here the TPSS-D2 functional was included rather than the TPSS, since we were unable to obtain stationary points for the TPSS functional without the D2 correction in chloroform and ethanol utilising the all electron 6-311G** basis set. This is a reasonable approximation since, as shown earlier in Table 5.1, the D2 correction does not affect ΔE_S and $V_{S, MAX}$ energies, but only the $I_3^- \cdots I_3^-$ interaction energy.

In Fig. 5.6 we see all the methods yield a linear dependence with R^2 values closest to 1, with the B97D functional giving the lowest R^2 value of the four methods shown. Even though the E_{INT} of MP2 was calculated with the a-TZ basis set and the $V_{S, MAX}$ with the 6-311G** basis set, we see that MP2 still yields a R^2 value showing a good fit to the data. Another way of interpreting Fig. 5.6 is that there is a linear relation between the ESP on the surface of the I_3^- ion and the electrostatic interaction component of the $I_3^- \cdots I_3^-$ interaction energy.

When the equations of the linear trend lines in Fig. 5.6 are compared, we observe that all three DFT functionals yield comparable gradients and *y*-intercepts. Furthermore, this similarity in the gradients show that the DFT functionals represented in Fig. 5.6 exhibit similar dependence on the dielectric constant and the effect it has on the total energy of the I_3^- ion.

Also, the MP2 method shows a different dependence when the gradients are compared, which may be a results of the $I_3^- \cdots I_3^-$ interaction energy used.

Interestingly, $V_{S,\,MAX}$ is best used for non-covalent interactions that are electrostatic in nature, however, the attractive forces between the I_3^- ions are a result of electron correlation, we still observe a linear relationship between the electrostatic potential on the surface of the I_3^- ion and the calculated $I_3^- \cdots I_3^-$ interaction energy. These results show that if the I_3^- ion interacts with electrostatic environment the ESP of the ion decreases resulting in a decrease in the repulsion between these ions. Furthermore, it was shown that the higher ΔE_S the less negative the ESP becomes on the surface of the molecule. This could explain with what is observed in the CSD where $I_3^- \cdots I_3^-$ close contacts, less than twice the vdW radii, are known to exist in the solid state.

To summarise, it was shown that even though σ-holes were discovered and are mostly known to exist for neutral molecules, σ-holes can exist in an overall negatively charged molecule where the σ-hole positioned at the tips of each of the terminal iodine atoms in the I_3^- ion remains the relatively more positive region of the ion. Furthermore, it was shown that $V_{S,\,MAX}$ of the σ-hole has a linear relationship to both the stabilisation provided by the surroundings and to the $I_3^- \cdots I_3^-$ interaction energy showing that the E_{INT} is highly dependent on electrostatic interactions the I_3^- ion has with its surroundings. Also, when the I_3^- ion interacts with the surroundings, be it solvent or surrounding molecules in the solid state, the overall negative electrostatic potential becomes less negative as the strength of these interactions between the ion and surroundings increases, thus decreasing the repulsion between the I_3^- ions. Although, this was done for the solvent, it seems reasonable to hypothesise that this study done in this Chapter could be extrapolated to the solid state with regards to the change in the ESP of the surface of the I_3^- ion by interaction with surrounding cations.

References

1.   Bulat, F., et al., *Quantitative analysis of molecular surfaces: areas, volumes, electrostatic potentials and average local ionization energies.* Journal of Molecular Modeling, 2010. **16**(11): p. 1679-1691.

2.   Bulat FA, T.-L.A., *WFA: A suite of programs to analyse wavefunctions*: unpublished.

3.   Murray JS, P.P., *Molecular Surfaces, van der Waals Radii and Electrostatic Potentials in Relation to Noncovalent Interactions.* Croatia Chemica Acta, 2009. **82**: p. 267-275.

4.   Clark, T., et al., *Halogen bonding: the σ-hole.* Journal of Molecular Modeling, 2007. **13**(2): p. 291-296.

5.   Politzer, P., J.S. Murray, and T. Clark, *Halogen bonding: an electrostatically-driven highly directional noncovalent interaction.* Physical Chemistry Chemical Physics, 2010. **12**(28): p. 7748-7757.

6.   Mohajeri, A., A.H. Pakiari, and N. Bagheri, *Theoretical studies on the nature of bonding in σ-hole complexes.* Chemical Physics Letters, 2009. **467**(4–6): p. 393-397.

7.   Murray, J., P. Lane, and P. Politzer, *Expansion of the σ-hole concept.* Journal of Molecular Modeling, 2009. **15**(6): p. 723-729.

CHAPTER 6

Atoms in Molecules analysis of the I_3^- ion and $I_3^- \cdots I_3^-$ in the gas phase and in an implicit solvent model

Introduction

In this chapter we will investigate the nature of three properties; electron density [$\rho_b(\boldsymbol{r})$], Laplacian of the electron density [$L(\rho_b(\boldsymbol{r}))$], (L is defined as $-\frac{1}{4}\nabla^2$), and the total energy density [$H_b(\boldsymbol{r})$], as defined by the theory Atoms in Molecules (AIM) [1, 2] at the intra- and intermolecular bond critical points (BCPs) for the I_3^- ion and $I_3^- \cdots I_3^-$ in the gas phase and in various solvents, utilising an implicit solvent model, with a wide range of dielectric constants. In particular, these three AIM parameters will be employed to aid in the understanding and classification of the $I^- \cdots I_2$ and $I_3^- \cdots I_3^-$ interaction in the gas phase and in solution. Furthermore, the investigation will look at how various DFT functionals, that yielded a range of I-I bond lengths, are comparable to MP2 when the three AIM parameters are considered, utilising the a-TZ basis set.

Fig. 6.1 – Two dimensional contour plot of the electron density of the I_3^- ion in the gas phase at the MP2/a-TZ level of theory, with the BCPs indicated as green spheres and the numbered atoms shown in purple

6.1. AIM analyses of the I_3^- ion

In Fig. 6.1 the electron density of the I_3^- ion in the gas phase where the electron density is shown in two-dimensions, with the bond critical points indicated as green spheres and atoms as purple spheres.

In order to study the properties of the I_3^- bond in the gas phase and in solvent various parameters at the two BCPs (shown in Fig. 6.1), were investigated where a subscript b indicates that the value of a particular parameter was obtained at a BCP. As mentioned earlier, the analyses will be focussing on the following AIM parameters positioned at the BCP: The electron density (ρ_b), the Laplacian of the ρ_b [$L(\rho_b)$] and the total energy density (H_b),

represented graphically in two dimensions in Fig. 6.1, Fig. 6.2 and Fig. 6.3 for the I_3^- ion in the gas phase.

Table 6.1 – The I_3^- ion bond length (Å), electron density (ρ_b) at the BCPs in (ea_0^{-3}), the Laplacian of the electron density [L(ρ_b)] in (ea_0^{-5}) and the total electronic energy density (H_b) in atomic units at the BCP for the I_3^- ion in the gas phase, chloroform, ethanol, water and *n*-methylformamide-mixture at the MP2/a-TZ level of theory.

solvent	Bond length (Å)	BCP #	Atoms	ρ_b (ea_0^{-3})	L(ρ_b) (ea_0^{-5})	H_b (au)
gas	2.924	1	I1 - I2	**0.0502**	**0.0318**	**-0.0117**
		2	I1 - I3	0.0502	0.0318	-0.0117
chloroform	2.915	1	I1 - I2	0.0509	0.0321	-0.0121
		2	I2 - I3	0.0509	0.0321	-0.0121
ethanol	2.915	1	I1 - I2	0.0509	0.0320	-0.0121
		2	I1 - I3	0.0509	0.0320	-0.0121
water	2.915	1	I1 - I2	0.0510	0.0320	-0.0121
		2	I1 - I3	0.0510	0.0320	-0.0121
n-methylformamide-mixture	2.915	1	I1 - I2	0.0510	0.0320	-0.0121
		2	I2 - I3	0.0510	0.0320	-0.0121

In Table 6.1 various paramaters are listed related to the BCPS shown in Fig. 6.1, where we note that the values for all the parameters at BCP #1 and #2 are identical for an I_3^- ion in a particular solvent due to the symmetry of the ion. We chose to study the I_3^- ion at the MP2/a-TZ level of theory to generate a high level of theory wave function and also to study the influence the solvent has on the selected AIM parameters. If we consider ρ_b for the I_3^- ion in the gas phase and various solvents, we observe an increase in the electron density of about 1.5 % when the I_3^- ion in gas phase is compared to chloroform. Furthermore, we don't see any substantial dependance of ρ_b on the dielectric constant when chloroform is compared to *n*-methylformamide-mix. This initial increase in ρ_b when the I_3^- ion is submerged in chloroform is a result of the decrease in bond length, then as the dielectric constant increases the bond length remains fairly constant, which was discussed earlier in section 3.1.1. This is also observed for the other AIM parameters where there is a change in the parameter's value from the gas phase to chloroform where after it remains constant as the dielectric constant increases. We observed increase in L(ρ_b) when the gas phase is compared to chloroform, with the opposite being true for H_b where the value becomes more negative by 3 % when the gas phase is compared to chloroform. This makes that the total energy density is most sensitive to the change in conditions of all the AIM parameters considered in Table 6.1.
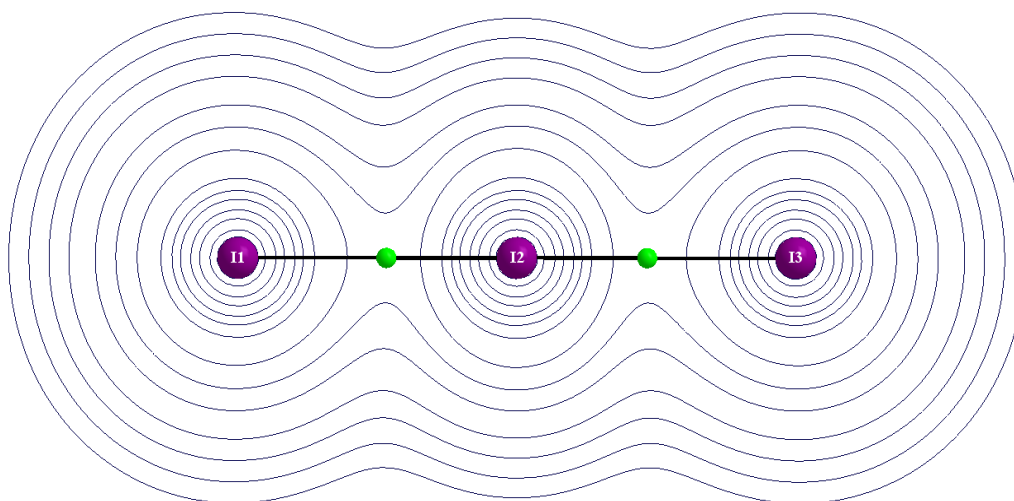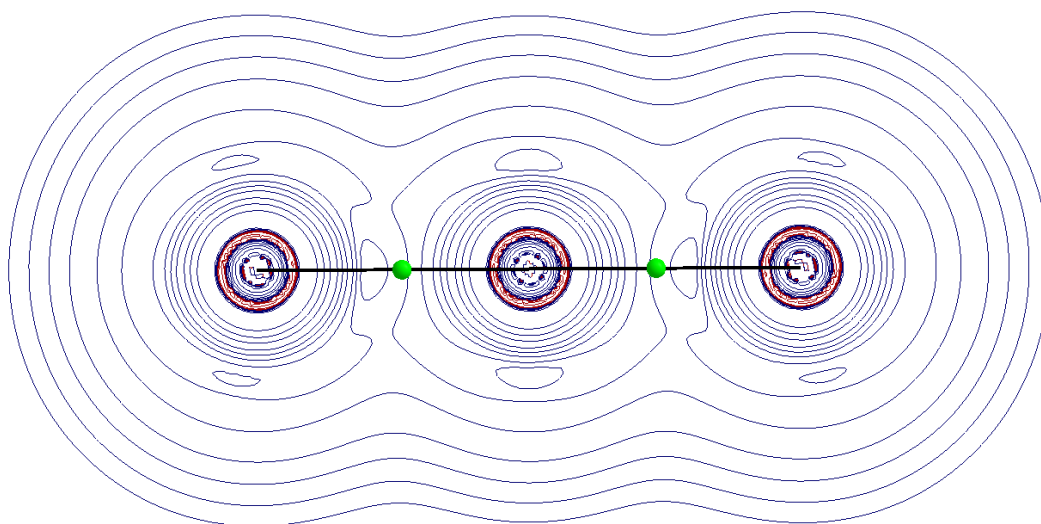
Fig. 6.2 – Two dimensional contour plot of the $L(\rho_b)$ of the I_3^- ion in the gas phase at the MP2/a-TZ level of theory with the bondpath indicated as black lines and the BCPs as green spheres.

Now that we have proven that the AIM parameters are not affected by the solvent by a substantial amount for the I_3^- ion, i.e. they do not exhibit dependence on the dielectric constant, only the parameters of the I_3^- ion in the gas phase listed in Table 6.1 will be considered and discussed.
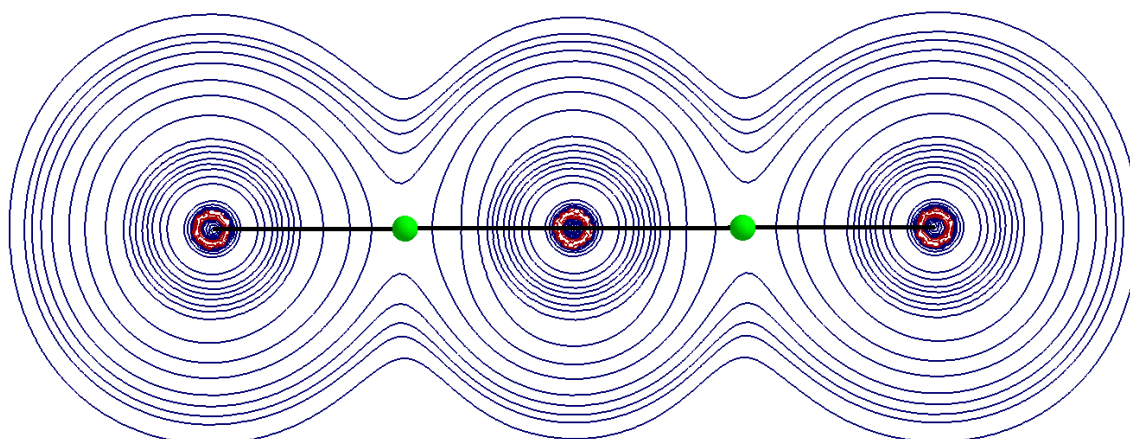
Fig. 6.3 – Two dimensional contour plot of the total energy density (H) of the I_3^- ion in the gas phase at the MP2/a-TZ level of theory with the bondpath indicated as a black line and the BCPs as green spheres.

Nakanishi *et al.* [3] conducted a theoretical study where they constructed plots utilising the total energy density (H_b) and the Laplacian of the electron density [$L(\rho_b)$] for better understanding of weak interactions and to allow classification as weak or strong interaction ranging from van der Waals (vdW) interactions, hydrogen bonding, charge transfer (CT) in molecular complexes, charge transfer in trigonal bipyramidal adducts (CT-TBP) to classical and strong covalent bonds. This was done by constructing a graph of the total energy density against Laplacian and assigning regions to each type of interaction or bond. Furthermore, since Br_3^- and Cl_3^- (classified as CT-TBP) were included in their study, our results can be

105

compared to what they found in order for us to 'classify' the strength of the dative bond present in I_3^-.

Table 6.2 – The bond length (Å), electron density (ρ_b) at the BCPs in (ea_0^{-3}), the Laplacian of the electron density [L(ρ_b)] in (ea_0^{-5}) and the total electronic energy density (H_b) in au at the BCP of the Cl_3^- and Br_3^- trihalides in the gas phase optimised at the MP2/6-311+G(2df, 2p) level of theory[a]

Trihalide	Bond length (Å)	ρ_b (ea_0^{-3})	$\Delta^2\rho_b$ (ea_0^{-5})	H_b (au)
[a]Cl_3^-	2.2924	0.0858	0.0942	-0.0279
[a]Br_3^-	2.5703	0.0641	0.0671	-0.0152

[a]Values obtained from [3]

In Table 6.2 we have included various AIM parameters obtained from the work of Nakanishi *et al.* where we see that as the optimised bond length increases from Br_3^- to Cl_3^-, both the electron density (ρ_b) and the Laplacian of the electron density [L(ρ_b)] decreases at the BCP, with the total energy density becoming less negative, which can be attributed to the increase in size of the atom. Naturally, one would then expect these trends visible in the AIM parameters to continue when considering the size of the iodine atom, which is true if we study the results listed in Table 6.1. Furthermore, we observe that all the values for the AIM parameters for Cl_3^-, Br_3^- and I_3^- listed in Table 6.1 and Table 6.2 are in the same order of magnitude and that the AIM parameters are comparable. Values obtained from the work done by Nakanishi *et al.* are listed in Table 6.3, showing typical ranges for each of the AIM parameters (ρ_b, L(ρ_b), H_b) to aid in the classification of the interaction by analysing the calculated AIM parameters for a particular molecule, in our case the I_3^- ion. Covalent bonds are classified as having a $H_b < 0$ and L(ρ_b) < 0 whereas ionic bonds have a $H_b > 0$ and L(ρ_b) > 0.

Table 6.3 – Typical ranges for $\rho_b(ea_0^{-3})$, L(ρ_b) in (ea_0^{-5}), H_b (au) for vdW interactions and the CT-TBP (trihalide ion)[a]

Interaction	ρ_b (ea_0^{-3})	$\Delta^2\rho_b$ (ea_0^{-5})	H_b (au)
Hydrogen Bonds	$0.01 < \rho_b < 0.04$	$0.04 < \nabla^2\rho_b < 0.12$	$-0.004 < H_b < 0.002$
van der Waals[a]	$0.00 < \rho_b < 0.01$	$0.00 < \nabla^2\rho_b < 0.04$	$0.000 < H_b < 0.002$
CT-TBP[a]	$0.03 < \rho_b < 0.1$	$-0.01 < \nabla^2\rho_b < 0.1$	$-0.06 < H_b < -0.003$

[a]Values obtained from [3]

We see from Table 6.3 that the calculated values listed in Table 6.1 fall within the defined ranges for a CT-TBP interaction and can thus conclude that the bond in the I_3^- ion exhibits these properties. We see that trihalides, in particular I_3^-, have a $H_b < 0$ and L(ρ_b) > 0, which, according to the classification proposed by Nakanishi *et al.* shows that the trihalide exhibits a

degree of covalent character, correlating with the study by Kloo and co-workers [4] where they calculated the bond order to be close to 0.5.

Now, we were interested to see if various DFT functionals yield similar results for the various AIM parameters to those obtained using MP2/a-TZ yielded, with MP2/a-TZ serving as a benchmark. Few DFT functionals that yielded comparable results to the CSD average for the I_3^- bond length (M06-2X and ωB97X), discussed earlier in Section 3.1.1, were chosen, as well as DFT functionals that both overestimate (BLYP, B3LYP) and underestimate (M06-HF and LC-ωPBE) the bond length of the I_3^- ion, when the CSD average (2.92 Å) is considered.

Table 6.4 – The bond length (Å), electron density (ρ_b) in (ea_0^{-3}), the Laplacian of the electron density [L(ρ_b)] in (ea_0^{-5}) and the total electronic energy density (H$_b$) in atomic units at the BCP for the I_3^- ion in the gas phase utilising various DFT functionals with the a-TZ basis set

DFT functional	Bond length (Å)	BCP #	Atoms	ρ_b (ea_0^{-3})	L(ρ_b) (ea_0^{-5})	H$_b$ (au)
M06-2X	2.924	1	I1 - I2	0.0494	0.0380	-0.0104
		2	I2 - I3	0.0494	0.0380	-0.0104
ωB97X	2.943	1	I1 - I2	0.0484	0.0360	-0.0098
		2	I2 - I3	0.0484	0.0360	-0.0098
M06-HF	2.841	1	I1 - I2	0.0543	0.0486	-0.0127
		2	I2 - I3	0.0543	0.0486	-0.0127
LC-ωPBE	2.898	1	I1 - I2	0.0521	0.0370	-0.0118
		2	I2 - I3	0.0521	0.0370	-0.0118
BLYP	3.044	1	I1 - I2	0.0397	0.0416	-0.0049
		2	I2 - I3	0.0397	0.0416	-0.0049
B3LYP	2.994	1	I1 - I2	0.0436	0.0406	-0.0068
		2	I2 - I3	0.0436	0.0406	-0.0068
PBE-D2	2.978	1	I1 - I2	0.0449	0.0421	-0.0073
		2	I2 - I3	0.0449	0.0421	-0.0073
TPSS-D2	2.981	1	I1 - I2	0.0443	0.0433	-0.0069
		2	I2 - I3	0.0443	0.0433	-0.0069

Results of the three selected AIM parameters of eight DFT functionals for the I_3^- ion are listed in Table 6.4. Along with the PBE-D2 functional due to its success in modelling the $I_3^- \cdots I_3^-$ interaction (discussed in Section 3.2.3.), and also to see if this accuracy is maintained in the calculation of the three AIM parameters. The meta-GGA, TPSS, has also been included to investigate if this DFT functional yields substantially different results from the other GGA functionals listed in Table 6.4.

If we consider the ρ_b values listed in Table 6.4, we see that the DFT functionals that yield bond lengths most comparable to the calculated CSD average and to the geometry of our AIM

parameter benchmark (MP2/a-TZ), M06-2X and ωB97X also reproduce the values for the electron density at the BCP (ρ_b) the best, with approximate deviation of 2 % and 4 %, respectively. Also, the DFT functionals that underestimate the bond length of the I_3^- ion (M06-HF and LC-ωPBE) overestimate ρ_b by approximately 8%, while the DFT functionals that overestimate the calculated CSD average (BLYP and B3LYP) for the I_3^- bond length underestimate the ρ_b when compared to MP2/a-TZ. The BLYP and B3LYP DFT functionals also yield the least comparable results for the ρ_b value with deviations of approximately 21 % and 13 %, respectively. We observe that the PBE-D2 and TPSS-D2 DFT functionals yield similar ρ_b results, with an approximate underestimation of about 11% from our MP2/a-TZ benchmark for both DFT functionals. However, we believe the similarity in electron density at the BCP for both the PBE-D2 and TPSS-D2 functionals are a result of the similarity in the optimised I_3^- bond length.

When we consider the $L(\rho_b)$ values listed in Table 6.4 for various DFT functionals, we observe that ωB97X yields the value closest to our MP2/a-TZ benchmark with an approximate deviation of 13 %, with one of the DFT functionals that underestimates the I_3^- bond length, LC-ωPBE, also yielding comparable results with an approximate deviation of 17 %. The deviations from the MP2/a-TZ benchmark of $L(\rho_b)$ for PBE-D2 and TPSS-D2 are 32 % and 36 %, respectively. Furthermore, the M06-HF DFT functional yields an even poorer result for $L(\rho_b)$, with a deviation of approximately 53 %.

If we consider the third AIM parameter listed in Table 6.4, H_b, we see that LC-ωPBE yields the value closest to our MP2/a-TZ benchmark, with an approximate deviation of less than 1 %, while M06-HF differs by approximately 9 %. We should mention that both the DFT functionals that yield comparable results to our MP/a-TZ benchmark underestimates the bond length of the I_3^- when compared to our CSD average (2.92 Å). If ρ_b is considered in Table 6.4, it seems that the underestimation in the bond length by M06-HF and LC-ωPBE functionals yields the highest electron density at the BCP, therefore this is also visible in the other AIM parameters where the other DFT functionals tend to underestimate the values for these parameters at a bond length equal or greater than what MP2/a-TZ yields (~ 2.92 Å). Furthermore, it can be seen that the DFT functional that yields the shortest I-I bond length for the I_3^- ion (M06-HF) yields the largest absolute values for each of the AIM parameters. The functional that yielded the least comparable results for H_b was the BLYP with a deviation of approximately 58 %. Despite this large deviation, all the calculated results for H_b listed in Table 6.4 remain within the borders of the typical range defined for H_b by Nakanishi *et al.*[3], shown in Table 6.3. Furthermore, if we consider all the results listed in Table 6.4 for all three AIM parameters, ρ_b, $L(\rho_b)$ and H_b, despite the respective deviations for each parameter

compared to our MP2/a-TZ benchmark, the results for all three parameters remain in the typical ranges for the CT-TBP interaction as defined by Nakanishi *et al.*[3] with LC-ωPBE yielding the most satisfactory results for all three AIM parameters listed in Table 6.4.

A)

B)

C)
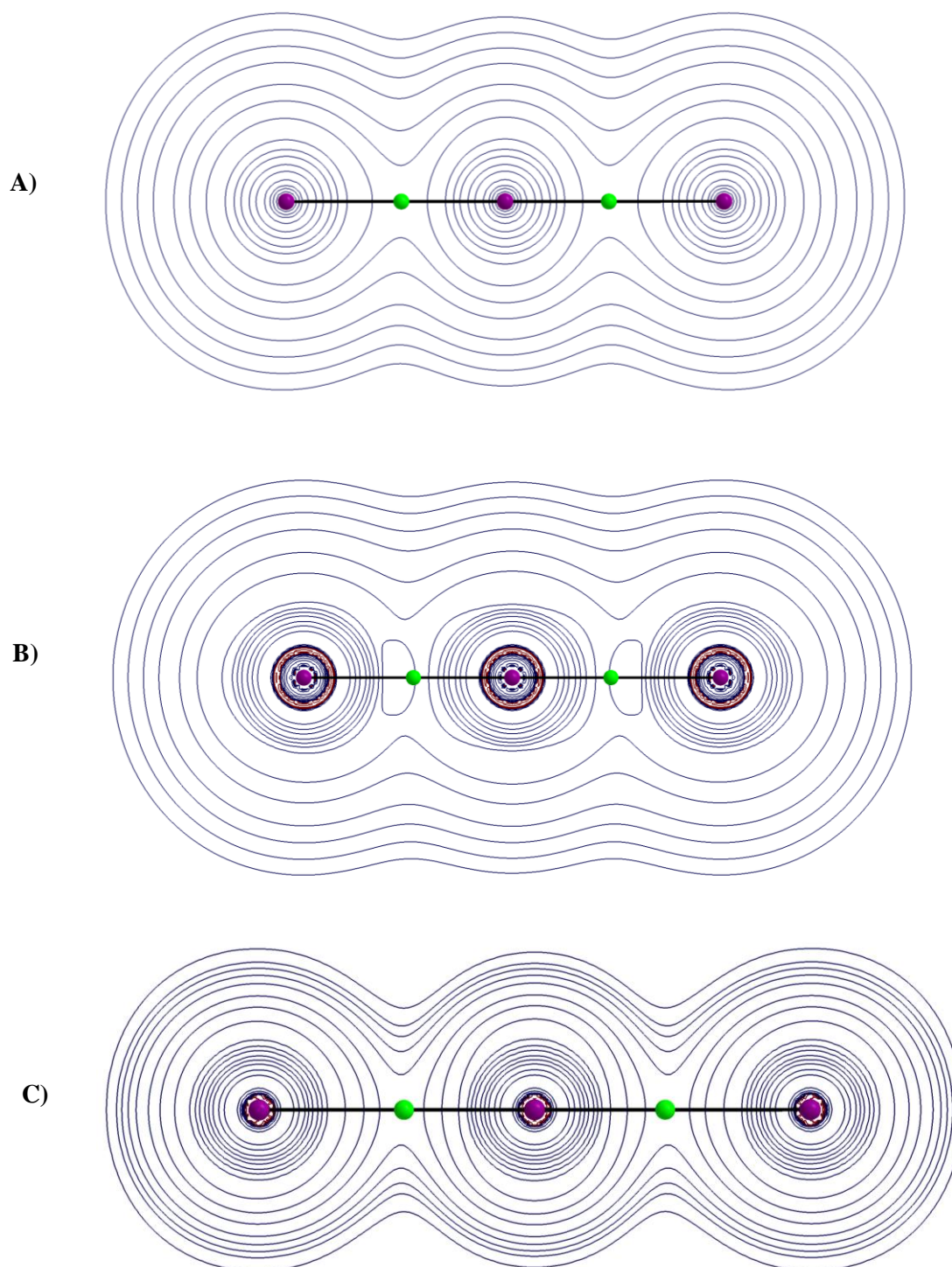
Fig. 6.4 – Two dimensional contour plots of A) electron density (ρ_b) at the BCPs in (ea_0^{-3}), B) the Laplacian of the electron density [L(ρ_b)] in (ea_0^{-5}) and C) the total electronic energy density (H_b) in atomic units at the BCP of the I_3^- in the gas phase at the LC-ωPBE/a-TZ level of theory. Atoms are indicated as purple spheres, BCPs as green spheres and the bondpath indicated as a black line.

In Fig. 6.4 we have included two dimensional contour plots of the the DFT functional, LC-ωPBE, which yields values for ρ_b, $L(\rho_b)$ and H_b closest to our MP2/a-TZ benchmark. However, we see that LC-ωPBE yields similar plots to MP2 for the ρ_b and H_b, but not for the $L(\rho_b)$ where we see the absence of the lone pairs on the side of the atoms perpendicular to the bondpath when Fig. 6.4 B) is compared to Fig. 6.2. This absence of the lone pairs shows that even though the LC-ωPBE yields comparable results, it does not yield a wave function of the same quality than the *ab initio* method, MP2.

Now that we have discussed the intramolecular interaction present in the I_3^- ion, we will focus on the intermolecular interaction found between the I_3^- dimer.

6.2. AIM analyses of the $I_3^-\cdots I_3^-$ interaction
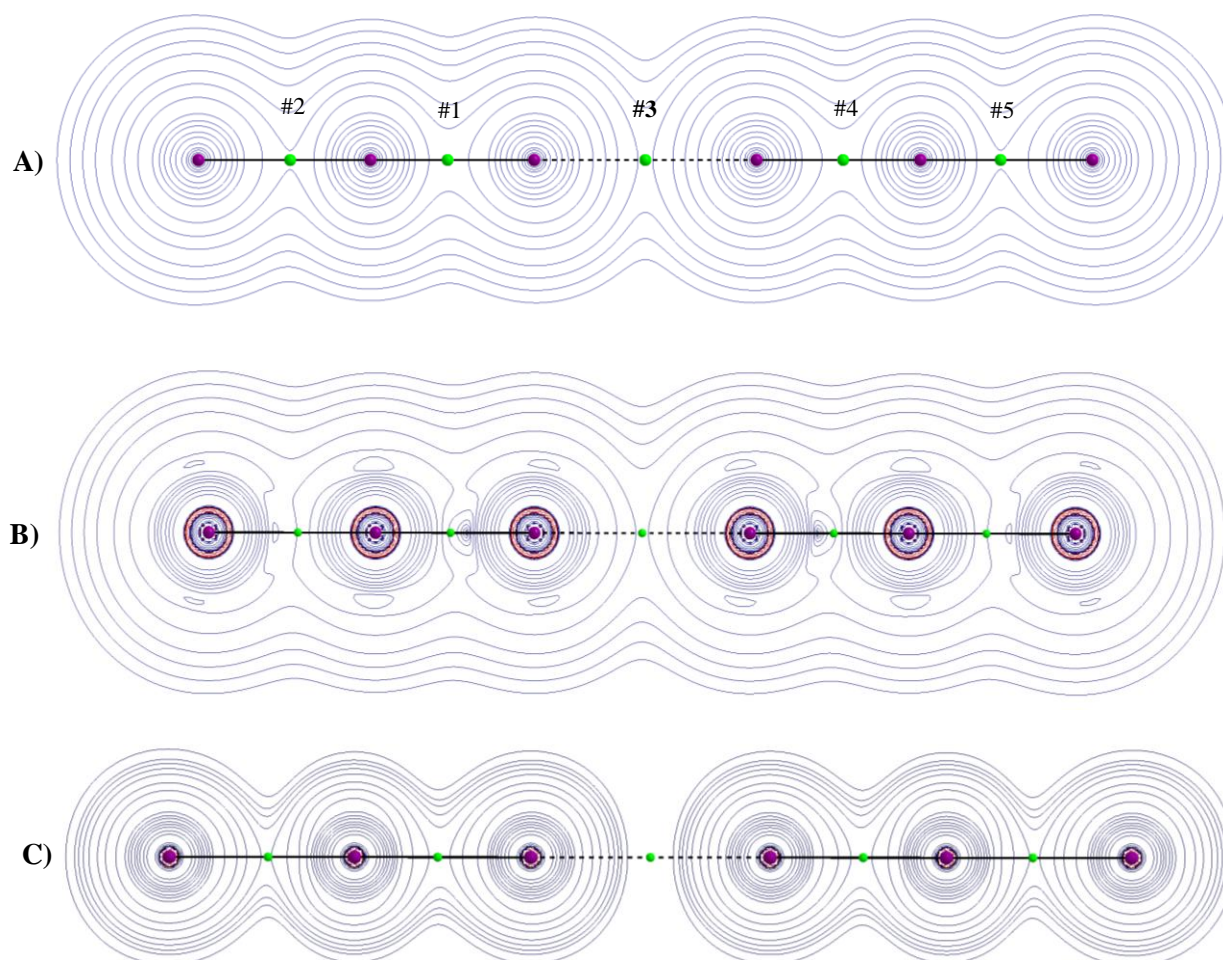
Fig. 6.5 – Two dimensional contour plots of A) electron density (ρ_b) at the BCPs in (ea_0^{-3}), B) the Laplacian of the electron density [$L(\rho_b)$] and C) the total electronic energy density (H_b) in atomic units at the BCP in (ea_0^{-5}) of the I_3^- dimer in the gas phase at the MP2/a-TZ level of theory, atoms are indicated as purple spheres, BCPs indicated as green spheres, the bondpath indicated by a (solid) black line and the atomic interaction line indicated by a dotted black line.

The calculated values for the ρ_b, $L(\rho_b)$ and H_b at these various BCPs are listed in Table 6.5 and shown in Fig. 6.5 we show a two dimensional plot of the electron density, the Laplacian and the total energy density for the I_3^- dimer in the gas phase numbered BCPs indicated as green spheres. Here the asymmetry of an individual I_3^- in the dimer is visible in the optimised structure in the gas phase. Surprisingly, even though the calculated $I_3^- \cdots I_3^-$ interaction energy (33.2 kcal/mol) at the MP2/a-TZ level of theory is highly repulsive, a BCP was obtained. Although, as mention earlier, this stationary point is spurious in nature (see Section 3.1.2. and 3.1.3.) , it would be interesting to study the characteristics of the three AIM parameters and also the change in the AIM parameters from gas phase to solvent, to verify the dependence of any changes on the dielectric constant of the environment.

Table 6.5 – The bond length (Å), $I_3^- \cdots I_3^-$ intermolecular distance (Å), electron density (ρ_b) in (ea_0^{-3}), the Laplacian of the electron density [$L(\rho_b)$] in in (ea_0^{-5}) and the total electronic energy density (H_b) in atomic units at various BCPs (shown in Fig. 6.5) of the I_3^- dimer in the gas phase, chloroform, ethanol, water and n-methylformamide-mixture at the MP2/a-TZ level of theory.

Gas/Solvent	Bond length (Å)	BCP #	ρ_b (ea_0^{-3})	$L(\rho_b)$ (ea_0^{-5})	H_b (au)
	2.873	1	0.0572	0.0164	-0.01556
	3.018	2	0.0412	0.0415	-0.00737
Gas	**3.901[a]**	**3**	**0.0072**	**0.0186**	**0.00067**
	2.873	4	0.0572	0.0164	-0.01556
	3.018	5	0.0412	0.0415	-0.00737
	2.885	1	0.0558	0.0198	-0.00014
	2.977	2	0.0445	0.0405	-0.00007
Chloroform	**3.574[a]**	**3**	**0.0132**	**0.0319**	**-0.00056**
	2.885	4	0.0558	0.0198	-0.00014
	2.977	5	0.0445	0.0405	-0.00007
	2.896	1	0.0545	0.0225	-0.00007
	2.958	2	0.0464	0.0387	-0.00003
Ethanol	**3.561[a]**	**3**	**0.0137**	**0.0328**	**-0.00031**
	2.896	4	0.0545	0.0225	-0.00007
	2.958	5	0.0464	0.0387	-0.00003
	2.898	1	0.0542	0.0232	-0.01385
	2.954	2	0.0468	0.0383	-0.00993
Water	**3.562[a]**	**3**	**0.0137**	**0.0328**	**0.00047**
	2.898	4	0.0542	0.0232	-0.01385
	2.954	5	0.0468	0.0383	-0.00993
	2.899	1	0.0541	0.0234	-0.01379
	2.953	2	0.0469	0.0381	-0.00999
n-methylformamide-mixture	**3.563[a]**	**3**	**0.0137**	**0.0328**	**0.00047**
	2.899	4	0.0541	0.0234	-0.01379
	2.953	5	0.0469	0.0381	-0.00999

[a]$I_3^- \cdots I_3^-$ Intermolecular distance and values of BCP in between the dimer

111

As mentioned before at the end of Section 3.1.1, the bond length of the individual I_3^- ion elongates by a negligible amount (~0.01 Å) and that one would thus expect this subtle change in geometry to have an effect on the AIM parameters. When the ρ_b, [$L(\rho_b)$] and H_b of the I_3^- ion are compared to average of the I_3^- dimer in the gas phase (excluding the values of BCP #3) at the MP2/a-TZ level of theory, a change of 2 %, 12 % and 1 % is observed, respectively. Despite this deviation in the AIM parameters for the I_3^- dimer compared to a single I_3^- ion, it remains within the ranges defined by Nakanishi *et al.* listed in Table 6.3 for the CT-TBP complexes [3]. Even though we observe this slight change in the bond characteristics, it remains as the same type of bond, thus our previous discussion applies and will not discuss this further.

Only the results of the three AIM parameters at the BCP #3 listed in Table 6.5 will be discussed and indicated as follows: ρ_{b3}, $L(\rho_{b3})$ and H_{b3}.

If we consider ρ_{b3} listed in Table 6.5, we see that when the I_3^- dimer is submerged in chloroform the electron density between the I_3^- ions increase by approximately 83 %, whereas it only increases by a further 4 % as the dielectric constant increases from chloroform to ethanol, and then remains constant for ethanol, water and *n*-methylformamide-mixture. When the ρ_{b3} values for the I_3^- dimer in the gas phase and in the various solvents are considered in Table 6.5, we see that only the ρ_{b3} of the gas phase falls within the range listed in Table 6.3 for vdW interactions as defined by Nakanishi *et al.* The other values for ρ_{b3} in the various solutions are the same order of magnitude but exhibit slightly higher electron densities than the 'typical range' of vdW interactions.

However, if we consider the values of $\nabla^2 \rho_{b3}$ listed in Table 6.5 we observe an increase in the calculated $\nabla^2 \rho_{b3}$ by approximately 71 % when the I_3^- dimer in gas phase is compared to chloroform. When the I_3^- dimer is modelled in ethanol the [$L(\rho_{b3})$] increases by 3% from the value in chloroform, and remains constant as the dielectric constant increases to 182. Surprisingly, all the calculated $L(\rho_{b3})$ values for the I_3^- dimer fall within the typical range for dispersion interactions listed in Table 6.3.

If we consider the calculated values for H_{b3} listed in Table 6.5 we observe that all the calculated values fall within the range defined by Nakanishi *et al.* for vdW interactions, except the H_{b3} values for the I_3^- dimer in chloroform and ethanol, which yield a slightly negative values. These values suggests that the calculated H_{b3} values are opposite in sign for the I_3^- dimer in chloroform and ethanol due to the fact that the values are so close to zero and may simply be a result of numerical noise.

Parthasarathi and co-workers [5] also performed an AIM study on hydrogen bonding where they illustrated that in general for weak hydrogen bonds and vdW interactions, $\rho_b < 0.02\ ea_0^{-3}$ and $L(\rho_b) < 0.01\ ea_0^{-5}$ and correlating with the typical range defined by Nakanishi *et al.*[3]. If we consider the range for ρ_b defined by Parthasarathi and co-workers [5], we observe that our calculated results for the electron density at the BCP between two molecules corresponds to a complex bound by dispersion interactions. However, our calculated results for $L(\rho_b)$ fall outside the range used by Parthasarathi and co-workers.

Bone and Bader [6] also point out in their theoretical study of van der Waals molecules using AIM that closed-shell interactions are characterised by a ρ_b of $\sim 10^{-3}$ au or less and $L(\rho_b)$ and H_b values are positive, also see references in [6].

If we consider the work of Parthasarathi and co-workers [3], Bone and Bader [6] and also the typical ranges defined by Nakanishi *et al.*[3] for the three AIM parameters (ρ_b, $L(\rho_b)$ and H_b), we then conclude that even though only the I_3^- dimer in the gas phase yields a value for the ρ_{b3} that lies within the typical range for vdW interactions, that all the calculated values for $L(\rho_{b3})$ correspond to those vdW interactions, while there is an inconsistent trend for the H_{b3} values, these results are substantial proof that the $I_3^- \cdots I_3^-$ interaction can be classified as a dispersion type interaction.

For comparison, we also investigated the ability of selected DFT functionals to produce comparable AIM parameters to MP2/a-TZ, that are indicative of vdW interactions. We selected to model the I_3^- dimer in *n*-methylformamide-mixture since this is where the $I_3^- \cdots I_3^-$ interaction is most stabilising.

Table 6.6 – The bond length (Å), $I_3^- \cdots I_3^-$ intermolecular distance (Å), electron density (ρ_b) in ea_0^{-3}, the Laplacian of the electron density [$L(\rho_b)$] and the total electronic energy density (H_b) in atomic units at various BCPs (shown in Fig. 6.5) in (ea_0^{-5}) of the I_3^- dimer in *n*-methylformamide-mixture for PBE-D2 and TPSS-D2 utilising the a-TZ basis set.

DFT functional	Bond length (Å)	BCP #	ρ_b (ea_0^{-3})	$L(\rho_b)$ (ea_0^{-5})	H_b (au)
PBE-D2	2.965	1	0.0461	0.0419	-0.00782
	2.987	2	0.0443	0.0431	-0.00702
	3.845[a]	**3**	**0.0093**	**0.0188**	**0.00049**
	2.965	4	0.0461	0.0419	-0.00782
	2.987	5	0.0443	0.0431	-0.00702
TPSS-D2	2.966	1	0.0457	0.0432	-0.00750
	2.990	2	0.0437	0.0444	-0.00666
	3.884[a]	**3**	**0.0087**	**0.0180**	**0.00053**
	2.966	4	0.0457	0.0432	-0.00750
	2.990	5	0.0437	0.0444	-0.00666

[a]$I_3^- \cdots I_3^-$ intermolecular distance, also BCP between I_3^- ions

Values of ρ_b, L(ρ_b) and H$_b$ for the I$_3^-$ dimer in *n*-methylformamide-mixture for the PBE-D2 and the meta-GGA functional TPSS-D2 are listed in Table 6.6. We observe that even though the I$_3^-$ dimer is modelled in solution, it yields results in the same order of magnitude as MP2/a-TZ in the gas phase. This may be due to the 'locality' of DFT theory and also be a contributing factor the low accuracy of DFT functionals when it comes to model of dispersion interactions.

If we compare the ρ_{b3} of the I$_3^-$ dimer for PBE-D2 and TPSS-D2 in Table 6.6 to the ρ_{b3} of the I$_3^-$ dimer in the gas phase at the MP2/a-TZ level of theory, we observe deviations of 29 % and 21 %, respectively, as opposed to the MP2/a-TZ values in *n*-methylformamide-mixture, where we observe 32 % and 36 % deviation, respectively. These values are nevertheless within the range expected for vdW interactions.

When we consider the L(ρ_{b3}) listed for PBE-D2 and TPSS-D2 in Table 6.6 we see that these DFT functionals yield results that deviate 1 % and 3 % from the L(ρ_{b3}) calculated using MP2/a-TZ in the gas phase, respectively. Furthermore, if the PBE-D2 and TPSS-D2 values are compared to L(ρ_{b3}) calculated using MP2/a-TZ in *n*-methylformamide-mixture, we note a deviation of 43 % and 45 %, respectively.

If we consider the third AIM parameter listed in Table 6.6, H$_{b3}$, we note that values obtained with PBE-D2 and TPPS-D2 deviates by 26 % and 21 %, and, 5% and 13% when compared to H$_{b3}$ of MP2/a-TZ in the gas phase and in *n*-methylformamide-mixture, respectively. In contrast to the MP2/a-TZ results which were inconsistent, these results support the identification of the I$_3^-$⋯I$_3^-$ interaction as dispersion based.

To summarise the DFT results, we observe that ρ_{b3} and L(ρ_{b3}) of both DFT functionals compare more closely to the corresponding values for MP2/a-TZ in the gas phase than in *n*-methylformamide-mixture. However, if we consider H$_{b3}$ for both DFT functionals it can be said that these values correspond better H$_{b3}$ value of the I$_3^-$ dimer in *n*-methylformamide-mixture at MP2/a-TZ level of theory than to the gas phase.

Nevertheless, the values calculated for the three AIM parameters utilising two particular DFT functionals agree with the characteristics of vdW interactions [3, 5, 6] and coincide with the ranges listed in Table 6.3.

The fact that these calculated values for the three AIM parameters at BCP #3 listed in Table 6.6 (ρ_{b3}, L(ρ_{b3}) and H$_{b3}$) results correlate so closely to previous work and that both WFT methods and DFT functionals all point to the same conclusion, which is that the I$_3^-$ ions interact with one another through dispersion interactions. These AIM results concur with our findings in Chapter 3, including the surface analysis results presented in Chapter 5 showing that the ESP on the surface decreases as the dielectric constant increases, thus decreasing

repulsion between I_3^- ions. Furthermore, it was shown that the electron density at BCP #3 listed in Table 6.6 is independent of the dielectric constant implying that the strength of the vdW interactions remain constant, thus supporting the conclusion we made in Chapter 3 and 5 where it was stated that the $I_3^- \cdots I_3^-$ interaction energy increased as a function of the dielectric constant due to the decrease in the electrostatic component of the total interaction energy with the dispersion interaction remaining constant as inherently dependent on the polarisation of the atoms involved.

To conclude, the MP2 results calculated for the three selected AIM parameters, ρ_b, $L(\rho_b)$ and H_b for the I_3^- ion coincides with the findings of Nakanishi *et al.* [3] where they investigated the nature of the bond present in Cl_3^- and Br_3^- ions and concluded it to be a CT-TBP adduct. When the DFT results are compared to MP2 for the three selected, we see that the DFTs functionals (M06-2X and ωB97X) yield comparable results (deviation 2 % and 4 %) for the electron density when the optimised geometries of the methods have comparable I-I bondlengths. Furthermore, we observe that the deviation from the MP2 benchmark increases to 13 % when $L(\rho_b)$ is considered for the ωB97X functional. When the third parameter, H_b, is considered we see that in general this parameter is least comparable to MP2, with the an increase in accuracy is observed when a DFT is considered which yields a shorter bond length to MP2. Despite this deviations present for the three AIM parameters, the calculated values for the various DFT functionals are within the typical ranges as defined by Nakanishi *et al.* [3]

When we compare ρ_{b3} and $L(\rho_{b3})$ for the I_3^- dimer calculated by MP2 in the gas phase to solution a substantial increase in the absolute value for each parameter is observed, which is due to the decrease in the $I_3^- \cdots I_3^-$ intermolecular distance. When the H_b is considered, we observe that when the $I_3^- \cdots I_3^-$ interaction energy is relatively close to zero (see Table 3.4), as is the case with chloroform (+3.18 kcal/mol) and ethanol (-3.19 kcal/mol), an inconsistency is observed for this parameter in Table 6.5. However, these values remain in the typical ranges defined by Nakanishi *et al.* [3]

When the calculated values of the two selected DFT functionals are compared to MP2, we observe that the DFT functionals yield comparable results for the $L(\rho_b)$ and H_b, but yields a value for ρ_{b3} an order of magnitude lower. This is different to what was found for the I_3^- ion, where the DFT functionals yielded comparable results for electron density and the Laplacian of the electron density.

These results show that the DFT functionals tested here are more reliable when utilised for intramolecular bonding of the I_3^- ion than the $I_3^- \cdots I_3^-$ intermolecular interaction, when the three selected AIM parameters are considered. However, both methods yield values leads us

to the same conclusion, that the I_3^- ion is a CT-TBP adduct and that the $I_3^- \cdots I_3^-$ intermolecular interaction is always dispersive in nature and remains relatively constant in the all the tested solvents. This supports our observations made in Chapter 3 where it was shown that as the dielectric constant increases, the electrostatic component of the total $I_3^- \cdots I_3^-$ interaction energy decreases and the attractive interactions is a result of the dispersion interactions present.

References

1.   Bader, R.F.W., *Atoms in Molecules*, in *Encyclopedia of Computational Chemistry*, A.N. Schleyer PvR, Kollman PA, Clark T, Schaefer HFS, Gasteiger J, Schreiner PR, Editor 1998, Wiley-VCH: Chichester. p. 64-87.

2.   Bader, R.F.W., *Atoms in molecules.* Accounts of Chemical Research, 1985. **18**(1): p. 9-15.

3.   Nakanishi, W., S. Hayashi, and K. Narahara, *Atoms-in-Molecules Dual Parameter Analysis of Weak to Strong Interactions: Behaviors of Electronic Energy Densities versus Laplacian of Electron Densities at Bond Critical Points.* The Journal of Physical Chemistry A, 2008. **112**(51): p. 13593-13599.

4.   Kloo, L., J. Rosdahl, and Per H. Svensson, *On the Intra- and Intermolecular Bonding in Polyiodides.* European Journal of Inorganic Chemistry, 2002. **2002**(5): p. 1203-1209.

5.   Parthasarathi, R., V. Subramanian, and N. Sathyamurthy, *Hydrogen Bonding without Borders: An Atoms-in-Molecules Perspective.* The Journal of Physical Chemistry A, 2006. **110**(10): p. 3349-3351.

6.   Bone, R.G.A. and R.F.W. Bader, *Identifying and Analyzing Intermolecular Bonding Interactions in van der Waals Molecules†.* The Journal of Physical Chemistry, 1996. **100**(26): p. 10892-10911.

Point charge calculations of a 'crystal'

Introduction

In this chapter three methods will be used to link the modelling of I_3^- in a highly polar solvent to that in an ionic crystalline environment, pointing out similarities that these vastly different environments have on the ion and the $I_3^- \cdots I_3^-$ interaction. It will be shown that a highly polar solvent can be used as an alternative and computationally less expensive way of modelling the $I_3^- \cdots I_3^-$ interaction compared to including the surrounding ionic molecules. This study will compare stabilisation energies and electrostatic potential (ESP) on the surface of the I_3^- ion and also utilising atoms in molecules (AIM).

7.1. Stabilisation Energy of the I_3^- ion

The relationship between the $I_3^- \cdots I_3^-$ interaction energy (E_{INT}) and the stabilisation (ΔE_S) provided by the solvent (for a single I_3^- ion) is shown in Fig. 7.1 at various levels of theory. The MP2/TZ level of theory was included as reference with the inclusion of MP2/a-TZ to illustrate that even though E_{INT} is overestimated the level of theory still yields comparable values for $V_{S,\ MAX}$. The PBE-D2 was included due to its success in modelling the $I_3^- \cdots I_3^-$ interaction energy when compared to the CCSD/a-TZ//MP2/TZ benchmark, seen in Chapter 3. The dTZ basis set was selected instead of the a-TZ for the PBE-D2 functional for the sake of clarity since the a-TZ basis set exactly overlays. This graph shows that both the WFT method, MP2, and the DFT method, PBE-D2, yield comparable gradients which illustrates that the solvent has the same effect on the energy and also the interaction energy. Furthermore, the *x*-intercept in Fig. 7.1 shows the stabilisation needed to make the $I_3^- \cdots I_3^-$ interaction energy favourable for a particular method. If we consider the method that yields the most accurate E_{INT}, MP2/TZ, we see that a stabilisation of approximately -41 kcal/mol is needed for the $I_3^- \cdots I_3^-$ interaction energy to become stabilising. Furthermore, we see that PBE-D2 yields comparable results, with a stabilisation of approximately -40.3 kcal/mol is needed to make E_{INT} favourable. In general, a stabilisation greater than -40 kcal/mol is needed for the $I_3^- \cdots I_3^-$ intermolecular interaction to become favourable. Naturally, a value greater than -40 kcal/mol for a single I_3^- in the solid state would be expected, since it is surrounded by cations. Note, that when MP2 is used with the a-TZ basis set, the amount of stabilisation energy needed is decreased by almost 3 kcal/mol due to an overestimation of the $I_3^- \cdots I_3^-$ interaction energy.
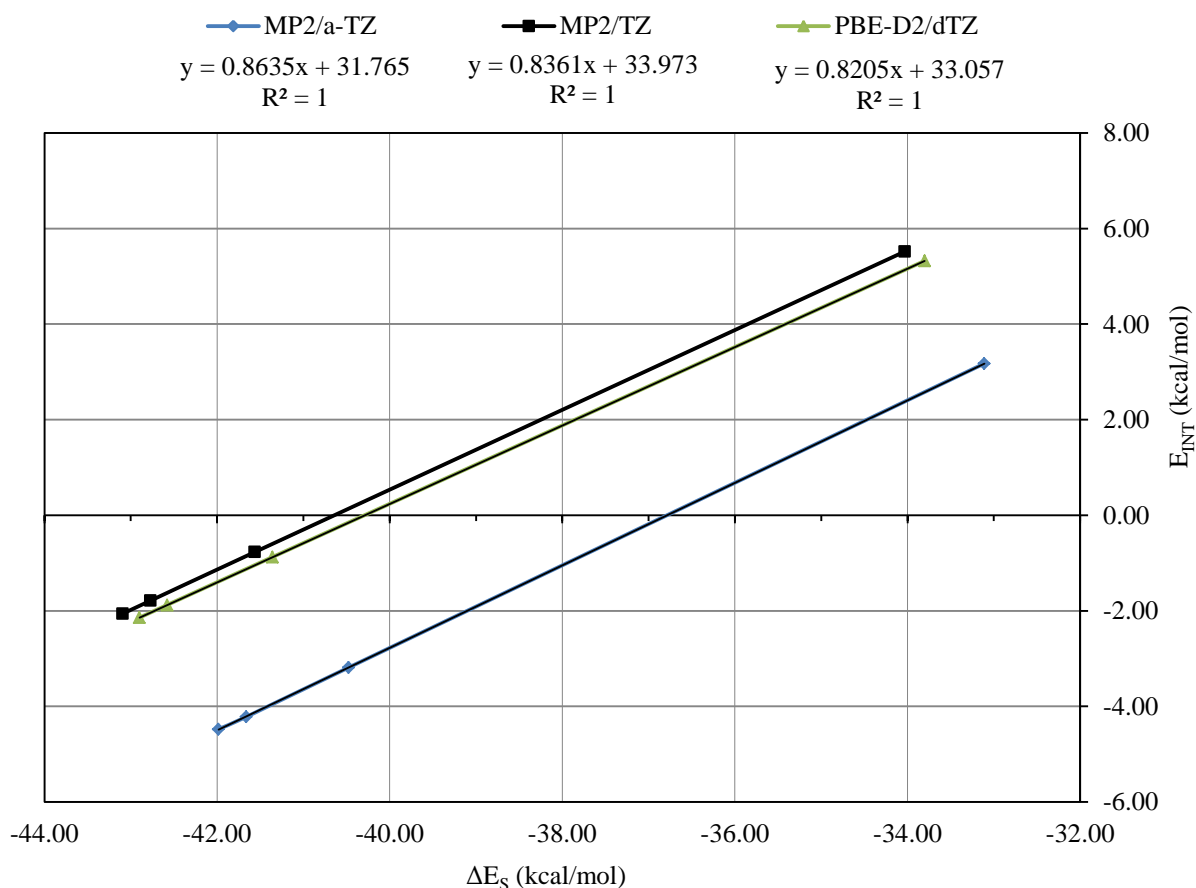
Fig. 7.1 – The $I_3^-\cdots I_3^-$ interaction energy (E_{INT}) plotted against the stabilisation (ΔE_S) provided by the four selected solvents (from left to right) *n*-methylformamide-mixture, water, ethanol and chloroform. The graph is constructed from data listed in Table 3.4.

To obtain a rough estimate of the stabilisation provided by the surrounding cations, it was decided that the four cations in the expanded unit cell (shown in Fig. 7.2) would be considered as the 'surroundings'. If a greater stabilisation is obtained for the expanded unit cell than for the *n*-methylformamide-mixture solvent, we can say with certainty that the stabilisation could only increase with an expansion in the size of the model, due to added electrostatic interactions. It was decided that the stabilisation for a single I_3^- in SETHAB would be calculated by taking all of the interaction energies between a single I_3^- with the other fragments in the expanded unit cell into account (see Fig. 7.2 and Table 7.1).

120
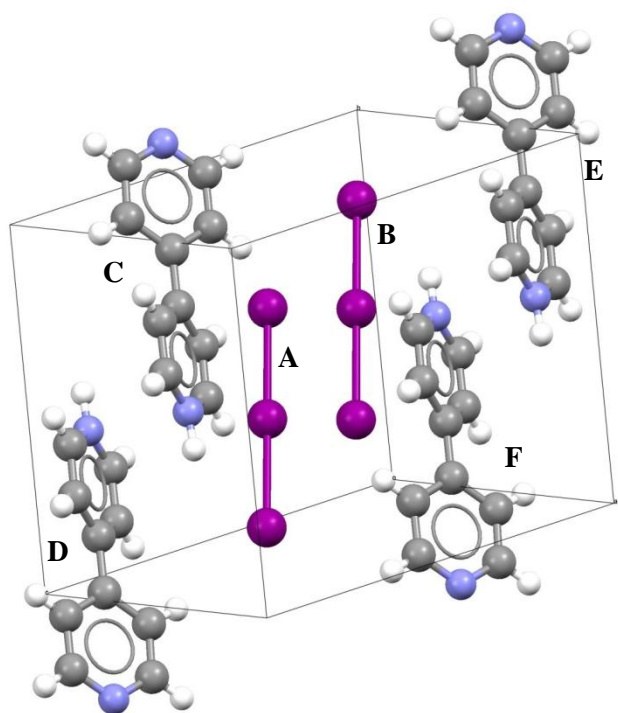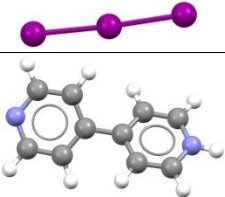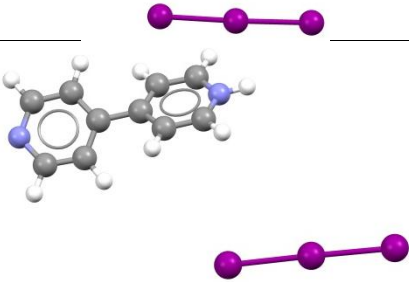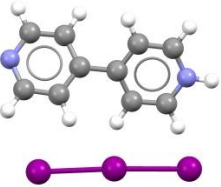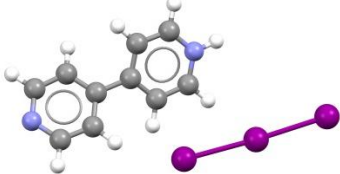
Fig. 7.2 – The expanded unit cell of SETHAB with the molecules numbered from A to F.

All the stabilisation energies of the various permutations (A-B, A-C, A-D, A-E, A-F) for a single I_3^- ion with neighbouring molecules shown in Fig. 7.2, are listed in Table 7.1.

Table 7.1 – All the stabilisation energies for ion A with molecules C, D, E, F and B shown in Fig. 7.2, with their corresponding stabilisation energies calculated with MP2 where the a-TZ basis set was utilised for the triiodides and the 3-21G basis set for C, N and H atoms.

Fragment **A** with **B, C**, **D**, **E** and **F**	Stabilisation Energy (kcal/mol)
	+48.88
	-74.24
	-40.86
	-74.84
	-70.03
TOTAL STABILISATION ENERGY	**-211.09**

The various stabilisations provided by each of the cations given in Table 7.1 are equal to or greater than that found for the I_3^- ion in *n*-methylformamide-mixture in almost all cases. Furthermore, when all of these interactions are summarised we see that the total stabilisation provided by the surroundings is almost four times the magnitude (-211 kcal/mol) of what is found for the I_3^- ion in a highly polar solvent, despite the high repulsion (+49 kcal/mol) present between the two I_3^- ions. This is substantially higher, also considering the size of the crystal model, than the -40 kcal/mol needed to make the $I_3^- \cdots I_3^-$ intermolecular interaction

stabilising favourable. Therefore, it seems reasonable to assume that if the I_3^- ions are separated by a distance less than twice the vdW radius in a crystalline environment the $I_3^- \cdots I_3^-$ interaction is highly likely to be favourable due to the stabilisation provided by the surroundings. The high value for the stabilisation calculated in Table 7.1 could be a result of double counting interactions. The stabilisation by the surroundings of -211 kcal/mol can therefore not be considered as a realistic or reliable result. Furthermore, if we revisit Fig. 3.4 where E_{INT} was plotted against the dielectric constant we saw that the $I_3^- \cdots I_3^-$ interaction energy converged to a specific value for each method, due to 'damping' of the electrostatic component within the total $I_3^- \cdots I_3^-$ interaction energy. This dependence of the $I_3^- \cdots I_3^-$ interaction energy on the dielectric was shown to be a result of the increased stability provided by the solvent. This stabilisation provided by the solvent is a result of the increase electrostatic interactions between the solute and the solvent which was found in Chapter 3 to 'dampen' the repulsive electrostatic component of the total $I_3^- \cdots I_3^-$ interaction energy. It was found that the 'dampening' effect converges to a maximum when the I_3^- dimer is submerged in n-methylformamide-mixture resulting in an $I_3^- \cdots I_3^-$ interaction energy of -2.06 kcal/mol. Furthermore, as mentioned before, the strength of the dispersion interaction is dependent on the polarisability of the atom under investigation, implying that even though the electrostatic repulsive term decreased even further, the total attractive $I_3^- \cdots I_3^-$ interaction energy would converge. Thus, it seems fair to assume that if the stabilisation provided by the surroundings exceeds the calculated value of -43 kcal/mol for n-methylformamide-mixture, the 'dampening' effect of the electrostatic component of the total $I_3^- \cdots I_3^-$ interaction energy should remain at a maximum, making the total $I_3^- \cdots I_3^-$ interaction energy only dependent on the dispersion interaction term.

7.2. Surface analysis of the I_3^- ion in a crystal

Before the surface of the I_3^- ion is discussed in the SETHAB crystal, let us briefly revisit selected results from the WFA-SAS analysis discussed in Chapter 5, which are summarised in Table 7.2 and extracted from Table 5.1. Results in Table 7.2 are graphically represented in Fig. 7.3.

Table 7.2 – E_{INT} (kcal/mol) and the average $V_{S, MAX}$ (kcal/mol) for the PBE-D2 and B97D functionals utilising the 6-311G** basis set in chloroform, ethanol, water and *n*-methylformamide-mixture.

	PBE-D2	B97D
Solvent	E_{INT} (kcal/mol)	
Chloroform (ε = 4.7113)	5.56	5.58
Ethanol (ε = 24.852)	-0.62	-0.45
Water (ε = 78.3553)	-1.62	-1.43
n-methylformamide-mix (ε = 181.56)	-1.89	-1.69
	Average $V_{S, MAX}$ (kcal/mol)	
Chloroform (ε = 4.7113)	-70.04	-69.80
Ethanol (ε = 24.852)	-69.34	-69.14
Water (ε = 78.3553)	-69.20	-69.00
n-methylformamide-mix (ε = 181.56)	-69.16	-68.96

The results for $V_{S, MAX}$ value listed in Table 7.2 is the average ESP of both σ-holes on the surface of the I_3^- ion, shows that as the $I_3^- \cdots I_3^-$ interaction energy increases, the ESP potential of the σ-hole becomes less negative, thus decreasing the repulsion between the I_3^- ions. When the *y*-intercepts for both DFT functionals are considered in Fig. 7.3, we can deduce that if the $V_{S, MAX}$ of the σ-hole on the surface of the I_3^- ion, it must be less negative (or greater than) than -69.35 kcal/mol or -69.20 kcal/mol for the PBE-D2 and B97D functionals, respectively in order for an attractive $I_3^- \cdots I_3^-$ interaction to be observed. We therefore expect the $V_{S, MAX}$ of the σ-hole of the I_3^- ion in the crystalline environment to be less than -69.4 kcal/mol.
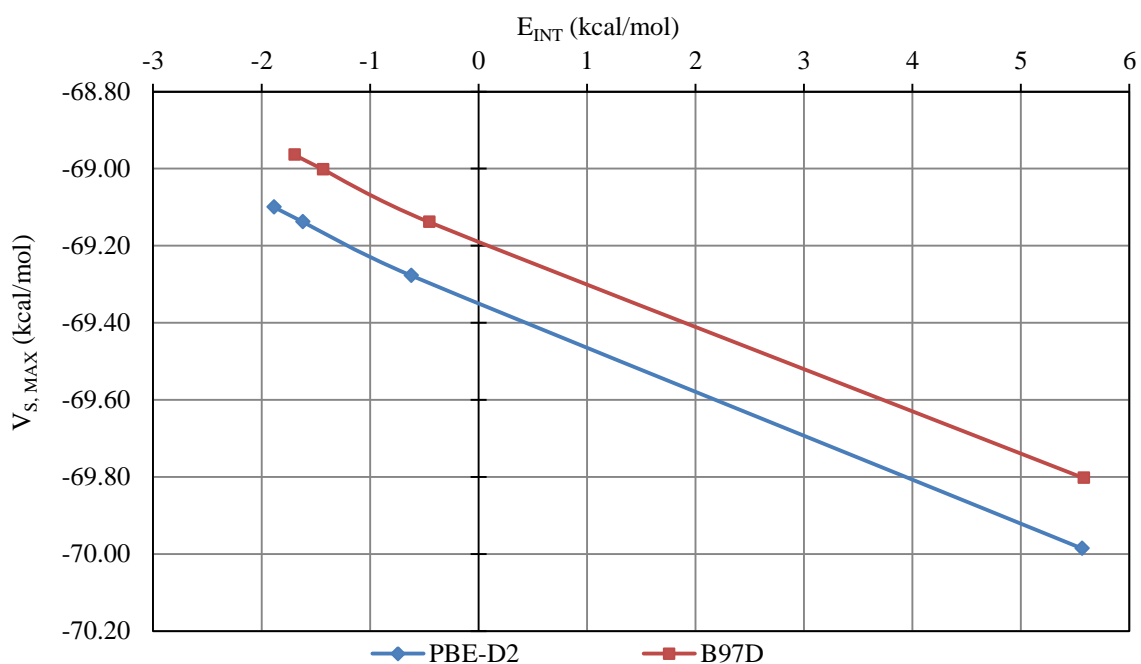
Fig. 7.3 – Relationship of $V_{S, MAX}$ (kcal/mol) of the σ-hole vs the $I_3^- \cdots I_3^-$ interaction energy for the PBE-D2 and B97D functionals utilising the 6-311G** basis set.

However, before we investigate this next aspect, we must consider how the SETHAB electrostatic environment is defined. The environment consists of the 3×3×3 units of the expanded unit cell shown in Fig. 7.2, where a central I_3^- ion (indicated in black in Fig. 7.4) was represented quantum mechanically with the surrounding atoms replaced by corresponding point charges (shown in Fig. 7.4). Mulliken charges were calculated for the expanded unit cell (shown in Fig. 7.2) and utilised to replace the atoms (shown as grey spheres in Fig. 7.4) with their corresponding point charges. This replacement of atoms with corresponding point charges mimics the electrostatics of the crystalline environment.
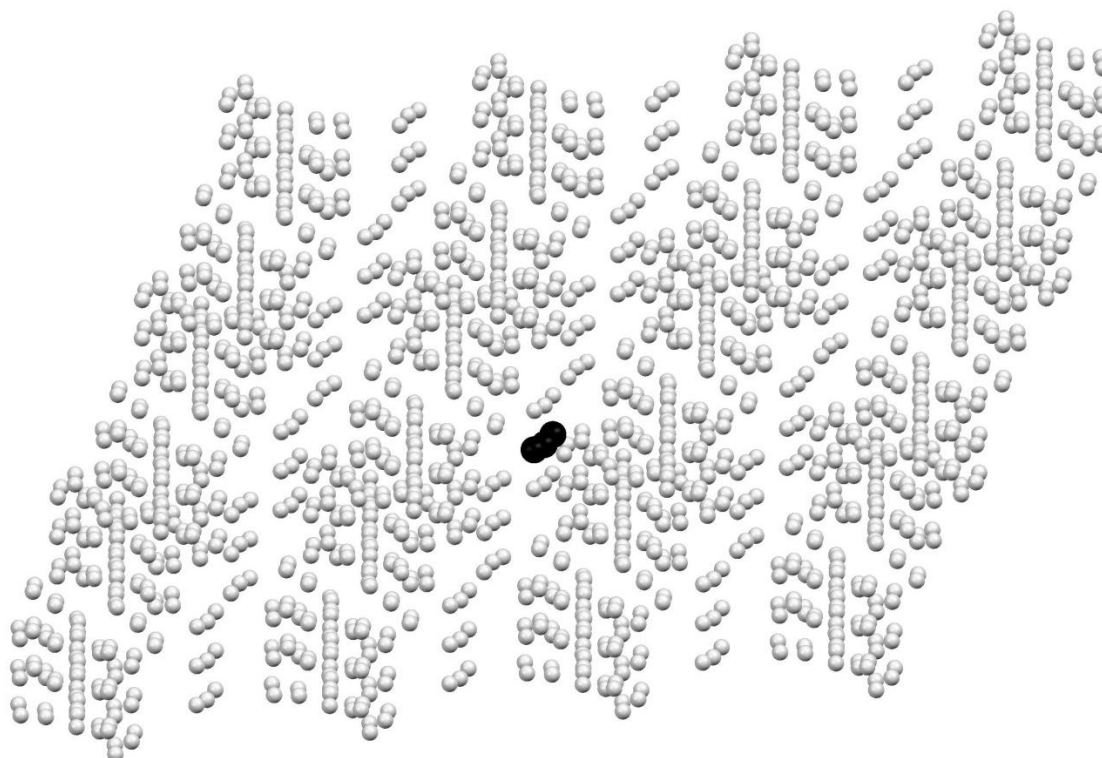
Fig. 7.4 – Point charge positions with their corresponding Mulliken charges (indicated as light grey spheres) for the extended unit cell surrounding the I_3^- ion (indicated in black).

The ESP surface for the I_3^- ion surrounded by the point charges indicated in Fig. 7.4, is shown in Fig. 7.5 for the PBE-D2 functional, where noticeable differences can be seen with respect to the position and size of the two σ-holes. When the electrostatic surface of the I_3^- ion (shown in Fig. 7.5 A) is compared to the I_3^- ion in solution and gas phase (shown in Fig. 5.2 and Fig. 7.5 B for comparison), the influence of the electrostatic environment on the ESP on the surface of the I_3^- ion is clearly visible. In the solid state, the ESP of the region on the surface of the I_3^- ion between the two σ-holes is less negative than in solution.

125
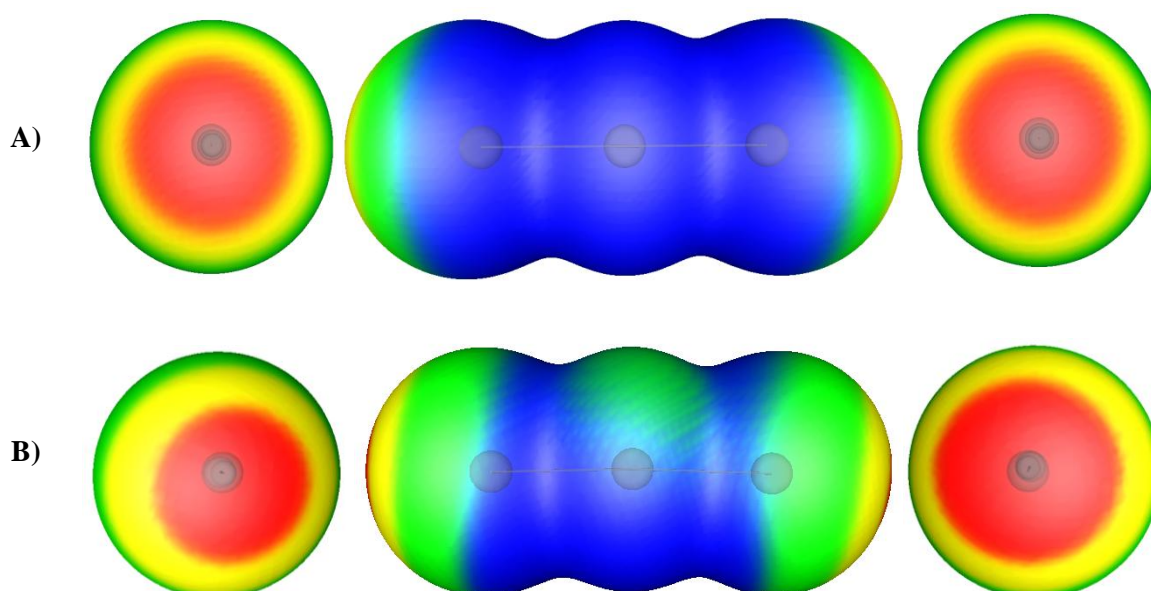
Fig. 7.5 – A) ESP surface of the I_3^- ion in the gas phase and the B) ESP surface of the I_3^- ion in SETHAB expanded in the *x*, *y* and *z* direction with three unit cells in each direction and all atoms replaced by point charges, at the PBE-D2/6-311G** levels of theory. The red regions (greater than -79 kcal/mol) indicate regions on the surface that are relatively less negative than the remainder of the molecule. The blue areas indicate regions that are more negative (-92.1 kcal/mol).

The average values for the $V_{S, MAX}$ critical points (CPs) located on the σ-hole, calculated for the I_3^- ion (shown in Fig. 7.6) within the SETHAB crystal structures are listed in Table 7.3.
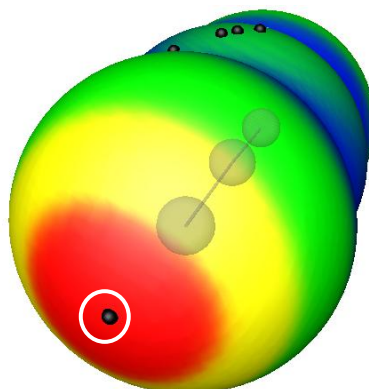
Fig. 7.6 - Critical points on the surface of the I_3^- ion, indicated as black spheres, within the SETHAB crystal structure environment at the PBE-D2/6-311G** level of theory.

The calculated values for $V_{S, MAX}$, listed in Table 7.3, were obtained with different Mulliken charges to make up the electrostatic environment that the I_3^- ion is exposed to within the SETHAB crystal. The ESP values of the two σ-holes are not identical as before in Chapter 5, resulting from terminal iodine atoms being in locally 'different' electrostatic environments due to the directionality of the surrounding cations. The calculated $V_{S, MAX}$ values coincide with the size of the σ-hole, resulting in larger σ-holes having less negative values than smaller σ-holes. All the charges were obtained from a single point energy calculation done on the extended unit cell, shown in Fig. 7.2, for a range of functionals. Charge set **1** was calculated with two basis set, where 6-311G** was used for I_3^- and 3-21G for C, N and H. Charge set **2**

was calculated utilising the 6-311G** basis set for all the atoms present. Charge set **3** was also calculated with the 6-311G** basis set for all the atoms, with the exception of the N-H bond length being optimised with QM (see Methodology), since MM failed to model it accurately, to investigate possible changes in the ESP of the σ-hole of the I_3^- ion.

Table 7.3 – $V_{S, MAX}$ (kcal/mol) of the σ-hole on the surface of the I_3^- ion within the SETHAB crystal, where the only differences are in the basis sets used to calculate charges. Electrostatic surfaces potentials are calculated utilising the PBE-D2 and B97D functionals with the 6-311G** basis set.

Charge set	Functional	$V_{S, MAX}$ (kcal/mol)	$V_{S, MAX}$ (kcal/mol)	Average $V_{S, MAX}$ (kcal/mol)
1[a]	PBE-D2	-66.60	-68.49	*-67.54*
	B97D	-68.49	-70.66	*-69.58*
2[b]	PBE-D2	-66.38	-68.61	-67.50
	B97D	-67.15	-68.76	-67.96
3[c]	PBE-D2	-66.38	-68.67	**-67.53**
	B97D	-67.15	-68.82	**-67.99**

[a]Charges calculated for Fig. 7.2, with the 6-311G** basis set for I and 3-21G basis set for C, N, H

[b]Charges calculated for Fig. 7.2, with the 6-311G** for I, C, N, H

[c]Charges calculated for Fig. 7.2, N-H bondlength set to 1.12 Å (B971 optimisation), charges calculated with 6-311G**

If we consider the calculated $V_{S, MAX}$ values for point charge set **1**, we note that if we were to compare the value of $V_{S, MAX}$ obtained with the B97D functional to the graph in Fig. 7.3, it indicates that the electrostatic environment does not stabilise the I_3^- ion sufficiently, thus suggesting the $I_3^- \cdots I_3^-$ interaction energy is not favourable. The opposite is true for the PBE-D2 functional. This inconsistency in the $V_{S, MAX}$ values for the two DFT functionals is a result of the Mulliken charges utilised as point charges which are not correctly calculated by the 3-21G basis set when compared to the 6-311G** basis set.

We see for charge set **2** and **3** the $V_{S, MAX}$ for both values indicate the ESP on the surface of the I_3^- ion is substantially less negative when compared to in a highly polar solvent ($V_{S, MAX} =$ ~ -69 kcal/mol see Fig. 7.3). This 2 kcal/mol increase, for both DFT functionals, in the value of $V_{S, MAX}$ indicates conclusively that the electrostatic environment provides sufficient stabilisation in order for the $I_3^- \cdots I_3^-$ intermolecular interaction to be favourable. Also, the value of $V_{S, MAX}$ means that the repulsive electrostatic component in the total $I_3^- \cdots I_3^-$ interaction energy is minimised. Furthermore, the HF $I_3^- \cdots I_3^-$ interaction energy as a function of the dielectric constant (shown in Fig. 3.4) illustrates that the decrease in the repulsive electrostatic component present in the total $I_3^- \cdots I_3^-$ interaction energy converges to 6 kcal/mol (achieved with a stabilisation provided by *n*-methylformamide-mixture of approximately -42 kcal/mol) concomitant with an increase in the total attractive $I_3^- \cdots I_3^-$ interaction energy. Since the $I_3^- \cdots I_3^-$ interaction energy is a result of dispersion interactions due to electron correlation and is limited to the number electrons and atoms involved, we believe that even though the

repulsive electrostatic component is even further decreased than in *n*-methylformamide-mixture, the interaction energy would not be greater than what is found for the I_3^- dimer in *n*-methylformamide-mixture at the CCSD/a-TZ/MP2/TZ level of theory. Thus far, our results for the $I_3^- \cdots I_3^-$ interaction energy in a highly polar solvent, seem to be representative of what is found in the solid state. We conclude that charge set **3** is the more accurate electrostatic representation of the three crystalline electrostatic environments listed in Table 7.3, despite the fact that charge set **3** yields a slightly greater negative average value for $V_{S, MAX}$ suggesting a decrease in stabilisation. However, we believe the hydrogen positions in charge set **3** alongside all the calculated Mulliken charges are a more realistic representation of the electrostatic environment of the SETHAB crystal.

A graph (Fig. 5.5) was constructed in Chapter 5, for selected solvents, which showed a linear relation between ΔE_S and $V_{S, MAX}$ (see Fig. 7.7). This graph will enable us to calculate an estimate for the stabilisation of the I_3^- ion provided by the crystal.

(1) y = -0.0924x - 72.9
R² = 0.9986

(2) y = -0.0961x - 73.272
R² = 0.9991

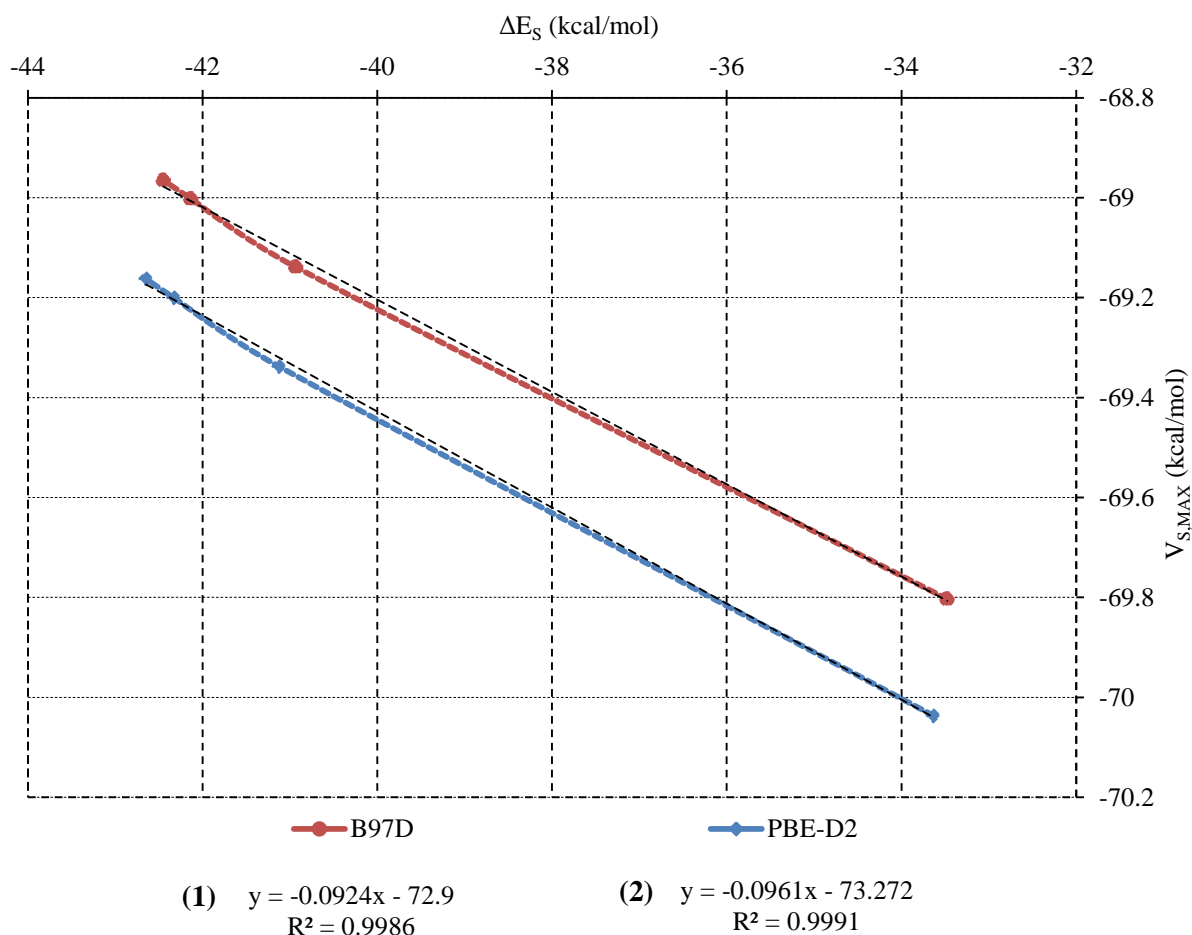**Fig. 7.7** – Linear relationship between ΔE_S (kcal/mol) and $V_{S, MAX}$ for B97D and PBE-D2 utilising the 6-311G** basis set.

The graph in Fig. 7.7 was obtained from Fig. 5.5, with the results for TPSS and MP2 omitted. The equations in Fig. 7.7 can be viewed as an alternative way of calculating the stabilisation provided by the crystal to our first attempt shown in Fig. 7.1, where the supramolecular

128

approach was followed by adding and subtracting selected parts in order to obtain a net stabilisation energy, which was found to be -211 kcal/mol. As mentioned before, this value of -211 kcal/mol is not considered as accurate, only an estimate. However, if we substitute the $V_{S, MAX}$ values calculated for the I_3^- listed in Table 7.3 for charge set **3** into the equations shown in Fig. 7.7, we could possibly obtain a more realistic value for the stabilisation energy provided by the crystalline environment for a single I_3^- ion.

From equation **1** for **B97D** in Fig. 7.7 ($x = \Delta E_S$ and y = $V_{S, MAX}$) we can obtain ΔE_S:

$$V_{S,MAX} = -67.99 \ kcal/mol$$

$$\Delta E_S = \frac{y + 72.9 \ kcal/mol}{-0.0924}$$

$$\boldsymbol{\Delta E_S = -53.14 \ kcal/mol}$$

If the same process if followed via equation **2** in Fig. 7.7 for PBE-D2, we obtain a value of **-59.75** kcal/mol. Calculated $V_{S, MAX}$ and ΔE_S values for the SETHAB crystal, utilising equations **1**and **2** in Fig. 7.7, are listed in Table 7.4. Calculated $V_{S, MAX}$, ΔE_S and E_{INT} values for the *n*-methylformamide-mixture are included for comparison. If the $V_{S, MAX}$ values in Table 7.4 for *n*-methylformamide-mixture and SETHAB are compared, we see that $V_{S, MAX}$ is approximately 2 % and 1 % less negative for PBE-D2 and B97D, respectively. These results obtained for ΔE_S through eq. **1** and **2**, listed in Table 7.4, indicate that the crystalline environment is approximately 10 kcal/mol more stabilising than the most polar solvent (*n*-methylformamide-mixture).

Table 7.4 − $V_{S, MAX}$ (kcal/mol), ΔE_S (kcal/mol) and E_{INT} (kcal/mol) in *n*-methylformamide-mixture and in the SETHAB crystal for PBE-D2 and B97D utilising the 6-311G** basis set.

	PBE-D2			B97D		
	$V_{S, MAX}$ (kcal/mol)	ΔE_S (kcal/mol)	E_{INT} (kcal/mol)	$V_{S, MAX}$ (kcal/mol)	ΔE_S (kcal/mol)	E_{INT} (kcal/mol)
n-methylformamide-mixture	-69.16	-42.65	-1.89	-68.96	-42.45	-1.70
Point charge set **3**	-67.53[a]	**-59.75**[b]	?	-67.99[a]	**-53.14**[b]	?

[a]Values obtained from Table 7.3

[b]Values obtained via $V_{S, MAX}$ utilising eq. 1 and 2 in Fig. 7.7

Both the PBE-D2 and B97D functionals indicate ΔE_S values for the I_3^- ion are larger in the point charge set than *n*-methylformamide-mixture. However, the calculated ΔE_S values for SETHAB via eq. **1** and **2** by substituting $V_{S, MAX}$ into the corresponding equation is substantially lower than the stabilisation energy calculated in Table 7.1 which was calculated by employing the supramolecular approach. It seems reasonable to assume that the ΔE_S values

listed in Table 7.4 are more representative of the stabilisation provided by the crystal structure than the -211 kcal/mol stabilisation energy listed in Table 7.1.

To broaden the scope of the investigation, an AIM analysis will be performed and compared to what was found in Chapter 6.

7.3. AIM analysis of the I_3^- ions in SETHAB

In this section two neighbouring I_3^- ions, as found in the SETHAB crystal structure, will be studied in various environments. It should be stressed that although $[I_3^-]_\infty$ chains are present in SETHAB, only two neighbouring I_3^- ions as found in the solid state will be studied. The environments are: the gas phase, the *n*-methylformamide-mixture solvent and in the SETHAB crystal (where the I_3^- ion will be surrounded by Charge set **4**). The two neighbouring I_3^- ions will be compared, as before in Chapter 6, by investigating the values for the three AIM properties: the electron density (ρ_b), the Laplacian of the electron density [$L(\rho_b)$] and the the total energy density (H_b), in various electrostatic environments.
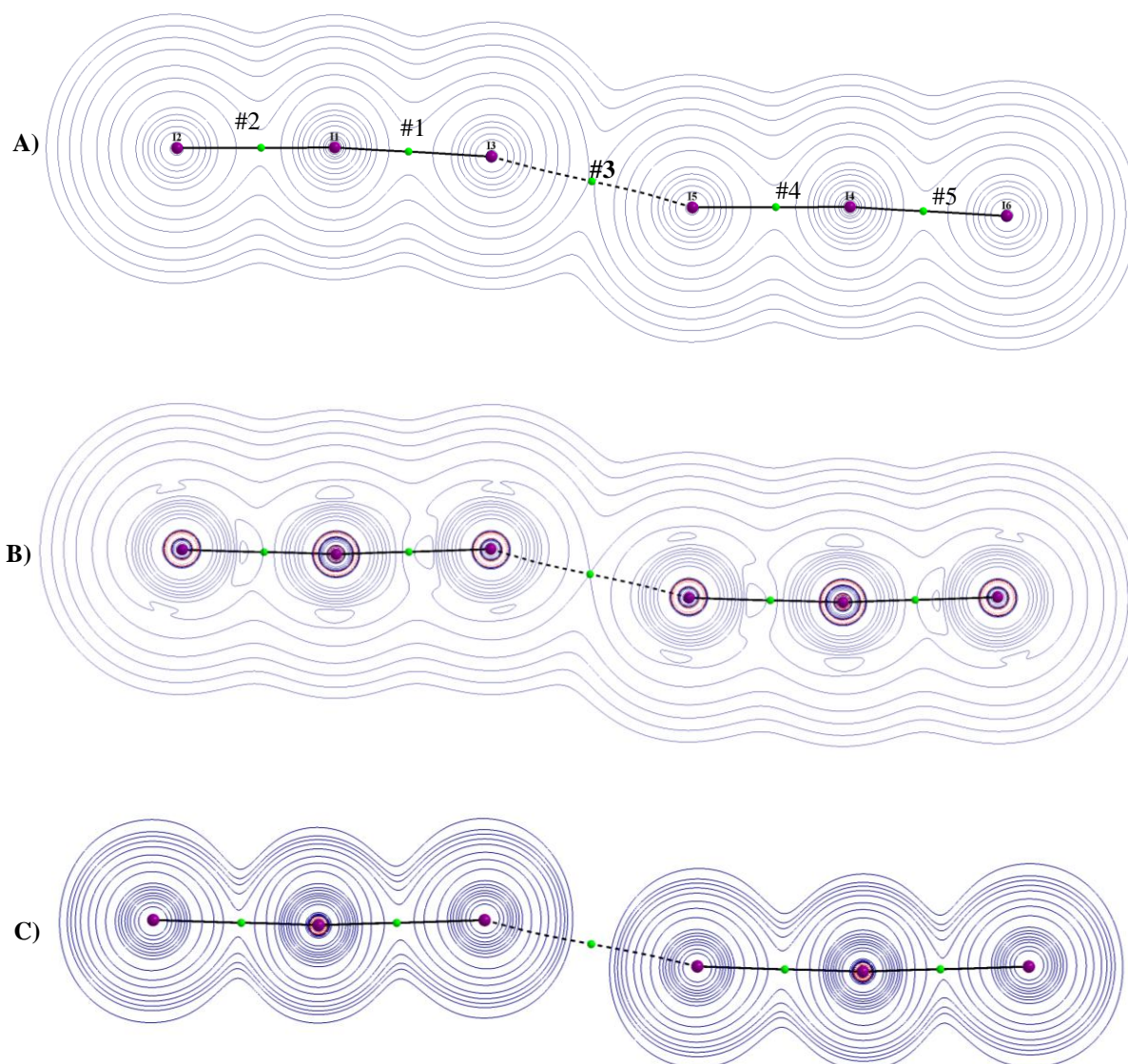
Fig. 7.8 – Two dimensional contour plots of A) the electron density (ρ_b) B) the Laplacian of the electron density [L(ρ_b)] and C) the total energy density (H$_b$) of two neighbouring I$_3^-$ ions, obtained from SETHAB, in the gas phase at the MP2/TZ level of theory with the numbered BCPs indicated as green spheres, atoms are shown in purple, bond path represented as solid black line represent and the atomic interaction line indicated as a dotted black line.

In Fig. 7.8 the three AIM parameters with the various BCPs are graphically represented by two dimensional contour plots for the geometry of two neighbouring I$_3^-$ ions found in SETHAB. The various bond lengths and calculated values for the three AIM parameters at the BCPs shown in Fig 7.6 are listed in Table 7.5 for three different environments. The values calculated for the three AIM parameters were calculated at the MP2/TZ level due to its success in calculating the I$_3^-\cdots$I$_3^-$ interaction energy when the CCSD/a-TZ//MP2/TZ benchmark is considered in Chapter 3. The a-TZ basis set was avoided due to its overestimation of the I$_3^-\cdots$I$_3^-$ interaction energy, which may then also result in an overestimation of the electron density at BCP #3. The discussion will mainly concern the

results for BCP #3 (indicated in bold Table 7.5), the remaining BCPs shown in Fig. 7.8 will be mentioned briefly.

Table 7.5 – The bondlength (Å), $I_3^- \cdots I_3^-$ intermolecular distance (Å), electron density (ρ_b), the Laplacian of the electron density [$L(\rho_b)$] and the total energy density (H_b) in au at various BCPs (shown in Fig. 7.8 A) at the MP2/TZ level of theory.

Surroundings	Bond length (Å)	BCP #	Atoms	ρ_b (ea_0^{-3})	$L(\rho_b)$ (ea_0^{-5})	H (au)
Gas phase	2.938	1	I1 - I3	0.0511	0.0223	-0.0120
	2.951	2	I1 - I2	0.0463	0.0408	-0.0095
	3.888	**3**	**I3 - I5**	**0.0078**	**0.0200**	**0.0008**
	2.951	4	I4 - I5	0.0499	0.0237	-0.0113
	2.938	5	I4 - I6	0.0475	0.0399	-0.0101
n-methyl-formamide-mixture	2.938	1	I1 - I3	0.0500	0.0281	-0.0114
	2.951	2	I1 - I2	0.0475	0.0353	-0.0101
	3.888	**3**	**I3 - I5**	**0.0082**	**0.0206**	**0.0007**
	2.951	4	I4 - I5	0.0486	0.0300	-0.0107
	2.938	5	I4 - I6	0.0488	0.0336	-0.0108
SETHAB	2.938	1	I1 - I2	0.0495	0.0270	-0.0112
	2.951	2	I1 - I3	0.0488	0.0348	-0.0107
	3.888	**3**	**I3 - I5**	**0.0084**	**0.0208**	**0.0007**
	2.951	4	I4 - I5	0.0483	0.0334	-0.0105
	2.938	5	I4 - I6	0.0500	0.0283	-0.0114

Note that the geometries of both triiodides in Fig. 7.8 are identical, thus only BCP #1 and #2 (analogous to BCP #4 and #5) will be briefly discussed with regards to the I-I bond. Our main interest is with the calculated values for the three AIM parameters at BCP #3 between the two I_3^- ions, and its behaviour with respect to the change in surroundings.

If the electron densities of BCP #1 and #2 for the three different surroundings in Table 7.5 is considered, we observe that all the calculated values falls within the range as defined by Nakanishi *et al.* (listed in Table 6.3 and repeated below for convenience) for CT-TBP bond types. In Chapter 6 it was shown that the electron density at the BCP of the I-I bond is not substantially affected when the I_3^- ion is submerged in a highly polar solvent.

Table 6.3 – Typical ranges for ρ_b (ea_0^{-3}), $L(\rho_b)$ in (ea_0^{-5}), H_b (au) for vdW interactions and the CT-TBP (trihalide ion)[a]

Interaction type	ρ_b (ea_0^{-3})	$L(\rho_b)$ (ea_0^{-5})	H_b (au)
Hydrogen Bonds	$0.01 < \rho_b < 0.04$	$0.04 < \nabla^2\rho_b < 0.12$	$-0.004 < H_b < 0.002$
van der Waals[a]	$0.00 < \rho_b < 0.01$	$0.00 < \nabla^2\rho_b < 0.04$	$0.000 < H_b < 0.002$
CT-TBP[a]	$0.03 < \rho_b < 0.1$	$-0.01 < \nabla^2\rho_b < 0.1$	$-0.06 < H_b < -0.003$

[a]values listed in Table 6.3 obtained from [1]

If the typical ranges for the Laplacian of the electron density and the total energy density are considered in Table 6.3, we see that all the results for both $L(\rho_b)$ and the H_b at the BCP #1 and #2 listed in Table 7.5 falls within the range defined by Nakanishi *et al.* for CT-TBP and vdW interactions, i.e. same as what was found in solvents [1].

If the three calculated ρ_{b3} values are considered in Table 7.5 an increases of approximately 6 % and 8 % are observed, relative to the gas phase, for *n*-methylformamide-mixture and the crystal environment, respectively. This increase in ρ_{b3} suggests, despite identical geometries being used, the $I_3^- \cdots I_3^-$ interaction energy becomes more stabilising from the gas phase to an ionic electrostatic environment in the solid state. Furthermore, we observe that both the Laplacian of the electron density at BCP #3 [$L(\rho_{b3})$] and the total energy density at BCP #3 (H_{b3}) falls within the defined range listed in Table 6.3, which further indicates that the $I_3^- \cdots I_3^-$ interaction is characterised as a vdW interaction. When $L(\rho_{b3})$ in the gas phase is compared to $L(\rho_{b3})$ in *n*-methylformamide-mixture and the crystal structure, increases of 3 % and 4 % are observed. If the values for H_{b3} are considered in Table 7.5, increases of 7 % and 10 % are observed for the I_3^- dimer *n*-methylformamide-mixture and the crystal structure when compared to the gas phase, respectively. As with the results in Chapter 6, we see that the value of H_{b3} are the most sensitive to the change in the environment. Interestingly, if the calculated values for ρ_{b3}, $L(\rho_{b3})$ and H_{b3} of $I_3^- \cdots I_3^-$ in *n*-methylformamide-mixture are compared to the crystal structure in Table 7.5, we see increases of 2.3 % and 1.2 % and a decrease of 2.5 %, respectively. The most significant finding, in Table 7.5, is the increase in the electron density between the two I_3^- ions when the dimer is modelled in a highly polar solvent and the dimer modelled in an ionic electrostatic environment, since, according to a theoretical study performed by Parthasarathi and co-workers [2] this suggests that the interaction energy will also increase. Utilising AIM theory Parthasarathi and co-workers showed that as the electron density increases at the BCP between two interacting molecules, the interaction energy increases in a linear fashion. However, this was applied across a broad range of dispersion interactions to strong hydrogen bonding.

The various calculated values for the three AIM parameters, with the geometry obtained for SETHAB, coincides with the typical ranges defined by Nakanishi *et al.*[1] for vdW interactions and proves that the I-I bond maintains it characteristics in substantially different electrostatic environments. Also, that the $I_3^- \cdots I_3^-$ interaction is present with a slightly lower electron density between the two I_3^- ions than what we found for the optimised structures in Chapter 6 (see Table 6.5), suggesting a decrease in the $I_3^- \cdots I_3^-$ interaction energy.

To summarise, in Section 7.1 we showed that the crystal structure environment stabilises the I_3^- ion substantially more than the implicit solvent models described in Chapter 3, but since our models used to calculate these ΔE_S values for the crystal were only an approximation of the crystal structure, the investigation was expanded to analyse the $V_{S, MAX}$ of the σ-hole of the I_3^- ion. Here, convincing evidence is presented for the ESP of the σ-hole on the surface of the I_3^- ion being approximately 2 kcal/mol less negative than for the I_3^- ion in the most polar solvent used in this study (*n*-methylformamide-mixture with a dielectric constant of ~182). This severe decrease in the $V_{S, MAX}$ of the σ-hole of I_3^- ion indicates that sufficient stabilisation is provided so that the $I_3^- \cdots I_3^-$ interaction to becomes favourable. The investigation was further supported by AIM results, where it was found that the electron densities at the BCP between the two I_3^- ions are comparable in *n*-methylformamide-mixture and the selected ionic electrostatic environment, with the ionic crystal yielding a slighter higher electron density at this BCP. This suggests that the $I_3^- \cdots I_3^-$ interaction energy is equal to or less stabilising than the -2 kcal/mol we obtained for the $I_3^- \cdots I_3^-$ interaction energy in *n*-methylformamide-mixture at the CCSD/a-TZ//MP2/TZ level of theory.

To expand the investigation even further, the $I_3^- \cdots I_3^-$ interaction was calculated in *n*-methylformamide-mixture, using geometries obtained from the crystal structure SETHAB. These $I_3^- \cdots I_3^-$ interaction energies are listed in Table 7.6 with MP2/TZ included as reference due to its low percentage deviation (~5 %) from the CCSD/a-TZ//MP2/TZ benchmark given in Chapter 3.

Table 7.6 – Calculated $I_3^- \cdots I_3^-$ interaction energies (E_{INT}) in *n*-methylformamide-mixture (ε = 181.56) using geometries obtained from SETHAB (shown in Fig. 7.8) for various methods utilising the a-TZ basis set.

Method	E_{INT} (kcal/mol)	% Deviation
MP2[a]	**-1.80**	0
HF	2.82	256.4
MP2	-3.63	101.3
PBE-D2	-1.87	3.8
B97D	-1.37	24.1

[a]the TZ basis set was used

When the MP2/TZ reference value is considered, we observe that the $I_3^- \cdots I_3^-$ interaction is less than what we found in Chapter 3 and believe this slight decrease in the interaction energy

is a result of the deviation from the optimised linear structures we observed for the solvent optimisations in various solvents of $I_3^- \cdots I_3^-$.

If the $I_3^- \cdots I_3^-$ interaction energy obtained with the two WFT methods, HF and MP2, utilising the a-TZ basis set we see that HF yields a repulsive $I_3^- \cdots I_3^-$ interaction energy with the MP2 overestimating the $I_3^- \cdots I_3^-$ interaction energy by more than 250 %. The results for HF/a-TZ and MP2/a-TZ coincide with our findings in Chapter 3 where these methods exhibited similar behaviour with regards to the interaction energy. As before in Chapter 3, the PBE-D2 functional yields the most comparable results for a particular benchmark, which in this case, is MP2/TZ. If the $I_3^- \cdots I_3^-$ interaction energy is considered for the B97D functional, we observe that as before in Chapter 3, this functional underestimates the $I_3^- \cdots I_3^-$ interaction energy when compared to a benchmark.

To summarise,

- Even though the calculated values for ΔE_S in a solvent with a dielectric constant of ~182 (*n*-methylformamide-mixture) are not comparable to the calculated values of ΔE_S for SETHAB given in Table 7.1, the solvent does provide sufficient stabilisation to damp the electrostatic repulsion between the I_3^- ions.

- The ESP potential on the surface of the I_3^- ion in solution is slightly more negative than what is found for the ionic crystal environment.

- The electron density at BCP 3# is slightly lower (yet comparable) for *n*-methylformamide-mixture compared to what is found for the SETHAB crystal, suggesting that the $I_3^- \cdots I_3^-$ interaction becomes more stabilising in the ionic crystal environment.

- The results in Chapter 3 suggest that *n*-methylformamide-mixture provides the necessary stabilisation for the $I_3^- \cdots I_3^-$ interaction to be favourable, thus making our calculated interaction energies in Table 7.6 a realistic approximation of utilising the *n*-methylformamide-mixture solvent to model the $I_3^- \cdots I_3^-$ interactions.

- All the results presented in this chapter strongly suggest that the cations or counterions can be omitted and replaced with an extremely polar solvent with a high dielectric constant as a pseudo-crystal environment providing the needed electrostatic stabilisation in order to make the $I_3^- \cdots I_3^-$ interaction favourable.

References

1.   Nakanishi, W., S. Hayashi, and K. Narahara, *Atoms-in-Molecules Dual Parameter Analysis of Weak to Strong Interactions: Behaviors of Electronic Energy Densities versus Laplacian of Electron Densities at Bond Critical Points.* The Journal of Physical Chemistry A, 2008. **112**(51): p. 13593-13599.

2.   Parthasarathi, R., V. Subramanian, and N. Sathyamurthy, *Hydrogen Bonding without Borders: An Atoms-in-Molecules Perspective.* The Journal of Physical Chemistry A, 2006. **110**(10): p. 3349-3351.

CHAPTER 8

Conclusions and Future Work

8.1. Conclusions

It has been shown that the $I_3^- \cdots I_3^-$ interaction does not exist in the gas phase, and therefore cannot be studied in this phase; even though a stationary point was obtained at the MP2/aug-cc-pVTZ-pp level of theory this was considered as an artefact. The $I_3^- \cdots I_3^-$ interaction has to be studied in a controlled electrostatic environment since there is evidence in the CSD for the existence of these anion-anion interactions. This marked the beginning of this investigation into this previously unexplained phenomenon.

As described in the third chapter, three parameters were utilised to measure the performance of various WFT and DFT methods, two of which are geometrical parameters determined from experimental structural data contained in the CSD: the I-I bond length [2.92(5) Å] of the I_3^- ion and the $I_3^- \cdots I_3^-$ intermolecular distance [3.80(10) Å]; with the third parameter being the $I_3^- \cdots I_3^-$ interaction energy calculated, in selected solvents, at the CCSD/aug-cc-pVTZ-pp//MP2/cc-pVTZ-pp level of theory. It was found that optimisations at the MP2/cc-pVTZ-pp level of theory yield results most comparable to the average values for both geometrical parameters obtained from the CSD, with less than 1 % deviation. Furthermore, MP2/ cc-pVTZ-pp yielded values for the $I_3^- \cdots I_3^-$ interaction energies closest to those obtained at the CCSD/aug-cc-pVTZ-pp //MP2/ cc-pVTZ-pp level of theory, with the greatest deviation from these values being 4 %. This makes MP2/cc-pVTZ-pp the best performing method for all three parameters defined.

The DFT optimisations of the I_3^- ion and $I_3^- \cdots I_3^-$ show that M06-2X yields values closest to the CSD average for the I_3^- bond length, while for the $I_3^- \cdots I_3^-$ intermolecular distance PBE-D2, BP86 and TPSS were most successful in reproducing the CSD average for the $I_3^- \cdots I_3^-$ intermolecular distance with a deviation under 2 %. We should mention that with the def2-TZVP basis set the I_3^- bond lengths and $I_3^- \cdots I_3^-$ intermolecular distances generally decrease when compared to the aug-cc-pVTZ-pp basis set. As might be expected, calculated $I_3^- \cdots I_3^-$ interaction energies become correspondingly more stabilising. If we only consider the interaction energy, E_{INT}, we can conclude that PBE-D2/aug-cc-pVTZ-pp came closest to the benchmark CCSD/aug-cc-pVTZ-pp //MP2/ cc-pVTZ-pp interaction energy in solution, being the only functional that does not underestimate this interaction. However, when we consider the DFT functionals investigated we notice that there is no one particular method that outperforms the others. We should add that we consider the $I_3^- \cdots I_3^-$ interaction energy to be the most decisive parameter in measuring a method's success due to the weak nature and type of this interaction. As a result, we can conclude that the PBE-D2 functional is the most

successful DFT functional, given its success in modelling the $I_3^- \cdots I_3^-$ intermolecular distance and interaction energy.

To summarise, we have identified a relatively inexpensive WFT method (MP2/cc-pVTZ-pp) which is able to successfully reproduce the experimental averages for the I-I bond length and for the intermolecular $I_3^- \cdots I_3^-$ distance, as well as the $I_3^- \cdots I_3^-$ interaction energy calculated at the CCSD/aug-cc-pVTZ-pp//MP2/cc-pVTZ-pp level of theory. Furthermore, we were able to identify a number of DFT functionals that give results for the geometrical parameters comparable to the experimental values, although only one method yielded a good value for the intermolecular interaction between the I_3^- ions.

Our solvent dependency studies indicated that anion-anion interactions can be favourable in the appropriate environment, and we have identified the minimum amount of energy (ΔE_s) needed, per I_3^- ion, for this interaction to become favourable, namely 40 kcal/mol. The last part of this section showed that the strength of the $I_3^- \cdots I_3^-$ interaction energy converges as the dielectric constant increases, which implies that the attractive interaction energy reaches a maximum regardless of the stabilisation provided by the surroundings. In Chapter 4 alternative electrostatic environments to the implicit solvent model were investigated to see if they could provide sufficient stability for the formation of the $I_3^- \cdots I_3^-$ interactions. Two alternatives were investigated: the electric field and the crystalline environment. All the optimisations were performed at a high level of theory, utilising MP2 in combination with large basis sets. The first part of the study was performed on the I_3^- ion, investigating the effect various strengths and directions of the electric field have on the optimised geometry. We saw that if the electric field is parallel to the I_3^- ion and is at a strength of 0.09 au one I-I bond breaks, resulting in I_2 and I^- fragments. When the direction of the field was adjusted perpendicular to the I_3^- ion, the strength could be increased to 0.13 au before one of the I-I bonds broke.

This difference in the strength of the field that can be applied with a change in orientation shows that the I_3^- ion is more stabilised by an electric field perpendicular to its bond axis than parallel to it. This study was expanded to $I_3^- \cdots I_3^-$ where lower strength electric fields were applied to minimise the geometrical distortion induced by the electric field. Despite decreasing the strength of the electric field substantially, no stationary points were obtained, thus suggesting that the directional nature of the electrostatic environment was the problem. In order to correct for this, the influences four different crystal structure models have on the geometry of the I_3^- ion were investigated in the second part of the chapter. Various optimisations of the I_3^- were performed with the positions of the cations kept stationary. It was observed that the optimised I-I bond length in the gas phase was consistently shorter than

139

what was found in the four crystal structure models. This decrease in the I-I bond length when the I_3^- ion wass placed in an electrostatic environment was also seen in Chapter 3 for the implicit solvent model studies. One particular result stood out, which is the optimisation of the I_3^- ion within crystal structure model **4**, where the B971 functional, which yields the most comparable I-I bond length in the gas phase to what is experimentally found for SETHAB, did not obtain a stationary point for $I_3^- \cdots I_3^-$ within an intermolecular distance twice the vdW radius of iodine (4.2 Å). However, we observed that PBE-D2 yields a stationary point for $I_3^- \cdots I_3^-$ within crystal structure model **4** with a very comparable $I_3^- \cdots I_3^-$ intermolecular distance, indicating the importance of dispersion interactions in these optimisations.

The work described in Chapter 5 consisted of the analysis of the electrostatic potential on the surface of the I_3^- ion as a function of the solvent. The WFA Surface Analysis Suite was utilised to investigate the surface of the I_3^- ion and correlate the ESP on the surface of the I_3^- to the $I_3^- \cdots I_3^-$ interaction energy (E_{INT}) and also stabilisation energy (ΔE_S) provided by the solvent. The surface potential ($V_{S, MAX}$) of the σ-hole supports our findings in Chapter 3 with respect to the HF $I_3^- \cdots I_3^-$ interaction energy, where the calculated E_{INT} at the HF/aug-cc-pVTZ-pp level of theory decreased as the dielectric constant increased, thus indicating a decrease in the (repulsive) electrostatic component of the total $I_3^- \cdots I_3^-$ interaction energy. This was indicated by $V_{S, MAX}$ becoming less negative as the dielectric constant increased. As a result, we observed an increase in the total $I_3^- \cdots I_3^-$ interaction energy along with the increase in the dielectric constant. Furthermore, this change in $V_{S, MAX}$ could be seen for both WFT and DFT methods indicating that both methods are similarly influenced by the effects of the electrostatic environment.

Following the surface analysis, AIM analysis was performed on the I_3^- ion and I_3^- dimer in Chapter 6. In this chapter three properties as defined by the AIM theory (electron density [$\rho_b(r)$], Laplacian of the electron density [$L(\rho_b(r))$] and the total energy density [$H_b(r)$]) were analysed at various BCPs of the I_3^- ion and $I_3^- \cdots I_3^-$. Various methods were tested including MP2, TPSS-D2 and PBE-D2, which all yield similar results when the I_3^- ion is considered. The I-I bond was found to be CT-TBP that exhibits partial covalent character, with the $I_3^- \cdots I_3^-$ interaction exhibiting typical van der Waals characteristics. The three AIM parameters were analysed for the $I_3^- \cdots I_3^-$ interaction as a function of the dielectric constant but, unfortunately, no substantial changes were observed from the gas phase to a highly polar solvent when MP2/aug-cc-pVTZ-pp is considered. Furthermore, we observe that the DFT functionals yield results more comparable to MP2/aug-cc-pVTZ-pp in the gas phase, which illustrates that DFTs are less sensitive to a change in the surroundings than the WFT method, MP2. Despite

these differences, the calculated results for the three AIM parameters coincide with those obtained with MP2, suggesting that the stabilising interactions between the I_3^- ions are dispersion interactions.

In the penultimate chapter, similarities in the influence that the surroundings have on the I_3^- ion and the $I_3^- \cdots I_3^-$ interaction were investigated. It was shown that the crystalline environment definitely provides the needed stabilisation for a single I_3^- ion in order for the $I_3^- \cdots I_3^-$ intermolecular interaction to become favourable. Furthermore, the AIM analysis illustrates that dispersion interactions are present between the I_3^- ions and that both the polar solvent selected and the crystalline environment have comparable effects on the electron density at the BCP between the two I_3^- ions in the dimer when compared to the gas phase. The utilisation of the ESP on the surface of the I_3^- ion in combination with the AIM results strongly suggests that the interactions present between the I_3^- ions are present if the intermolecular distance is within twice the vdW radius of Iodine. Furthermore, we showed that the crystalline environment provides substantially more stabilisation than *n*-methylformamide-mixture, which implies that the crystalline environment substantially decreases the contribution of the repulsive electrostatic term to the total attractive $I_3^- \cdots I_3^-$ interaction energy resulting in a favourable $I_3^- \cdots I_3^-$ interaction. Even though the *n*-methylformamide-mixture does not provide the same amount of stabilisation energy to the I_3^- ion, the solvent does provide sufficient stabilisation in order to keep the contribution of the electrostatic repulsive term to the total $I_3^- \cdots I_3^-$ interaction energy to a minimum. Thus, it seems reasonable to model the $I_3^- \cdots I_3^-$ interaction energy, found in the solid state, by utilising the *n*-methylformamide-mixture solvent as a pseudo-crystalline environment.

To summarise, geometrical data were obtained for the I-I bond length and the $I_3^- \cdots I_3^-$ intermolecular distance as reference by utilising the structural data available in the CSD. To our knowledge, structural data for the I-I bondlength, $I_3^- \cdots I_3^-$ intermolecular distance or the $I_3^- \cdots I_3^-$ interaction energy have yet not been calculated in the gas phase or in solution. Consequently, methods had to be identified which were able to yield comparable results for the I-I bond length and the $I_3^- \cdots I_3^-$ intermolecular distance compared to what is found in the solid state, and particularly, the $I_3^- \cdots I_3^-$ interaction energy due to its weak nature. Furthermore, it was important to explore methods that are less expensive than MP2 and CCSD, to enable the study of these ions in the crystalline environment where experimental data are available for comparison. As a result, numerous DFT functionals were tested, along with two high quality basis sets, aug-cc-pVTZ-pp and def2-TZVP. It was shown that the implicit solvent model could be used as a preliminary experiment to test the accuracy of a particular method

for calculating the $I_3^-\cdots I_3^-$ interaction energy. This was shown in Chapter 4, where the influence of various crystal structure models was investigated on the geometry of the I_3^- ion and also the geometry of two neighbouring I_3^- ions in a crystal structure model. The B971 functional was considered due to its excellent ability to reproduce the I-I bond length found in the crystal structure under investigation in the gas phase, while the PBE-D2 functional was chosen for its ability to model the $I_3^-\cdots I_3^-$ interaction in solution. As the Chapter progressed we observed that B971 consistently outperforms the other functionals when only the I-I bond length is considered, except for when $I_3^-\cdots I_3^-$ is optimised in crystal structure model **4**, where we see that B971 and PBE-D2 yield intermolecular distances of 7.3 Å and 3.84 Å, respectively. This substantial difference is a result of the inability of B971 to model the $I_3^-\cdots I_3^-$ interaction accurately, while changing the PES surface significantly as the stability provided by the environment increases. This influences the ability of a particular method to obtain a stationary point. This dependence on the electrostatic environment was seen in Chapter 3, where some functionals yield a stationary point in water but not in ethanol, since water has a higher dielectric constant and thus provides added stability. Furthermore, it was also shown in Chapter 3 that B971 yields an $I_3^-\cdots I_3^-$ interaction energy of +0.502 kcal/mol in ethanol compared to the $I_3^-\cdots I_3^-$ interaction energy calculated by PBE-D2 of -0.875 kcal/mol, utilising the def2-TZVP basis set (keep in mind that PBE-D2 was the DFT functional most successful in modelling the $I_3^-\cdots I_3^-$ interaction energy).

The AIM analysis performed in Chapter 6 proved that the $I_3^-\cdots I_3^-$ interaction energy is stabilised by dispersion interactions in the gas phase and in the four selected solvents. It was shown that the electron density at a particular BCP is dependent on the interatomic distance, and, to a lesser extent, on the dielectric constant. However, a substantial increase in the electron density at the BCP separating two I_3^- ions was observed for the I_3^- dimer when it was placed in a solvent. This increase of electron density at the BCP separating the I_3^- dimer was also observed in Section 7.3 where two neighbouring I_3^- ions in the SETHAB crystal structure, were placed in *n*-methylformamide-mixture and in a point charge electrostatic environment representing the crystal structure.

It was also shown that the ESP on the surface ($V_{S, MAX}$) of the I_3^- ion correlates linearly to the calculated $I_3^-\cdots I_3^-$ interaction energy and also to the ΔE_S in four selected solvents. $V_{S, MAX}$ was shown to become less negative as the total $I_3^-\cdots I_3^-$ interaction increased, correlating with the 'damping' of the repulsive electrostatic component. Since the increase in ΔE_S indicates an increase in the stabilisation provided by the surroundings, which was shown to coincide with a decrease in the repulsive electrostatic component of the total $I_3^-\cdots I_3^-$ interaction energy,

$V_{S,\ MAX}$ could also be utilised to implicitly calculate ΔE_S, which indicates how 'damped' the repulsion is. This strategy was employed in Chapter 7, where $V_{S,\ MAX}$ was obtained for the I_3^- ion in the solid state, showing that the $I_3^- \cdots I_3^-$ intermolecular interaction is highly likely to be favourable in the SETHAB crystal.

As mentioned before, we postulate that it is reasonable to model the $I_3^- \cdots I_3^-$ interaction energy in the solid state by utilising the *n*-methylformamide-mixture as a pseudo-crystalline environment providing sufficient stabilisation and 'damping' of the repulsive electrostatic term present in the total $I_3^- \cdots I_3^-$ interaction energy to make the $I_3^- \cdots I_3^-$ interaction favourable. Our postulate is supported by the HF interaction energy in Fig. 3.4 where the HF $I_3^- \cdots I_3^-$ interaction energy represents the 'damping' provided by the electrostatic surroundings.

In Fig. 3.4 a convergence is observed, which implies that even though the stabilisation (ΔE_S) increases, from *n*-methylformamide-mixture to the crystalline environment, the 'damping' of the electrostatic component in the $I_3^- \cdots I_3^-$ interaction energy is sufficient so that the attractive dispersion interactions present between the I_3^- ions can predominate. Furthermore, in Fig. 3.4, we observe that the $I_3^- \cdots I_3^-$ interaction energy also converges, since the electrostatic component is 'damped' and that the stabilising interactions, i.e. dispersion interactions, are dependent on the polarisability of the atoms present and therefore have a 'maximum' interaction energy. Our AIM results for the neighbouring $I_3^- \cdots I_3^-$ ions in the SETHAB crystal was consistent with the calculated $I_3^- \cdots I_3^-$ interaction energy, utilising the *n*-methylformamide-mixture as surroundings, where a decrease at BCP #3, was observed which then corresponds to a decrease in the $I_3^- \cdots I_3^-$ interaction energy.

8.2. Future work

Future work entails performing optimisations of the I_3^- ion and I_3^- dimer in various solvent at high levels of theory (CCSD and CCSD(T) in combination with the aug-cc-pVTZ-pp or aug-cc-pVQZ-pp basis sets) in order to obtain a benchmark for the $I_3^- \cdots I_3^-$ interaction energy. Another important aspect is to obtain DFT functionals able to model the $I_3^- \cdots I_3^-$ interaction energy accurately in solution in order to investigate the solid state. We propose employing the D3 dispersion correction, which has been incorporated into a wider number of DFT functionals, to study its effects on the optimised I-I bond length, $I_3^- \cdots I_3^-$ intermolecular distances and $I_3^- \cdots I_3^-$ interaction energy in various solvents. Furthermore, we believe our postulate should be expanded to other crystalline systems containing $[I_3^-]_\infty$ chains where we can employ *n*-methylformamide-mixture as a substitute for the crystalline electrostatic environment. This can be done by studying the Electrostatic Surface Potential of the I_3^- ion in

other crystalline environments where $[I_3^-]_\infty$ chains are present, and also utilising AIM to correlate $I_3^- \cdots I_3^-$ interaction energies in the solid state to those in solution.

We have shown that by utilising the ESP at a particular CP, for an ion within a point charge "crystal", it is possible to obtain the stabilisation energy provided by the ionic environment by means of extrapolation from values obtained in various PCM solvent environments and strongly believe that this can be applied to other ionic compounds, e.g. to study cation-cation interactions. If the stabilisation energy, calculated through the proposed extrapolation method, is sufficient to 'damp' the repulsive electrostatic term we can model the intermolecular interactions between ions with the same sign in charge, by submerging the system in *n*-methylformamide-mixture as a pseudo-crystalline environment and calculating the intermolecular interaction energy using the geometry found in the solid state. This study of intermolecular interaction energies between ions with the same sign in charge could even be expanded to cases where interactions are implied by short intermolecular interactions are implied by short intermolecular contact distances (within the sum of the vdW radii) in the solid state. However, this method can <u>only</u> be applied to intermolecular interactions which have repulsive electrostatic terms adding to the total intermolecular interaction energy.

Appendix A

Supplementary Information

Supplementary Information

Supplementary tables S1-5 containing optimised and average bond lengths for the I_3^- dimer at various levels of theory and basis sets.

Table S1 – Optimised and average bond lengths (Å) of the I_3^- dimer utilising MP2 in combination with various basis sets in the gas phase, ethanol and water.

Basis set	Solvent	Bond length (Å)				Average bond length (Å)
		R_1	R_2	R_3	R_4	
dTZ	ethanol	2.948	2.882	2.882	2.948	2.915
	water	2.944	2.885	2.885	2.944	2.914
a-TZ	gas	3.018	2.873	2.873	3.018	2.946
	ethanol	2.958	2.896	2.896	2.958	2.927
	water	2.954	2.898	2.898	2.954	2.926
TZ	ethanol	2.946	2.893	2.893	2.946	2.919
	water	2.942	2.896	2.896	2.942	2.919
a-DZ	ethanol	3.017	2.970	2.970	3.017	2.993
	water	3.012	2.974	2.974	3.012	2.993
DZ	ethanol	3.003	2.964	2.964	3.003	2.984
	water	2.999	2.967	2.967	2.999	2.983

Table S2 – Optimised and average bond lengths (Å) of the I_3^- dimer utilising various DFT functionals with the a-TZ basis set in ethanol.

Solvent	**ETHANOL**	Bond length (Å)				Average bond length (Å)
Basis set	**a-TZ**	R_1	R_2	R_3	R_4	
Functional	PBE	2.996	2.961	2.961	2.996	2.979
	PBE-D2	2.992	2.961	2.961	2.992	2.977
	ωB97X	3.024	2.862	2.862	3.023	2.943
	ωB97XD	2.975	2.910	2.910	2.975	2.942
	B971	2.978	2.942	2.942	2.978	2.960
	B97D	3.042	3.004	3.004	3.042	3.023
	BP86	3.006	2.971	2.971	3.006	2.989
	BP86-D2	3.004	2.972	2.972	3.004	2.988
	B3LYP	-	-	-	-	-
	B3LYP-D2	3.016	2.967	2.967	3.016	2.992
	TPSS	2.999	2.961	2.961	2.999	2.980
	TPSS-D2	2.997	2.962	2.962	2.997	2.979
	BLYP-D2	3.067	3.022	3.022	3.067	3.045
	PBE0	2.953	2.915	2.915	2.953	2.934
	M06	2.996	2.939	2.939	2.996	2.968
	M06-HF	2.865	2.812	2.812	2.865	2.838
	M06-2X	2.952	2.890	2.890	2.952	2.921
	LC-ωPBE	2.936	2.851	2.851	2.936	2.893
	B972	-	-	-	-	-
	X3LYP	2.996	2.967	2.967	2.996	2.982

Table S3 - Optimised and average bond lengths (Å) of the I_3^- dimer utilising various DFT functionals with the a-TZ basis set in water.

Solvent	WATER	Bond length (Å)				Average bond length (Å)
Basis set	a-TZ	R_1	R_2	R_3	R_4	
Functional	PBE	2.993	2.964	2.964	2.993	2.978
	PBE-D2	2.988	2.964	2.964	2.988	2.976
	ωB97X	3.132	2.804	2.804	3.132	2.968
	ωB97XD	2.965	2.918	2.918	2.965	2.941
	B971	2.973	2.946	2.946	2.973	2.959
	B97D	3.037	3.008	3.008	3.037	3.022
	BP86	3.003	2.974	2.974	3.003	2.988
	BP86-D2	2.999	2.975	2.975	2.999	2.987
	B3LYP	2.991	2.977	2.977	2.991	2.984
	B3LYP-D2	3.010	2.972	2.972	3.010	2.991
	TPSS	2.996	2.964	2.964	2.996	2.980
	TPSS-D2	2.992	2.965	2.965	2.992	2.978
	BLYP-D2	3.060	3.026	3.026	3.060	3.043
	PBE0	2.948	2.918	2.918	2.948	2.933
	M06	2.989	2.944	2.944	2.989	2.967
	M06-HF	2.861	2.815	2.815	2.861	2.838
	M06-2X	2.946	2.894	2.894	2.946	2.920
	LC-ωPBE	2.924	2.861	2.861	2.924	2.892
	B972	2.957	2.943	2.943	2.957	2.950
	X3LYP	2.992	2.971	2.971	2.992	2.981

Table S4 - Optimised and average bond lengths (Å) of the I_3^- dimer utilising various DFT functionals with the dTZ basis set in ethanol.

Solvent	**ETHANOL**	Bond length (Å)				Average bond length (Å)
Basis set	**dTZ**	R_1	R_2	R_3	R_4	
Functional	PBE	2.957	2.993	2.957	2.993	2.975
	PBE-D2	2.957	2.988	2.957	2.988	2.972
	ωB97X	2.797	3.135	2.919	2.944	2.949
	ωB97XD	2.907	2.970	2.907	2.970	2.938
	B971	2.938	2.975	2.938	2.975	2.956
	B97D	3.000	3.040	3.000	3.040	3.020
	BP86	2.967	3.003	2.967	3.003	2.985
	BP86-D2	2.968	2.999	2.968	2.999	2.983
	B3LYP	-	-	-	-	-
	B3LYP-D2	2.964	3.013	2.964	3.013	2.988
	TPSS	2.957	2.995	2.957	2.995	2.976
	TPSS-D2	2.958	2.992	2.958	2.992	2.975
	BLYP-D2	3.019	3.063	3.019	3.063	3.041
	PBE0	2.911	2.949	2.911	2.949	2.930
	M06	2.935	2.996	2.935	2.996	2.965
	M06-HF	2.810	2.859	2.810	2.859	2.834
	M06-2X	2.888	2.947	2.888	2.947	2.918
	LC-ωPBE	2.855	2.922	2.855	2.922	2.888
	B972	-	-	-	-	-
	X3LYP	2.964	2.994	2.964	2.994	2.979

Table S5 - Optimised and average bond lengths (Å) of the I_3^- dimer utilising various DFT functionals with the dTZ basis set in water.

Solvent	**WATER**	Bond length (Å)				Average bond length (Å)
Basis set	**dTZ**	R_1	R_2	R_3	R_4	
Functional	PBE	2.959	2.989	2.959	2.989	2.974
	PBE-D2	2.960	2.984	2.960	2.984	2.972
	ωB97X	2.782	3.169	2.965	2.899	2.954
	ωB97XD	2.916	2.959	2.916	2.959	2.938
	B971	2.942	2.970	2.942	2.970	2.956
	B97D	3.004	3.033	3.004	3.033	3.019
	BP86	2.969	2.999	2.969	2.999	2.984
	BP86-D2	2.971	2.995	2.971	2.995	2.983
	B3LYP	2.974	2.990	2.974	2.990	2.982
	B3LYP-D2	2.968	3.007	2.968	3.007	2.988
	TPSS	2.960	2.992	2.960	2.992	2.976
	TPSS-D2	2.961	2.987	2.961	2.987	2.974
	BLYP-D2	3.023	3.057	3.023	3.057	3.040
	PBE0	2.914	2.944	2.914	2.944	2.929
	M06	2.941	2.988	2.941	2.988	2.964
	M06-HF	2.814	2.854	2.814	2.854	2.834
	M06-2X	2.893	2.941	2.893	2.941	2.917
	LC-ωPBE	2.859	2.917	2.859	2.917	2.888
	B972	2.939	2.953	2.940	2.953	2.946
	X3LYP	2.967	2.990	2.967	2.990	2.979

Digital Supplementary Information

The attached CD contains all the Gaussian output files generated in this study, where files have been included in directories according to chapter. Filenames of the output files are descriptive of the theory and solvent used according to the following legend:

Chapter 3 (also Chapter 4, 5, 6)

The first part of the *.log filename indicates the system under investigation e.g. "I3_" or "lin_I3" indicates a single I_3^- ion and I_3^- dimer that was optimised, respectively. This is then usually followed by the method and basis set, "B3LYP_aug_cc_pVTZ_pp". The last part of the filename indicates the solvent, e.g. "SCRF_ethanol". If the "SCRF_" part is omitted in the file name it implies that the calculation has been done in the gas phase.

The filenames for the linear PES scans of the I_3^- dimer are indicated by a "2_I3_linear" and followed by the method and basis set, e.g. "MP2_cc_pVTZ_pp. Again, the presence of "SCRF_" indicates whether or not it has been performed in the gas phase or in solution.

Chapter 4

Example: 2_I3_4_SETHAB_VERT_B971_def2TZVP_OPT_I_LanL2DZ_x.log.

The "2_I3_" part indicates the amount of triiodides in the model, the "_4_" indicates there are four cations, "SETHAB" is the refcode. The "VERT" (or "lin") after the word "SETHAB" in the filename indicates the positions of the triiodides relative to one another. "B971" indicates the functional used, "_def2TZVP_OPT_I" indicates the def2-TZVP basis set has been used for the optimisation of the triiodide positions, whereas the the "LanL2DZ" (Gaussian uses D95V basis set for 1st row elements if LanL2DZ is selected as basis set) indicates the basis set used for the other atoms present in the optimisation.

The "EF_Z_10_130" indicates that an electric field is present (EF) and that the direction is along the Z-axis, with the "10_130" indicating the range of the strength of the electric field (10 = 0.001 au).

Chapter 7

Example: lin_I3_SETHA B_343_MP2_cc_pVTZ_pp_chk_wfx.log

"lin_I3_SETHAB" indicates that the geometry of an I_3^- dimer was obtained from the SETHAB crystal and a single point energy calculation of the dimer was performed. The "343" indicates that the dimer is surrounded by a point charge environment (where all the atoms have been replaced by point charges except for the dimer) where the expanded unit cell was expanded to $3 \times 4 \times 3$ in the crystallographic axes *a*, *b* and *c*. If the filename contains an "SCRF" it means that the triiodides are submerged in solution utilising the crystal structure geometry.

The following Gaussian output files are included in the digital supplementary information:

Chapter_3

DFT

I3_dimer

Ethanol

DFT_aug-cc-pVTZ-pp

lin_I3_B3LYP_aug_cc_pVTZ_pp_SCRF_ethanol.log

lin_I3_B3LYP_D2_aug_cc_pVTZ_pp_SCRF_ethanol_x.log

lin_I3_B971_aug_cc_pVTZ_pp_SCRF_ethanol_x.log

lin_I3_B972_aug_cc_pVTZ_pp_SCRF_ethanol_x_DIST_Pos_03.log

lin_I3_B97D_aug_cc_pVTZ_pp_SCRF_ethanol_x.log

lin_I3_BLYP_aug_cc_pVTZ_pp_SCRF_ethanol.log

lin_I3_BLYP_D2_aug_cc_pVTZ_pp_SCRF_ethanol.log

lin_I3_BP86_aug_cc_pVTZ_pp_SCRF_ethanol_DIST_Pos_03.log

lin_I3_BP86_D2_aug_cc_pVTZ_pp_SCRF_ethanol_DIST_Pos_03.log

lin_I3_LC-wPBE_aug_cc_pVTZ_pp_SCRF_ethanol_x.log

lin_I3_M062X_aug_cc_pVTZ_pp_SCRF_ethanol_x_DIST_Pos_03.log

lin_I3_M06_aug_cc_pVTZ_pp_SCRF_ethanol.log

lin_I3_M06HF_aug_cc_pVTZ_pp_SCRF_ethanol_x.log

lin_I3_PBE1PBE_aug_cc_pVTZ_pp_SCRF_ethanol.log

lin_I3_PBEPBE_aug_cc_pVTZ_pp_SCRF_ethanol.log

lin_I3_PBEPBE_D2_aug_cc_pVTZ_pp_SCRF_ethanol.log

lin_I3_TPSSTPSS_aug_cc_pVTZ_pp_SCRF_ethanol_FX.log

lin_I3_TPSSTPSS_D2_aug_cc_pVTZ_pp_SCRF_ethanol_FX.log

lin_I3_wB97X_aug_cc_pVTZ_pp_SCRF_ethanol_x_DIST_Pos_03.log

lin_I3_wB97XD_aug_cc_pVTZ_pp_SCRF_ethanol_x.log

lin_I3_X3LYP_aug_cc_pVTZ_pp_SCRF_ethanol.log

DFT_def2-TZVP

lin_I3_B3LYP_D2_def2TZVP_SCRF_ethanol.log

lin_I3_B3LYP_def2TZVP_SCRF_ethanol.log

lin_I3_B971_def2TZVP_SCRF_ethanol_FX.log

lin_I3_B972_def2TZVP_SCRF_ethanol_x.log

lin_I3_B97D_def2TZVP_SCRF_ethanol_x.log

lin_I3_BLYP_D2_def2TZVP_SCRF_ethanol.log

lin_I3_BLYP_def2TZVP_SCRF_ethanol.log

lin_I3_BP86_D2_def2TZVP_SCRF_ethanol.log

lin_I3_BP86_def2TZVP_SCRF_ethanol_x.log

lin_I3_LC-wPBE_def2TZVP_SCRF_ethanol_x.log

lin_I3_M062X_def2TZVP_SCRF_ethanol_x.log

lin_I3_M06_def2TZVP_SCRF_ethanol.log

lin_I3_M06HF_def2TZVP_SCRF_ethanol_x.log

lin_I3_PBE1PBE_def2TZVP_SCRF_ethanol_DIST_Pos_03.log

lin_I3_PBEPBE_D2_def2TZVP_SCRF_ethanol_x.log

lin_I3_PBEPBE_def2TZVP_SCRF_ethanol.log

lin_I3_TPSSTPSS_D2_def2TZVP_SCRF_ethanol.log

lin_I3_TPSSTPSS_def2TZVP_SCRF_ethanol.log

lin_I3_wB97XD_def2TZVP_SCRF_ethanol_x.log

lin_I3_wB97X_def2TZVP_SCRF_ethanol.log

lin_I3_X3LYP_def2TZVP_SCRF_ethanol.log

Water

DFT_aug-cc-pVTZ-pp

lin_I3_B3LYP_aug_cc_pVTZ_pp_SCRF_water_x.log

lin_I3_B3LYP_D2_aug_cc_pVTZ_pp_SCRF_water_x.log

lin_I3_B971_aug_cc_pVTZ_pp_SCRF_water.log

lin_I3_B972_aug_cc_pVTZ_pp_SCRF_water_x.log

lin_I3_B97D_aug_cc_pVTZ_pp_SCRF_water_x.log

lin_I3_BLYP_aug_cc_pVTZ_pp_SCRF_water_x.log

lin_I3_BLYP_D2_aug_cc_pVTZ_pp_SCRF_water_2x.log

lin_I3_BP86_aug_cc_pVTZ_pp_SCRF_water_x.log

lin_I3_BP86_D2_aug_cc_pVTZ_pp_SCRF_water_DIST_Pos_03_x.log

lin_I3_LC-wPBE_aug_cc_pVTZ_pp_SCRF_water_x.log

lin_I3_M062X_aug_cc_pVTZ_pp_SCRF_water_DIST_Pos_03.log

lin_I3_M06_aug_cc_pVTZ_pp_SCRF_water.log

lin_I3_M06HF_aug_cc_pVTZ_pp_SCRF_water_x.log

lin_I3_PBE1PBE_aug_cc_pVTZ_pp_SCRF_water.log

lin_I3_PBEPBE_aug_cc_pVTZ_pp_SCRF_water.log

lin_I3_PBEPBE_D2_aug_cc_pVTZ_pp_SCRF_water.log

lin_I3_TPSSTPSS_aug_cc_pVTZ_pp_SCRF_water_FX.log

lin_I3_TPSSTPSS_D2_aug_cc_pVTZ_pp_SCRF_water_FX.log

lin_I3_wB97X_aug_cc_pVTZ_pp_SCRF_water.log

lin_I3_wB97XD_aug_cc_pVTZ_pp_SCRF_water.log

lin_I3_X3LYP_aug_cc_pVTZ_pp_SCRF_water.log

DFT_def2-TZVP

lin_I3_B3LYP_D2_def2TZVP_SCRF_water.log

lin_I3_B3LYP_def2TZVP_SCRF_water.log

lin_I3_B971_def2TZVP_SCRF_water_x.log

lin_I3_B972_def2TZVP_SCRF_water_x.log

lin_I3_B97D_def2TZVP_SCRF_water_DIST_Pos_03.log

lin_I3_BLYP_D2_def2TZVP_SCRF_water.log

lin_I3_BLYP_def2TZVP_SCRF_water_DIST_Pos_03.log

lin_I3_BP86_D2_def2TZVP_SCRF_waterDIST_Pos_03.log

lin_I3_BP86_def2TZVP_SCRF_water_x.log

lin_I3_LC-wPBE_def2TZVP_SCRF_water_x.log

lin_I3_M062X_def2TZVP_SCRF_water_x.log

lin_I3_M06_def2TZVP_SCRF_water.log

lin_I3_M06HF_def2TZVP_SCRF_water.log

lin_I3_PBE1PBE_def2TZVP_SCRF_water_x.log

lin_I3_PBEPBE_D2_def2TZVP_SCRF_water.log

lin_I3_PBEPBE_def2TZVP_SCRF_water.log

lin_I3_TPSSTPSS_D2_def2TZVP_SCRF_water.log

lin_I3_TPSSTPSS_def2TZVP_SCRF_water.log

lin_I3_wB97XD_def2TZVP_SCRF_water.log

lin_I3_wB97X_def2TZVP_SCRF_water.log

lin_I3_X3LYP_def2TZVP_SCRF_water.log

I3_ion

Chloroform_and_n_Methylformamide

DFT_aug-cc-pVTZ-pp

I3_B97D_aug_cc_pVTZ_pp_SCRF_Chloroform.log

I3_B97D_aug_cc_pVTZ_pp_SCRF_n_Methyl_formamide_mix.log

I3_PBEPBE_D2_aug_cc_pVTZ_pp_SCRF_Chloroform.log

I3_PBEPBE_D2_aug_cc_pVTZ_pp_SCRF_n_Methyl_formamide_mix.log

I3_TPSSTPSS_D2_aug_cc_pVTZ_pp_SCRF_Chloroform.log

I3_TPSSTPSS_D2_aug_cc_pVTZ_pp_SCRF_n_Methyl_formamide_mix.log

DFT_def2-TZVP

I3_B97D_def2TZVP_SCRF_Chloroform.log

I3_B97D_def2TZVP_SCRF_n_Methyl_formamide_mix.log

I3_PBEPBE_D2_def2TZVP_SCRF_Chloroform.log

I3_PBEPBE_D2_def2TZVP_SCRF_n_Methyl_formamide_mix.log

I3_TPSSTPSS_D2_def2TZVP_SCRF_Chloroform.log

I3_TPSSTPSS_D2_def2TZVP_SCRF_n_Methyl_formamide_mix.log

Ethanol

DFT_aug-cc-pVTZ-pp

I3_B3LYP_aug_cc_pVTZ_pp_SCRF_ethanol_FX.log

I3_B3LYP_D2_aug_cc_pVTZ_pp_SCRF_ethanol_FX.log

I3_B971_aug_cc_pVTZ_pp_SCRF_ethanol.log

I3_B972_aug_cc_pVTZ_pp_SCRF_ethanol.log

I3_B97D_aug_cc_pVTZ_pp_ethanol.log

I3_BLYP_aug_cc_pVTZ_pp_SCRF_ethanol.log

I3_BLYP_D2_aug_cc_pVTZ_pp_SCRF_ethanol.log

I3_BP86_aug_cc_pVTZ_pp_SCRF_ethanol.log

I3_BP86_D2_aug_cc_pVTZ_pp_SCRF_ethanol_FX.log

I3_LC-wPBE_aug_cc_pVTZ_pp_SCRF_ethanol.log

I3_M062X_aug_cc_pVTZ_pp_SCRF_ethanol.log

I3_M06_aug_cc_pVTZ_pp_SCRF_ethanol.log

I3_M06HF_aug_cc_pVTZ_pp_SCRF_ethanol.log

I3_PBE1PBE_aug_cc_pVTZ_pp_SCRF_ethanol.log

I3_PBEPBE_aug_cc_pVTZ_pp_SCRF_ethanol_FX.log

I3_PBEPBE_D2_aug_cc_pVTZ_pp_SCRF_ethanol_FX.log

I3_TPSSTPSS_aug_cc_pVTZ_pp_SCRF_ethanol_FX.log

I3_TPSSTPSS_D2_aug_cc_pVTZ_pp_SCRF_ethanol_FX.log

I3_wB97X_aug_cc_pVTZ_pp_SCRF_ethanol.log

I3_wB97XD_aug_cc_pVTZ_pp_SCRF_ethanol.log

I3_X3LYP_def2TZVP_SCRF_ethanol_x.log

DFT_def2-TZVP

I3_B3LYP_D2_def2TZVP_SCRF_ethanol.log

I3_B3LYP_def2TZVP_SCRF_ethanol.log

I3_B971_def2TZVP_SCRF_ethanol.log

I3_B972_def2TZVP_SCRF_ethanol.log

I3_B97D_def2TZVP_SCRF_ethanol.log

I3_BLYP_D2_def2TZVP_SCRF_ethanol.log

I3_BLYP_def2TZVP_SCRF_ethanol.log

I3_BP86_D2_def2TZVP_SCRF_ethanol.log

I3_BP86_def2TZVP_SCRF_ethanol.log

I3_LC-wPBE_def2TZVP_SCRF_ethanol.log

I3_M062X_def2TZVP_SCRF_ethanol.log

I3_M06_def2TZVP_SCRF_ethanol.log

I3_M06HF_def2TZVP_SCRF_ethanol.log

I3_PBE1PBE_def2TZVP_SCRF_ethanol.log

I3_PBEPBE_D2_def2TZVP_SCRF_ethanol.log

I3_PBEPBE_def2TZVP_SCRF_ethanol.log

I3_TPSSTPSS_D2_def2TZVP_SCRF_ethanol.log

I3_TPSSTPSS_def2TZVP_SCRF_ethanol.log

I3_wB97XD_def2TZVP_SCRF_ethanol.log

I3_wB97X_def2TZVP_SCRF_ethanol.log

I3_X3LYP_def2TZVP_SCRF_ethanol_x.log

Gas Phase

DFT_aug-cc-pVTZ-pp

I3_B3LYP_aug_cc_pVTZ_pp_FX.log

I3_B3LYP_D2_aug_cc_pVTZ_pp_FX.log

I3_B971_aug_cc_pVTZ_pp.log

I3_B972_aug_cc_pVTZ_pp.log

I3_B97D_aug_cc_pVTZ_pp.log

I3_BLYP_aug_cc_pVTZ_pp.log

I3_BLYP_D2_aug_cc_pVTZ_pp.log

I3_BP86_aug_cc_pVTZ_pp.log

I3_BP86_D2_aug_cc_pVTZ_pp_FX.log

I3_LC-wPBE_aug_cc_pVTZ_pp.log

I3_M062X_aug_cc_pVTZ_pp.log

I3_M06_aug_cc_pVTZ_pp.log

I3_M06HF_aug_cc_pVTZ_pp.log

I3_PBE1PBE_aug_cc_pVTZ_pp.log

I3_PBEPBE_aug_cc_pVTZ_pp_FX.log

I3_PBEPBE_D2_aug_cc_pVTZ_pp_FX.log

I3_PBEPBE_D2_def2TZVP.log

I3_TPSSTPSS_aug_cc_pVTZ_pp_FX.log

I3_TPSSTPSS_D2_aug_cc_pVTZ_pp_FX.log

I3_wB97X_aug_cc_pVTZ_pp.log

I3_wB97XD_aug_cc_pVTZ_pp.log

I3_X3LYP_aug_cc_pVTZ_pp.log

DFT_def2-TZVP

I3_B3LYP_D2_def2TZVP.log

I3_b3lyp_def2TZVP.log

I3_B971_def2TZVP.log

I3_B972_def2TZVP.log

I3_B97D_def2TZVP.log

I3_BLYP_D2_def2TZVP.log

I3_BLYP_def2TZVP.log

I3_BP86_D2_def2TZVP.log

I3_BP86_def2TZVP.log

I3_LC-wPBE_def2TZVP.log

I3_M062X_def2TZVP.log

I3_M06_def2TZVP.log

I3_M06HF_def2TZVP.log

I3_PBE1PBE_def2TZVP.log

I3_PBEPBE_D2_def2TZVP.log

I3_PBEPBE_def2TZVP.log

I3_TPSSTPSS_D2_def2TZVP.log

I3_TPSSTPSS_def2TZVP.log

I3_wB97XD_def2TZVP.log

I3_wB97X_def2TZVP.log

I3_X3LYP_def2TZVP.log

Water

DFT_aug-cc-pVTZ-pp

I3_B3LYP_aug_cc_pVTZ_pp_SCRF_water_FX.log

I3_B3LYP_D2_aug_cc_pVTZ_pp_SCRF_water_FX.log

I3_B971_aug_cc_pVTZ_pp_SCRF_water.log

I3_B972_aug_cc_pVTZ_pp_SCRF_water.log

I3_B97D_aug_cc_pVTZ_pp_water.log

I3_BLYP_aug_cc_pVTZ_pp_SCRF_water.log

I3_BLYP_D2_aug_cc_pVTZ_pp_SCRF_water.log

I3_BP86_aug_cc_pVTZ_pp_SCRF_water.log

I3_BP86_D2_aug_cc_pVTZ_pp_SCRF_water_FX.log

I3_LC-wPBE_aug_cc_pVTZ_pp_SCRF_water.log

I3_M062X_aug_cc_pVTZ_pp_SCRF_water.log

I3_M06_aug_cc_pVTZ_pp_SCRF_water.log

I3_M06HF_aug_cc_pVTZ_pp_SCRF_water.log

I3_PBE1PBE_aug_cc_pVTZ_pp_SCRF_water.log

I3_PBEPBE_aug_cc_pVTZ_pp_SCRF_water_FX.log

I3_PBEPBE_D2_aug_cc_pVTZ_pp_SCRF_water_FX.log

I3_TPSSTPSS_aug_cc_pVTZ_pp_SCRF_water_FX.log

I3_TPSSTPSS_D2_aug_cc_pVTZ_pp_SCRF_water_FX.log

I3_wB97X_aug_cc_pVTZ_pp_SCRF_water.log

I3_wB97XD_aug_cc_pVTZ_pp_SCRF_water.log

I3_X3LYP_aug_cc_pVTZ_pp_SCRF_water.log

DFT_def2-TZVP

I3_B3LYP_D2_def2TZVP_SCRF_water.log

I3_B3LYP_def2TZVP_SCRF_water.log

I3_B971_def2TZVP_SCRF_water.log

I3_B972_def2TZVP_SCRF_water.log

I3_B97D_def2TZVP_SCRF_water.log

I3_BLYP_D2_def2TZVP_SCRF_water.log

I3_BLYP_def2TZVP_SCRF_water.log

I3_BP86_D2_def2TZVP_SCRF_water.log

I3_BP86_def2TZVP_SCRF_water.log

I3_LC-wPBE_def2TZVP_SCRF_water.log

I3_M062X_def2TZVP_SCRF_water.log

I3_M06_def2TZVP_SCRF_water.log

I3_M06HF_def2TZVP_SCRF_water.log

I3_PBE1PBE_def2TZVP_SCRF_water.log

I3_PBEPBE_D2_def2TZVP_SCRF_water.log

I3_PBEPBE_def2TZVP_SCRF_water.log

I3_TPSSTPSS_D2_def2TZVP_SCRF_water.log

I3_TPSSTPSS_def2TZVP_SCRF_water.log

I3_wB97XD_def2TZVP_SCRF_water.log

I3_wB97X_def2TZVP_SCRF_water.log

I3_X3LYP_def2TZVP_SCRF_water.log

PES_scans

Gas Phase

2_I3_linear_scan_B97D_aug_cc_pVTZ_pp.log

2_I3_linear_scan_PBE_aug_cc_pVTZ_pp.log

2_I3_linear_scan_PBE_D2_aug_cc_pVTZ_pp.log

Solution

2_I3_linear_scan_PBE_D2_aug_cc_pVTZ_pp_SCRF_chloroform.log

2_I3_linear_scan_PBE_D2_aug_cc_pVTZ_pp_SCRF_ethanol.log

2_I3_linear_scan_PBE_D2_aug_cc_pVTZ_pp_SCRF_n_Methyl_formamide_mix.log

2_I3_linear_scan_PBE_D2_aug_cc_pVTZ_pp_SCRF_water.log

WFT

I3_dimer

CCSD

Single-Point Energy Calculations

lin_I3_CCSD_aug_cc_pVTZ_pp_SCRF_Chlorofrom_x.log

lin_I3_CCSD_aug_cc_pVTZ_pp_SCRF_ethanol_2x.log

lin_I3_CCSD_aug_cc_pVTZ_pp_SCRF_ethanol_x.log

lin_I3_CCSD_aug_cc_pVTZ_pp_SCRF_n_Methyl_formamide_mix_x.log

lin_I3_CCSD_aug_cc_pVTZ_pp_SCRF_water_2x.log

lin_I3_CCSD_aug_cc_pVTZ_pp_SCRF_water_x.log

lin_I3_CCSD_aug_cc_pVTZ_pp_x.log

MP2

Gas Phase

lin_I3_BSSE_MP2_aug_cc_pVTZ_pp_x.log

lin_I3_MP2_aug_cc_pVTZ_pp_FX.log

Solution

lin_I3_MP2_aug_cc_pVDZ_pp_SCRF_ethanol_x.log

lin_I3_MP2_aug_cc_pVDZ_pp_SCRF_water_FX.log

lin_I3_MP2_aug_cc_pVTZ_pp_SCRF_ethanol_x.log

lin_I3_MP2_aug_cc_pVTZ_pp_SCRF_water_FX_DIST_Pos_03.log

lin_I3_MP2_cc_pVDZ_pp_SCRF_ethanol_x.log

lin_I3_MP2_cc_pVDZ_pp_SCRF_water_FX_DIST_pos_03.log

lin_I3_MP2_cc_pVTZ_pp_SCRF_ethanol_x.log

lin_I3_MP2_cc_pVTZ_pp_SCRF_water_FX_x.log

lin_I3_MP2_def2TZVP_SCRF_ethanol.log

lin_I3_MP2_def2TZVP_SCRF_water.log

I3_ion

CCSD

Gas Phase

Optimisation

I3_CCSD_aug_cc_pVTZ_pp_3x.log

Single-Point Energy Calculations

I3_CCSD_aug_cc_pVTZ_pp_2x.log

I3_CCSD_aug_cc_pVTZ_pp_x.log

Solution

Optimisation

I3_CCSD_aug_cc_pVTZ_pp_SCRF_chloroform_2x.log

I3_CCSD_aug_cc_pVTZ_pp_SCRF_ethanol_2x.log

I3_CCSD_aug_cc_pVTZ_pp_SCRF_n_Methyl_formamide_mix_2x.log

I3_CCSD_aug_cc_pVTZ_pp_SCRF_water_3x.log

Single-Point Energy Calculations

I3_CCSD_aug_cc_pVTZ_pp_SCRF_chloroform_x.log

I3_CCSD_aug_cc_pVTZ_pp_SCRF_ethanol.log

I3_CCSD_aug_cc_pVTZ_pp_SCRF_ethanol_x.log

I3_CCSD_aug_cc_pVTZ_pp_SCRF_n_Methyl_formamide_mix_x.log

I3_CCSD_aug_cc_pVTZ_pp_SCRF_water_2x.log

I3_CCSD_aug_cc_pVTZ_pp_SCRF_water_x.log

MP2

Gas Phase

I3_MP2_aug_cc_pVDZ_pp_FX.log

I3_MP2_aug_cc_pVTZ_pp_FX.log

I3_MP2_cc_pVDZ_pp_FX.log

I3_MP2_cc_pVTZ_pp_FX.log

I3_MP2_def2TZVP.log

Solution

I3_MP2_aug_cc_pVDZ_pp_SCRF_ethanol_FX.log

I3_MP2_aug_cc_pVDZ_pp_SCRF_water_FX.log

I3_MP2_aug_cc_pVTZ_pp_SCRF_Chloroform.log

I3_MP2_aug_cc_pVTZ_pp_SCRF_ethanol_FX.log

I3_MP2_aug_cc_pVTZ_pp_SCRF_n_Methyl_formamide_mix.log

I3_MP2_aug_cc_pVTZ_pp_SCRF_water_FX.log

I3_MP2_cc_pVDZ_pp_SCRF_ethanol_FX.log

I3_MP2_cc_pVDZ_pp_SCRF_water_FX.log

I3_MP2_cc_pVTZ_pp_FX.log

I3_MP2_cc_pVTZ_pp_SCRF_Chloroform.log

I3_MP2_cc_pVTZ_pp_SCRF_ethanol_FX.log

I3_MP2_cc_pVTZ_pp_SCRF_n_Methyl_formamide_mix.log

I3_MP2_cc_pVTZ_pp_SCRF_water_FX.log

I3_MP2_def2TZVP_SCRF_ethanol.log

I3_MP2_def2TZVP_SCRF_water_x.log

PES_scans

Gas Phase

2_I3_linear_scan_MP2_aug_cc_pVTZ_pp.log

2_I3_linear_scan_MP2_cc_pVTZ_pp.log

Solution

2_I3_linear_scan_MP2_cc_pVTZ_pp_SCRF_chloroform.log

2_I3_linear_scan_MP2_cc_pVTZ_pp_SCRF_ethanol.log

2_I3_linear_scan_MP2_cc_pVTZ_pp_SCRF_n_Methyl_formamide_mix.log

2_I3_linear_scan_MP2_cc_pVTZ_pp_SCRF_water.log

Chapter_4

Crystal Optimisation

I3_gas-phase

I3_b3lyp_3-21G.log

I3_B971_def2TZVP.log

I3_B97D_3-21G.log

I3_HF_3-21G.log

I3_MP2_3-21G.log

I3_PBEPBE_D2_def2TZVP.log

Optimisations_Crystal_1

I3_2_SETHAB_b3lyp_3-21G_OPT_I_x.log

I3_2_SETHAB_B971_def2TZVP_OPT_I_LanL2DZ_x.log

I3_2_SETHAB_B97D_3-21G_OPT_I_x.log

I3_2_SETHAB_HF_3-21G_OPT_I.log

I3_2_SETHAB_MP2_3-21G_OPT_I_x.log

Optimisations_Crystal_2

2_I3_3_SETHAB_b3lyp_3-21G_OPT_I_x.log

2_I3_3_SETHAB_B971_def2TZVP_OPT_I_LanL2DZ_x.log

2_I3_3_SETHAB_HF_3-21G_OPT_I_x.log

Optimisations_Crystal_3

2_I3_4_SETHAB_VERT_b3lyp_3-21G_OPT_I_x.log

2_I3_4_SETHAB_VERT_B971_def2TZVP_OPT_I_LanL2DZ_x.log

2_I3_4_SETHAB_VERT_HF_3-21G_OPT_I_x.log

Optimisations_Crystal_4

2_I3_4_SETHAB_lin_B971_def2TZVP_OPT_I_LanL2DZ_new_x.log

2_I3_4_SETHAB_lin_PBE_D2_def2TZVP_OPT_I_LanL2DZ.log

Electric Field Optimisations

I3_dimer

electric_field_y-direction

lin_I3_MP2_aug_cc_pVDZ_pp_EF_X_10_130.log

lin_I3_MP2_aug_cc_pVDZ_pp_EF_X_2_8.log

lin_I3_MP2_aug_cc_pVDZ_pp_EF_X_4_8.log

lin_I3_MP2_aug_cc_pVTZ_pp_EF_X_10_x.log

lin_I3_MP2_aug_cc_pVTZ_pp_EF_X_2_8.log

lin_I3_MP2_aug_cc_pVTZ_pp_EF_X_4_8.log

lin_I3_MP2_cc_pVDZ_pp_EF_X_10_130.log

lin_I3_MP2_cc_pVDZ_pp_EF_X_2_8.log

lin_I3_MP2_cc_pVDZ_pp_EF_X_4_8.log

lin_I3_MP2_cc_pVTZ_pp_EF_X_10_x.log

lin_I3_MP2_cc_pVTZ_pp_EF_X_2_8.log

lin_I3_MP2_cc_pVTZ_pp_EF_X_4_8.log

electric_field_z-direction

lin_I3_MP2_aug_cc_pVDZ_pp_EF_Z_10_130.log

lin_I3_MP2_aug_cc_pVDZ_pp_EF_Z_50_130.log

lin_I3_MP2_aug_cc_pVTZ_pp_EF_Z_10_130.log

lin_I3_MP2_aug_cc_pVTZ_pp_EF_Z_50_130.log

lin_I3_MP2_cc_pVDZ_pp_EF_Z_10_130.log

lin_I3_MP2_cc_pVDZ_pp_EF_Z_50_130.log

lin_I3_MP2_cc_pVTZ_pp_EF_Z_10_130.log

lin_I3_MP2_cc_pVTZ_pp_EF_Z_50_130.log

I3_ion

electric_field_y-direction

I3_MP2_aug_cc_pVDZ_pp_EF_X_10_210.log

I3_MP2_aug_cc_pVDZ_pp_EF_X_2_8.log

I3_MP2_aug_cc_pVTZ_pp_EF_X_10_210.log

I3_MP2_aug_cc_pVTZ_pp_EF_X_2_8.log

I3_MP2_cc_pVDZ_pp_EF_X_10_210.log

I3_MP2_cc_pVDZ_pp_EF_X_2_8.log

I3_MP2_cc_pVTZ_pp_EF_X_10_210.log

I3_MP2_cc_pVTZ_pp_EF_X_2_8.log

electric_field_z-direction

I3_MP2_aug_cc_pVDZ_pp_EF_Z_10_210.log

I3_MP2_aug_cc_pVTZ_pp_EF_Z_10_210.log

I3_MP2_cc_pVDZ_pp_EF_Z_10_210.log

I3_MP2_cc_pVTZ_pp_EF_Z_10_210.log

Chapter_5

B97D

I3_dimer

lin_I3_B97D_6_311Gss_SCRF_Chloroform.log

lin_I3_B97D_6_311Gss_SCRF_ethanol.log

lin_I3_B97D_6_311Gss_SCRF_n_Methyl_formamide_mix.log

lin_I3_B97D_6_311Gss_SCRF_water.log

I3_ion

I3_B97D_6_311Gss_chk_wfn.log

I3_B97D_6_311Gss_SCRF_chloroform_chk_wfn.log

I3_B97D_6_311Gss_SCRF_ethanol_chk_wfn.log

I3_B97D_6_311Gss_SCRF_n-Methyl_formamide_mix_chk_wfn.log

I3_B97D_6_311Gss_SCRF_water_chk_wfn.log

MP2

I3_ion

I3_MP2_6_311Gss_chk_wfn.log

I3_MP2_6_311Gss_SCRF_chloroform_chk_wfn.log

I3_MP2_6_311Gss_SCRF_ethanol_chk_wfn.log

I3_MP2_6_311Gss_SCRF_n-Methyl_formamide_mix_chk_wfn.log

I3_MP2_6_311Gss_SCRF_water_chk_wfn.log

PBE-D2

I3_dimer

lin_I3_PBE_D2_6_311Gss_SCRF_Chloroform.log

lin_I3_PBE_D2_6_311Gss_SCRF_ethanol.log

lin_I3_PBE_D2_6_311Gss_SCRF_n_Methyl_formamide_mix.log

lin_I3_PBE_D2_6_311Gss_SCRF_water.log

I3_ion

I3_PBEPBE_D2_6_311Gss_chk_wfn.log

I3_PBEPBE_D2_6_311Gss_SCRF_chloroform_chk_wfn.log

I3_PBEPBE_D2_6_311Gss_SCRF_ethanol_chk_wfn.log

I3_PBEPBE_D2_6_311Gss_SCRF_n-Methyl_formamide_mix_chk_wfn.log

I3_PBEPBE_D2_6_311Gss_SCRF_water_chk_wfn.log

TPSS

I3_dimer

lin_I3_TPSS_6_311Gss_SCRF_Chloroform.log

lin_I3_TPSS_6_311Gss_SCRF_Ethanol.log

lin_I3_TPSS_6_311Gss_SCRF_n_Methyl_formamide_mix.log

lin_I3_TPSS_6_311Gss_SCRF_Water.log

I3_ion

I3_TPSS_6_311Gss_chk_wfn.log

I3_TPSS_6_311Gss_SCRF_chloroform_chk_wfn.log

I3_TPSS_6_311Gss_SCRF_ethanol_chk_wfn.log

I3_TPSS_6_311Gss_SCRF_n-Methyl_formamide_mix_chk_wfn.log

I3_TPSS_6_311Gss_SCRF_water_chk_wfn.log

TPSS-D2

I3_dimer

lin_I3_TPSS_6_311Gss_D2_SCRF_n_Methyl_formamide_mix.log

lin_I3_TPSS_D2_6_311Gss_SCRF_Chloroform.log

lin_I3_TPSS_D2_6_311Gss_SCRF_Ethanol.log

lin_I3_TPSS_D2_6_311Gss_SCRF_Water.log

I3_ion

I3_TPSS_D2_6_311Gss_chk_wfn.log

I3_TPSS_D2_6_311Gss_SCRF_chloroform_chk_wfn.log

I3_TPSS_D2_6_311Gss_SCRF_ethanol_chk_wfn.log

I3_TPSS_D2_6_311Gss_SCRF_n-Methyl_formamide_mix_chk_wfn.log

I3_TPSS_D2_6_311Gss_SCRF_water_chk_wfn.log

Chapter_6

I3_dimer

DFT

lin_I3_PBE_D2_aug_cc_pVTZ_pp_SCRF_n_Methyl_formamide_chk_wfx.log

lin_I3_TPSS_D2_aug_cc_pVTZ_pp_SCRF_n_Methyl_formamide_chk_wfx.log

WFT

lin_I3_MP2_aug_cc_pVTZ_pp_chk_wfx.log

lin_I3_MP2_aug_cc_pVTZ_pp_SCRF_chloroform_chk_wfx.log

lin_I3_MP2_aug_cc_pVTZ_pp_SCRF_ethanol_chk_wfx.log

lin_I3_MP2_aug_cc_pVTZ_pp_SCRF_n_Methyl_formamide_chk_wfx.lo

lin_I3_MP2_aug_cc_pVTZ_pp_SCRF_water_chk_wfx.log

I3_ion

DFT

I3_B3LYP_aug_cc_pVTZ_pp_chk_wfx.log

I3_BLYP_aug_cc_pVTZ_pp_chk_wfx.log

I3_LC_wPBE_aug_cc_pVTZ_pp_chk_wfx.log

I3_M06_2X_aug_cc_pVTZ_pp_chk_wfx.log

I3_M06HF_aug_cc_pVTZ_pp_chk_wfx.log

I3_PBE_D2_aug_cc_pVTZ_pp_chk_wfx.log

I3_TPSS_D2_aug_cc_pVTZ_pp_chk_wfx.log

I3_wB97X_aug_cc_pVTZ_pp_chk_wfx.log

WFT

MP2_aug-cc-pVTZ-pp

I3_MP2_aug_cc_pVTZ_pp_chk_wfx.log

I3_MP2_aug_cc_pVTZ_pp_SCRF_chloroform_chk_wfx.log

I3_MP2_aug_cc_pVTZ_pp_SCRF_ethanol_chk_wfx.log

I3_MP2_aug_cc_pVTZ_pp_SCRF_n_Methyl_formamide_chk_wfx.log

I3_MP2_aug_cc_pVTZ_pp_SCRF_water_chk_wfx.log

Chapter_7

AIM

lin_I3_SETHAB_343_MP2_cc_pVTZ_pp_chk_wfx.log

lin_I3_SETHAB_MP2_cc_pVTZ_pp_chk_wfx.log

lin_I3_SETHAB_MP2_cc_pVTZ_pp_SCRF_n_methylformamide_mix_chk_wfx.log

Charge_sets

Charge_set_1

I3_SETHAB_333_B97D_6_311Gss_chk_wfn.log

I3_SETHAB_333_PBE_D2_6_311Gss_chk_wfn.log

Charge_set_2

I3_SETHAB_333_B97D_6_311Gss_chk_wfn_x.log

I3_SETHAB_333_PBE_D2_6_311Gss_chk_wfn_x.log

Charge_set_3

I3_SETHAB_333_B97D_6_311Gss_chk_wfn_2x.log

I3_SETHAB_333_PBE_D2_6_311Gss_chk_wfn_2x.log

Solution

B97D

I3_dimer

lin_I3_B97D_6_311Gss_SCRF_Chloroform.log

lin_I3_B97D_6_311Gss_SCRF_ethanol.log

lin_I3_B97D_6_311Gss_SCRF_n_Methyl_formamide_mix.log

lin_I3_B97D_6_311Gss_SCRF_water.log

I3_ion

I3_B97D_6_311Gss_SCRF_chloroform_chk_wfn.log

I3_B97D_6_311Gss_SCRF_ethanol_chk_wfn.log

I3_B97D_6_311Gss_SCRF_n-Methyl_formamide_mix_chk_wfn.log

I3_B97D_6_311Gss_SCRF_water_chk_wfn.log

PBE-D2

I3_dimer

lin_I3_PBE_D2_6_311Gss_SCRF_Chloroform.log

lin_I3_PBE_D2_6_311Gss_SCRF_ethanol.log

lin_I3_PBE_D2_6_311Gss_SCRF_n_Methyl_formamide_mix.log

lin_I3_PBE_D2_6_311Gss_SCRF_water.log

I3_ion

I3_PBEPBE_D2_6_311Gss_SCRF_chloroform_chk_wfn.log

I3_PBEPBE_D2_6_311Gss_SCRF_ethanol_chk_wfn.log

I3_PBEPBE_D2_6_311Gss_SCRF_n-Methyl_formamide_mix_chk_wfn.log

I3_PBEPBE_D2_6_311Gss_SCRF_water_chk_wfn.log

Table_7.1_Fragments

1_SETHAB_MP2_aug_cc_pVTZ_pp_I_3_21G.log

2_I3_SETHAB_VERT_MP2_aug_cc_pVTZ_pp_I_3_21G.log

I3_SETHAB_A_MP2_aug_cc_pVTZ_pp_I_3_21G.log

I3_SETHAB_B_MP2_aug_cc_pVTZ_pp_I_3_21G.log

I3_SETHAB_C_MP2_aug_cc_pVTZ_pp_I_3_21G.log

I3_SETHAB_D_MP2_aug_cc_pVTZ_pp_I_3_21G.log

I3_SETHAB_MP2_aug_cc_pVTZ_pp_SP.log

Table_7.6

    DFT

        I3_dimer

2_I3_SETHAB_lin_B97D_aug_cc_pVTZ_pp_SCRF_n_methformamide_mix.log

2_I3_SETHAB_lin_PBE_D2_aug_cc_pVTZ_pp_SCRF_n_methformamide_mix.log

        I3_ion

        I3_SETHAB_B97D_aug_cc_pVTZ_pp_SCRF_n_methformamide_mix.log

I3_SETHAB_PBE_D2_aug_cc_pVTZ_pp_SCRF_n_methformamide_mix.log

MP2

        I3_dimer

2_I3_SETHAB_lin_MP2_aug_cc_pVTZ_pp_SCRF_n_methformamide_mix.log

2_I3_SETHAB_lin_MP2_cc_pVTZ_pp_SCRF_n_methformamide_mix.log

        I3_ion

        I3_SETHAB_MP2_aug_cc_pVTZ_pp_SCRF_n_methformamide_mix.log

        I3_SETHAB_MP2_cc_pVTZ_pp_SCRF_n_methformamide_mix.log